VERSLAGEN EN VERHANDELINGEN

REPORTS AND TRANSACTIONS

NATIONAAL LUCHT- EN RUIMTEVAART-LABORATORIUM

NATIONAL AERO- AND ASTRONAUTICAL RESEARCH INSTITUTE

AMSTERDAM

*

XXX - 1965

PREFACE

This volume of Reports and Transactions contains a selection of reports completed in recent years.
The investigations reported in TR G.28, TR G.32 and TR T.83 have been performed under contract for the Netherlands Aircraft Development Board (NIV). Reports TR W.7 and TR W.8 have been prepared for the Ministry of Defence (Air Force). The permission for publication is herewith acknowledged.
Reports MP.216 and MP.222 contain the results of an investigation initiated and sponsored by the Netherlands Department of Civil Aviation and carried out under supervision of the Study Group on Airport Lighting.
In addition to the reports which are collected at more or less regular intervals in the volumes of Reports and Transactions, numerous others are published on subjects studied by the NLR.
A complete list of publications issued from 1921 through 1963 is available upon request.

Amsterdam, November 1965

A. J. Marx

(Director)

CONTENTS

C.C.L. Class. D 023: D 201

REPORT NLR-TR G. 28

Determination of shapes for minimum drag for a given lift and base area in linearized supersonic flow*)

by

F. van der Walle and P. J. Zandbergen

Summary

This report presents a new method to find shapes that attain minimum wave drag under certain constraints. The constraints considered here are given values for the base area and the lift. The configuration is assumed to be embedded in a volume enclosed by two opposing circular Mach cones, one going through the most forward point of the configuration, the other through the rim of the base. The flow field inside this volume is entirely governed by the perturbation velocities on the Mach cone through the base. In fact, the method deals with the procedure to determine the value of these velocities. Once the velocity distribution along the Mach cone is known the flow field and thus the shape of possible configurations can be found by applying characteristic methods.

Two cases are considered; in the first only the value of the base area is prescribed, while in the second also the lift is given. As an example, the shape and the axis inclinations of a possible ring-wing configuration are calculated.

The analysis is based on linearized supersonic flow theory. However, the method can also be adapted to non-linear flows around shapes with circular cross-sections.

This investigation has been performed under contract with the Netherlands Aircraft Development Board.

Contents

List of symbols

A	— projected base area
a	— ratio of ring-wing lift and total lift
b	— distance between F and the center of pressure (see figure 1)
$B(x)$	— source strength
c	— ring-wing chord
$c_1 \ldots c_6$	— constants
cn	— Jacobian elliptic function
c_{p_2}	— pressure coefficient
d	— diameter of a circular base area
D	— drag
E	— Legendre's incomplete elliptic integral of the second kind
i	— axis inclination
K	— complete elliptic integral of the first kind
L	— lift
l	— length of straight line joining Mach cone vertices (see figure 1)
l_F	— length of fuselage
M	— Mach number

*) This report is a revised version of report G.10, completed in August '58 and recently declassified.

$\mathscr{M}$	— moment about point F (see figure 1)	u_1	— incomplete elliptic integral of the first kind
m	— mass flow	V_N	— velocity normal to Mach cone
n	— $= \dfrac{L}{\rho_1 U_1^2 R_c^2}$	x	— axial coordinate
p	— pressure	y	— $=x-x_1$
$q=\frac{1}{2}\rho_1 U_1^2$	— dynamic pressure	β	— $=\sqrt{M_1^2-1}$
r	— radius	η	— variation of φ
R	— ring-wing radius	λ	— constant
R_c	— radius of intersecting circle of two Mach cones	μ	— Mach angle
R_E	— radius of base contour	Π	— Legendre's integral of the third kind
S	— surface of Mach cone	ρ	— density
sn	— Jacobian elliptic function	φ	— $=rw_i$
U	— axial velocity	$\Delta\varphi$	— $=\varphi_{\text{outside}}-\varphi_{\text{inside}}$
V	— radial velocity	ψ	— meridian angle
W	— tangential velocity		
u	— $=u_0+u_i \cos\psi = \beta^2 \dfrac{U_2-U_1}{U_1}$		
v	— $=v_0+v_i \cos\psi = \beta \dfrac{V_2}{U_1}$		
w	— $=w_0+w_i \sin\psi = \beta \dfrac{W_2}{U_1}$		

Indices

0	applies to minimum drag case
1	applies to forward Mach cone
2	applies to aft Mach cone
i	applies to minimum induced drag case
outside	applies to outside surface or ring wing
inside	applies to inside surface of ring wing

1 Introduction

One of the problems that has always been a challenge to the aerodynamicist is to find shapes that attain a low drag under certain constraints. Especially if a configuration is considered that flies at supersonic speed this problem becomes important. The reason is that in that case a form of drag occurs, which does not exist at subsonic speed. This is the wave drag, generated in fact by the shockwaves, which are one of the more spectacular aspects of supersonic flow. It will be evident that the search has been to find methods to reduce this drag.

Now, fortunately, the problem of finding shapes for minimum wave drag is not so complicated as, say, finding shapes for minimum viscous drag. This explains why much work has been done on it, particularly as far as axially symmetric bodies are concerned. In the latter case, most of the solutions are obtained by using the concept of a potential field as generated by a distribution of singularities along the axis of the body. The shape of this body is usually found by solving an integral equation by purely analytical methods. (see for instance ref. 1).*)

However, such methods are only applicable to rather simple problems and give rise to great difficulties for more complicated shapes. In order to escape these difficulties one would like to have a different approach to the problem of finding shapes for minimum wave drag, giving rise to a formulation of the optimum conditions which even in complicated cases lead to a simple calculation procedure for finding the shape. Now this approach can be found by considering the following arguments.

It is known that the flow field around a given axially symmetric body with or without axis inclination can be found by using linearized methods of characteristics (refs. 2 and 3). It is further known that the flow field can be calculated if the velocities along two characteristics which intersect each other are given. Now the conditions along the characteristic surface through the vertex of the body are given by the fact that the incoming stream is uniform. If it were possible to express the optimum conditions in terms of the perturbation velocities along a characteristic surface intersecting the first one, it would be possible to construct the flow field inside these characteristic surfaces, which in its turn determines the shape of the optimum body. The purpose of this report is to show that this approach is indeed successful and to present some results found by this new method.

The optimum shape will be determined for a configuration that lies within two circular Mach cones. The straight line joining the vertices is assumed to be parallel to the undisturbed stream. The base contour is a closed curve that lies on the surface of the aft Mach cone. It is not assumed beforehand that the base area is flat, only its projection on a plane perpendicular to the direction of the undisturbed stream has a prescribed value A. Owing to the presence of a body-wing system within the volume enclosed by the two Mach cones disturbance velocities will be generated on the surface of the aft Mach cone. Applying the momentum theorem to the enclosed volume, the lift L, the drag D and the moment $\mathscr{M}$ can be expressed as integrals along the aft Mach cone. The problem which will now be investigated is to determine the conditions for minimum drag when the lift and the base area

*) Needless to say that all these problems are solved by using the linearized potential equation. This equation is also the base of the investigations described in this report.

have prescribed values. This results in a number of requirements for the disturbance velocities on the aft Mach cone.

When the drag is minimized the following conditions for the disturbance velocities have to be satisfied:

a) The mass of air flowing through the forward Mach cone must be equal to that flowing through the aft Mach cone.

b) A suitable combination of the equations of motion and the continuity equation.

The reason for the choice of the particular control volume bounded by two opposing Mach cones is, in fact, that the last condition furnishes equations for the disturbance velocities and its derivatives along the Mach cone only. This makes it possible to calculate the distribution of these velocities along the control surface explicitly.

The report includes two main sections.

Section 2 derives the expressions for the lift, the drag and the moment as found by applying the momentum theorem and gives the equation for the mass flow together with the characteristic equations along the aft Mach cone.

Section 3 consists of two parts. In the first the optimum conditions along the aft Mach cone are derived for purely axially symmetric flow; thus the lift L equals zero, while the base area A has a prescribed value. In the second part the case is considered when also the lift L has a prescribed value. In both cases the results are elucidated by calculating an example.

2 Derivation of the expressions for the lift, the drag, the moment, the mass flow and of the characteristic equations

In this section the expressions for the drag, the lift and the moment are derived by using momentum theorems. It is shown that these quantities can be written as integrals over functions of the disturbance velocities on the aft Mach cone. A similar expression is derived for the base area by using the mass flow equation, while furthermore the so-called characteristic equations are established.

The coordinate system has been defined in figure 1. The cylindrical coordinates of a point P are: x, r and ψ.

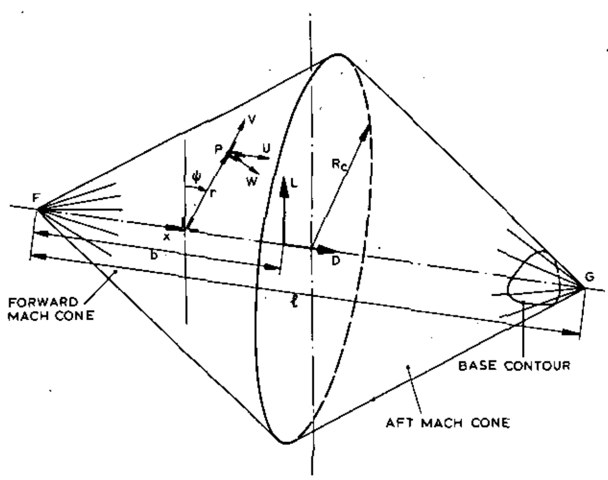

Fig. 1. Definition of the coordinate system.

The velocities in a point P are:

a) the axial velocity U,

b) the radial velocity V,

c) the tangential velocity W.

The conditions in the undisturbed stream will be indicated by an index 1, those on the aft Mach cone by an index 2.

Applying the momentum theorem to the air within the control volume, the following expressions are obtained for the lift L, and the drag D:

$$L+\int_{S_1} p_1 \cos\mu \cos\psi \, dS + \int_{S_2} p_2 \cos\mu \cos\psi \, dS = \int_{S_2} \rho_2 V_{N_2}(W_2 \sin\psi - V_2 \cos\psi) dS . \quad (1)$$

$$D+p_1 \cdot A + \int_{S_2} p_2 \sin\mu dS - \int_{S_1} p_1 \sin\mu dS = \int_{S_1} \rho_1 V_{N_1} U_1 dS - \int_{S_2} \rho_2 V_{N_2} U_2 dS = -\int_{S_2} \rho_2 V_{N_2}(U_2 - U_1) dS . \quad (2)$$

The term $p_1 \cdot A$ represents the force due to a pressure p_1 on the base area, while D is the drag without base drag and friction drag.

Applying the moment of momentum theorem, the following expression for the moment $\mathcal{M}=L\cdot b$ is found:

$$L\cdot b+\int_{S_2}(p_2-p_1)(-r\cos\psi\sin\mu+x\cos\psi\cos\mu)\mathrm{d}S=\int_{S_2}\rho_2 V_{N_2}(U_2 r\cos\psi-V_2 x\cos\psi+W_2 x\sin\psi)\mathrm{d}S \quad (3)$$

Here b is the distance between F and the center of pressure (see figure 1). In the above formula the following symbols are used:

p = pressure
ρ = density
S_1 = surface of forward Mach cone
S_2 = surface of aft Mach cone outside of base contour
V_{N_1} = velocity normal to surface of forward Mach cone (positive when directed inwards)
$\cos\mu=\dfrac{\beta}{\sqrt{\beta^2+1}}$ and $\sin\mu=\dfrac{1}{\sqrt{\beta^2+1}}$, while $\beta=\sqrt{M_1^2-1}$.
V_{N_2} = velocity normal to surface of aft Mach cone (positive when directed outwards)

In addition, we have:

$$V_{N_1}=U_1\sin\mu \quad (4)$$

$$V_{N_2}=U_2\sin\mu+V_2\cos\mu \quad (5)$$

$$\int_{S_1}p_1\cos\mu\cos\psi\,\mathrm{d}S=\int_{S_2}p_1\cos\mu\cos\psi\,\mathrm{d}S=0 \quad (6)$$

$$c_{p_2}=\frac{p_2-p_1}{q}=-2\frac{U_2-U_1}{U_1}-\left(\frac{V_2}{U_1}\right)^2+\beta^2\left(\frac{U_2-U_1}{U_1}\right)^2-\left(\frac{W_2}{U_1}\right)^2 \quad (7)$$

with:

$$q=\tfrac{1}{2}\rho_1 U_1^2 \quad (8)$$

$$\rho_2=\rho_1\left(1-M_1^2\frac{U_2-U_1}{U_1}\right) \quad (9)$$

$$x=2\beta R_c-\beta r \quad (10)$$

Substitution of equations (4)–(10) included in equations (1), (2) and (3) and introduction of the dimensionless quantities:

$$u=\beta^2\frac{U_2-U_1}{U_1} \quad (11)\text{a}$$

$$v=\beta\frac{V_2}{U_1} \quad (11)\text{b}$$

$$w=\beta\frac{W_2}{U_1} \quad (11)\text{c}$$

yields, when higher-order terms are neglected:
for the lift:

$$\frac{L}{\rho_1 U_1^2}=\frac{1}{\beta\sqrt{\beta^2+1}}\int_{S_2}\{(u-v)\cos\psi+w\sin\psi\}\mathrm{d}S\ ; \quad (12)$$

for the drag:

$$\frac{D}{\rho_1 U_1^2}=\frac{1}{2\beta^2\sqrt{\beta^2+1}}\int_{S_2}\{(u-v)^2+w^2\}\mathrm{d}S\ ; \quad (13)$$

for the distance b:

$$\frac{b\cdot L}{\rho_1 U_1^2}=\frac{1}{\sqrt{\beta^2+1}}\int_{S_2}\left[2R_c\{(u-v)\cos\psi+w\sin\psi\}-r\{2(u-v)\cos\psi+w\sin\psi\}\right]\mathrm{d}S\,, \quad (14)$$

where R_c is the radius of the intersecting circle of the two Mach cones (see figure 1).

Considering that $dS = \sqrt{\beta^2+1}\, r\, dr\, d\psi$, equations (12), (13) and (14) can be written as follows:

$$\frac{L}{\rho_1 U_1^2} = \frac{1}{\beta} \iint_{S_2} \{(u-v)\cos\psi + w\sin\psi\}\, r\, dr\, d\psi\,, \tag{15}$$

$$\frac{D}{\rho_1 U_1^2} = \frac{1}{2\beta^2} \iint_{S_2} \{(u-v)^2 + w^2\}\, r\, dr\, d\psi\,, \tag{16}$$

$$\frac{b\cdot L}{\rho_1 U_1^2} = \iint_{S_2} [2R_c\{(u-v)\cos\psi + w\sin\psi\} - r\{2(u-v)\cos\psi + w\sin\psi\}]\, r\, dr\, d\psi\,, \tag{17}$$

or, when (15) is substituted in (17):

$$\frac{b}{\beta R_c} = 2 - \frac{\iint_{S_2} \{2(u-v)\cos\psi + w\sin\psi\}\, r^2\, dr\, d\psi}{R_c \iint_{S_2} \{(u-v)\cos\psi + w\sin\psi\}\, r\, dr\, d\psi}\,. \tag{18}$$

As already mentioned in the introduction, the disturbance velocities must satisfy the following conditions:

(a) *The mass flow* through both Mach cones must be the same, i.e.

$$\int_{S_1} \rho_1 V_{N_1} dS = \int_{S_2} \rho_2 V_{N_2} dS\,. \tag{19}$$

After substitution of equations (4), (5) and (9) this can be simplified to:

$$\frac{S_1 - S_2}{\sqrt{\beta^2+1}} = \iint_{S_2} (v-u)\, r\, dr\, d\psi\,. \tag{20}$$

The expression $\frac{S_1 - S_2}{\sqrt{\beta^2+1}}$ represents the difference between the projection of the Mach cone areas S_1 and S_2 on a plane perpendicular to the x-axis, so that:

$$\frac{S_1 - S_2}{\sqrt{\beta^2+1}} = A\,, \tag{21}$$

where A is the projected base area.

The final equation for the base area can therefore be written as:

$$A = \iint_{S_2} (v-u)\, r\, dr\, d\psi\,. \tag{22}$$

From the derivation of the expressions for L, D, $\mathcal{M}$ and A it is evident that no explicit use has been made of the property that the forward boundary of the control volume is a Mach cone. The sole condition used is that no disturbance velocities are generated in front of this Mach cone. This means that the wing-body configuration cannot extend ahead of this Mach cone. It is not necessary, on the other hand, for the wing and body noses to lie on this forward Mach cone.

However, from the derivation of the optimum velocity distribution along the aft Mach cone it will appear that *at least one* contour part of the configuration has to start on the forward Mach cone.

It will be seen from the derivation of equation (22) that the same equation is valid for configurations consisting of a nose inlet on the forward Mach cone. In this more general case the quantity A is equal to the difference between projected base area and projected inlet area. All the results derived in this report are applicable to this more general case.

(b) *The continuity equation and irrotationality condition*:

The continuity equation is, in cylindrical coordinates:

$$\frac{\partial(\rho U)}{\partial x} + \frac{\partial(\rho U)}{\partial r} + \frac{\rho V}{r} + \frac{1}{r}\frac{\partial(\rho W)}{\partial\psi} = 0\,. \tag{23}$$

After substituting equation (9) and again introducing the quantities (11) this can be written as:

$$-\beta\frac{\partial u}{\partial x} + \frac{\partial v}{\partial r} + \frac{v}{r} + \frac{\partial w}{r\,\partial\psi} = 0 \tag{24}$$

The conditions for irrotational flow are:

$$\frac{\partial U}{\partial r} = \frac{\partial V}{\partial x} \quad \text{or} \quad \frac{\partial u}{\partial r} = \beta \frac{\partial v}{\partial x} \tag{25a}$$

$$\frac{\partial rW}{\partial x} = \frac{\partial U}{\partial \psi} \quad \text{or} \quad \beta \frac{\partial rw}{\partial x} = \frac{\partial u}{\partial \psi} \tag{25b}$$

$$\frac{\partial rW}{\partial r} = \frac{\partial V}{\partial \psi} \quad \text{or} \quad \frac{\partial rw}{\partial r} = \frac{\partial v}{\partial \psi} \tag{25c}$$

The equations (24) and (25) will now be applied to the disturbance quantities on the surface of the aft Mach cone.

Differentiations along the aft Mach cone surface surface will be indicated by:

$$\frac{\mathrm{d}}{\mathrm{d}x}, \frac{\mathrm{d}}{\mathrm{d}r} \text{ and } \frac{\mathrm{d}}{\mathrm{d}\psi}.$$

Then:

$$\frac{\mathrm{d}(rw)}{\mathrm{d}x} = \frac{\partial(rw)}{\partial x} - \frac{1}{\beta}\frac{\partial(rw)}{\partial r} = \frac{1}{\beta}\frac{\partial u}{\partial \psi} - \frac{1}{\beta}\frac{\partial v}{\partial \psi} = \frac{1}{\beta}\frac{\mathrm{d}(u-v)}{\mathrm{d}\psi}.$$

Therefore, equations (25)b and (25)c lead to the following conditions for the velocities on the aft Mach cone:

$$\frac{\mathrm{d}(rw)}{\mathrm{d}x} = \frac{1}{\beta}\frac{\mathrm{d}(u-v)}{\mathrm{d}\psi} = -\frac{1}{\beta}\frac{\mathrm{d}(rw)}{\mathrm{d}r}. \tag{26}$$

From equations (24) and (25)a we easily obtain:

$$\frac{\mathrm{d}u}{\mathrm{d}x} = \frac{\partial u}{\partial x} - \frac{1}{\beta}\frac{\partial u}{\partial r} = \frac{\partial u}{\partial x} - \frac{\partial v}{\partial x}$$

and

$$\frac{\mathrm{d}v}{\mathrm{d}r} = \frac{\partial v}{\partial r} - \beta\frac{\partial v}{\partial x}.$$

Substitution of these two equations in (24) leads to:

$$\frac{\mathrm{d}u}{\mathrm{d}r} + \frac{1}{r}\frac{\mathrm{d}(vr)}{\mathrm{d}r} = -\frac{\mathrm{d}w}{r\,\mathrm{d}\psi}. \tag{27}$$

Equations (26) and (27) are the so-called characteristic equations, which have to be fulfilled along every forward-directed Mach cone.

The problem under consideration is to minimize the expression for the drag (eq. 16) whilst keeping the lift (eq. 15) and the base area (eq. 22) at a prescribed value and, at the same time, fulfilling the characteristic equations (26) and (27).

A comparison of equations (15), (16), (22), (26) and (27) reveals that equations (15), (16), (22) and (26) are completely determined by the quantities $(u-v)$ and w. The only relation between u and v is given by equation (27). It is possible, therefore, first to determine the optimum distribution of $(u-v)$ and w on the surface S_2 from equations (15), (16), (22) and (26). Afterwards the quantities u and v can be determined from the known solutions for $(u-v)$ and w by means of equation (27).

3 The optimum conditions along the aft Mach cone

3.1 *The minimum drag for a given base area*

When it is only specified that the drag should be at a minimum for a given projected base area A, equations (16), (22), (26) and (27) have to be considered. Inspection of equations (16) and (22) reveals that this problem is analogous to the wellknown problem of minimizing the induced drag of a plane wing for a given lift in incompressible flow.

According to equation (22) a mean value for $(v-u)$ is prescribed on the surface S_2, whereas equation (16) shows that the drag is given by a mean value of $(v-u)^2+w^2$.

Considering only equations (16) and (22), therefore, it is evident that the optimum values for $(u-v)$ and w are:

$$(u-v)_{\text{opt}} = u_0 - v_0 = c_1 \quad \text{(constant)} \tag{28}$$

$$w_{\text{opt}} = w_0 = 0\,. \tag{29}$$

The subscript 0 denotes the optimum distribution of the perturbation quantities for the minimum drag case.

As relations (28) and (29) also satisfy equation (26), they represent the correct solution of the problem.

Substitution of eqs. (28) and (29) in eq. (15) shows that the first-order terms of the lift are zero in this case, which could be expected a priori.

The constant c_1 can be determined by substituting equation (28) in equation (22). The result is:

$$c_1 = -\frac{A}{\pi R_c^2} \tag{30}$$

with R_c = radius of the intersecting circle of the two Mach cones (see figure 1).

In accordance with the linearized approach the base dimensions have been neglected with respect to R_c in deriving equation (30).

Substitution of (28), (29) and (30) in (27) gives:

$$2\frac{\mathrm{d}v_0}{\mathrm{d}r} + \frac{v_0}{r} = 0\,. \tag{31}$$

Integration of (31) results in:

$$v_0 = c_2 \cdot r^{-\frac{1}{2}} \tag{32}$$

Combining (28), (30) and (32) gives for u:

$$u_0 = c_2 \cdot r^{-\frac{1}{2}} - \frac{A}{\pi R_c^2}\,. \tag{33}$$

The constant c_2 is determined by the requirement that equation (27) is also valid for the transition of the disturbed flow along the aft Mach cone to the undisturbed flow at $r = R_c$.

On the forward Mach cone the flow is undisturbed and thus $u = v = 0$.

From equation (27) it can be concluded therefore that on the aft Mach cone for $r = R_c$:

$$u_0 + v_0 = 0\,. \tag{34}$$

Equations (32), (33) and (34) yield for the constant c_2:

$$c_2 = \frac{A}{\pi R_c^2} \cdot \frac{R_c^{\frac{1}{2}}}{2}\,. \tag{35}$$

The expressions for u and v on the aft Mach cone become:

$$u_0 = \frac{A}{\pi R_c^2}\left(\frac{1}{2}\sqrt{\frac{R_c}{r}} - 1\right), \tag{36}$$

$$v_0 = \frac{A}{2\pi R_c^2}\sqrt{\frac{R_c}{r}}\,. \tag{37}$$

The drag of an optimum configuration can be found by substitution of eq. (28), (29) and (30) in eq. (16).

The result is:

$$\frac{D_0}{\rho_1 U_1^2} = \frac{A^2}{2\pi\beta^2 R_c^2}\,. \tag{38}$$

Again the base dimensions have been neglected with respect to R_c. The expression for R_c is:

$$R_c = \frac{l}{2\beta}, \tag{39}$$

where l is the length of the straight line joining the two vertices F and G of the Mach cones (see figure 1).

Therefore:

$$\frac{D_0}{\rho_1 U_1^2} = \frac{2A^2}{\pi l^2},$$

or:

$$\frac{D_0}{q} = \frac{4A^2}{\pi l^2}, \tag{40}$$

with q = dynamic pressure.

In the case of a circular base area of diameter d the drag coefficient of the optimum shape becomes:

$$\frac{D_0}{qA} = \left(\frac{d}{l}\right)^2. \tag{41}$$

It should be stressed that in deriving expression (40) no assumptions have been made regarding the shape of the configuration. The only requirement is that the shape gencrates disturbance velocities on the aft Mach cone according to equations (36) and (37).

These disturbance velocities are axially symmetric with respect to the line FG (see figure 1).

One possible solution for the optimum shape problem is therefore given by an axially symmetric shape.

However, in principle also less simple shapes are possible with the same minimum drag value.

When a pointed fuselage alone is considered it is most probable, however, that only an axially symmetric fuselage can realize the disturbance velocity distribution given by equations (36) and (37).

In this case the results can be compared with those of Heaslett and Fuller in ref. 1. These authors have restricted their analysis beforehand to axially symmetric fuselages. The drag given by equation (40) is exactly the same as their result.

Instead of the fairly simple equations (36) and (37), however, they find a more complicated expression containing elliptic functions that cannot be reduced to the form of equations (36) and (37).

A critical examination of the final results of ref. 1 reveals that the derivation of these results involves an error. A correct derivation based on the approach of ref. 1 is given in appendix B. The correct solution for the disturbance velocities in the region between the two Mach cones does contain elliptic functions; on the surface of the aft Mach cone, however, these functions degenerate into the simple expressions (36) and (37) of this report.

From equations (36) and (37) it follows that for $r = R_c$ the disturbance velocities u_0 and v_0 are different from zero. This means that the optimum configuration, when consisting only of a fuselage without nose inlet must have a blunt nose, as the nose shock strength becomes zero for a pointed fuselage in the linearized approach. This is confirmed by the well-known characteristic of optimum body shapes (as, for instance, the von Kàrman ogive).

As already remarked, the optimum configuration does not necessarily consist of a fuselage only.

An axially symmetric fuselage with a ring wing is also possible (see figure 2).

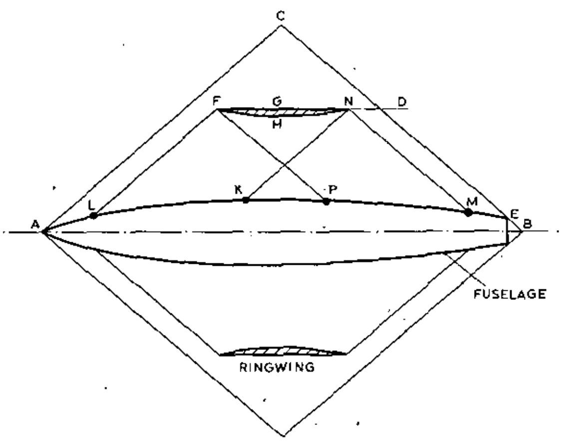

Fig. 2. General body-ring wing configuration.

The following remarks can be added:

a) The diameter and the length of the ring wing can be chosen arbitrarily. The combination must be such, however, that the ring wing lies within the two Mach cones.

b) The contour parts AL and ME of the fuselage and FGN of the ring wing are completely determined by the known velocity distribution along characteristics AC and CE.

c) Of the four remaining contour parts, FHN, LK, KP and PM, two can be chosen arbitrarily; the others are then determined by the velocity distribution along AC and CE.

This means that for instance the ring-wing thickness distribution and the shape of the front part of the fuselage can be chosen arbitrarily, whilst the drag will remain equal to the minimum value predicted by equation (40).

This freedom in the choice of parts of the contours is an essential consequence of the presence of a ring wing. When the ring-wing nose F lies on the forward Mach cone it is not even necessary that the fuselage nose be situated in point A (see figure 3). The shape $A'K$, indicated by a dotted line, leads to the same minimum drag given by equation (40).

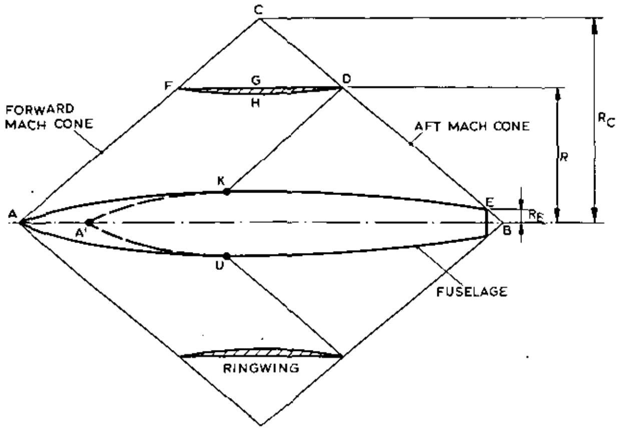

Fig. 3. Body-ring wing configuration with wing leading edge on forward Mach cone.

On the other hand, it is not necessary for the ring-wing leading edge to lie on the front Mach cone AC nor is it necessary for the ring-wing trailing edge to lie on the aft Mach cone. In that case, however, the fuselage nose must lie in the vertex of the forward Mach cone. Of course, the shape of the two chosen contour parts influences the pressure distribution and the shape of the other parts.

An example of an optimum fuselage ring-wing combination is shown in figure 4a. The front part of the fuselage has been chosen as that of a parabolic fuselage with a slenderness ratio of 9. The ring-wing thickness is 2% and the Mach number 2.5.

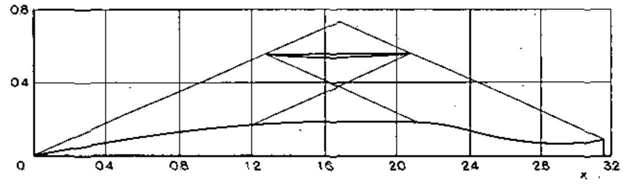

Fig. 4a. Optimum fuselage-ring wing combination for $M = 2.5$.

The contour and the pressure distribution have been determined by means of the linearized graphical characteristics method of Erdmann and Oswatitsch (ref. 2).

The minimum drag according to equation (40) is, for this configuration, given by:

$$\frac{D_0}{qA} = .00285\,. \tag{42}$$

The drag coefficient for a parabolic fuselage of the same front shape and a base area of 18.4% of the frontal area appears to be .520.

The possibility of this large decrease in drag is a direct consequence of the flow phenomena at supersonic speeds.

In supersonic flow the pressure distribution around a fuselage is characterized by positive pressures on the front part and negative pressures on most of the aft part of the fuselage. Owing to the existence of a ring wing around a fuselage the pressures over the rear of the fuselage are increased (see figure 4c). The pressure distribution resembles rather the type peculiar to subsonic flows in that the positive drag of the front part is compensated by a negative drag of the aft part. However, the discontinuous behaviour of the pressure distribution is typical of supersonic flows only.

Summarizing, it may be stated that it is always possible to design a fuselage ring-wing combination for which the drag is equal to the very low value given by equation (40), whilst freedom exists in the choice of a large part of the contour. From the pressure distributions of figure 4b and 4c it may further be concluded that, apart from the leading edge region of the ring-wing inner contour, the only possible difficulty with respect to the boundary layer flow is connected with the sharp pressure rise on the fuselage; everywhere else the pressure gradient is always negative or zero.

The small region with a positive pressure gradient on the ring-wing inner side can be removed by more selective shaping of the ring-wing thickness distribution.

In the case of figure 4c the sudden increase in c_p amounts to .15. It may be expected that this pressure rise can be withstood by a turbulent boundary layer without introducing separation.

A final remark should be made regarding the very small value of the drag coefficients derived from equation (40). This small value is a consequence of the optimization of the configuration; it means that the lowest-order

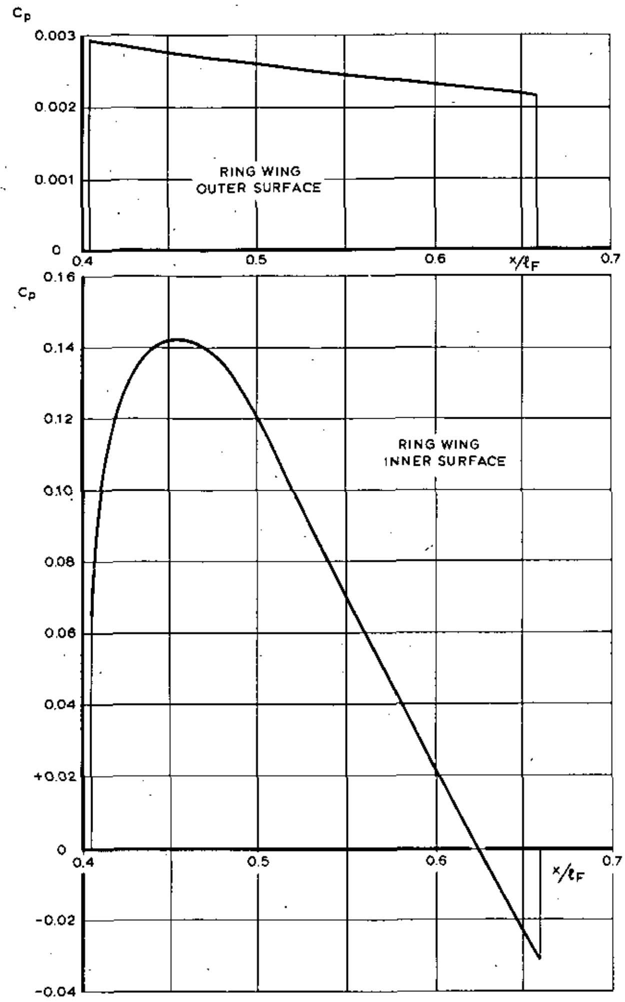

Fig. 4b. Pressure distribution along the ring wing for the optimum fuselage-ring wing combination of fig. 4a.

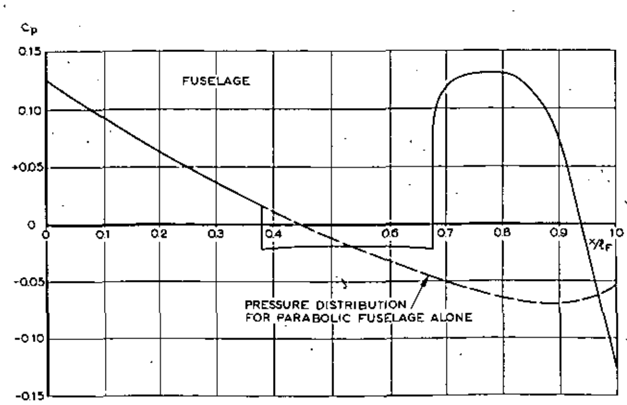

Fig. 4c. Pressure distribution on the fuselage contour of the optimum configuration of fig. 4a.

terms in the drag equation nearly cancel each other. For a reasonable estimate of the exact drag value, therefore, it will be necessary to include higher-order terms in the drag equation. The result will probably be a higher drag than predicted by equation (40); however, the reduction in drag will be appreciable anyway.

In addition, it can be remarked that the influence of the shape on the base drag has not been considered.

The approach used here for designing optimum body-ring wing combinations can be employed also in other fields.

One interesting application would be in the field of engine inlets at supersonic Mach numbers (see figure 5). In designing these inlets it is often necessary to compromise between the requirements for optimum pressure recovery and those for minimum nacelle drag, spillage drag, etc.

When the engine inlet is equipped with a ring wing, as shown in figure 6, it is possible to design the inner contours for maximum pressure recovery without having to compromise for nacelle drag, etc. The resultant

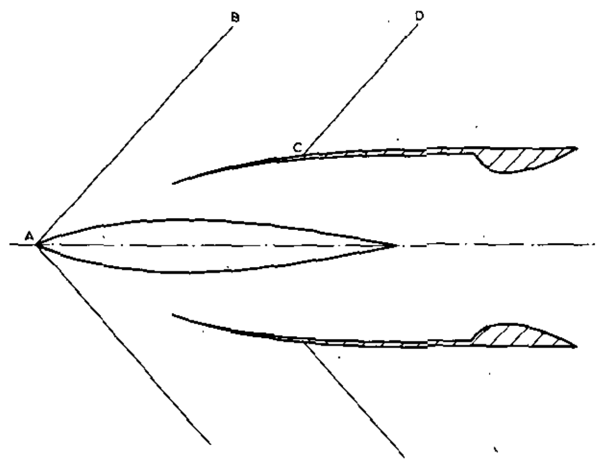

Fig. 5. Supersonic engine inlet configuration.

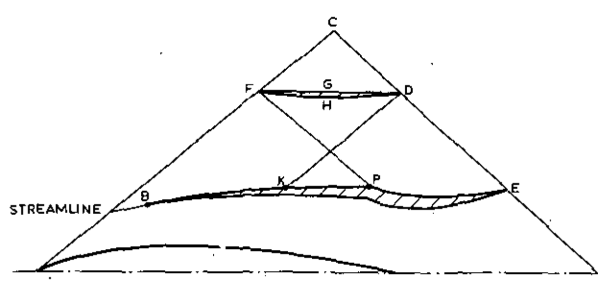

Fig. 6. Supersonic engine inlet configuration with ring wing.

nacelle drag and spillage drag is minimized to the low figure given by eq. (40) by the introduction of the ring wing and the indentation PE on the aft side of the engine cowling (see figure 6).

Here again, one is free to choose contour parts BK and FHD, whereas parts FGD, KP and PE are prescribed by the optimum velocity distribution along CE.

The quantity A of equation (40) is in this case:

A = base area of engine nacelle minus cross-sectional area of undisturbed stream tube area ending at inlet lip B.

3.2 *The minimum induced drag for a given lift for wing-body configurations with circular cross-sections*

The determination of the optimum shape for minimum induced drag for a given lift will be restricted to shapes with circular cross-sections.

In this case the dependence of the disturbance quantities u, v and w on the independent variables r and ψ can be expressed as follows:

$$u = u_0 + u_i \cos\psi \tag{43a}$$

$$v = v_0 + v_i \cos\psi \tag{43b}$$

$$w = w_i \sin\psi\,. \tag{43c}$$

The lift vector is assumed to lie in the meridian plane $\psi = 0$ (see fig. 1). u_0, u_i, v_0, v_i and w_i are functions of r only.

Substitution of (43)a, b and c in eq. (16) gives:

$$\frac{D}{\rho_1 U_1^2} = \frac{1}{2\beta^2}\left[\iint_{S_2}(u_0 - v_0)^2 r\,dr\,d\psi + \iint_{S_2}\left\{(u_i - v_i)^2\cos^2\psi + w_i^2\sin^2\psi\right\} r\,dr\,d\psi\right] = \frac{D_0}{\rho_1 U_1^2} + \frac{D_i}{\rho_1 U_1^2} \tag{44}$$

The cross products of the symmetric and asymmetric quantities cancel out after integration, as they contain uneven powers of $\cos\psi$ and $\sin\psi$.

The induced drag D_i becomes:

$$\frac{D_i}{\rho_1 U_1^2} = \frac{1}{2\beta^2} \iint_{S_2} \left\{(u_i - v_i)^2 \cos^2\psi + w_i^2 \sin^2\psi\right\} r\mathrm{d}r\mathrm{d}\psi = \frac{\pi}{2\beta^2} \int_E^C \left\{(u_i - v_i)^2 + w_i^2\right\} r\mathrm{d}r. \tag{45}$$

The points E and C are defined in figure 2.

Substitution of (43)a, b and c in eq. (15) gives for the lift:

$$\frac{L}{\rho_1 U_1^2} = \frac{1}{\beta}\left[\iint_{S_2} \left\{(u_0 - v_0)\cos\psi + w_0 \sin\psi\right\} r\mathrm{d}r\mathrm{d}\psi + \iint_{S_2} \left\{(u_i - v_i)\cos^2\psi + w_i \sin^2\psi\right\} r\mathrm{d}r\mathrm{d}\psi\right],$$

or:

$$\frac{L}{\rho_1 U_1^2} = \frac{\pi}{\beta} \int_E^C (u_i - v_i + w_i)\, r\mathrm{d}r. \tag{46}$$

Substitution of eq. (43)a, b and c in eq. (22) leads to:

$$A = \iint_{S_2} (v_0 - u_0)\, r\mathrm{d}r\mathrm{d}\psi + \iint_{S_2} (v_i - u_i)\cos\psi r\mathrm{d}r\mathrm{d}\psi = \iint_{S_2} (v_0 - u_0)\, r\mathrm{d}r\mathrm{d}\psi. \tag{47}$$

This equation does not result in a relation for the asymmetric flow quantities. Introducing eq. (43)a, b and c in (26) and (27) results in the following expressions for the asymmetric flow quantities:

$$\frac{\mathrm{d}(rw_i)}{\mathrm{d}r} = u_i - v_i \qquad \text{on } CE, \tag{48}$$

$$\frac{\mathrm{d}u_i}{\mathrm{d}r} + \frac{1}{r}\frac{\mathrm{d}(v_i r)}{\mathrm{d}r} = -\frac{w_i}{r} \quad \text{on } CE. \tag{49}$$

The problem at hand, therefore, is to minimize the induced drag D_i, given by eq. (45), for a given value of the lift L, according to eq. (46), while equations (48) and (49) have to be satisfied.

Here again it is sufficient first to consider equations (45), (46) and (48) in order to find the optimum distributions for $u_i - v_i$ and w_i on S_2.

Subsequently the optimum distribution of u_i and v_i can be deduced from this result with the help of eq. (49).

From equation (48) it can be seen that a function φ exists such that

$$\varphi = rw_i, \tag{50}$$

and

$$\varphi_r = u_i - v_i.$$

Transformed into the variable φ, the problem is therefore to minimize the induced drag given by (see eq. 45):

$$\frac{D_i}{\rho_1 U_1^2} = \frac{\pi}{2\beta^2} \int_E^C \left(\frac{\varphi^2}{r^2} + \varphi_r^2\right) r\mathrm{d}r, \tag{51}$$

the given lift following from (see eq. (46)):

$$\frac{L}{\rho_1 U_1^2} = \frac{\pi}{\beta} \int_E^C \left(\frac{\varphi}{r} + \varphi_r\right) r\mathrm{d}r. \tag{52}$$

Equation (48) is satisfied automatically by the introduction of φ.

The problem can therefore be formulated as that of finding the optimum distribution of φ along the characteristic line CE (see figure 2).

The following boundary conditions have to be fulfilled:

a) The quantity φ is equal to zero for $r = R_c$ as the tangential disturbance quantity w_i is zero in the undisturbed stream and is continuous in C (no transverse pressure discontinuities are present in the flow around axially symmetric shapes).

b) In point D or, in general, in the intersecting point of the characteristic CE with a vortex sheet emanating from a trailing edge a discontinuity in φ is possible. The jump $\Delta\varphi$ in φ when crossing point D is related directly to the total lift carried by the ring wing.

If the ratio ring-wing lift/total lift is put equal to a, it can be shown that (see appendix C):

$$\Delta\varphi = -\frac{a\beta}{\pi R}\frac{L}{\rho_1 U_1^2}, \tag{53)a}$$

with

$$\Delta\varphi = \varphi_{\text{outside}} - \varphi_{\text{inside}}, \tag{53)b}$$

and R = ring-wing radius.

It is shown in appendix A that the optimum distribution of φ has to satisfy the following equation along CD as well as along DE:

$$\varphi_{rr} + \frac{1}{r}\varphi_r - \frac{\varphi}{r^2} = 0, \tag{54}$$

with the boundary conditions:

a)	$r = R_c$	$\varphi = 0$		(55)a
b)	$r = R$	$\varphi_r = -\lambda$	on both sides of the vortex sheets	(55)b
c)	$r = R_E$	$\varphi_r = -\lambda$		(55)c

where λ is a constant, as yet undetermined.

The general solution of equation (34) is:

$$\varphi = c_3 \cdot r + \frac{c_4}{r}. \tag{56}$$

The constants c_3 and c_4 on part CD of characteristic CE (see figure 2) can be determined with the aid of boundary conditions (55)a and (55)b.

The resultant expression for φ becomes along CD:

$$\varphi = -\lambda r \frac{1 - \left(\frac{R_c}{r}\right)^2}{1 + \left(\frac{R_c}{R}\right)^2}, \tag{57)a}$$

and hence:

$$w_i = \frac{\varphi}{r} = -\lambda \frac{1 - \left(\frac{R_c}{r}\right)^2}{1 + \left(\frac{R_c}{R}\right)^2}, \tag{57)b}$$

and

$$u_i - v_i = \varphi_r = -\lambda \frac{1 + \left(\frac{R_c}{r}\right)^2}{1 + \left(\frac{R_c}{R}\right)^2}, \tag{57)c}$$

i.e. along CD the term $(u_i - v_i + w_i)$ in eq. (46) is a constant.

The values for constants c_3 and c_4 in eq. (56) along DE can be determined in a similar way from boundary conditions (55)b and (55)c. The resultant expression for φ is:

$$\varphi = -\lambda r, \tag{58)a}$$

and hence:

$$w_i = \frac{\varphi}{r} = -\lambda, \tag{58)b}$$

and:

$$u_i - v_i = \varphi_r = -\lambda. \tag{58)c}$$

In this region also $u_i - v_i + w_i$ is a constant; it is different, however, from the value along CD owing to the discontinuity in w_i in point D.

The constant λ can be determined by substitution of (57)b and c and (58)b and c in equation (52):

$$\frac{L}{\rho_1 U_1^2} = \frac{\pi}{\beta}\left[\int_{R_E}^{R} -2\lambda r\,dr + \int_{R}^{R_c} \frac{-2\lambda r\,dr}{1 + \left(\frac{R_c}{R}\right)^2}\right] = \frac{\pi\lambda}{\beta}\left\{\frac{-2R_c^2}{1 + \left(\frac{R_c}{R}\right)^2} + R_E^2\right\}.$$

The analysis is restricted to linearized flow, i.e. $R_E/R_c \ll 1$.

Thus, the expression can be simplified to:

$$\frac{L}{\rho_1 U_1^2} = \frac{-2\pi\lambda R_c^2}{\beta\left\{1 + \left(\frac{R_c}{R}\right)^2\right\}},$$

or:

$$\lambda = -\frac{\beta}{2\pi R_c^2}\left\{1 + \left(\frac{R_c}{R}\right)^2\right\}\frac{L}{\rho_1 U_1^2}. \tag{59}$$

Substituting equations (57)a and (58)a in equations (53)a and b gives for the jump in φ across the ring-wing vortex sheet:

$$\Delta\varphi = -\lambda R\frac{1 - \left(\frac{R_c}{R}\right)^2}{1 + \left(\frac{R_c}{R}\right)^2} + \lambda R = 2\lambda R\left\{\frac{\left(\frac{R_c}{R}\right)^2}{1 + \left(\frac{R_c}{R}\right)^2}\right\} = -\frac{a\beta}{\pi R}\frac{L}{\rho_1 U_1^2}.$$

Substitution of (59) in this expression yields for the lift parameter:

$$a = \frac{\text{ring-wing lift}}{\text{total lift}} = 1, \tag{60a}$$

i.e. the total lift must be carried by the ring wing alone.

The net lift of the fuselage is zero in the optimum configuration.

Substitution of equations (57)b, (57)c, (58)b and (58)c in equation (17) gives for the distance b between the center of pressure and the vertex of the forward Mach cone:

$$\frac{b}{\beta R_c} = 2 - \frac{\iint_{S_2}\left\{2(u_i - v_i)\cos^2\psi + w_i\sin^2\psi\right\}r^2\,\mathrm{d}r\,\mathrm{d}\psi}{R_c\iint_{S_2}\left\{(u_i - v_i)\cos^2\psi + w_i\sin^2\psi\right\}r\,\mathrm{d}r\,\mathrm{d}\psi} =$$

$$= 2 - \frac{\int_{R_E}^{R_c}\left\{2(u_i - v_i) + w_i\right\}r^2\,\mathrm{d}r}{R_c\int_{R_E}^{R_c}\left\{(u_i - v_i) + w_i\right\}r\,\mathrm{d}r} =$$

$$= 2 - \frac{\int_{R_E}^{R} - 3\lambda r^2\,\mathrm{d}r + \int_{R}^{R_c}\lambda\frac{-3 - \left(\frac{R_c}{r}\right)^2}{1 + \left(\frac{R_c}{R}\right)^2}r^2\,\mathrm{d}r}{R_c\left[\int_{R_E}^{R} - 2\lambda r\,\mathrm{d}r + \int_{R}^{R_c}\frac{-2\lambda r\,\mathrm{d}r}{1 + \left(\frac{R_c}{R}\right)^2}\right]} = 1.$$

Therefore

$$b = \beta R_c = \tfrac{1}{2}l, \tag{60b}$$

where l is the distance between the vertices of the two Mach cones (see fig. 1), i.e. *the lift vector lies in the plane of the intersecting circle of the two Mach cones.*

u_i and v_i can be determined with the aid of equation (49). Substitution of (57)b and (57)c in (49) leads, for region CD, to the expression:

$$\frac{2\mathrm{d}u_i}{\mathrm{d}r} + \frac{u_i}{r} = \frac{\lambda}{r}\frac{1 - \left(\frac{R_c}{r}\right)^2}{1 + \left(\frac{R_c}{R}\right)^2} + \frac{2\lambda}{r}\frac{\left(\frac{R_c}{r}\right)^2}{1 + \left(\frac{R_c}{R}\right)^2} - \frac{\lambda}{r}\frac{1 + \left(\frac{R_c}{r}\right)^2}{1 + \left(\frac{R_c}{R}\right)^2} = 0. \tag{61}$$

The general solution for u_i is:

$$u_i = \frac{c_5}{\sqrt{r}}, \tag{62a}$$

and therefore with eq. (57)c:

$$v_i = \frac{c_5}{\sqrt{r}} + \lambda \frac{1 + \left(\frac{R_c}{r}\right)^2}{1 + \left(\frac{R_c}{R}\right)^2}. \tag{62b}$$

For the same reasons that led to equation (34) the boundary condition for u_i and v_i in point C is:

$$u_i + v_i = 0 \quad \text{for} \quad r = R_c. \tag{62c}$$

The final expressions for u_i and v_i are therefore:

$$u_i = \frac{-\lambda}{1 + \left(\frac{R_c}{R}\right)^2} \sqrt{\frac{R_c}{r}}, \tag{63a}$$

$$v_i = \frac{-\lambda}{1 + \left(\frac{R_c}{R}\right)^2} \left[\sqrt{\frac{R_c}{r}} - 1 - \left(\frac{R_c}{r}\right)^2\right], \tag{63b}$$

with λ given by equation (59).

Substitution of (58)b and c in (49) results in:

$$2\frac{\mathrm{d}u_i}{\mathrm{d}r} + \frac{u_i}{r} = \frac{\lambda}{r} - \frac{\lambda}{r} = 0 \quad \text{on} \quad DE.$$

The solution is:

$$u_i = \frac{c_6}{\sqrt{r}}, \tag{64a}$$

and:

$$v_i = \frac{c_6}{\sqrt{r}} + \lambda. \tag{64b}$$

The constant c_6 is determined by the boundary condition that u_i and v_i are continuous in D ($r = R$). Thus, combining eq. (64)a and (63)a for $r = R$ gives:

$$\frac{c_6}{\sqrt{R}} = \frac{-\lambda}{1 + \left(\frac{R_c}{R}\right)^2} = \sqrt{\frac{R_c}{R}}. \tag{65}$$

Substitution of (65) in (64)a and (64)b yields for DE:

$$u_i = -\lambda\sqrt{\frac{R_c}{r}} \frac{1}{1 + \left(\frac{R_c}{R}\right)^2}, \tag{66a}$$

and

$$v_i = \frac{-\lambda}{1 + \left(\frac{R_c}{R}\right)^2} \left\{\sqrt{\frac{R_c}{r}} - 1 - \left(\frac{R_c}{R}\right)^2\right\}. \tag{66b}$$

Upon equation (59) being introduced into equations (57)b, (63)a and b, (58)b and (66)a and b the results can be summarized as follows:

Along CD		Along DE	
$u_i = \frac{\beta}{2\pi R_c^2}\frac{L}{\rho_1 U_1^2}\sqrt{\frac{R_c}{r}}$ or $\frac{u_i}{n} = \frac{\beta}{2\pi}\sqrt{\frac{R_c}{r}}$	(67)a	$u_i = \frac{\beta}{2\pi R_c^2}\frac{L}{\rho_1 U_1^2}\sqrt{\frac{R_c}{r}}$ or $\frac{u_i}{n} = \frac{\beta}{2\pi}\sqrt{\frac{R_c}{r}}$	(68)a
$v_i = \frac{\beta}{2\pi R_c^2}\frac{L}{\rho_1 U_1^2}\left\{\sqrt{\frac{R_c}{r}} - 1 - \left(\frac{R_c}{r}\right)^2\right\}$ or $\frac{v_i}{n} = \frac{\beta}{2\pi}\left\{\sqrt{\frac{R_c}{r}} - 1 - \left(\frac{R_c}{r}\right)^2\right\}$	(67)b	$v_i = \frac{\beta}{2\pi R_c^2}\frac{L}{\rho_1 U_1^2}\left\{\sqrt{\frac{R_c}{r}} - 1 - \left(\frac{R_c}{R}\right)^2\right\}$ or $\frac{v_i}{n} = \frac{\beta}{2\pi}\left\{\sqrt{\frac{R_c}{r}} - 1 - \left(\frac{R_c}{R}\right)^2\right\}$	(68)b
$w_i = \frac{\beta}{2\pi R_c^2}\frac{L}{\rho_1 U_1^2}\left\{1 - \left(\frac{R_c}{r}\right)^2\right\}$ or $\frac{w_i}{n} = \frac{\beta}{2\pi}\left\{1 - \left(\frac{R_c}{r}\right)^2\right\}$	(67)c	$w_i = \frac{\beta}{2\pi R_c^2}\frac{L}{\rho_1 U_1^2}\left\{1 + \left(\frac{R_c}{R}\right)^2\right\}$ or $\frac{w_i}{n} = \frac{\beta}{2\pi}\left\{1 + \left(\frac{R_c}{R}\right)^2\right\}$	(68)c

$$\text{with } n = \frac{L}{\rho_1 U_1^2 R_c^2}$$

The disturbance velocities given by equations (67)a–(68)c incl. can be obtained by an inclination i of the axis of the ring wing or fuselage with respect to the undisturbed flow. The inclination i will be different for ring wing and fuselage and in general i will be a function of the axial coordinate x.

The required axis inclination i is dependent, of course, upon the chosen thickness distribution of ring wing and fuselage. The result obtained can, therefore, be summarized as follows:

a) The zero-lift drag can be minimized by determining a suitable thickness distribution for the fuselage and ring wing (see section 3.1).
b) For this optimum thickness distribution the optimum axis inclination i can be determined from the results derived in this section.
   It is equally possible, however, to apply these results to another thickness distribution than the optimum one. In that case the zero-lift drag will not be optimum but the induced drag will have the optimum value connected with the disturbance velocities given by eq. (67)a–(68)c incl.

Just as is the case for u_0 and v_0 in the minimum drag configuration at zero lift, the disturbance velocities u_i and v_i are different from zero in point C.

When the ring-wing leading edge lies on the forward Mach cone (as in figure 3) the axis inclination of the nose station, necessary to generate these velocities in C, is different from zero but finite. However, in case these velocities must be generated by a sharp fuselage nose, as for instance in the configuration of figure 2, an infinitely large value of the local axis inclination is necessary. This is analogous to the blunt nose of fuselages for optimum zero-lift drag (see section 3.1).

For the configuration shown in figure 2 the following qualitative remarks can be made:
(a) The axis inclinations of the ring wing and of fuselage parts AL and ME are completely determined by the known velocity distributions along AC and CE.
(b) Of the three contour parts LK, KP and PM of the fuselage, the inclination of only one can be chosen arbitrarily, with the restriction that the value for w_i in point D is prescribed (see eq. (68)c). This means that fuselage part LK must generate sufficient upwash or downwash in flow-field $LKDHF$ in order that the total ring-wing lift has the prescribed value.

The freedom in the choice of the axis inclinations is smaller than that in the choice of the thickness distribution, due to the fact that in remark (a) the axis inclination is assumed to be the same for the outer and inner surfaces of the ring wing.

This restriction is not necessary for a ring wing with a blunt trailing edge, in which case, therefore, the freedom in the choice of the axis inclinations is larger.

For the optimum fuselage-ring-wing combination shown in figure 4a axis inclinations i that yield the velocity distributions given by equations (67)a–(68)c have been determined by means of the graphical linearized characteristics method of ref. 2 with the extensions of ref. 3.

The results have been plotted in figure 7a; the corresponding lift loading is represented in figure 7b. The quantity u_i/n on the inner side of the fuselage has been chosen to vary linearly with x.

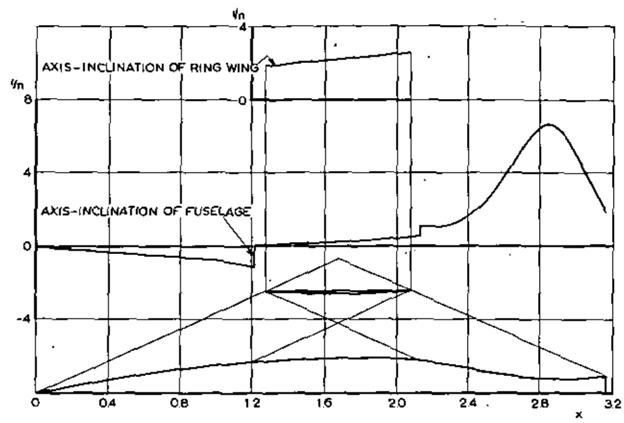

Fig. 7a. The axis inclinations for the optimum configuration of figure 4a.

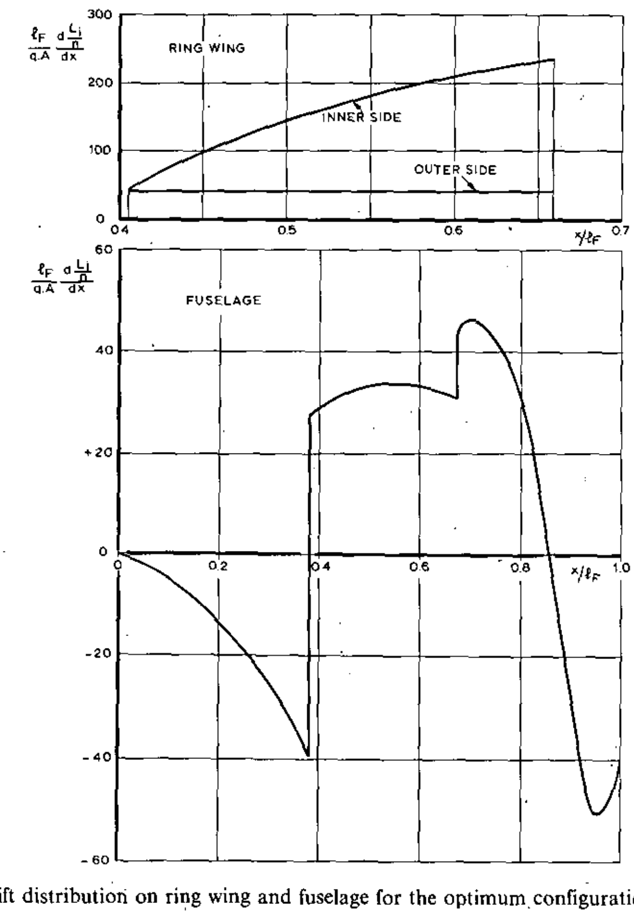

Fig. 7b. The lift distribution on ring wing and fuselage for the optimum configuration of figure 4a.

As the disturbance velocities along characteristic CE are proportional to the desired lift, the quantities u_i/n, v_i/n, w_i/n are used to calculate values for i/n rather than i.

The induced drag distribution is shown in figure 7c. Both lift and induced drag distributions are plotted dimensionless in the forms:

$$\frac{l_F}{qA}\frac{\mathrm{d}\left(\frac{L_i}{n}\right)}{\mathrm{d}x} \quad \text{and} \quad \frac{l_F}{qA}\frac{\mathrm{d}\left(\frac{D_i}{n^2}\right)}{\mathrm{d}x},$$

respectively with l_F = fuselage length.

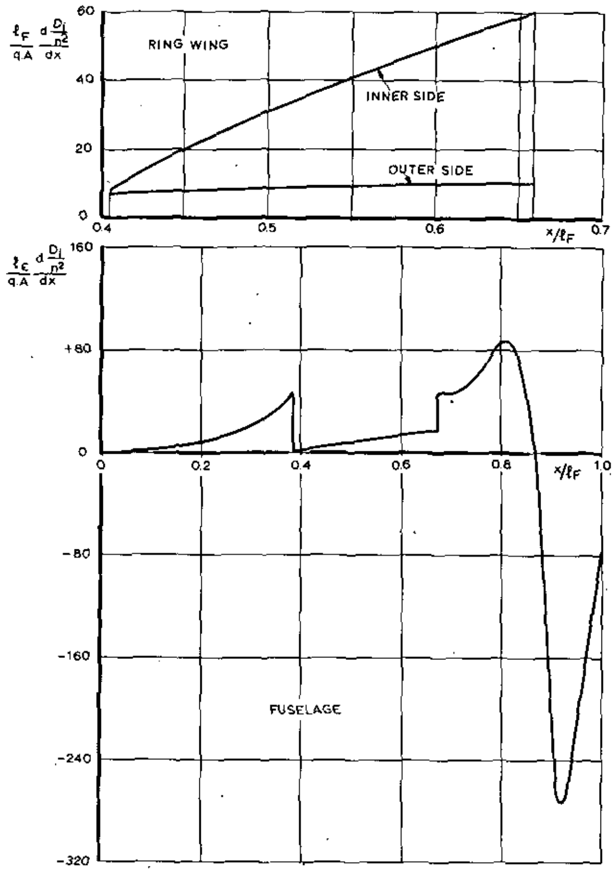

Fig. 7c. The induced drag distribution for the optimum configuration of figure 4a.

It may be remarked that the total lift of the fuselage is not zero as it should be according to equation (60)a. The reason is that the linearized characteristics method which has been used for the determination of the axis inclination is not accurate enough when flow around a fuselage is considered.

A more detailed treatment of this problem is given in ref. 8.

The induced drag is obtained by substitution of equations (57)b and c, (58)b and c, and (59) in eq. (51). The result is:

$$\frac{D_i}{\rho_1 U_1^2} = \frac{\pi\lambda^2}{2\beta^2}\left[\int_{R_E}^{R} 2r\,dr + \int_{R}^{R_c} \frac{2+2\left(\frac{R_c}{r}\right)^4}{\left\{1+\left(\frac{R_c}{R}\right)^2\right\}^2}\,r\,dr\right] =$$

$$= \frac{\pi}{2\beta^2}\,\frac{\beta^2}{4\pi^2}\left(\frac{L}{\rho_1 U_1^2 R_c^2}\right)^2\left\{1+\left(\frac{R_c}{R}\right)^2\right\}^2\left[R^2-R_E^2+\frac{R_c^2-R^2-R_c^2+\frac{R_c^4}{R^2}}{\left\{1+\left(\frac{R_c}{R}\right)^2\right\}^2}\right],$$

as $R_E \ll R$ and $R_E \ll R_c$ this can be simplified to:

$$\frac{D_i}{\rho_1 U_1^2 R_c^2} = \frac{1}{4\pi}\left(\frac{L}{\rho_1 U_1^2 R_c^2}\right)^2\left\{1+\left(\frac{R_c}{R}\right)^2\right\}, \tag{69a}$$

or:

$$\frac{D_i}{\rho_1 U_1^2} = \frac{1}{4\pi}\left(\frac{L}{\rho_1 U_1^2}\right)^2 \frac{1+\left(\frac{R_c}{R}\right)^2}{R_c^2}. \tag{69b}$$

It follows from (69)a and b that for a given value of R_c the induced drag is at a minimum when $R=R_c$. In this case, however, the ring-wing length is zero and the lift is concentrated in an infinitely small region. The absolute value of the local axis inclinations of the fuselage necessary to produce this result are infinitely large. In practice, therefore, the solution is not valid for values of R too close to R_c. From figure 8 it follows that the induced drag does not increase too rapidly when R/R_c is decreased from 1. It is noted that the induced drag given by equation

(69)b for $R=R_c$ is exactly the same as that given in ref. 9 for the optimum wing system within a double Mach-cone space. The important point to note is that, according to the results given here, such low induced-drag values can be realized without necessitating the use of very large wing surfaces (see figure 8).

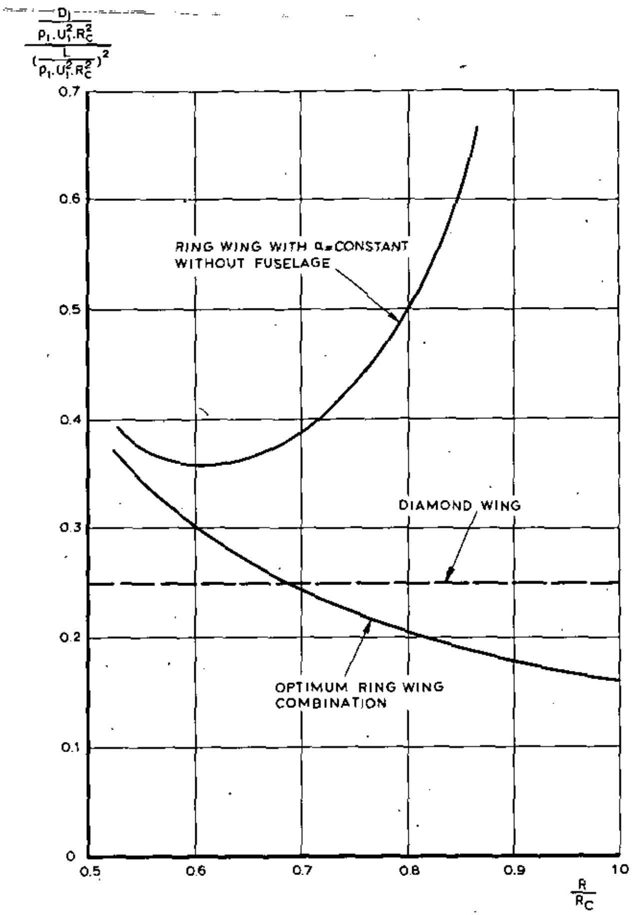

Fig. 8. The induced drag for the optimum configuration as a function of R/R_c, compared with the ring wing at constant angle of attack and the diamond wing.

Use has to be made, however, of the interference effects between fuselage and ring wing in order to realize the optimum velocity distribution on the aft Mach cone.

The optimum value for the induced drag can be compared with that of a ring wing without fuselage at a constant angle of attack and with a chord $c=2\beta(R_c-R)\leqq 2\beta R$; i.e. the maximum chord possible within the two Mach cones. This has been computed by the graphical characteristics method of ref. 2.

In figure 8 the quantity $\frac{D_i/\rho_1 U_1^2 R_c^2}{L/(\rho_1 U_1^2 R_c^2)^2}$ has been plotted against R/R_c for both cases. It is evident that an appreciable reduction in induced drag is possible.

The induced-drag value for the diamond wing of maximum dimensions within the two Mach cones (span $=2R_c$ and length $=2\beta R_c$) is indicated by the dashed horizontal line in figure 8.

The induced drag of the optimum ring-wing configuration is smaller than that of the maximum-sized diamond wing for values of R/R_c greater than .68.

In the optimum configuration, however, the fuselage lift loading is partly positive, partly negative, whereas the net lift of the fuselage is zero (see figure 7b).

The realization of the above-mentioned favourable interference effect on the induced drag depends, therefore, on the possibility for the fuselage boundary layer to withstand the associated pressure distributions.

4 Conclusions

It has been shown that the requirement for a configuration enclosed between two circular Mach cones with a given base area to be optimum with respect to drag is that the disturbance velocities generated on the aft Mach cone have to be axially symmetric. With body-ring-wing combinations the same minimum drag can be realized as with the optimum axially symmetric fuselage alone, whilst a certain freedom exists in the choice of part of the shape. Furthermore, a method has been presented to determine the optimum axis inclinations for a body-ring-wing combination for minimum induced drag at a given lift. An expression has been given for this minimum induced drag as a function of the ring-wing diameter and the length of the body. It is shown that through the optimum choice of body axis and ring-wing axis inclinations an appreciable reduction over the induced drag of a ring wing alone can be obtained. In the optimum configuration the net lift of the fuselage appears to be zero.

5 Acknowledgements

The authors wish to express their sincere thanks to Prof. Dr. R. Timman for his valuable comments which have been to the benefit of the final form of this report.

6 References

[1] Heaslett, M. A. and Fuller, F. B., Axially symmetric shapes with minimum wave drag. National Advisory Committee for Aeronautics, report TR 1256, 1956.

[2] Erdmann, S. F. and Oswatitsch, K., A graphical linearized characteristics method for symmetric and unsymmetric flow around axially symmetric fuselages and ring wings (in German). Zeitschrift für Flugwissenschaften 1954; Volume 8; pages 201–215.

[3] Walle, F. van der, Graphical determination of the stationary forces on body-annular wing configurations with circular cross-sections. National Aeronautical Research Institute, report TN-G.9, 1958.

[4] Byrd, P. P. and Friedman, M. D., Handbook of elliptic integrals for engineers and physicists. Lange, Maxwell and Springer Ltd., 1954.

[5] Walle, F. van der, Determination of the interference effects between a ring wing and an axially symmetric fuselage. National Aeronautical Research Institute, report TN-G.7, 1958.

[6] Ehlers, F. E., The lift and moment on a ring concentric to a cylindrical body in supersonic flow. Journal of the Aeronautical Sciences, April 1955, pages 239–248.

[7] Courant, R. und Hilbert, D., Methoden der Mathematischen Physik, Band 1. Springer Verlag 1924.

[8] Zandbergen, P. J., Investigations on the supersonic flow around bodies. National Aeronautical Research Institute, report TR-G.25, October 1962.

[9] Graham, E. W., Lagerstrom, P. E., Licher, R. M. and Beane, B. J., A theoretical investigation of the drag of generalized aircraft configurations in supersonic flow. NACA. TM 1421 January, 1957.

APPENDIX A

Determination of the equations for the optimum distribution of the potential φ on the aft Mach cone

According to equations (51) and (52) of section 3.2 the optimum distribution of φ is a distribution that minimizes the expression:

$$\int_{R_E}^{R_c} \left\{\left(\frac{\varphi}{r}\right)^2 + \varphi_r^2\right\} r\,\mathrm{d}r\,, \tag{A.1}$$

for a given value of:

$$\int_{R_E}^{R_c} \left\{\frac{\varphi}{r} + \varphi_r\right\} r\,\mathrm{d}r\,. \tag{A.2}$$

The boundary conditions are (see section 3.2):

$$\text{for } r=R_c\,, \qquad \varphi=0\,, \tag{A.3}$$

whereas for $r=R$ a discontinuity in φ exists with:

$$\Delta\varphi=\varphi_{\text{outside}}-\varphi_{\text{inside}}=-\frac{a\beta}{\pi R}\,\frac{L}{\rho_1 U_1^2}\,, \tag{A.4}$$

where a is a constant, as yet undetermined (see App. C).

In order to solve this variational problem a variation η of the function φ is considered. η also must satisfy eq. (A.3).

For optimum conditions to exist, it is known from variational theory that the following equation must be satisfied (see, for instance, ref. 7.):

$$\delta\int_{R_E}^{R_c}\left\{\left(\frac{\varphi}{r}\right)^2+\varphi_r^2\right\} r\,\mathrm{d}r+2\lambda\int_{R_E}^{R_c}\left(\frac{\varphi}{r}+\varphi_r\right) r\,\mathrm{d}r=0\,,$$

where λ is a constant.

Therefore, for every small value of η:

$$\int_{R_E}^{R_c}\left\{2\,\frac{\mathrm{d}\varphi}{\mathrm{d}r}\,\frac{\mathrm{d}\eta}{\mathrm{d}r}+\frac{2}{r^2}\,\varphi\eta\right\} r\,\mathrm{d}r+2\lambda\int_{R_E}^{R_c}\left\{\frac{\mathrm{d}\eta}{\mathrm{d}r}+\frac{\eta}{r}\right\} r\,\mathrm{d}r=0\,. \tag{A.5}$$

Integration by parts of the first term gives:

$$\int_{R_E}^{R_c} 2\,\frac{\mathrm{d}\varphi}{\mathrm{d}r}\,\frac{\mathrm{d}\eta}{\mathrm{d}r}\,r\,\mathrm{d}r=\int_{R_E}^{R_c} 2\,\frac{\mathrm{d}\varphi}{\mathrm{d}r}\,r\,\mathrm{d}\eta=2r\eta\,\frac{\mathrm{d}\varphi}{\mathrm{d}r}\Big/_{\substack{\text{on}\\ \text{boundaries}}}-\int_{R_E}^{R_c}2\eta\,\frac{\mathrm{d}\varphi}{\mathrm{d}r}\,\mathrm{d}r-\int_{R_E}^{R_c}2r\,\frac{\mathrm{d}^2\varphi}{\mathrm{d}r^2}\,\eta\,\mathrm{d}r\,. \tag{A.6}$$

The third term of equation (A.5) yields in the same way:

$$\int_{R_E}^{R_c}\frac{\mathrm{d}\eta}{\mathrm{d}r}\,r\,\mathrm{d}r=\int_{R_E}^{R_c} r\,\mathrm{d}\eta=r\eta\Big/_{\substack{\text{on}\\ \text{boundaries}}}-\int_{R_E}^{R_c}\eta\,\mathrm{d}r\,. \tag{A.7}$$

Substituting eq. (A.6) and (A.7) in (A.5):

$$-2\int_{R_E}^{R_c}\left\{r\cdot\varphi_{rr}+\varphi_r-\frac{\varphi}{r}\right\}\eta\,\mathrm{d}r+\left(2\lambda\eta r+2\eta r\,\frac{\mathrm{d}\varphi}{\mathrm{d}r}\right)\Big/_{\substack{\text{on}\\ \text{boundaries}}}=0. \tag{A.8}$$

Equation (A.8) must be satisfied for every small value of η; the necessary conditions for this are:

$$r\varphi_{rr}+\varphi_r-\frac{\varphi}{r}=0 \quad\text{or}\quad \varphi_{rr}+\frac{1}{r}\,\varphi_r-\frac{\varphi}{r^2}=0\,, \tag{A.9}$$

and on those boundaries where $\eta\neq 0$ (i.e. $r=R_E$ and $r=R$):

$$\lambda+\frac{\mathrm{d}\varphi}{\mathrm{d}r}=0 \quad\text{or}\quad \frac{\mathrm{d}\varphi}{\mathrm{d}r}=-\lambda\,. \tag{A.10}$$

The boundary condition for $r=R_c$, where $\eta\equiv 0$, is given by eq. (A.3).

APPENDIX B

Comparison with the results of ref. 1 for the minimum zero lift drag of an axially symmetric fuselage

The source strength found in ref. 1 for pointed fuselages is in the notation of this report (see eq. (70)b of ref. 1):

$$B(x) = \frac{2U_1}{\beta^2}\left(\frac{R_E}{R_c}\right)^2 \sqrt{x(l-x)}\,, \tag{B.1}$$

or:

$$B'(x) = \frac{U_1}{\beta^2}\left(\frac{R_E}{R_c}\right)^2 \frac{l-2x}{\sqrt{x(l-x)}}, \tag{B.2}$$

where the prime denotes differentiation with respect to x.

The disturbance velocity in axial direction is:

$$\frac{U-U_1}{U} = -\frac{1}{2\pi}\int_0^{x-\beta r} \frac{1}{\beta^2}\left(\frac{R_E}{R_c}\right)^2 \frac{l-2x_1}{\sqrt{x_1(l-x_1)}} \frac{dx_1}{\sqrt{(x-x_1)^2-\beta^2 r^2}},$$

or:

$$-2\pi\beta^2 \frac{U-U_1}{U_1}\left(\frac{R_c}{R_E}\right)^2 = \int_0^{x-\beta r}\sqrt{\frac{l-x_1}{x_1}}\frac{dx_1}{\sqrt{(x-x_1)^2-\beta^2r^2}} + $$

$$- \int_0^{x-\beta r}\sqrt{\frac{x_1}{l-x_1}}\frac{dx_1}{\sqrt{(x-x_1)^2-\beta^2r^2}}, \tag{B.3}$$

with the substitution of $y=x-x_1$ and using eq. (B.1) this becomes:

$$-2\pi u\left(\frac{R_c}{R_E}\right)^2 = \int_{\beta r}^{x}\sqrt{\frac{l-x+y}{x-y}}\frac{dy}{\sqrt{y^2-\beta^2r^2}} - \int_{\beta r}^{x}\sqrt{\frac{x-y}{l-x+y}}\frac{dy}{\sqrt{y^2-\beta^2r^2}}. \tag{B.4}$$

In the region between the two Mach cones is:

$$x-\beta r>0 \quad \text{and} \quad x+\beta r \leqq l\,,$$

or:

$$x>\beta r \quad \text{and} \quad l-x\geqq \beta r\,.$$

Hence: $x>\beta r>-\beta r \geqq -(l-x)$.

Therefore, the first integral of equation (B.4) can be written as:

$$\int_b^a \sqrt{\frac{t-d}{(a-t)(t-b)(t-c)}}\,dt \quad \text{with} \quad a>b>c\geqq d\,.$$

According to ref. 4 (eq. 256.13 and 339.01) this is equal to:

$$(b-d)g\int_0^{u_1}\frac{\mathrm{dn}^2 u\,du}{1-\alpha^2\mathrm{sn}^2 u} = \frac{(b-d)g}{\alpha^2}\left[k^2u_1+(\alpha^2-k^2)\Pi(\varphi,\alpha^2,k)\right], \tag{B.5}$$

with: $a=x$ $\qquad k^2 = \dfrac{(a-b)(c-d)}{(a-c)(b-d)} = \dfrac{(x-\beta r)(l-x-\beta r)}{(x+\beta r)(l-x+\beta r)}$,

$b=\beta r$

$c=-\beta r$ $\qquad \alpha^2 = \dfrac{x-\beta r}{x+\beta r} > k^2$,

$d=-(l-x)$ $\qquad \varphi = \sin^{-1}\sqrt{\dfrac{(a-c)(a-b)}{(a-b)(a-c)}} = \dfrac{\pi}{2}$,

$$g = \frac{2}{\sqrt{(a-c)(b-d)}} = \frac{2}{\sqrt{(x+\beta r)(l-x+\beta r)}}.$$

The second integral of equation (B.4) can be written as:

$$\int_b^a\sqrt{\frac{a-t}{(t-b)(t-c)(t-d)}}\,dt = (a-b)g\int_0^{u_1}\frac{\mathrm{cn}^2u\,du}{1-\alpha^2\mathrm{sn}^2u} = \frac{(a-b)}{\alpha^2}\cdot g\left[u_1+(\alpha^2-1)\Pi(\varphi,a^2,k)\right]. \tag{B.6}$$

(see ref. 4 eq. 256.14 and 338.01).

Substitution of (B.5) and (B.6) in (B.4) yields:

$$-2\pi u\left(\frac{R_c}{R_E}\right)^2=\frac{2}{\sqrt{(x+\beta r)(l-x+\beta r)}}\left[\frac{l-x+\beta r}{a^2}k^2K-\frac{x-\beta r}{a^2}K\right]+$$

$$+\frac{2}{\sqrt{(x+\beta r)(l-x+\beta r)}}\left[(l-x+\beta r)\left(1-\frac{k^2}{\alpha^2}\right)-(x-\beta r)\left(1-\frac{1}{\alpha^2}\right)\right]\Pi\left(\frac{\pi}{2},\ \alpha^2,k\right), \qquad \text{(B.7)}$$

or:

$$-2\pi u\left(\frac{R_c}{R_E}\right)^2=\frac{2}{\sqrt{(x+\beta r)(l-x+\beta r)}}\left[\left\{l-2(x+\beta r)\right\}K+4\beta r\Pi\left(\frac{\pi}{2},\ \alpha^2,k\right)\right]. \qquad \text{(B.8)}$$

On the aft Mach cone: $x+\beta r=l$ or $k=0$.

Then: $K=\dfrac{\pi}{2}$

and $$\Pi\left(\frac{\pi}{2},\ \alpha^2,0\right)=\lim_{k\to 0}\int_0^{\pi/2}\frac{\mathrm{d}\vartheta}{(1-\alpha^2\sin^2\vartheta)\sqrt{1-k^2\sin^2\vartheta}}=$$

$$=\int_0^{\pi/2}\frac{\mathrm{d}\vartheta}{1-\alpha^2\sin^2\vartheta}=\frac{\pi/2}{\sqrt{1-\alpha^2}}=\sqrt{\frac{x+\beta r}{2\beta r}}\cdot\frac{\pi}{2}=\sqrt{\frac{l}{2\beta r}}\cdot\frac{\pi}{2}.$$

Substituting this in (B.8) yields:

$$-2\pi u\left(\frac{R_c}{R_E}\right)^2=\frac{2}{\sqrt{2\beta rl}}\left[-l\cdot\frac{\pi}{2}+4\beta r\sqrt{\frac{l}{2\beta r}}\cdot\frac{\pi}{2}\right]$$

or:

$$u=-\left(\frac{R_E}{R_c}\right)^2\left[1-\tfrac{1}{2}\sqrt{\frac{R_c}{r}}\right], \qquad \text{(B.9)}$$

where $l=2\beta R_c$ has been substituted.

Equation (B.9) is exactly the same result as eq. (36).

The radial velocity V is determined by:

$$\frac{\beta^2 V}{U_1}\left(\frac{R_c}{R_E}\right)^2=\beta\cdot v\left(\frac{R_c}{R_E}\right)^2=\frac{1}{2\pi r}\int_0^{x-\beta r}\frac{(x-x_1)(l-2x_1)\mathrm{d}x_1}{\sqrt{x_1(l-x_1)}\sqrt{(x-x_1)^2-\beta^2r^2}},$$

or:

$$\beta\cdot 2\pi rv\left(\frac{R_c}{R_E}\right)^2=\int_0^{x-\beta r}(x-x_1)\sqrt{\frac{l-x_1}{x_1}}\frac{\mathrm{d}x_1}{\sqrt{(x-x_1)^2-\beta^2r^2}}+$$

$$-\int_0^{x-\beta r}(x-x_1)\sqrt{\frac{x_1}{l-x_1}}\frac{\mathrm{d}x_1}{\sqrt{(x-x_1)^2-\beta^2r^2}}.$$

With $y=x-x_1$ this equation becomes:

$$\beta\cdot 2\pi rv\left(\frac{R_c}{R_E}\right)^2=\int_{\beta r}^{x}y\sqrt{\frac{l-x+y}{x-y}}\frac{\mathrm{d}y}{\sqrt{y^2-\beta^2r^2}}-\int_{\beta r}^{x}y\sqrt{\frac{x-y}{l-x+y}}\frac{\mathrm{d}y}{\sqrt{y^2-\beta^2r^2}}=$$

$$=\int_{\beta r}^{x}\sqrt{\frac{l-x+y}{x-y}}\sqrt{\frac{y+\beta r}{y-\beta r}}\,\mathrm{d}y-\beta r\int_{\beta r}^{x}\sqrt{\frac{l-x+y}{x-y}}\frac{\mathrm{d}y}{\sqrt{y^2-\beta^2r^2}}-\int_{\beta r}^{x}\sqrt{\frac{x-y}{l-x+y}}\sqrt{\frac{y+\beta r}{y-\beta r}}\,\mathrm{d}y+$$

$$+\beta r\int_{\beta r}^{x}\sqrt{\frac{l-x+y}{x-y}}\frac{\mathrm{d}y}{\sqrt{y^2-\beta^2r^2}}. \qquad \text{(B.10)}$$

The first integral of eq. (B.10) can be written as (see ref. 4 eq. 256.16 and 362.17):

$$(b-c)(b-d)g\int_0^{u_1}\frac{\mathrm{dn}^2u\,\mathrm{d}u}{(1-\alpha^2\,\mathrm{sn}^2u)^2}=$$

$$=(b-c)(b-d)g\left[\frac{-1}{2\alpha^2(\alpha^2-1)}\left\{\alpha^2E+(k^2-\alpha^2)K+(2\alpha^2-\alpha^4-k^2)\cdot\Pi\left(\frac{\pi}{2},\ \alpha^2,k\right)\right\}\right]. \qquad \text{(B.11)}$$

The third integral is, according to ref. 4 (eq. 362.16):

$$(a-b)(b-c)g\int_0^{u_1}\frac{\mathrm{cn}^2 u\,\mathrm{d}u}{(1-\alpha^2\,\mathrm{sn}^2 u)^2} =$$

$$= (a-b)(b-c)g\left[\frac{1}{2\alpha^2(k^2-\alpha^2)}\left\{\alpha^2 E+(k^2-\alpha^2)K+(2k^2\alpha^2-\alpha^4-k^2)\,\Pi\left(\frac{\pi}{2},\ \alpha^2, k\right)\right\}\right]. \quad \text{(B.12)}$$

Substitution of eq. (B.11) and (B.12) in (B.10) leads to:

$$\beta\cdot 2\pi r v\left(\frac{R_c}{R_E}\right)^2 = \frac{2}{\sqrt{(x+\beta r)(l-x+\beta r)}}\left[(l-x+\beta r)(x+\beta r)E\left(\frac{\pi}{2},\ k\right) - \beta r l K\right]. \quad \text{(B.13)}$$

For $x+\beta r=l$ this is equal to:

$$\beta\cdot 2\pi r v\left(\frac{R_c}{R_E}\right)^2 = \frac{2}{\sqrt{2\beta r l}}\left\{2\beta r l\frac{\pi}{2} - \beta r l\cdot\frac{\pi}{2}\right\},$$

or:

$$v=\tfrac{1}{2}\left(\frac{R_E}{R_c}\right)^2\sqrt{\frac{R_c}{r}}. \quad \text{(B.14)}$$

Equation (B.14) is exactly equal to eq. (37).

APPENDIX C

Determination of the discontinuity in φ across the vortex sheet aft of a ring wing

To a first approximation, the lift of a ring wing with radius R can be written as (see ref. 2 eq. (35)):

$$\frac{L}{\rho_1 U_1^2} = \frac{\pi R}{\beta^2}\left\{\int\limits_{\substack{\text{outer}\\ \text{surface}}} u_i\,\mathrm{d}x - \int\limits_{\substack{\text{inner}\\ \text{surface}}} u_i\,\mathrm{d}x\right\}. \quad \text{(C.1)}$$

Within the linearized approximation the integrals in eq. (C.1) are equal to (see ref. 2):

$$\int u_i\,\mathrm{d}x = -\beta\{R(w_i)_{\text{trailing edge}} - R(w_i)_{\text{leading edge}}\} =$$

$$= -\beta\{\varphi_{\text{trailing edge}} - (Rw_i)_{\text{leading edge}}\}. \quad \text{(C.2)}$$

Substituting (C.2) in (C.1) we get:

$$\frac{L}{\rho_1 U_1^2} = \frac{\pi R}{\beta}\{\varphi_{\text{inside}} - \varphi_{\text{outside}}\},$$

or:

$$\Delta\varphi = \frac{-\beta}{\pi R}\,\frac{L}{\rho_1 U_1^2} \quad \text{(C.3)}$$

with:

$$\Delta\varphi = \varphi_{\text{outside}} - \varphi_{\text{inside}}. \quad \text{(C.4)}$$

When the ring-wing trailing edge does not extend to the aft Mach cone equation (C.3) is still valid, as the discontinuity in φ across the vortex sheet is constant (see refs. 3 and 5).

C.C.L. Class. D 023 B 27

REPORT NLR-TR G. 32

A programme for the construction of a "first characteristic" Flow around a cone with or without inclination

by

J. Maasdam and P. J. Zandbergen

Summary

This report gives a programme for the determination of the flow around a circular cone. Both the cases of zero-inclination and of a small inclination have been considered. The programme is written in the international machine language ALGOL and can therefore be operated on any computer having an ALGOL compiler.

The purpose of this investigation was mainly to provide an accurate solution for these conical flows in view of their application as initial data along a "first characteristic". These data will enable the determination of the flow field around an axially symmetric configuration having a nose contour which may be considered as conical along a certain distance from the vertex.

The programme is discussed in detail and some results obtained by it are included as an example.

This investigation has been performed under contract with the Netherlands Aircraft Development Board.

Contents

List of symbols

M — Mach number
P — Stagnation pressure ratio
U, V, W — Velocity components
a — Speed of sound
c_p — Pressure coefficient
p — Pressure
$u, u'', \bar{u}$; $v, v'', \bar{v}$; w'' — Velocity components
α — Perturbation angle
β — $\sqrt{M^2-1}$
γ — Ratio of specific heats
ε — Angle of inclination
ϑ — Angular spherical coordinate
ρ — Density
ψ — Angular coordinate

Symbols used in the Algol programme:

eps — Accuracy
g — Identical with γ: ratio of specific heats
hw, hwt — Semi shock wave angle estimations
hs — Semi top angle
n — Number of steps
m0 — Mach number of the undisturbed flow
Ms — Machnumber at the cone surface
P2 — Perturbation P'' of the quantity P
cp2 — Perturbation cp_s'' of the quantity cp
u2,v2,w2 — The quantities u'',v'',w''
rdvdxf, rdvdxb — The quantities $r(\delta v/\delta x)_f$ and $r(\delta v/\delta x)_b$
a — The quantity α

1 Introduction

Since the introduction of the electronic computer, the possibilities for the study of flow fields around certain kinds of configurations have increased enormously. Only ten years ago, no other practical solutions were available than those based on the so-called linearized potential theory. Although a few other general schemes were known, their application was prohibited, because of the large amount of time and money involved.

Especially in the field of the computation of supersonic flow regions the assistance furnished by electronic computers is more or less crucial to the solution of certain problems. In the following lines this statement will be discussed in more detail.

As is known by now, for a reliable solution of the flow field around a certain configuration, the use of linearized theory is not permissible in most cases. To remedy this situation use has to be made of the governing non-linear differential equations. Fortunately an attractive numerical scheme can be developed for the computation of the solution of these equations. This scheme is based on the concept of characteristic surfaces. These are in fact the surfaces separating the region where a disturbance occurring in a certain point is experienced from the region where it is not. At this moment the calculation schemes for the supersonic flow around two-dimensional and axially-symmetric configurations have obtained a high degree of generality. The development of such schemes for three-dimensional flow fields is still in its earliest phase, due to the enormous difficulties attached to it.

Since the differential-equations are non linear, the computation of the values in a certain point can be achieved only by an iterative procedure. This is why the use of electronic computers is necessary. Even then much skill is required to make the numerical scheme and the programme in such a way that the computation time and thus the costs are not unreal.

In order to use such schemes, we have to start from a set of initial data. From the general theory of hyperbolic equations it is known that for given initial data along a surface, not coinciding with a characteristic surface, a solution can be constructed in the neighbourhood of this surface. This solution, however, cannot be extended outside the volume enclosed by the characteristic surfaces through the boundary of the region for which the initial data are given. A sketch of this situation is given in fig. 1. For practical cases the situation is totally different.

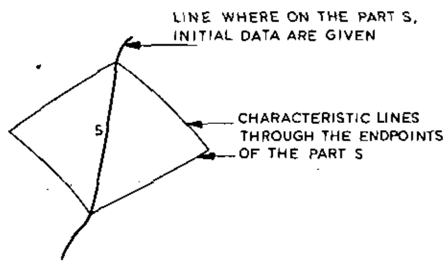

Fig. 1. The largest region where a solution exists.

There it will be required to calculate the flow field around a given configuration and for a given Mach number of the undisturbed stream. Along the surface of the configuration the flow quantities are related to each other because this surface is a stream surface. It can be shown then that the construction of the flow field with the method of characteristics is possible only if the values of the flow quantities are known along a certain surface in this flow field. This may be a characteristic surface as well. The determination of such a surface is in fact the key to the solution of the whole problem. It is evident from fig. 2 that we should have such a situation if we knew the

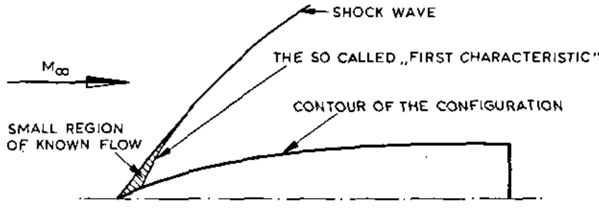

Fig. 2. The initial data necessary for the computation of the flow field.

flow field around the small region near the nose of the configuration. Then it is possible to obtain the flow quantities along a characteristic surface, which is necessary for the construction of the complete flow-field. As we deal in the following only with cases for which the flow is axially or quasi-axially symmetric we will refer to this surface as to the "first characteristic". In the case of pointed bodies this means that the flow is conical in a small region near the nose. It must be observed that this does not necessarily mean that the configuration itself has to be axially-symmetric.

The study of the flow around cones has been very extensive, and in fact already in 1933 a solution, based on non linear differential equations, was obtained by Taylor and Maccoll (ref. 1). A table of computed results was published in 1947 by Kopal and his staff (ref. 2). It is interesting to note that this table was computed with the aid of ordinary desk computers. Further progress was made when Stone succeeded in solving the problem for the flow around an inclined cone by using the technique of superimposing a small perturbation term on the purely axially-symmetric flow (ref. 3). This solution was tabulated by Kopal as well (ref. 4).

The question may be raised now, if there is any need to present here once more a rather thorough investigation of such flows. However, these conical solutions are so important, because of the fact that they furnish the initial conditions necessary for the determination of the whole flow field. It will then be clear that for a reliable solution, these initial data have to be known accurately. Moreover it will be necessary to have the ability to determine these initial conditions for arbitrary values of semi-top angle, ratio of specific heats and the Mach number of the undisturbed stream. Such a solution can be obtained in principle by interpolating in the tables of refs. 2 and 4. Besides of causing a large amount of work, this solution will almost always be too inaccurate for the use it is intended for.

It was therefore decided to develop a very universal programme for the calculation of the flow around cones with and without inclination. This program gives all the information along the "first characteristic".

Although a second order perturbation theory for cones at large angles of yaw has been developed, this case will not be considered because of the fact that no method exists for the calculation of more general flow fields using this second order theory.

The purpose of this report is to present the details of the above mentioned universal programme and the way followed to formulate it.

Therefore, the first part of this report gives a review of the theoretical formulation of these problems and discusses the requirements for the programme.

The programme itself and the numerical schemes on which it is built will be described afterwards. It has been presented in this report in the form of an ALGOL programme, because this is an internationally accepted machine language.

The original programme, however, was written in the code of the computer actually in use at the NLR, since this works faster than ALGOL.

The main features of the programme are shown in a block diagram. An example is discussed to show the results which can be obtained.

2 The formulation of the conical problems to be solved

In this section the differential equations and the boundary conditions that govern the flow around circular cones will be reviewed both for the cases of zero and non-zero inclination. In this presentation, only those formulae are given which pertain to the problem.

2.1 *The case of zero inclination*

In fig. 3 the coordinate systems for analysing this case are presented, namely the spherical system (R, ϑ) and the system (x, r). The velocities in these systems are $(\bar{u}, \bar{v})$ and (u, v) respectively. The semi-top angle of the cone

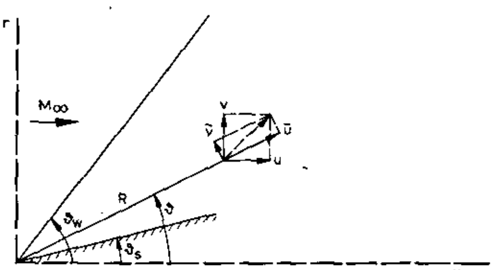

Fig. 3. Coordinate systems and related velocities.

surface is given by ϑ_s, while ϑ_w denotes the half angle of the shock-wave. M_∞ is the Mach number of the undisturbed stream.

The differential equations governing the problem are given by

$$\frac{d\bar{v}}{d\vartheta} + \bar{u} = \frac{\bar{a}^2(\bar{u}+\bar{v}\cot\vartheta)}{\bar{v}^2-\bar{a}^2} \qquad (2.1)a$$

$$\frac{d\bar{u}}{d\vartheta} - \bar{v} = 0 \qquad (2.1)b$$

where the local speed of sound $\bar{a}$ is given by

$$\bar{a}^2 = \left(\frac{1}{M_\infty^2} + \frac{\gamma-1}{2}\right) U_\infty^2 - \frac{\gamma-1}{2} (\bar{u}^2 + \bar{v}^2) \tag{2.2}$$

and U_∞ is the velocity of the undisturbed stream.

In most of the applications, use will be made of the velocity components u and v which are non-dimensional. The following relations exist

$$\bar{u} = U_\infty \{ \quad u \cos \vartheta + v \sin \vartheta \} \tag{2.3)a}$$

$$\bar{v} = U_\infty \{ -u \sin \vartheta + v \cos \vartheta \} \tag{2.3)b}$$

The system of differential equations is then transformed into

$$\frac{\mathrm{d}u}{\mathrm{d}\vartheta} = \frac{-a^2 v}{(v \cos \vartheta - u \sin \vartheta)^2 - a^2} \tag{2.4)a}$$

$$\frac{\mathrm{d}v}{\mathrm{d}\vartheta} = -\cot \vartheta \frac{\mathrm{d}u}{\mathrm{d}\vartheta} \tag{2.4)b}$$

where

$$a^2 = \frac{1}{M_\infty^2} + \frac{\gamma-1}{2} - \frac{\gamma-1}{2} (u^2 + v^2) . \tag{2.5}$$

The boundary conditions pertain to the cone surface and the shock wave respectively. The condition for the cone surface to be a stream surface is given by

$$u = v \cot \vartheta_s . \tag{2.6}$$

The conditions at the shockwave are given by

$$u - 1 = -v \tan \vartheta_w \tag{2.7)a}$$

$$u - 1 = \frac{2}{\gamma+1} \frac{1 - M_\infty^2 \sin^2 \vartheta_w}{M_\infty^2} . \tag{2.7)b}$$

The equations (2.4)–(2.7) contain the complete description of the problem.

We will first discuss some of its features. As has been said in the introduction in most cases the Mach number M_∞, the semi-top angle ϑ_s and the value of γ will be given. It is clear that the problem is, to solve the two non-linear differential equations (2.4) given the edge conditions (2.6) and (2.7)b, while the value of the shock angle ϑ_w defined by eq. (2.7)a is still unknown. This can only be achieved by an iteration procedure. One of the more easy schemes is the following.

Choose a value for u at $\vartheta = \vartheta_s$. From eq. (2.6) v can be calculated and hence it is possible to start the solution of the differential eqs. (2.4)a and b. The solution procedure is continued until a value of ϑ is reached which satisfies eq. (2.7)a. From eq. (2.7)b there follows then the value of M_∞. In general this will not be equal to the prescribed value. Hence by choosing a slightly different value of u at $\vartheta = \vartheta_s$, an iteration with respect to M_∞ can be made, until a certain required accuracy is obtained. Another probably more attractive scheme is to choose a value for ϑ_w. Then from eq. (2.7)b the value of u can be computed and from eq. (2.7)a the value of v. The solution can now be started and continued until $\vartheta = \vartheta_s$, where in general eq. (2.6) will not be satisfied. In that case an iteration with respect to $\vartheta = \vartheta_w$ is performed until eq. (2.6) is satisfied.

Although there is in principle no difference between the two methods, the latter appears to be the better one.

When the value of the shock-wave angle is determined, it is possible to calculate the rise in entropy, accompanying the shockwave.

This can be expressed in terms of the ratio P of the stagnation pressures behind and before the shockwave.

$$P = \left[\frac{(\gamma+1) M_\infty^2 \sin^2 \vartheta_w}{(\gamma-1) M_\infty^2 \sin^2 \vartheta_w + 2}\right]^{\gamma/(\gamma-1)} \left[1 + \frac{2\gamma}{\gamma+1} (M_\infty^2 \sin^2 \vartheta_w - 1)\right]^{-1/(\gamma-1)} \tag{2.8}$$

Once the velocities u and v are known as a function of ϑ it is possible to construct a first characteristic by using the equation for the characteristic direction. For a positive slope the direction is given by

$$\frac{\mathrm{d}r}{\mathrm{d}x} = \frac{u + \beta v}{\beta u - v} \tag{2.9}$$

where

$$\beta = \sqrt{\frac{u^2+v^2}{a^2} - 1}\,.$$

Usually, as an initial condition, the coordinate x of a point at the cone surface will be given. In constructing a characteristic a difficulty is encountered, which should be discussed here. In solving the differential equations use will be made of a difference method based upon a certain stepwidth $\Delta\vartheta$. At first sight, it may seem advantageous to use a constant stepwidth, since a variety of numerical schemes has been developed for that particular case. However, in that case the points lying on the first characteristic are distributed unequally as is shown in fig. 4, especially for low Mach numbers and small values of the semi top-angle.

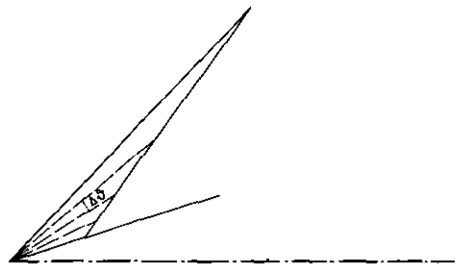

Fig. 4. Stepwidth ΔX on first characteristic for constant value of $\Delta\vartheta$.

Since this characteristic has to be used for the calculation of the flow-field such a distribution is not very appropriate. It is desirable to have a distribution with a more or less constant stepwidth Δx. (Although a better numerical accuracy is obtained with a constant stepwidth $\Delta\vartheta$ for the same number of points). In that case the stepwidth $\Delta\vartheta$ cannot be held constant but has to vary from point to point. Therefore a numerical scheme has to be used which permits the continuous change of the stepwidth $\Delta\vartheta$. The actual choice made will be discussed in the section devoted to the description of the programme. First we will proceed to the theoretical formulation for the case of an inclined cone.

2.2 The case of non-zero inclination

The flow around a cone with a small angle of inclination ε can be determined by superimposing a perturbation term on the axially-symmetric flow. Taking into account only terms linear in ε a scheme can be developed for the determination of the first order perturbation velocities. Such a scheme has been given by Stone in ref. 3. For a good understanding it is necessary to recall its main features, although for a more thorough presentation the reader is referred to refs. 3 and 5. The problem is solved not for the actual flow field, but for a so-called transformed field which is obtained by transforming the conditions on the actual boundaries to conditions along the surface of cone and shock wave for the axially symmetric case. It is assumed that the total velocities in a spherical coordinate system are given by

$$U = \bar{u}+\varepsilon x \cos\psi \tag{2.10a}$$

$$V = \bar{v}+\varepsilon y \cos\psi \tag{2.10b}$$

$$W = \varepsilon z \sin\psi\,. \tag{2.10c}$$

As is shown in ref. 3 the inclined shape of the shock wave again is a cone with an angle of inclination given by $\alpha\varepsilon$. The coefficient α follows from the analysis, and is dependent on the quantity d. This quantity defines the perturbation in the ratio of the stagnation pressures. If the total ratio is defined by P_1 then

$$P_1 = P\left\{1-\varepsilon\,\frac{d}{\gamma-1}\cos\psi\right\}. \tag{2.11}$$

Before turning to the equations used in this report, we will first give the system of equations derived by Stone for this case

$$\frac{d^2x}{d\vartheta^2} + A\,\frac{dx}{d\vartheta} + Bx+Cd=0 \tag{2.12a}$$

$$\frac{dx}{d\vartheta} - y=0 \tag{2.12b}$$

$$x+z\sin\vartheta - \frac{Cd\sin^2\vartheta}{1+\lambda\bar{v}} = 0 \tag{2.12c}$$

where

$$A = \cot\vartheta + \lambda[(\bar{u}+\bar{v}\cot\vartheta)\{(\gamma+1)\lambda\bar{v}+2\}+\bar{v}\cot\vartheta]$$

$$B = 1-\cot^2\vartheta + \lambda[\lambda(\gamma-1)\bar{u}(\bar{u}+\bar{v}\cot\vartheta) - \bar{v}\cot^2\vartheta]$$

$$C = \frac{1+\lambda\bar{v}}{(\gamma-1)\sin^2\vartheta}\sqrt{-\bar{v}\bar{p}\sin\vartheta}\int_{\vartheta_w}^{\vartheta}\frac{\bar{p}\sin\varphi}{\{\sqrt{-\bar{v}\bar{p}\sin\varphi}\}^3}\,d\varphi$$

The quantity λ, the pressure $\bar{p}$ and the density $\bar{\rho}$ are given by

$$\lambda = \frac{\bar{v}}{\bar{a}^2-\bar{v}^2}, \quad \bar{p} = \frac{1}{\gamma M_\infty^2}(a^2 M_\infty^2)^{\gamma/(\gamma-1)}\cdot P \quad \text{and} \quad \bar{\rho} = (a^2 M_\infty^2)^{1/(\gamma-1)}\cdot P\,.$$

From a numerical point of view the quantity C causes difficulties because the integrand is highly singular for $\vartheta=\vartheta_s$ (since $\bar{v}$ tends to zero as $-2\bar{u}(\vartheta-\vartheta_s)$) although C itself remains finite. This difficulty will be discussed and solved in the following presentation of the same formulae but now based on the cylindrical flow quantities given by u'', v'', w'' and P''. The total values are then given by

$$u_1 = u+\varepsilon u''\cos\psi \tag{2.13)a}$$
$$v_1 = v+\varepsilon v''\cos\psi \tag{2.13)b}$$
$$w_1 = \varepsilon w''\sin\psi \tag{2.13)c}$$
$$P_1 = P+\varepsilon P''\cos\psi \tag{2.13)d}$$

The relations between the two systems have the following form

$$x = u''\cos\vartheta+v''\sin\vartheta \tag{2.14)a}$$
$$y = -u''\sin\vartheta+v''\cos\vartheta \tag{2.14)b}$$
$$z = w'' \tag{2.14)c}$$
$$d = -(\gamma-1)\frac{P''}{P} \tag{2.14)d}$$

The system now reduces to a set of two simultaneous first-order differential equations for u'' and v''.

$$\frac{du''}{d\vartheta} + a^2\mu\cot\vartheta u'' - \mu^2 v(v\cos\vartheta - u\sin\vartheta)\{(\gamma-1)(v\cos\vartheta - u\sin\vartheta)\cdot$$
$$\cdot(uu''+vv'') + 2a^2(v''\cos\vartheta - u''\sin\vartheta)\} + C'\frac{P''}{P'} = 0 \tag{2.15)a}$$

$$\cot\vartheta\frac{du''}{d\vartheta} + \frac{dv''}{d\vartheta} = 0 \tag{2.15)b}$$

where

$$C' = \frac{a^2\mu}{\sin\vartheta}\sqrt{-\bar{v}\bar{p}\sin\vartheta}\int_{\vartheta_w}^{\vartheta}\frac{\bar{p}\sin\varphi}{\{\sqrt{-\bar{v}\bar{p}\sin\varphi}\}^3}\,d\varphi \quad \text{and} \quad \mu = \frac{1}{a^2-(v\cos\vartheta-u\sin\vartheta)^2}$$

By partial integration this highly singular integral can be written in a much easier form, as regards numerical computation.

$$C' = \frac{a^2\mu}{\sin\vartheta}\left\{-\frac{a^2}{\gamma(u\cos\vartheta+v\sin\vartheta)} + \frac{a_{\vartheta_w}^2\sqrt{(a^2)^{1/(\gamma-1)}\{u\sin\vartheta-v\cos\vartheta\}\sin\vartheta}}{\gamma\cos\vartheta_w\sqrt{(a_{\vartheta_w}^2)^{\gamma/(\gamma-1)}\{u_w\sin\vartheta_w-v_w\cos\vartheta_w\}\sin\vartheta_w}} + \right.$$
$$\left. + C''\sqrt{(a^2)^{1/(\gamma-1)}\{u\sin\vartheta-v\cos\vartheta\}\sin\vartheta}\right\} \tag{2.16)a}$$

where

$$C'' = \int_{\vartheta_w}^{\vartheta}\frac{\sqrt{u\sin\varphi-v\cos\varphi}}{\sqrt{(a^2)^{1/(\gamma-1)}\sin\varphi}}\,\frac{a^2}{\gamma(u\cos\varphi+v\sin\varphi)^2}\cdot\left\{1-\frac{(\gamma-1)\mu v}{\sin\varphi}(u\cos\varphi+v\sin\varphi)\right\}d\varphi\,. \tag{2.16)b}$$

As can be seen the value of C' for $\vartheta=\vartheta_s$ is given by the first term of eq. (2.16)a, while the integral C'' does not give any difficulty for the numerical calculation. Due to the fact that the first derivate of C' becomes infinite at

$\vartheta = \vartheta_s$, a succesful integration of the differential equations (2.15) is possible only when a more thorough investigation is made of the solution in the region near to the body. This analysis has been given in appendix A.

The set of equations (2.15) can be solved now for a given set boundary conditions, given by

$$u'' = + \frac{a^2 \sin\vartheta \cos\vartheta}{\gamma(\gamma+1)v^2} \{(\gamma-1)v + 6 \sin\vartheta \cos\vartheta\} \frac{P''}{P} \quad \text{for} \quad \vartheta = \vartheta_w \tag{2.17a}$$

$$v'' = -u'' \cot\vartheta + \frac{a^2 P''}{\gamma v P} \quad \text{for} \quad \vartheta = \vartheta_w \tag{2.17b}$$

while on the cone surface $\vartheta = \vartheta_s$ it can be prescribed that

$$v'' - u'' \tan\vartheta_s + \frac{2u}{\cos^2\vartheta_s} = 0\,. \tag{2.18}$$

It must be observed that some of the equations contain the hitherto unknown constant P''. Due to the linearity of the equations it is quite obvious that the system can be solved easily by considering the quantities $(u''/P'')P$ and $(v''/P'')P$. Then eqs. (2.17) are sufficient to start the solution, calculating just as in the axially symmetric case, from the shock wave surface towards the cone surface. The value of P'' and hence those of the quantities u'' and v'' themselves follow from eq. (2.18) once the solution has been continued until $\vartheta = \vartheta_s$.

The tangential perturbation velocity w'' is given by

$$w'' = -u'' \cot\vartheta - v'' - \frac{P''}{a^2 \mu P} C' \tag{2.19}$$

while the quantity α, representing the inclination of the shock wave follows from

$$\alpha = \frac{a^2 P'' \cos\vartheta \sin\vartheta}{\gamma v^2 P} \quad \text{for} \quad \vartheta = \vartheta_w\,. \tag{2.20}$$

It should be observed that contrary to the definition used by Stone, the angle ε is considered as positive if the axis is deflected downwards (fig. 5).

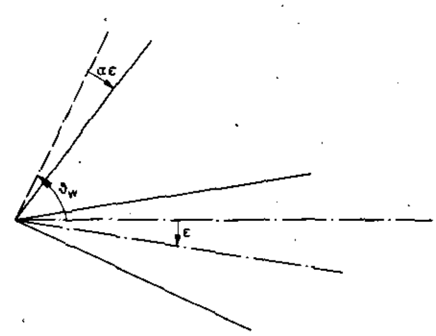

Fig. 5. Position of cone surface and shock wave for a positive angle of attack.

The formula given above for the flow around a cone with and without inclination contain the information needed to construct the programme, at least in principle. This programme will be discussed in the following.

3 Discussion of the programme

This section consists of two parts, the first giving the general layout of the programme in connection with the requirements to be met, while the second part gives more detailed information about the programme itself.

3.1 *Preliminary considerations*

In order to construct a programme, it is needed to formulate what kind of input data will occur and what is the best form in which the output data can be given. Furthermore some details which have not been considered in the foregoing analysis will have to be discussed.

As has been said in the introduction the purpose of the programme is to give a set of initial data for the construction of the flow-field around an axially symmetric or quasi-axially symmetric configuration. Then nearly always the Mach number M_∞, the semi-top angle ϑ_s of the nose and the ratio of specific heats γ will be given.

These data, however, are not sufficient for the construction of a characteristic; in addition the axial coordinate of the point at the cone surface through which the characteristic passes has to be given. Although it is possible to construct a forward facing or a backward facing characteristic, only the latter case is considered here. Moreover we have to recall the fact that the computation includes an iteration with respect to the initially unknown quantity ϑ_w, being the semi-top angle of the shock surface. Therefore, it is necessary to provide two estimated values for ϑ_w. Starting with these values the iteration procedure, which includes the computation of the complete axially-symmetric solution for each step, can be performed automatically. Obviously much work can be saved by using a very close estimate. To facilitate this, diagrams have been given in figures 6 and 7, prescribing the values of ϑ_w as a function of M_∞ and ϑ_s for two values of γ. In each case there is a lower limit for ϑ_w given by

$$\vartheta_w > \sin^{-1}\frac{1}{M_\infty}. \tag{3.1}$$

Another point which has to be referred to with respect to the input data is the following. Not always one will be interested in obtaining the flow field for an inclined cone. Thus it is feasible to give as input data a code for

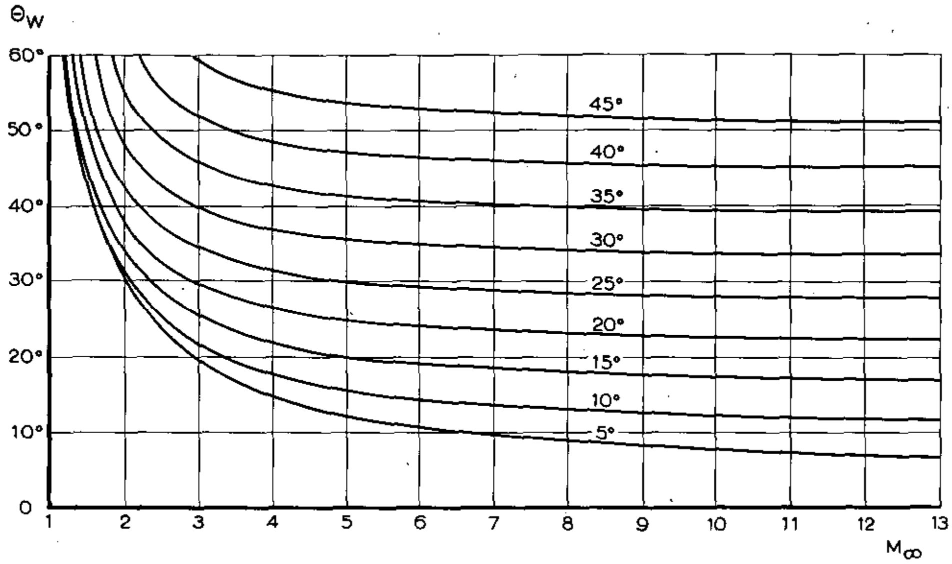

Fig. 6. The shock wave angle ϑ_w as a function of Mach number M and semi-top angle ϑ_s for $\gamma = 1.405$.

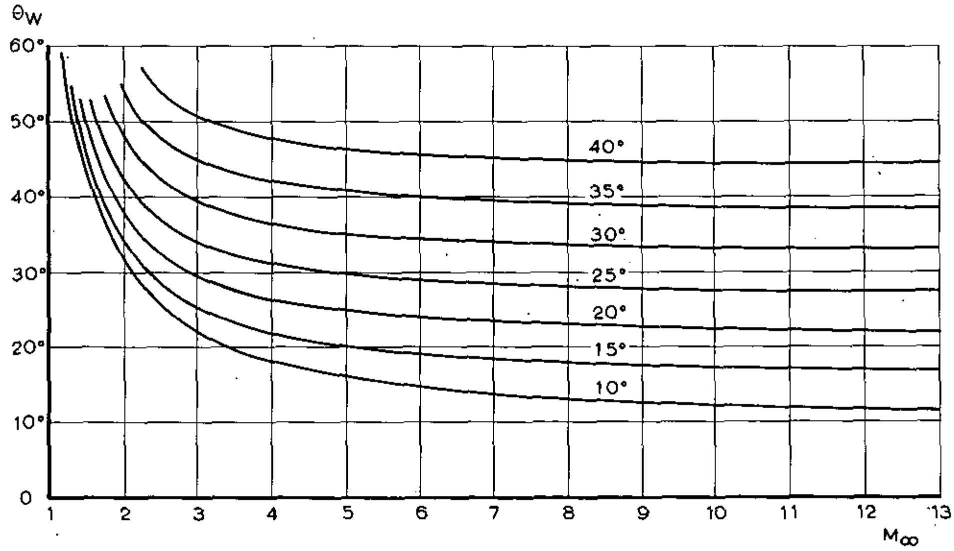

Fig. 7. The shock wave angle ϑ_w as a function of Mach number M and semi-top angle ϑ_s for $\gamma = 4/3$.

either "zero inclination" or "non-zero inclination". In the first case the programme will compute the axially-symmetric flow and stop, while in the second case it will continue with the computation of the inclined field. (As will be clear from the theoretical description, the latter field cannot be computed without a knowledge of the axially-symmetric flow). Since, as has already been remarked a constant stepwidth $\Delta\vartheta$ gives a better accuracy for the same number of steps compared to a method where Δx along the first characteristic is approximately constant, the programme is made such that by a suitable input code either the one or the other possibility is used. The most common form for the output data will be a table giving the geometry of the characteristic constructed and the velocity distribution along it. Thus for the axially-symmetric flow the table will consist of a set of columns giving the corresponding values of u, v, x and r. For the "non-zero inclination" case the set of values will be u, v, u'', v'', w'', x and r. However, this is not the complete set of quantities which are needed, since, as follows from ref. 5, for the computation of the flow around an inclined body also the values of $r(\delta v/\delta x)_b$ and $r(\delta v/\delta x)_f$ have to be known. These quantities are the derivatives with respect to x of the radial axially-symmetric velocity v along the constructed characteristic and along the set of characteristics intersecting this characteristic, respectively. They are given by the following formula

$$r\left(\frac{\delta v}{\delta x}\right)_b = a^2 \mu v \cos^2 \vartheta \left\{\tan \vartheta - \frac{u+\beta v}{\beta u - v}\right\} \tag{3.2)a}$$

$$r\left(\frac{\delta v}{\delta x}\right)_f = a^2 \mu v \cos^2 \vartheta \left\{\tan \vartheta + \frac{u-\beta v}{\beta u + v}\right\}. \tag{3.2)b}$$

In addition it seems advantageous to give a set of quantities characterizing the solution. For the axially-symmetric case these are, the shock wave semi-top angle ϑ_w, the ratio of stagnation pressures P, the coefficient c_{p_s} and the Mach number M_s, both on the cone surface. The latter two are given by

$$c_{p_s} = \frac{2}{\gamma M_\infty^2} \left\{(a^2 M_\infty^2)^{\gamma/(\gamma-1)} P - 1\right\}_{\vartheta=\vartheta_s} \tag{3.3}$$

$$M_s = \sqrt{\frac{u^2+v^2}{a^2}} \quad \text{for} \quad \vartheta=\vartheta_s \tag{3.4}$$

For the inclined field this set will be completed by giving the values of the shock wave inclination factor α and the perturbation terms P'' and c''_{p_s} where the latter quantity is defined by

$$c_{p_1} = c_p + \varepsilon c''_p \cos \psi . \tag{3.5}$$

The value of c''_{p_s} is given by

$$c''_{p_s} = \left\{c_p + \frac{2}{\gamma M_\infty^2}\right\} \left[\frac{P''}{P} - \gamma \frac{uu''+vv''}{a^2}\right]. \tag{3.6}$$

This is as far as the input and output data are concerned.

The problem which comes next is, by which method the differential equations should be integrated. As has been argumented in section 2.1 the methods available are dependent on the choice of the stepwidth. For the computation of the flow-field an approximately constant stepwidth Δx would be desirable. This means that $\Delta\vartheta$ is no longer constant and hence that any scheme for integrating differential equations using starting procedures is prohibitive. Then only those remain which are based on the method of Runge-Kutta. In the current programme use has been made of the fourth order version of this method.

To obtain an approximately equal stepwidth Δx the following procedure has been followed. Through a point at the shockwave a straight line has been drawn, tangent to the backward facing characteristic at this point. This line has been intersected by a set of lines through the vertex of the cone, such that along it a number of points is obtained with equal stepwidth Δx. In this way a distribution of stepwidth $\Delta\vartheta$ is obtained which can be expressed by the following formula, where n is the total number of steps required to cover the region $\vartheta_w - \vartheta_s$ and k is the index given to the kth step.

$$\Delta\vartheta_k = -\tan^{-1} \frac{n \sin(\vartheta_w - \vartheta_s) \sin(\alpha-\vartheta_s) \sin(\alpha-\vartheta_w)}{k(k-1)\sin^2(\vartheta_w-\vartheta_s) - n(2k-1)\sin(\vartheta_w-\vartheta_s)\sin(\alpha-\vartheta_s)\cdot\cos(\alpha-\vartheta_w) + n^2 \sin^2(\alpha-\vartheta_s)}. \tag{3.7}$$

The angle α is given, according to the above explanation by

$$\tan \alpha = \frac{u+\beta v}{\beta u - v} \quad \text{for} \quad \vartheta=\vartheta_w . \tag{3.8}$$

Although eq. (3.7) will not give an exactly equal stepwidth Δx along the characteristic, it may be expected that this distribution leads to an acceptable order of constancy of this stepwidth. Another point to be discussed, in connection with the computation procedure, is the following. When calculating the inclined field, the application of Runge-Kutta's method requires the knowledge of the quantities u and v at the middle of the step. This necessitates the computation of a double number of points for the axially-symmetric field. Since the knowledge of the results at the middle of the step is not necessary for a set of accurate values, these values do not occur in the output data. They are used and handled in the programme in a rather elegant way, as will be explained later.

Last but not least something should be said about the required and obtained accuracy of the program. A prescribed accuracy $\bar{\varepsilon}$ is given for the fulfillment of the boundary condition (2.6), while the integrations are performed following a procedure which has an error proportional to the fifth power of the stepwidth. The actual accuracy can best be checked by performing a computation with half the step. The differences will give an indication of the accuracy, and a quick determination can usually be made about the number of points required to obtain a given accuracy.

The analysis of the programme itself, will be given in the next section, with the aid of the appendices, B and C containing a flow diagram and the programme respectively.

3.2 *Analysis of the programme*

Before giving a description of the total programme, the most important parts of it are described first, since this will be of great help in understanding its layout.

3.2.1 *Description of the most important parts of the programme*

The programme, roughly speaking, consists of a number of procedures, the performance of which is controlled by so-called "labels". The results are stored in "arrays". In order to be able to make a certain choice, use is made of "switches".

(a) *Procedures*:

— The procedure dudv(h, u, v) computes the derivatives of u and v at the angle h after eqs. (2.4)a and b. This procedure is called in by the integration procedure. Note that the ALGOL notation for ϑ is h. A full list of the correspondence between the various symbols is contained in the list of symbols.

— The procedure du2 dv2 (h, u2, v2) calculates the derivatives of u'' and v'' at the angle h, after eqs. (2.15)a and b. The quantities u and v necessary for this computation, are taken from the array H (see below). This procedure also is called in by the integration procedure only.

— The procedure df1df2(h, f_1, f_2) calculates the derivatives of f and $\bar{f}$ at the angle h, according to eqs. A(4)a and A(4)c. This procedure is used only for the integration of the last step of the functions u'' and v''. The same remark pertains to the following procedure.

— The procedure dg1dg2(h, g_1, g_2) calculates the derivatives of g and $\bar{g}$ at the angle h, according to eqs. A(4)b and A(4)d.

— The procedure integrate (dh, Y, h, u, v) integrates with stepwidth dh, the differential equations specified by the procedure Y(dudv, du2 dv2, df1df2 or dg1dg2). These are the equations (2.4)a and b, (2.15)a and b and A(4) respectively. The integration is performed by applying the method of Runge-Kutta in its fourth order version. This means that the procedure Y for the determination of the derivatives has to be called in four times at one integration step, although always with other parameters.

— The procedure integrate (dh, Y, h, u, v) integrates with stepwidth dh, the differential equations specified by the procedure Y (dudy or du2dv2). These are the equations (2.4)a and b or (2.15)a and b respectively. The integration is performed by applying the method of Runge-Kutta in its fourth order version. This means that the procedure Y for the determination of the derivatives has to be called in four times at one integration step, although always with other parameters.

— The procedure integral (dh, h, u,v) effects the computation of the expression C' as given by eq. (2.16)a. This expression contains the integral C'' (eq. (2.16)b) which has to be evaluated between ϑ_w and ϑ. The computation is performed by using the trapezoidal rule. To this end the last obtained integral (C2) is kept in the store and the following (C3) is added.

— Finally the procedure betas (u,v) calculates the quantity β (see eq. (2.9)) for the given values of u and v.

(b) *Arrays*:

— The array result (0:n+1, 1:6) is the matrix in which the computed values of ϑ, u, v, $u''P/P''$, $v''P/P''$ and $w''P/P''$ are stored. Hence this matrix has six columns, while it has $n+2$ rows to store the appropriate quantities belonging to the coordinates ϑ_w, ϑ_w+dh_1, $\vartheta_w+dh_1+dh_2 \ldots \vartheta_w+dh_1+dh_2+\ldots+dh_n=\vartheta_s$. Thus the matrix has one row more than is necessary for the storage of the coordinates. This has a special reason which will become clear subsequently. In the case of zero inclination the u is stored in the second column and the v is stored in the third column. (These quantities are also stored in the fourth and fifth column, but this is due to the peculiar scheme used for the non-zero inclination case).

In the case of non-zero inclination not only the values of u and v have to be calculated at ϑ_w+dh_1, $\vartheta_w+dh_1+dh_2$, etc. but also at $\vartheta_w+\frac{1}{2}dh_1$, $\vartheta_w+dh_1+\frac{1}{2}dh_2$, etc. The storage of the values of u and v at the center of the stepwidth is carried out by using a two-fold count, by which the results appear in the fourth and fifth column of the array. This procedure will be presented in some more detail when describing the programme itself.

When these results are known it is possible to calculate the values of u'', v'' and w'' at the different coordinates. They are stored in the fourth, fifth and sixth column, thus deleting the former information on the fourth and fifth column which is no longer necessary.

— The array H is used in two different ways.

During the computation of the axially-symmetric field (u and v) the values of the estimates of the shockwave

semi-angle ϑ_w are stored at H[0] and H[1] while the corresponding values of the quantity $u - v \cot \vartheta_s$ are stored at H[2] and H[3]. These data are necessary for the interpolation of a new ϑ_w. During the calculation of the inclined field the array is used together with the procedure du2dv2. Then it contains the values of u and v at the points ϑ, $\vartheta + \frac{1}{2}h$ and $\vartheta + h$, as well as the values of the quantity C′ at these points. (The values at $\vartheta + \frac{1}{2}\mathrm{d}h$ are stored twice, hence the array consists of 12 places).
The array c2[0:3] is used to store the values of the integral C″ when calculating the last step with the functions $f, \bar{f}, g$ and $\bar{g}$.

(c) *Switches*:
There are four switches: zero, first, switch and theta.
The switch "zero" indicates either $z=0$ (zero is false) or $z \neq 0$ (zero is true). The first case means that only the axially-symmetric field is calculated while in the second case also the inclined field is calculated.
The switch "first" is in part independently used when iterating the value of ϑ_w, where it controls the interpolation between two estimated values.
Furthermore it is used conditionally, since for $z \neq 0$ it controls the value of the quantity C′ at the cone surface (at the surface C′ must equal zero).
The switch "switch" is conditional, that means that it is only used when $z \neq 0$. It controls the calculation of u and v at half the interval.
The switch "theta" indicates either th$=0$ (theta is false) or th$\neq 0$ (theta is true). In the first case the flow is calculated with an approximately constant stepwidth Δx, while in the second case the stepwidth in ϑ direction is constant.

(d) *Labels*:
The following labels have been used.
AA Start of the integration cycle for the zero inclination-velocity field.
BB Sublabel of AA, controls the integration cycle for the determination of the quantities u and v for $x \neq 0$, hence when also the values halfway of the interval dh are needed.
CC Computation of the initial values of u and v.
DD Interpolation of a new value of ϑ_w.
EE Start of the integration cycle for the determination of u'', v'' and w'' (inclined field).
FF Start of output.
GG Output of the data characterizing the solution.
HH Integration of the last step when determining u'', v'' and w''.

(e) *Special procedures*:
PUNLCR : punches new line, carriage return on the output tape.
FIXP (n,m,x) : punches the fixed point number x with n figures before and m figures after the point.
FLOP (n,m,x): punches the floating point number x with a mantisse of n figures and an exponent of m figures.
PUTEXT 1 ($\nless$ text $\ngtr$): punches the text between the strings.
Since the material, which is necessary for the understanding of the programme has been covered now, we can give a more extensive analysis of the performance of the programme.

3.2.2 *Description of the programme*
This section is based on the flow diagram contained in appendix B and the programme itself contained in appendix C.
The programme begins with reading the input data: m0, g, hs, hw, hwt, x, eps, n, z and th (see list of symbols).
The switches: zero, first switch, and theta are set.
The programme starts the calculation by computing the initial values of u and v at the shock wave. They are stored in the array result $(0:n+1, 1:6)$. After the calculation of some constants necessary for the computation of the dh distribution, two counts i and j are set. The programme proceeds by computing the first step dh (label AA). This quantity is halved if "zero=true" thus enabling the determination of u and v halfway of the interval. Then one integration step is performed and this is repeated, in the manner to be described next until $\vartheta = \vartheta_s$.
Assume that the $(k-1)$th step has been performed. The situation will be then as described in the array results for the two cases $z=0$ and $z \neq 0$.

$z=0$

ϑ_{k-1}	U_{k-1}	V_{k-1}	U_{k-1}	V_{k-1}

$z \neq 0$

ϑ_{k-1}	U_{k-1}	V_{k-1}	$U_{k-\frac{1}{2}}$	$V_{k-\frac{1}{2}}$
			U_{k-1}	V_{k-1}

Note that the results for $z \neq 0$ for the values of u and v halfway the interval $(\vartheta_{k-2}, \vartheta_{k-1})$ are stored in the fourth and fifth column on the row ϑ_{k-1}. We will now consider the calculation of the next values for u and v in both cases. At the end of the step $(k-1)$ in both cases the counts i and j are set equal to k. The programme now executes one integration step being dh for $z=0$ and dh/2 for $z \neq 0$. The results are stored as follows: u in (i,2) and (j,4) and v in (i,3) and (j,5). The array results will now be as follows.

$z=0$

ϑ_{k-1}	U_{k-1}	V_{k-1}	U_{k-1}	V_{k-1}
ϑ_k	U_k	V_k	U_k	V_k

$z \neq 0$

ϑ_{k-1}	U_{k-1}	V_{k-1}	$U_{k-\frac{3}{2}}$	$V_{k-\frac{3}{2}}$
$\vartheta_{k-\frac{1}{2}}$	$U_{k-\frac{1}{2}}$	$V_{k-\frac{1}{2}}$	$U_{k-\frac{1}{2}}$	$V_{k-\frac{1}{2}}$

Hence for $z=0$, simply the following row is calculated, while at the end of this step the counts i and j are both increased with one unit to $k+1$. In the case $z \neq 0$ the situation is a little more complicated. In the row k the results u and v halfway of the interval $(\vartheta_{k-1}, \vartheta_k)$ are stored. Note that the values U_{k-1} and V_{k-1} in the fourth and fifth column of this row are deleted and replaced by $U_{k-\frac{1}{2}}$ and $V_{k-\frac{1}{2}}$. After the calculation of the first half of the step, the count j is increased one unit and the calculation of the second half of the step is performed. When the results are stored after this step, the array takes the following shape

$z \neq 0$

ϑ_{k-1}	U_{k-1}	V_{k-1}	$U_{k-\frac{3}{2}}$	$V_{k-\frac{3}{2}}$
ϑ_k	U_k	V_k	$U_{k-\frac{1}{2}}$	$V_{k-\frac{1}{2}}$
			U_k	V_k

Hence the first three columns of the kth row are deleted and replaced while also the fourth and fifth column of the row $(k-1)$ are used. The situation is now similar to that shown in the array result after the calculation of the step $(k-1)$. Therefore the calculation can proceed in the same way from here on, when it is increased by one unit and j is decreased by the same amount, thus setting them both equal to $k+1$.

If $i=n+1$ the programme tests the boundary condition. If it is not satisfied the whole program is repeated with a new value of $\vartheta_w(h_w t)$. By using the first four places of the array H, an iteration procedure is performed until finally the boundary condition is satisfied for a given accuracy eps. In that case the quantities P and c_p are calculated, while also the characteristic through the given point x is computed. In the case of zero inclination the quantities M_∞, ϑ_s, γ and n together with the appropriate text is punched. The j count is set equal to zero and the programme jumps to label FF.

In the case of non-zero inclination the inclined velocity field has to be computed now. First the initial values of $u''P/P''$, $v''P/P''$ and $w''P/P''$ are computed for $\vartheta=\vartheta_w$ and the value of the integrand of C'' at the shock is determined. The quantities $u''P/P''$, $v''P/P''$ and $w''P/P''$ are stored in the array result (0:n+1, 1:6) at the places (0,4), (0,5) and (0,6) respectively.

The programme starts the integration cycle for u'' and v'' at label EE. At this label the j count is increased by one unit and the necessary dh is computed by subtraction of results (j,0) and (j−1, 0).

The integrals (C'') from ϑ_w to $\vartheta_w - \frac{1}{2}\Delta\vartheta$ and from ϑ_w to $\vartheta_w - \Delta\vartheta$ are stored in the array H just as the values of u and v necessary for the execution of one integration step. This integration step is now performed and the results are stored at (j,4), (j,5) and (j,6). The first two results replace the values for u and v halfway of the interval considered. As long as $j \leqslant n-1$ the programme proceeds with the determination of the solution u'', v'' and w'' by repeating the same operation. If $j=n$, the programme jumps to label HH and performs the last integration step by using the appropriate formula for determining $f, \bar{f}$, g and $\bar{g}$. Finally the values of P'' and Cp'' are computed. Then just as for $z=0$ the quantities M_∞, ϑ_s, γ and n are punched together with the necessary text and the programme jumps to label FF.

The programme punches the values of u, v, x and r along the characteristic and if $z \neq 0$ also the values of u'', v'', w'', $r\,(dv/dx)_b$ and $r\,(dv/dx)_f$. At last the characteristic quantities ϑ_w, P, c_p and M_s are punched and if $z \neq 0$ also P'', c_p'' and α.

3.3 *Some results*

In the tables 1.a and 1.b the results of routine computations with the programme has been given for $z=0$, i.e. axially-symmetric flow for the cases th=0 (Δx is constant) and th=1 ($\Delta\vartheta$ is constant) respectively. The results in these tables appear in standard form, as they are produced by the computer facilities themselves.

TABLE 1a Conical flow without inclination, dx is constant

Mo	hs	g	n
+4.154	+ .3490658	+1.405	+20

u	v	x	r
+.85257060	+.31031027	+ .02000000	+ .00727940
+.85543845	+.30254320	+ .02047374	+ .00766938
+.85804702	+.29566974	+ .02095232	+ .00805636
+.86044160	+.28951580	+ .02143575	+ .00844094
+.86265664	+.28395176	+ .02192416	+ .00882372
+.86471901	+.27887859	+ .02241775	+ .00920525
+.86665016	+.27421903	+ .02291678	+ .00958605
+.86846746	+.26991164	+ .02342159	+ .00996665
+.87018527	+.26590686	+ .02393255	+ .01034754
+.87181557	+.26216409	+ .02445009	+ .01072923
+.87336849	+.25864973	+ .02497470	+ .01111222
+.87485269	+.25533559	+ .02550691	+ .01149702
+.87627564	+.25219785	+ .02604729	+ .01188414
+.87764387	+.24921613	+ .02659650	+ .01227410
+.87896311	+.24637287	+ .02715522	+ .01266745
+.88023844	+.24365282	+ .02772422	+ .01306477
+.88147441	+.24104260	+ .02830436	+ .01346665
+.88267514	+.23853038	+ .02889656	+ .01387374
+.88384435	+.23610560	+ .02950183	+ .01428671
+.88498550	+.23375879	+ .03012133	+ .01470632
+.88610177	+.23148134	+ .03075630	+ .01513335

hw	P	cp	Ms
+ .4572599	+.79813095	+.26694736	+2.9630267

TABLE 1b Conical flow without inclination, dh is constant

Mo	hs	g	n
+4.154	+ .3490658	+1.405	+20

u	v	x	r
+.85257060	+.31031027	+ .02000000	+ .00727940
+.85423750	+.30576857	• .02026905	+ .00750175
+.85588349	+.30135780	+ .02055217	+ .00773320
+.85751232	+.29706406	+ .02085047	+ .00797447
+.85912753	+.29287473	+ .02116522	+ .00822637
+.86073248	+.28877817	+ .02149783	+ .00848980
+.86233045	+.28476353	+ .02184994	+ .00876578
+.86392464	+.28082059	+ .02222336	+ .00905546
+.86551830	+.27693956	+ .02262021	+ .00936017
+.86711469	+.27311094	+ .02304290	+ .00968141
+.86871723	+.26932538	+ .02349424	+ .01002091
+.87032950	+.26557350	+ .02397749	+ .01038070
+.87195535	+.26184576	+ .02449650	+ .01076313
+.87359898	+.25813223	+ .02505581	+ .01117097
+.87526505	+.25442236	+ .02566086	+ .01160754
+.87695883	+.25070475	+ .02631823	+ .01207683
+.87868639	+.24696674	+ .02703596	+ .01258367
+.88045486	+.24319395	+ .02782405	+ .01313408
+.88227280	+.23936963	+ .02869511	+ .01373556
+.88415070	+.23547370	+ .02966535	+ .01439775
+.88610177	+.23148134	+ .03075613	+ .01513326

hw	P	cp	Ms
+ .4572599	+.79813095	+.26694737	+2.9630267

The tables give the quantities u, v, x and r along a characteristic through the point $x=0.02$, from the surface to the shock wave. In the tables 2.a and 2.b the results for the same cases are given for $z \neq 0$. The top row has the same designation as for $z=0$. The tables give the quantities: u, v, u'', v'', w'', $r\,(dv/dx)_b$, $r\,(dv/dx)_f$, x and r in that order. The designations in the top and bottom row are given in the list of symbols.

TABLE 2a Conical flow with inclination, dx is constant

Mo	hs	g	n
+4.154	+ .3490658	+1.405	+20

u	v	u2	v2	w2	rdvdxb	rdvdxf	x	r
+.85257060	+.31031027	+ .99390846	−1.56927553	− .77153427	−.12795191$_{10}$+0	+.98412767$_{10}$−1	+ .02000000	+ .00727940
+.85543845	+.30254320	+ .97282659	−1.51216304	− .81234416	−.11732449$_{10}$+0	+.10080936$_{10}$+0	+ .02047374	+ .00766938
+.85804702	+.29566974	+ .95522686	−1.46577947	− .79373509	−.10865619$_{10}$+0	+.10329128$_{10}$+0	+ .02095232	+ .00805636
+.86044160	+.28951580	+ .94047841	−1.42786984	− .77024069	−.10143277$_{10}$+0	+.10586206$_{10}$+0	+ .02143575	+ .00844094
+.86265664	+.28395176	+ .92805784	−1.39666472	− .74628844	−.95307685$_{10}$−1	+.10852532$_{10}$+0	+ .02192416	+ .00882372
+.86471901	+.27887860	+ .91757156	−1.37086555	− .72317604	−.90038243$_{10}$−1	+.11128498$_{10}$+0	+ .02241775	+ .00920525
+.86665015	+.27421903	+ .90872218	−1.34950972	− .70132651	−.85449066$_{10}$−1	+.11414553$_{10}$+0	+ .02291678	+ .00958605
+.86846746	+.26991164	+ .90128222	−1.33187254	− .68084383	−.81410044$_{10}$−1	+.11711213$_{10}$+0	+ .02342159	+ .00996665
+.87018527	+.26590686	+ .89507574	−1.31740065	− .66170301	−.77822491$_{10}$−1	+.12019066$_{10}$+0	+ .02393255	+ .01034754
+.87181557	+.26216409	+ .88996554	−1.30566668	− .64382645	−.74610115$_{10}$−1	+.12338787$_{10}$+0	+ .02445009	+ .01072923
+.87336849	+.25864973	+ .88584420	−1.29633782	− .62711759	−.71712947$_{10}$−1	+.12671139$_{10}$+0	+ .02497470	+ .01111222
+.87485269	+.25533559	+ .88262772	−1.28915381	− .61147629	−.69083157$_{10}$−1	+.13016993$_{10}$+0	+ .02550691	+ .01149702
+.87627564	+.25219785	+ .88025094	−1.28391121	− .59680590	−.66682100$_{10}$−1	+.13377333$_{10}$+0	+ .02604729	+ .01188414
+.87764387	+.24921613	+ .87866429	−1.28045204	− .58301629	−.64478185$_{10}$−1	+.13753272$_{10}$+0	+ .02659650	+ .01227410
+.87896311	+.24637287	+ .87783140	−1.27865559	− .57002492	−.62445316$_{10}$−1	+.14146072$_{10}$+0	+ .02715522	+ .01266745
+.88023844	+.24365283	+ .87772741	−1.27843251	− .55775688	−.60561725$_{10}$−1	+.14557165$_{10}$+0	+ .02772422	+ .01306477
+.88147441	+.24104260	+ .87833791	−1.27972058	− .54614453	−.58809094$_{10}$−1	+.14988175$_{10}$+0	+ .02830436	+ .01346665
+.88267514	+.23853038	+ .87965822	−1.28248182	− .53512689	−.57171878$_{10}$−1	+.15440958$_{10}$+0	+ .02889656	+ .01387374
+.88384435	+.23610560	+ .88169310	−1.28670071	− .52464896	−.55636785$_{10}$−1	+.15917632$_{10}$+0	+ .02950183	+ .01428671
+.88498550	+.23375879	+ .88445685	−1.29238335	− .51466104	−.54192359$_{10}$−1	+.16420633$_{10}$+0	+ .03012133	+ .01470632
+.88610177	+.23148134	+ .88797373	−1.29955744	− .50511814	−.52828657$_{10}$−1	+.16952772$_{10}$+0	+ .03075630	+ .01513335

hw	P	cp	Ms	P2	cp2	a
+ .4572599	+.79813095	+.26694737	+2.9630267	+1.44716230	− 1.25367132	+ .86441042

TABLE 2b Conical flow with inclination, d*h* is constant

Mo	hs	g	n
+4.154	+ .3490658	+1.405	+20

u	v	u2	v2	w2	rdvdxb	rdvdxf	x	r
+.85257060	+.31031027	+ .99391106	−1.56927458	− .77154095	−.12795191$_{10}$+0	+.98412767$_{10}$−1	+ .02000000	+ .00727940
+.85423750	+.30576857	+ .98145552	−1.53535464	− .81481965	−.12162570$_{10}$+0	+.99766319$_{10}$−1	+ .02026905	+ .00750175
+.85588349	+.30135780	+ .96971607	−1.50387400	− .81008352	−.11578210$_{10}$+0	+.10121121$_{10}$+0	+ .02055217	+ .00773320
+.85751232	+.29706406	+ .95870864	−1.47485527	− .79837712	−.11036180$_{10}$+0	+.10275693$_{10}$+0	+ .02085047	+ .00797447
+.85912753	+.29287473	+ .94840681	−1.44813350	− .78358621	−.10531494$_{10}$+0	+.10441423$_{10}$+0	+ .02116522	+ .00822637
+.86073248	+.28877817	+ .93878318	−1.42356761	− .76718308	−.10059918$_{10}$+0	+.10619537$_{10}$+0	+ .02149783	+ .00848980
+.86233045	+.28476353	+ .92981557	−1.40103588	− .74989496	−.96178285$_{10}$−1	+.10811447$_{10}$+0	+ .02184994	+ .00876578
+.86392464	+.28082059	+ .92148899	−1.38043967	− .73213123	−.92020973$_{10}$−1	+.11018786$_{10}$+0	+ .02222336	+ .00905546
+.86551830	+.27693956	+ .91379655	−1.36170422	− .71414008	−.88100059$_{10}$−1	+.11243462$_{10}$+0	+ .02262021	+ .00936017
+.86711469	+.27311094	+ .90674029	−1.34477924	− .69607844	−.84391718$_{10}$−1	+.11487725$_{10}$+0	+ .02304290	+ .00968141
+.86871723	+.26932538	+ .90033219	−1.32963980	− .67804740	−.80874920$_{10}$−1	+.11754245$_{10}$+0	+ .02349424	+ .01002091
+.87032950	+.26557350	+ .89459559	−1.31628819	− .66011179	−.77530946$_{10}$−1	+.12046225$_{10}$+0	+ .02397749	+ .01038070
+.87195535	+.26184576	+ .88956725	−1.30475706	− .64231165	−.74342996$_{10}$−1	+.12367546$_{10}$+0	+ .02449650	+ .01076313
+.87359898	+.25813223	+ .88530036	−1.29511432	− .62466932	−.71295844$_{10}$−1	+.12722966$_{10}$+0	+ .02505581	+ .01117097
+.87526505	+.25442236	+ .88186875	−1.28747059	− .60719376	−.68375544$_{10}$−1	+.13118387$_{10}$+0	+ .02566086	+ .01160754
+.87695883	+.25070475	+ .87937309	−1.28199022	− .58988331	−.65569152$_{10}$−1	+.13561246$_{10}$+0	+ .02631823	+ .01207683
+.87868639	+.24696674	+ .87794992	−1.27890781	− .57272716	−.62864465$_{10}$−1	+.14061056$_{10}$+0	+ .02703596	+ .01258367
+.88045486	+.24319395	+ .87778524	−1.27855303	− .55570602	−.60249757$_{10}$−1	+.14630223$_{10}$+0	+ .02782405	+ .01313408
+.88227280	+.23936963	+ .87913532	−1.28138914	− .53879181	−.57713477$_{10}$−1	+.15285281$_{10}$+0	+ .02869511	+ .01373556
+.88415070	+.23547370	+ .88235987	−1.28807414	− .52194655	−.55243900$_{10}$−1	+.16048837$_{10}$+0	+ .02966535	+ .01439775
+.88610177	+.23148134	+ .88797693	−1.29956213	− .50511996	−.52828657$_{10}$−1	+.16952772$_{10}$+0	+ .03075613	+ .01513326

hw	P	cp	Ms	P2	cp2	a
+ .4572599	+.79813095	+.26694737	+2.9630267	+1.44716751	− 1.25368218	+ .86441353

It should be noted that the data necessary for an operator to use the program are: M_∞, γ, ϑ_s, ϑ_w, ϑ_{w2}, x, eps, n, z and th. With this set of quantities the results are completely determined.

4 Conclusions

This report contains a programme for the computation of the axially-symmetric flow, and for the perturbations to be superimposed on this field due to a small angle of inclination.

For purposes of general usefulness the programme has been written in the international machine language ALGOL and should be operative on all computers having an ALGOL compiler, except for minor changes to be made due to the peculiarities of the actual ALGOL compiler. The programme is contained in appendix C of the report.

It was decided to write this programme in the present form because of its importance for delivering the initial values along a characteristic for the calculation of the flow around a configuration having a nose shape which may be considered as conical for some distance from the vertex.

The first part of the report gives a compilation of the governing equations, together with the formula for all those quantities which seem of interest.

The second part is devoted almost entirely to a rather detailed description of the programme. First the requirements which must be fulfilled by the programme are discussed, after which it is shown how all these requirements are met in the actual programme. Although written with a view to the applications intended at the NLR, it is constructed in such a way that it can be changed to meet special requirements without large alterations of its basic lay-out.

The necessary data which enable the operation of the programme are the Mach number of the undisturbed stream M_∞ the value γ of the ratio of the specific heats, the semi-top-angle ϑ_s, two estimates for the semi-shock angle ϑ_{w_1} and ϑ_{w_2} the coordinate x through which the desired characteristic passes, the desired accuracy eps, the number n of points along the characteristic, the quantity z, which by taking the values 0 and 1 determines the calculation of the zero-inclination and non zero-inclination case respectively and the quantity th which governs the choice of a variable or constant stepwidth $\Delta\vartheta$.

Four examples of results obtained with the programme are given. All data necessary for proceeding with the calculation of the velocity field around a configuration by the method of characteristics are supplied by these results.

In conclusion the authors want to express the hope that their programme will be used as frequently as the now famous tables of Kopal, which in a sense are superseded by this programme, for all those, who want a larger accuracy than these tables afford.

5 References

[1] Taylor, G. I. and Maccoll, J. W., The air pressure on a cone moving at high speeds. Proceedings of the Royal Society (A) **139** (1933) 278–310.
[2] Kopal, Z., Tables of supersonic flow around cones. M.I.T. Technical Report no. 1 1947.
[3] Stone, A. H., On supersonic flow past a slightly yawing cone. Journal of Mathematics and Physics **27** (1948) April.
[4] Kopal, Z., Tables of supersonic flow around yawing cones. M.I.T. Technical Report no. 3 1947.
[5] Zandbergen, P. J., Investigations on the supersonic flow around bodies. NLR report TR-G.25 October 1962.

APPENDIX A

The integration of the last step

A thorough investigation of the equations (2.15) reveals that they are not very well adapted to be solved by a Runge-Kutta method in the surrounding of $\vartheta=\vartheta_s$. This because of the fact that the second derivatives of u'' and v'' behave as follows

$$\frac{d^2 u''}{d\vartheta^2} \approx 0\left(\frac{1}{\sqrt{\vartheta-\vartheta_s}}\right) \tag{A(1)}$$

Omitting the details of the analysis it is found that the following relations are valid

$$u'' = f(\vartheta)+(\sqrt{-\bar{v}})^3 g(\vartheta) \tag{A(2)a}$$

$$v'' = \bar{f}(\vartheta)+(\sqrt{-\bar{v}})^3 \bar{g}(\vartheta) \tag{A(2)b}$$

$$C' = p(\vartheta)+\sqrt{-\bar{v}}\, q(\vartheta) \tag{A(2)c}$$

$$C'' = C_0'' \ +(\sqrt{-\bar{v}})^3 \bar{q}(\vartheta) \tag{A(2)d}$$

It should be observed that $\sqrt{-\bar{v}} \approx 0(\sqrt{\vartheta-\vartheta_s})$, while it is assumed that the other functions occurring are regular in $\vartheta-\vartheta_s$.

Using the equations (2.16) it is readily found that

$$C_0 = C''_{\vartheta=\vartheta_s} = \int_{\vartheta_w}^{\vartheta_s} \frac{\sqrt{u \sin\varphi - v\cos\varphi}}{\sqrt{(a^2)^{1/(\gamma-1)}}\sin\varphi} \cdot \frac{a^2}{\gamma(u\cos\varphi+v\sin\varphi)^2}\left\{1-\frac{(\gamma-1)\mu v}{\sin\varphi}(u\cos\varphi+v\sin\varphi)\right\} d\varphi \tag{A(3)a}$$

$$p(\vartheta) = \frac{a^2\mu}{\sin\vartheta}\left[-\frac{a^2}{\gamma(u\cos\vartheta+v\sin\vartheta)}+\bar{q}(\vartheta)\bar{v}^2\sqrt{(a^2)^{1/(\gamma-1)}\sin\vartheta}\right] \tag{A(3)b}$$

$$q(\vartheta) = \frac{a^2\mu}{\sin\vartheta}\left[\frac{a_w^2}{\gamma\cos\vartheta_w\sqrt{(a_w^2)^{1/(\gamma-1)}(-\bar{v}_w)\sin\vartheta_w}}+C_0\right]\sqrt{(a^2)^{1/(\gamma-1)}\sin\vartheta} \tag{A(3)c}$$

Substitution of the equations A(2) into the system of equations (2.15) and equating to zero the coefficient of $\sqrt{-\bar{v}}$ and the rest in each differential equation gives rise to the following system of equations

$$\frac{df}{d\vartheta} + a^2\mu\cot\vartheta\cdot f - \mu^2 v\bar{v}\{(\gamma-1)\bar{v}(uf+v\bar{f})+2a^2(\bar{f}\cos\vartheta - f\sin\vartheta)\} + p\frac{P''}{P} = 0 \tag{A(4)a}$$

$$-\bar{v}\frac{dg}{d\vartheta}+\tfrac{3}{2}g\left\{\bar{u}-\frac{a^2(\bar{u}+\bar{v}\cot\vartheta)}{\bar{v}^2-a^2}\right\} - \bar{v}a^2\mu\cot\vartheta\cdot g + {} $$
$$+\mu^2 v\bar{v}^2\{(\gamma-1)\bar{v}(ug+v\bar{g})+2a^2(\bar{g}\cos\vartheta - g\sin\vartheta)\} + q\frac{P''}{P} = 0 \tag{A(4)b}$$

$$\cot\vartheta\frac{df}{d\vartheta}+\frac{d\bar{f}}{d\vartheta} = 0 \tag{A(4)c}$$

$$-\bar{v}\frac{dg}{d\vartheta}\cot\vartheta + \tfrac{3}{2}\left\{\bar{u}-\frac{a^2(\bar{u}+\bar{v}\cot\vartheta)}{\bar{v}^2-a^2}\right\}(g\cot\vartheta+\bar{g}) - \bar{v}\frac{d\bar{g}}{d\vartheta} = 0 \tag{A(4)d}$$

The next problem to be solved is the determination of the necessary boundary conditions. Due to the particular nature of the problem these conditions are given by the equations themselves. A careful analysis of the equations A(4)b and A(4)d gives as a result

$$g = -\frac{q}{3\bar{u}}\frac{P''}{P} \qquad \text{for} \quad \vartheta=\vartheta_s \tag{A(5)a}$$

$$\bar{g} = -g\cot\vartheta_s \qquad \text{for} \quad \vartheta=\vartheta_s \tag{A(5)b}$$

This means that the functions g and $\bar{g}$ can be solved in principle by starting at $\vartheta=\vartheta_s$. However, the necessary values of $\mathrm{d}g/\mathrm{d}\vartheta$ and $\mathrm{d}\bar{g}/\mathrm{d}\vartheta$ cannot be obtained directly from the equations, since their coefficients become zero for $\vartheta=\vartheta_s$. This difficulty can be solved by differentiating the equations A(4)b and A(4)d and evaluating the result at $\vartheta=\vartheta_s$. It is found then that

$$\frac{\mathrm{d}g}{\mathrm{d}\vartheta}=\tfrac{1}{10}\bar{g} \qquad \text{for} \quad \vartheta=\vartheta_s \tag{A(6)a}$$

$$\frac{\mathrm{d}\bar{g}}{\mathrm{d}\vartheta}=g\left\{\frac{3}{5\sin^2\vartheta_s}+\tfrac{1}{10}\cot^2\vartheta_s\right\} \qquad \text{for} \quad \vartheta=\vartheta_s \tag{A(6)b}$$

It will be discussed now in which way the above derived equations can be used to find the quantities u'' and v''. If it is assumed, that these quantities are known up to a certain angle ϑ_n the procedure is as follows.

Using the equations A(4)b and A(4)d together with A(5) and A(6) the functions g and $\bar{g}$ can be determined without difficulties by using a Runge-Kutta procedure from ϑ_s unto ϑ_n. With the aid of the equations A(2)a and A(2)b and from the known values of u'', v'' g and $\bar{g}$ at $\vartheta=\vartheta_n$ the starting values for f and $\bar{f}$ are obtained. Then using eqs. A(4)a and A(4)c the quantities f and $\bar{f}$ are determined for the interval $\vartheta_n \rightarrow \vartheta_s$. Finally the values for u'' and v'' in this interval are obtained by using the equations A(2)a and A(2)b.

In the program as given in this report only the last step has been treated in the manner described here.

APPENDIX B

Flow-diagram

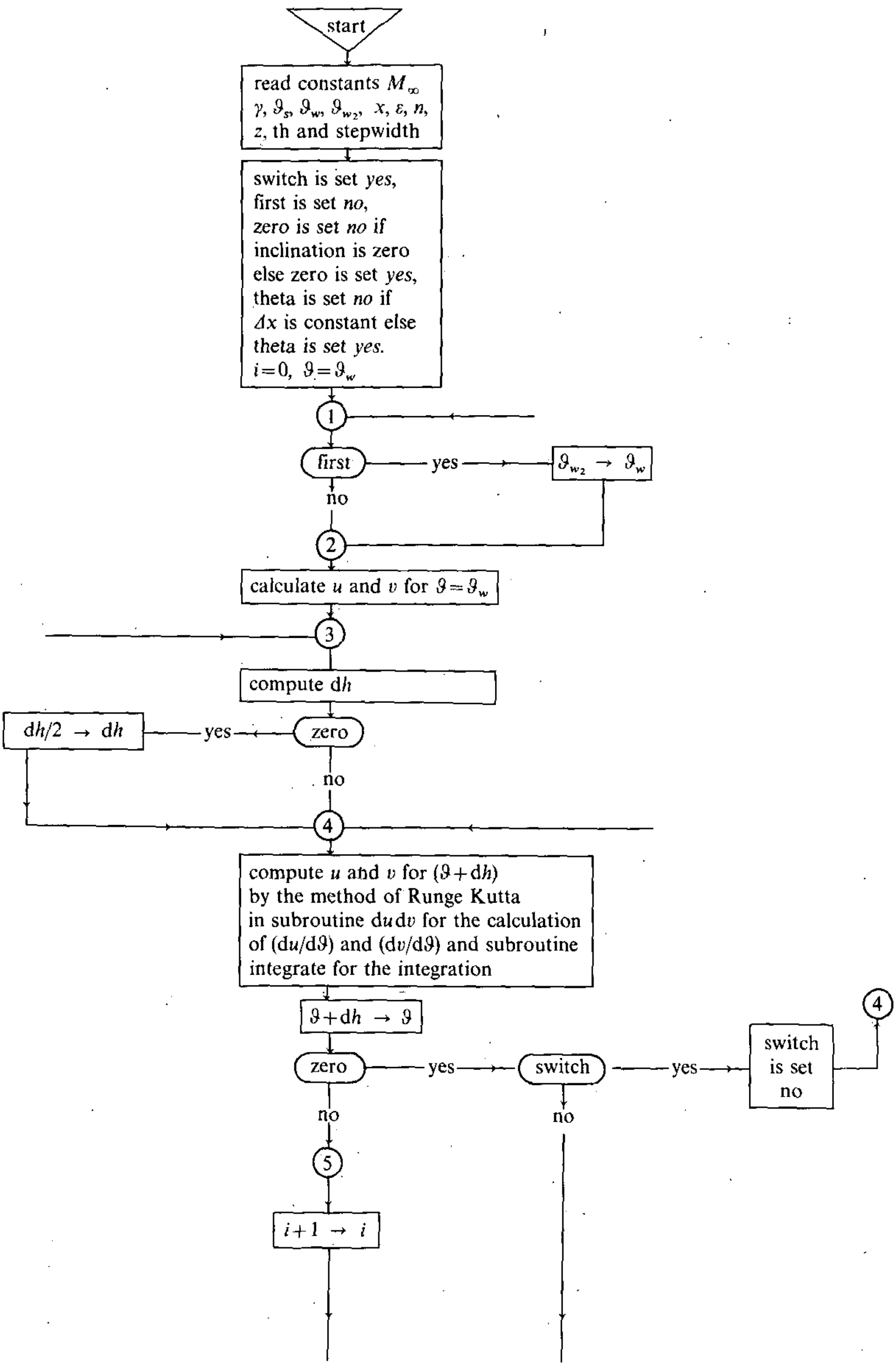

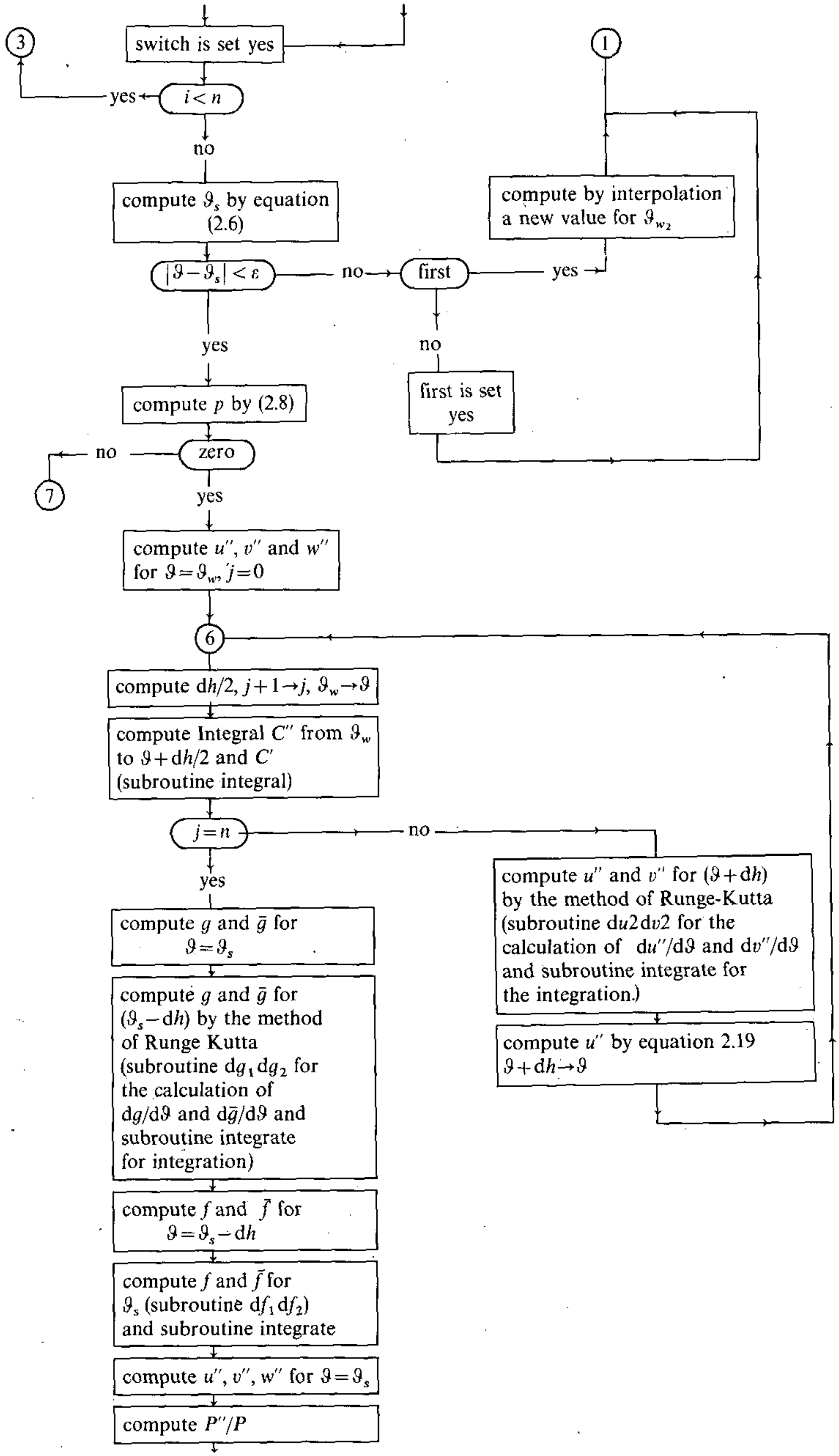

3
switch is set yes
yes
$i<n$
no
1
compute ϑ_s by equation (2.6)
compute by interpolation a new value for ϑ_{w_2}
$|\vartheta-\vartheta_s|<\varepsilon$
no
first
yes
yes
no
compute p by (2.8)
first is set yes
no
zero
7
yes
compute u'', v'' and w'' for $\vartheta=\vartheta_w$, $j=0$
6
compute $dh/2$, $j+1\rightarrow j$, $\vartheta_w\rightarrow\vartheta$
compute Integral C'' from ϑ_w to $\vartheta+dh/2$ and C' (subroutine integral)
$j=n$
no
yes
compute u'' and v'' for $(\vartheta+dh)$ by the method of Runge-Kutta (subroutine du2dv2 for the calculation of $du''/d\vartheta$ and $dv''/d\vartheta$ and subroutine integrate for the integration.)
compute g and $\bar{g}$ for $\vartheta=\vartheta_s$
compute u'' by equation 2.19 $\vartheta+dh\rightarrow\vartheta$
compute g and $\bar{g}$ for (ϑ_s-dh) by the method of Runge Kutta (subroutine dg_1dg_2 for the calculation of $dg/d\vartheta$ and $d\bar{g}/d\vartheta$ and subroutine integrate for integration)
compute f and $\bar{f}$ for $\vartheta=\vartheta_s-dh$
compute f and $\bar{f}$ for ϑ_s (subroutine df_1df_2) and subroutine integrate
compute u'', v'', w'' for $\vartheta=\vartheta_s$
compute P''/P

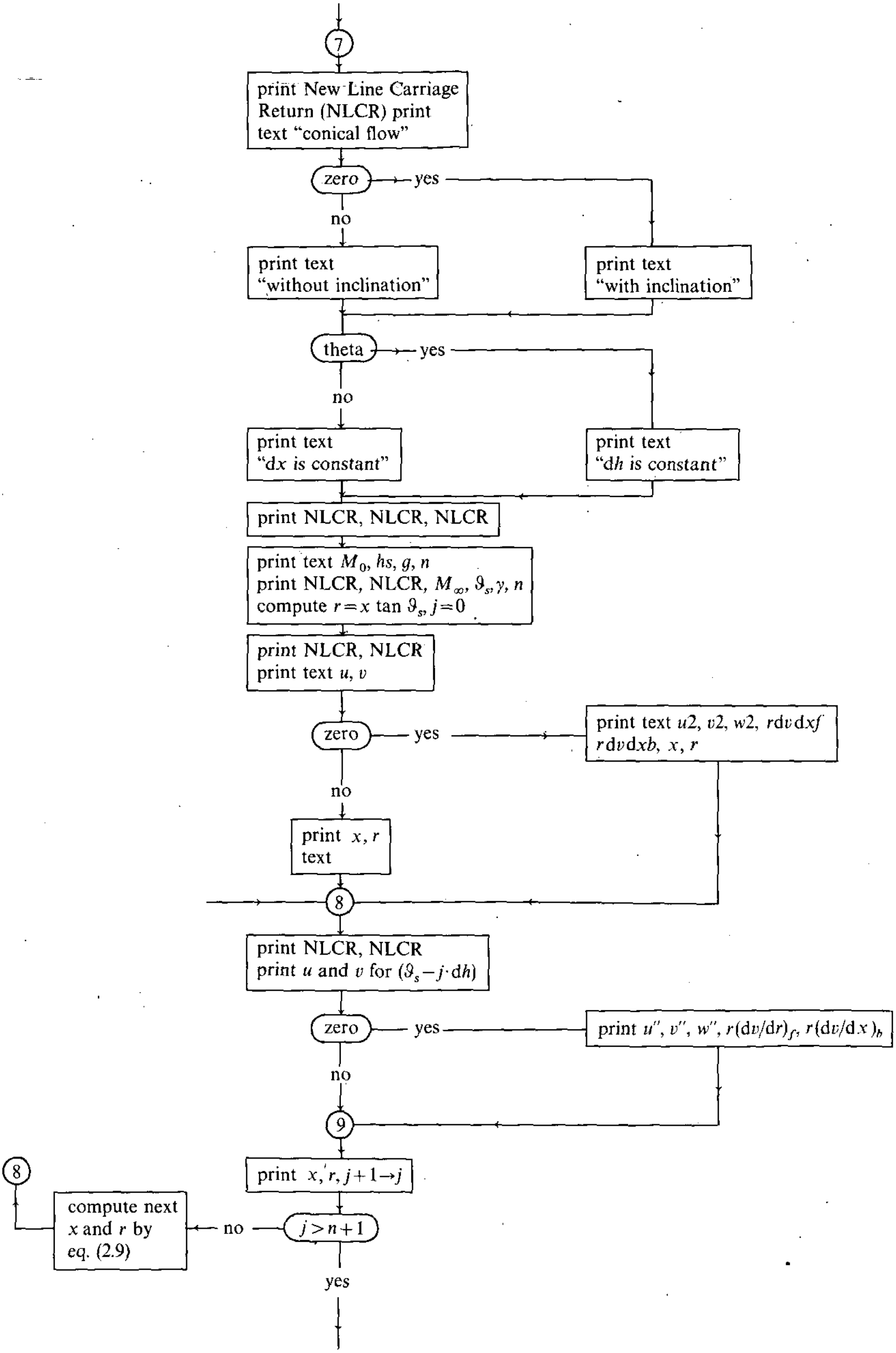
7
print New Line Carriage Return (NLCR) print text "conical flow"
zero
yes
no
print text "without inclination"
print text "with inclination"
theta
yes
no
print text "dx is constant"
print text "dh is constant"
print NLCR, NLCR, NLCR
print text M_0, hs, g, n
print NLCR, NLCR, M_∞, ϑ_s, γ, n
compute $r=x \tan \vartheta_s$, $j=0$
print NLCR, NLCR
print text u, v
zero
yes
print text u2, v2, w2, rdvdxf rdvdxb, x, r
no
print x, r text
8
print NLCR, NLCR
print u and v for $(\vartheta_s - j \cdot dh)$
zero
yes
print u'', v'', w'', $r(dv/dr)_f$, $r(dv/dx)_b$
no
9
print x, r, $j+1 \rightarrow j$
$j>n+1$
no
compute next x and r by eq. (2.9)
8
yes

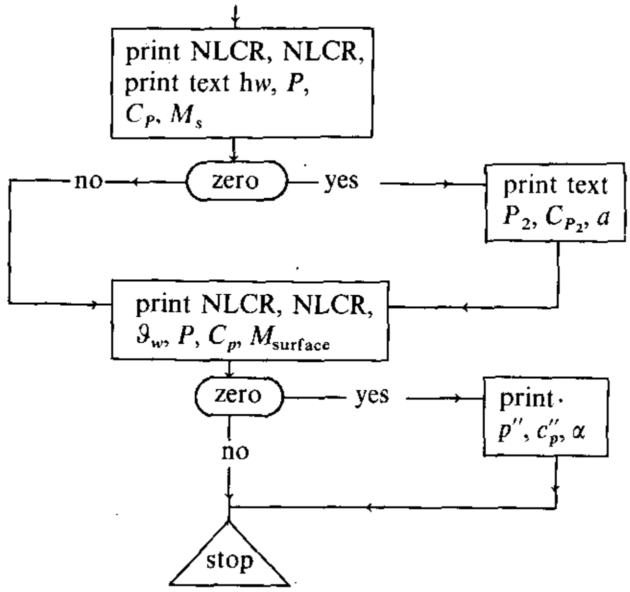
print NLCR, NLCR,
print text hw, P,
C_P, M_s
no
zero
yes
print text
P_2, C_{P_2}, a
print NLCR, NLCR,
ϑ_w, P, C_p, M_{surface}
zero
yes
print
p'', c_p'', α
no
stop

```
begin   real  m0, g, hs, hw, x, du, dv, k, l, a2, hwt, P, u, v, C1, C2, m, s, c, t,C4,g10,g20,g12,g22,dg1,dg2,df1,df2,f12,f22,a2s,
              p, q, r,  C3, P2, beta,l1,l2,l3,l4,k1,k2,k3,k4,h,dh,eps;
        integer  n,j, i, z, th;
        boolean zero, switch, first, theta;
        real  array  H [0:11], c2[0:3];

       procedure  du dv (h, u, v);  real h, u, v;
             begin  a2 := 1/(m0 × m0) + (g-1)×(1-(u × u)-(v×v))/2;
                    du := (-a2)×v/(( v× cos (h)- u× sin (h)) ↑ 2 - a2);
                    dv := (cos (h)/ sin (h)) ×( - du)
             end;

       procedure du2 dv2 (h,u2,v2); real h,u2,v2;
             begin   i:= i+1 ;a2:=1/(m0×m0) + (g-1)×(1-(H[4+i]×H[4+i])-(H[8+i]×H[8+i]))/2;
                     s:= sin (h);c:=cos(h); t:=H[i+8]×c-H[i+4]×s;m:=1/(a2-t×t);
                     du:=m×m× H[ i+8] ×t×((g-1)×t×(H[4+i]×u2+H[8+i]×v2)+2×a2×(v2×c-u2×s))-a2×m×c×u2/s-H[i];
                     dv:=du ×(-c)/s;
             end;

       procedure  df1df2(h,f1,f2); real h,f1,f2;
             begin   i:=i+1; a2:=1/(m0×m0)+(g-1)×(1-H[4+i]×H[4+i]-H[8+i]×H[8+i])/2;
                     s:=sin(h); c:=cos(h); t:=H[8+i]×c-H[4+i]×s; m:=1/(a2-t×t);
                     du:=df1:=-a2×m×c/s×f1+m×m×H[8+i]×t×(+(g-1)×t×(H[4+i]×f1+H[8+i]×f2)+2×a2×(f2×c-f1×s))
                     -a2×m/s×(-a2/(g×(H[4+i]×c+H[8+i]×s))+(c2[3-i]-c2[0])×sqrt(-t×a2↑(1/(g-1))×s));
                     dv:=df2:=-c/s×df1;
             end;

       procedure dg1dg2(h,g1,g2); real h,g1,g2;
             begin   i:=i+1; a2:=1/(m0×m0)+(g-1)×(1-H[7-i]×H[7-i]-H[11-i]×H[11-i])/2;
                     s:=sin(h); c:=cos(h); t:=H[11-i]×c-H[7-i]×s; m:=1/(a2-t×t);
                     r:=H[7-i]×c+H[11-i]×s; a2s:=1/(m0×m0)+(g-1)×(1-r×r-t×t)/2;
                     du:=dg1:= if i= 1 then 0.1×g2 else (1.5×g1×(r-a2s×(r+t×c/s)/(t×t-a2s))-t×a2×m×c/s×g1+m×m×H[11-i]×t×t×((g-1)×t×(H[7-i]×g1
                     +H[11-i]×g2)+2×a2×(g2×c-g1×s))+a2×m×C4×sqrt(a2↑(1/(g-1))/s))/t;
                     dv:=dg2:= if i = 1 then 0.6×g1/(s×s)-c/s×dg1 else -dg1×c/s+1.5×(r-a2s×(r+t×c/s)/(t×t-a2s))×(g1×c/s+g2)/t
             end;

       procedure  integrate (dh, Y ,h, u, v);  real  dh, h, u, v;  procedure  Y;
             begin Y(h, u, v); k1:= dh×du; l1:= dh×dv; Y((h+dh/2), (u+k1/2), (v+l1/2)); k2:=dh×du;
                     l2:=dh×dv; Y((h+dh/2), (u+k2/2), (v+l2/2)); k3:=dh×du; l3:=dh×dv; Y((h+dh), (u+k3), (v+l3));
                     k4:=dh×du; l4:=dh×dv;k:=(k1+2×k2+2×k3+k4)/6;  l:=(l1+2×l2+2×l3+l4)/6
             end;

       procedure  integral (dh, h, u, v); real  dh, h, u, v;
             begin s:=sin (h);c:=cos(h);a2:=1/(m0×m0)+(g-1)×(1-u×u-v×v)/2;t:=u×s-v×c;m:=1/(a2-t×t);q:=u×c+v×s; C2:=C2+C3×dh/2;
                     if j ≠ n then begin C3:=+sqrt(t)×a2/(g×q×q×sqrt((a2↑(1/(g-1)))×s))×(1-(g-1)×m×v×q/s);
                     r:=sqrt((a2↑(1/(g-1)))×t×s);
                     C2:=C2+C3×dh/2; C1:=a2×m/s×(r×p-a2/(g×q)+r×(C2));    end;
             end;

       procedure betas (u, v); real u, v;
             begin beta:= sqrt(1/((1/(m0×m0)+(g-1)/2)/(u×u+v×v)-(g-1)/2)-1)
             end;
```

```
m0:=read; g:=read; hs:=read; hw:=read; hwt:=read; x:=read;eps:=read; n:=read; z:=read; th:=read; first:=false; switch:=true; zero:=¬(z=0); theta:=¬(th=0);

begin real u0, v0, dh, a, u02, v02, cp, cp2;
      array result [0:(n+1),1:6];

CC:   if first then begin  H[0]:=H[1]; H[2]:=H[3]; hw:=hwt; end;
      s:=sin(hw); u0:=result[0,2]:=1+2×(1/(m0×m0)-s×s)/(g+1); v0:=result[0,3]:=(1-u0)×cos(hw)/s; result[0,1]:=hw;
      betas(u0, v0);a:=arctan((u0+beta×v0)/(beta×u0-v0)); c:=sin(a-hs); s:=sin(hw-hs); p:=n×s×c; q:=p×cos(a-hw);
      p:=p×sin(a-hw); r:=(n×c); r:=r×r; t:=s×s; i:=j:=1;

AA:   dh:=if theta then (hs-hw)/n else(-arctan(p/(i×(i-1)×t-(2×i-1)×q+r)));   if zero then dh:=dh/2;

BB:   integrate (dh, du dv,result [j-1, 1], result[j-1, 2], result [j-1, 3]);result[i, 2]:=result[j, 4]:=result[j-1, 2]+k;
         result[i, 3]:=result[j, 5]:=result[j-1, 3]+1; result[i, 1]:=result[j-1, 1]+dh;  j:=j+1;
                if  zero then
                          begin if switch then
                                          begin switch:=false; goto BB
                                          end;
                          end;
                if zero then j:=j-1; i:=i+1; switch:=true; if i ≤n then goto AA;
                H[1]:=hw;H[3]:=result [n, 2]-result [n, 3]×cos(result[n, 1])/sin(result[n, 1]);
                if abs (H[3])> eps then
                                begin if first then goto DD; first:=true; goto CC;
DD:                                   hwt:=(H[2]×H[1]-H[0]×H[3])/(H[2]-H[3]);goto CC;
                                end;
                s:=sin(hw); P:=((((g+1)×m0×m0×s×s)/((g-1)×m0×m0×s×s+2))↑(g/(g-1)))/((1+(2×g/(g+1))×(m0×m0×s×s-1))↑(1/(g-1)));
                c:=cos(hw); a2:=1/(m0×m0)+(g-1)×(1-(u0×u0)-(v0×v0))/2; cp2:=a2;
                if zero then
                        begin u02:=result [0, 4]:=(a2×s×c/(g×(g+1)×v0×v0))×((g-1)×v0+6×s×c);C2:=H[3]:=0; H[7]:=u0; first:=true;
                              v02:=result[0, 5]:=(-u02)×c/s+a2/(g×v0);H[11]:=v0; p:=a2/(g×c×sqrt((a2↑(1/(g-1)))×(u0×s-v0×c)×s));
                              j:=0;  C3:=0; integral((result[1, 1]-result[0, 1])/4. hw, u0, v0);a:=a2×c×s/(g×v0×v0); result[0,6]:=a2/((-g)×v0); C2:=0;
EE:                           j:=j+1; H[0]:=H[3]; H[4]:=H[7]; H[8]:=H[11]; hwt:=(result[j, 1]-result[j-1, 1])/2;
                              integral (hwt, result[j-1, 1]+hwt, result[j, 4], result[j, 5]); H[1]:=H[2]:=C1; H[5]:=H[6]:=result[j, 4];
                              H[9]:=H[10]:=result[j, 5]; if j=n then c2[2]:=c2[1]:=C2; integral(hwt, result[j-1, 1]+2×hwt, result[j, 2], result[j, 3]);
                              H[3]:=C1; H[7]:=result[j, 2]; i:=(-1);  H[11]:=result[j, 3];
                              if j=n-1 then c2[3]:= C2;
                              if j=n   then begin c2[0]:= C2; goto HH end;
                              integrate (2×hwt, du2  dv2, result[j-1, 1], result[j-1, 4], result[j-1, 5]);
                              result[j, 4]:=result[j-1, 4]+k; result[j, 5]:=result[j-1, 5]+1; result[j, 6]:=result[j, 4]×(-c)/s-result[j, 5]-C1/(a2×m);
```

```
          goto EE;
HH:                              C4:=cp2/(g×cos(hw)×sqrt(cp2↑(1/(g-1))×sin(hw)×(u0×sin(hw)-v0×cos(hw))))+c2[0];
                                 g10:=-a2×m×C4×sqrt(a2↑(1/(g-1))/s)/(3×q);
                                 g20:=-g10×c/s; integrate(-2×hwt, dg1dg2, result[n,1], g10,g20); g12:=g10+k; g22:= g20+1;
                                 f12:= result[n-1,4]-sqrt(-t)↑3×g12;
                                 f22:=result[n-1,5]-sqrt(-t)↑3×g22;
                                 i:=-1; integrate(2×hwt,df1df2,result[n-1,1],f12,f22);
                                 result[n,4]:=f12+k+sqrt(-t)↑3×g10;
                                 result[n,5]:=f22+1+sqrt(-t)↑3×g20;
                                 result[n,6]:=-result[n,4]×c/s-result[n,5]+a2/(g×s×(H[7]×c+H[11]×s));
                                 P2:=(2×result[n,2])/((result[n,4]×s/c-result[n,5])×c×c); a:=a×P2;
                             end; PUNLCR; PUTEXT1(⟨Conical flow⟩);
                    if zero then PUTEXT1(⟨ with inclination⟩) else
                        PUTEXT1 (⟨ without inclination⟩);
                    if theta then PUTEXT1(⟨, dh is constant⟩) else
                        PUTEXT1(⟨, dx is constant⟩); PUNLCR; PUNLCR; PUNLCR;
                        PUTEXT1(⟨   Mo      hs      g     n⟩); PUNLCR; PUNLCR; FIXP(1,3,m0); FIXP(1,7,result[n, 1]); FIXP(1,3,g); FIXP(2,0,n);r:=x×sin(hs)/cos(hs); j:=0;
                             PUNLCR;PUNLCR;PUTEXT1(⟨      u         v⟩);
                             if zero then PUTEXT1(⟨         u2         v2         w2         rdvdxb         rdvdxf         x         r⟩) else
                             PUTEXT1(⟨          x          r⟩);

FF:                 PUNLCR; PUNLCR; FIXP(0,8,result[n-j, 2]); FIXP(0,8,result[n-j, 3]);
                    if zero then
                            begin  FIXP(1,8,result[n-j, 4]×P2); FIXP(1,8,result[n-j, 5]×P2); FIXP(1,8,result[n-j, 6]×P2); s:=sin(result[n-j, 1]);
                                 c:=cos(result[n-j, 1]); a2:=1/(m0×m0)+(g-1)×(1-result[n-j, 3]×result[n-j, 3]-result[n-j, 2]×result[n-j, 2])/2;
                                 t:=c×result[n-j, 3]-s×result[n-j, 2]; betas(result[n-j, 2], result[n-j, 3]); m:=(a2/(a2-t×t))×result[n-j, 3]×c×c;
                                 FLOP(8,1,(s/c-(result[n-j, 2]+beta×result[n-j, 3])/(beta×result[n-j, 2]-result[n-j, 3]))×m);
                                 FLOP(8,1,(s/c+(result[n-j, 2]-beta×result[n-j, 3])/(beta×result[n-j, 2]+result[n-j, 3]))×m);
                            end;
                    FIXP(1,8,x); FIXP(1,8,r); j:=j+1; if j ≥ n+1 then goto GG; betas ((result[n-j, 2]+result[n-j+1, 2])/2, (result[n-j, 3]+result[n-j+1, 3])/2);
                    t:=((result[n-j, 2]+result[n-j+1, 2])/2+beta×(result[n-j, 3]+result[n-j+1, 3])/2)/(beta×(result[n-j, 2]
                    +result[n-j+1, 2])/2-(result[n-j, 3]+result[n-j+1, 3])/2);
                    x:=(r-t×x)/(sin(result[n-j, 1])/cos(result[n-j, 1])-t); r:=x×sin(result[n-j, 1])/cos(result[n-j, 1]); goto FF;

GG:                 a2:=1/(m0×m0)+(g-1)×(1-result[n, 2]↑2-result[n, 3]↑2)/2; cp:=(2/(g×m0×m0))×(((a2×m0×m0)↑(g/(g-1)))×P-1);
                    PUNLCR; PUNLCR; PUTEXT1(⟨     hw          P          cp          Ms⟩);
                    if zero then PUTEXT1(⟨          P2          cp2          a⟩);
                    PUNLCR; PUNLCR; FIXP(1,7,result[0, 1]); FIXP(0,8,P); FIXP(0,8,cp); FIXP(1,7,sqrt((result[n, 2]×result[n, 2]+result[n, 3]×result[n, 3])/a2));
                    if zero then
                             begin FIXP(1,8,P2×P); FIXP(3,8,(cp+2/(g×m0×m0))×P2 × (1-g × (result[n, 2] × result[n, 4] + result[n, 3] × result[n, 5])/a2));  FIXP(1,8,a)
                             end;
  end
  end
```

REPORT NLR-MP. 216

Flight operational evaluation of approach and runway lighting

by

J. B. de Boer and ir. T. van Oosterom

Summary:

The effectiveness of 3 systems for approach and runway lighting – basically 2 existing centre line and crossbar systems and a Netherlands proposal – has been judged on the basis of data on the quality of the approach and landing and on the pilot's effort to carry them out. These data have been recorded during flight tests executed by a group of 18 pilots from different countries.

A specially designed screen has been installed behind the cockpit window to simulate visibility in marginal weather conditions.

An interpretation procedure has been developed by which the mass of recorded data could be reduced to a numerical form, suitable for statistical analysis. This analysis gives rise to a preference of the Netherlands system over the 2 others investigated with regard to directional information and height guidance when passing the threshold. No preference was found with respect to the approach height before the threshold and the quality of the landing.

Pilots' comments have also been collected, but only general conclusions could be drawn on the basic principles of the different configurations.

Contents

1. Introduction

During the last few years representatives of the Netherlands have repeatedly made proposals for improving existing visual aids at international conferences on standardization of airport lighting. The purpose of this lighting is to give the pilot the visual information which he needs during the approach and landing manoeuvre in order to perform a successful landing, even when weather conditions, especially fog, deprive him of the natural visual references. These proposals are based on several considerations, founded primarily on extensive experience and critical study of the typical merits and imperfections of standardized systems for approach and runway lighting. Secondly, there is the need, becoming more and more economically pressing, for lowering the weather limits imposed for safety reasons and hence for making the regularity of scheduled airline operations less dependent on weather conditions at destination. Lastly, the light systems must satisfy the demands posed by future aircraft types, due to the increase in speed and decrease in manoeuvrability during landing.

In other countries, e.g. the USA, the UK and Australia, visual aids for approach and landing are also a subject of extensive study and research. All these studies are characterized by the point of view that the guidance required during the *approach* is available from standardized patterns. The configuration of lights applied before the threshold of the runway according to these standards is assumed to offer a suitable solution to the problem although the desire to land at still lower limits always remains. The studies carried out in the USA and the UK, for example, have therefore been concentrated on trying to find the right configuration of lights in the *landing zone*, i.e. in the vicinity of the ideal aiming point for touch-down. On the other hand, the views expressed by Netherlands experts in international circles for a considerable time past, are based on the principle that the *approach and runway* lighting configuration ought to form an *integrated* guidance system. This implies that considering the efficiency of a single part — e.g. the lay-out of the lights in the landing zone — isolated from the system as a whole, can hardly lead to effective improvement.

Until recently, these ideas have been put forward as a result of theoretical studies and on the basis of experiments performed with models. In order to be able to support the Netherlands proposals with the convincing power of practical experience, the Netherlands Department of Civil Aviation set up a study group of experts

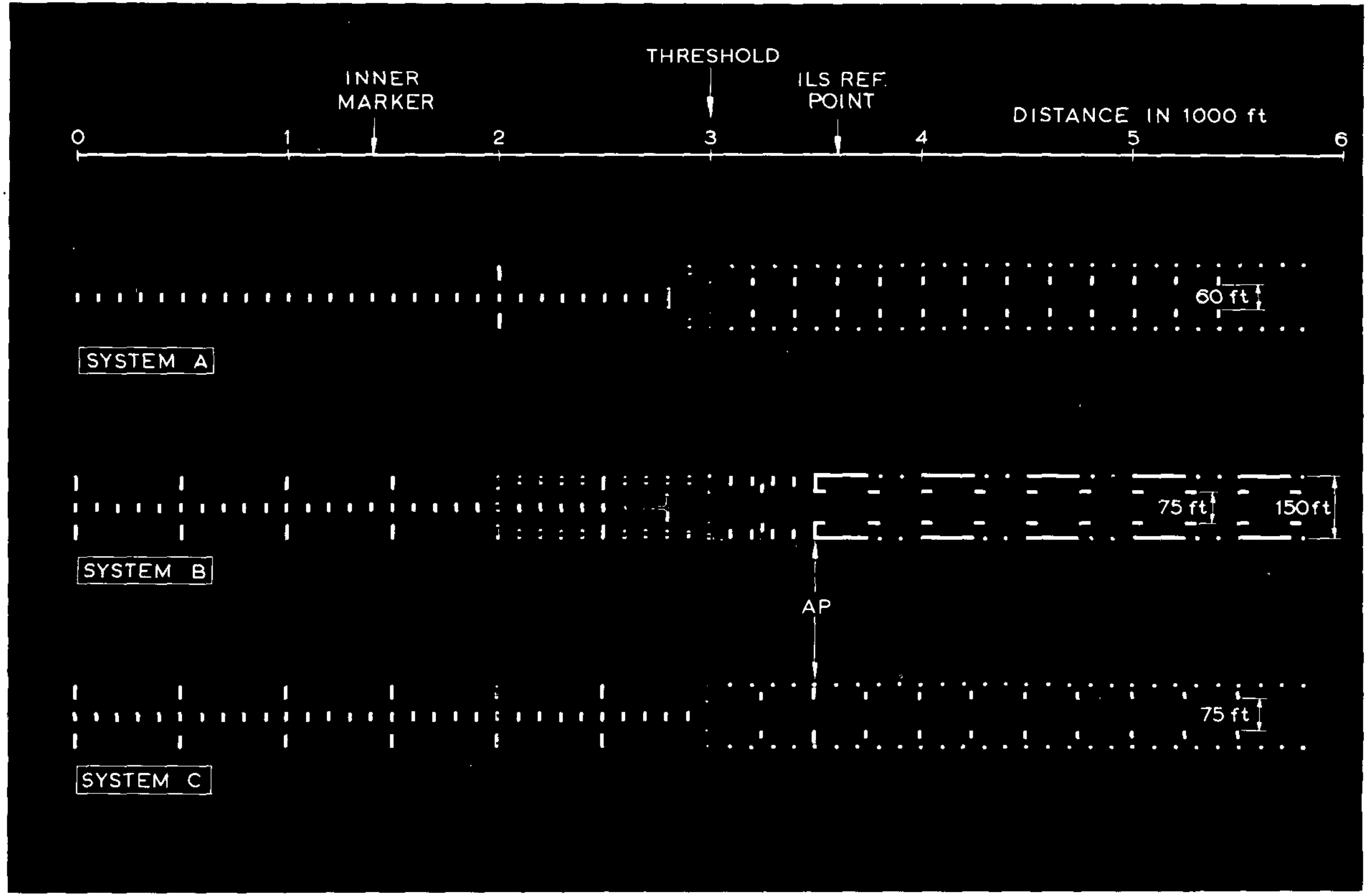

Fig. 1. Investigated light configurations.

interested in this problem [4]). The task of the study group was to conduct flight tests for the purpose of evaluating the quality of a visual aid system conforming to the Netherlands proposals in comparison with that of systems hitherto accepted as international standards for this subject. To this end, the study group was allowed to carry out a flight test programme and consequently to install the necessary experimental equipment on Eelde Airport, a modern airfield in the northern part of the Netherlands, extremely well suited for this purpose because of its low traffic density at night and its facilities as standard alternate to Schiphol Airport (Amsterdam).

The following pages contain a description of the test procedure worked out by the study group and applied in this investigation, followed by a survey and an analysis of the results obtained.

2. Description of evaluated light configurations

With respect to approach lighting, the International Civil Aviation Organization (ICAO) has restricted its recommendations to the 'centre line and crossbars' pattern showing, by means of rows of lights before the threshold the extended runway centre line in combination with at least one 'crossbar' perpendicular to this line. Two variants of this system are considered acceptable: the system favoured by the Airline Pilots' Association (ALPA) and the Calvert system.

The chief characteristic of the ALPA system is that one long crossbar is located 1000 feet before the threshold, whereas the Calvert system has a number of long crossbars at distances of 500 feet. The basic idea of the Netherlands proposal is to create an integration of non-visual and visual aids and of guidance during the approach as well as during the landing. To realize these principles the Netherlands system, contrary to both configurations mentioned above, has an additional double row of red barrettes before the threshold and a red T, interrupting the centre line over the last 500 feet before the threshold. The purpose of this proposal is to obtain a better height and roll guidance, particularly in the phase immediately preceding the flare-out. In order to continue roll guidance until touch-down and to 'fill up the black hole' in this final stage of the landing manoeuvre, the double row is extended between threshold and aiming point [5]).

The flight tests were conducted to compare the light configuration according to the Netherlands proposal with 2 centre line and crossbar systems as standardized by ICAO. The Netherlands system has been completed by a two-gauge longitudinal system in the deceleration zone, the 2 other configurations by visual aids in the landing and deceleration zone according to existing systems in the UK and the USA. The 3 complete configurations have been illustrated in fig. 1, from which the following details can be seen:

System A. This configuration contains the ALPA approach system, consisting of barrettes of lights at distances of 100 feet over a length of 3000 feet along the centre line of the runway before the hard surface and of one 150 feet long crossbar of lights at a distance of 1000 feet before the green-marked runway threshold. This approach system has been completed by a 60-feet narrow gauge runway light pattern with lateral barrettes at longitudinal distances of 200 feet over a length of 2400 feet.

System C. In this configuration the centre line and crossbars system of Eelde Airport is incorporated, which consists of the same centre line configuration as system A with additional 150-feet long crossbars every 500 feet [6]). The crossbar located at 1000 feet before the green-marked runway threshold consists of red lights. The system has been supplemented by runway lights in accordance with a principle indicated by the Royal Aircraft Establishment (UK): a 75-feet narrow gauge system with lateral barrettes at longitudinal distances of 250 feet over a length of 2500 feet. The aiming point for touch-down (AP in fig. 1) is indicated by large barrettes.

System B. This system differs from the preceding configuration by an additional double row lateral barrettes at intervals of 100 feet, beginning in red at 1000 feet before the runway threshold and extending in white from the threshold to the aiming point. A red T interrupts the centre line over the last 500 feet before the runway threshold. The threshold is emphasized by green longitudinal bars 250 feet in length. The runway lighting according to the Netherlands proposal differs from the previous systems by a change-over from the white lateral bars to white longitudinal bars beyond the aiming point. These longitudinal bars are placed in a 150-feet wide gauge system, each bar being 250 feet long with gaps of 250 feet, and in a 75-feet narrow gauge system of longitudinal elements 50 feet in length with gaps of 200 feet. Moreover, the aiming point is emphasized by lateral bars between the inner and the outer gauges, resulting in a double L-shaped pattern.

It should be mentioned that, as shown in fig. 1, the Netherlands system installed at Eelde Airport had only 1 block 500 feet in length between the runway threshold and the aiming point instead of 2 blocks of 500 feet each, as recommended for normal circumstances. This single length of 500 feet was selected in the tests at Eelde on account of the local site of the ILS reference point and the desire to bring the ideal aiming point of the

[4]) The study group was composed of experts representing:
- the Netherlands Department of Civil Aviation (RLD),
- the National Aeronautical and Astronautical Research Institute (NLR),
- Schiphol Airport Authority,
- Eelde Airport Inc.,
- the Netherlands Illuminating Engineering Society (NSvV),
- the Laboratory of the Coastal Lighting Service,
- the National Aeromedical Centre,
- KLM-Royal Dutch Airlines and
- the Lighting Laboratory of N.V. Philips' Gloeilampenfabrieken.

[5]) Further discussion of the motives which have led to the various configurations is beyond the scope of the present paper. More details of the principles of visual guidance during landing underlying the Netherlands proposal have been put forward at various ICAO and IATA meetings.

[6]) In accordance with the approach light configurations on civil aerodromes in the Netherlands, the crossbars are of equal length.

visual configuration as close as possible to the ILS reference point.

Many of the lights required for the 3 configurations to be compared were already available at Eelde Airport in the permanent light system installed there. Actually, this contained all the lights needed for the approach configuration of system C (see fig. 1). The necessary extension of this system for the landing zone and the provisions for switching to the other 2 configurations were obtained by adding an experimental installation.

One of the lights used before the threshold or along the outer edges of the runway is shown in fig. 2 in front of one of the runway lights forming part of the permanent installation. It consists of a very light wire frame in which a prefocussed incandescent lamp with mirrored bulb is suspended and to which a colour filter can be attached. As a number of these lights had always to be combined into a long or short crossbar (see fig. 1), the lights were mounted on timber boards as illustrated in fig. 3. Immediately prior to the tests, these boards could be placed at points previously marked on or in front of the runway. This ensured correct positioning and adjustment of the light bars.

The experimental lights for the inner gauge of the landing mat consisted of a thin transparent plastic housing containing a miniature tubular line lamp in a small reflector. A permanent magnet mounted in the base of the light permitted it to be stuck to a thin steel plate glued on the runway surface. As the light distribution is fan shaped in azimuth, its orientation in this direction is not critical. This construction allowed the lights to be quickly placed before and removed after the tests. The whole assembly is of such light construction that no damage could be done to the tyres of an aircraft running across.

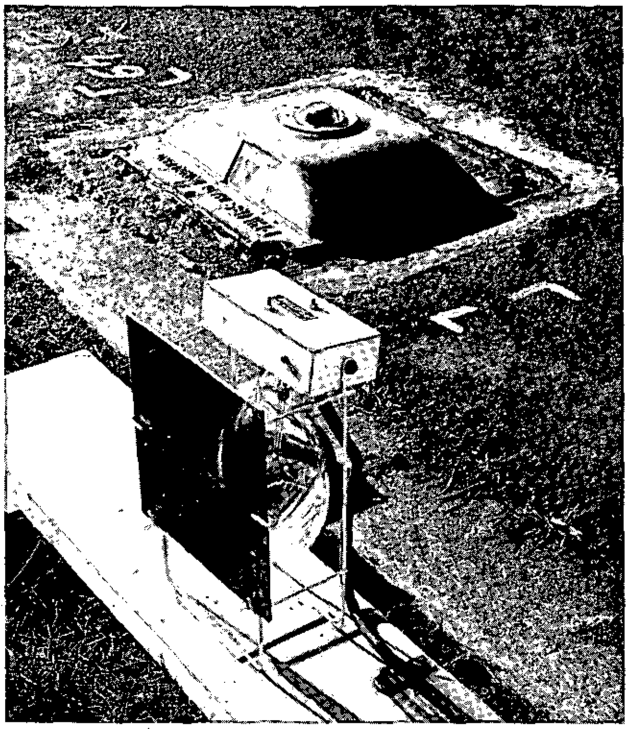

Fig. 2. One of the experimental lights (bottom) and one of the runway lights (top) out of the permanent installation.

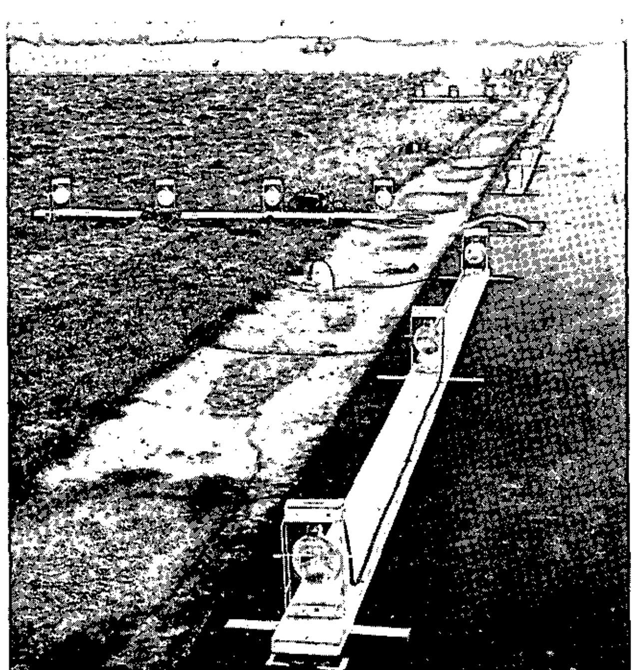

Fig. 3. Experimental lights mounted on timber boards.

3. Procedure of evaluation tests

The principle of the procedure followed in the evaluation tests is that the effectiveness of the guidance obtained from a certain configuration of lights during the approach and landing must for a given type of aircraft be apparent from

1. the quality of the approach,
2. the quality of the landing,
3. the pilot's effort to carry out the approach and landing.

The effectiveness may, moreover, be illustrated by the pilot's judgement and understanding of the guidance obtained.

The quality of the approach and landing as well as the pilot's effort and judgement will be greatly influenced not only by the effectiveness of the guidance of a certain configuration of lights but also by the prevailing weather and by the initial flight condition of the aircraft. Moreover, the performance of different pilots, even if flying under exactly the same condition, will by no means be the same. Fundamentally, the test procedure, therefore, must be such that data, enabling the above mentioned 3 criteria to be assessed, are recorded in marginal weather (real or simulated) with a number of pilots large enough to eliminate personal influence on the final results and for different initial flight conditions. A complete evaluation should, moreover, be based on tests with different types of aircraft. The present investigation, however, had for practical reasons to be restricted to one aircraft (type C-47).

In experiments of this nature the influence of the *weather* is perhaps the most troublesome problem. For the purpose of the investigation these tests have to be performed under marginal and invariable visibility conditions, which, however, occur but seldom. In view of the continuity and the reliability of the tests, therefore, it is of utmost importance to find a method of simulating consistent marginal conditions. This simulation has been achieved by fitting, immediately behind the cockpit window, a movable screen, especially designed for the purpose of limiting the pilot's visual field to obtain a constant visual range such as prevails in homogeneous fog, independent of the longitudinal attitude and the height of the aircraft. For this constant visual range the rather low value of 1000 feet has been chosen in order to emphasize possible differences in guidance characteristics of the light patterns to be compared. A detailed description of the movable screen and its control mechanism has been given in chapter 4 together with some illustrations indicating what part of the light configurations is visible to the pilot underneath the lower edge of the screen from different points on the flight path. In order to simulate seeing conditions in fog as realistically as possible, a reduced value of the luminous intensity of the lights was chosen. Moreover, a neutral and a slightly diffusing filter were placed before the pilot's eyes. This simulation of seeing conditions in fog requires a meteorological visibility during the test flights of at least 2 miles. Details of this part of the fog simulation have also been given in chapter 4.

In order to eliminate the influence of *personal characteristics* of the pilot as far as possible, the number of pilots involved in the tests must be such that the overall result can be regarded as characteristic for a great many pilots. The scatter of the results of a preliminary investigation carried out with 5 pilots, indicated that at least 15 pilots should be included in investigations of this type, if each pilot carries out one test flight on each light pattern and from each initial position (see below), as was planned for this investigation.

To ensure that the results would not be entirely dependent upon the influence of the drill followed by a particular company, 18 pilots from 10 different companies, organizations and government institutes (see Appendix I) participated in the tests. Sixteen of these pilots performed a complete set of approaches according to the test flight programme to be mentioned here below; 2 pilots could not complete their tests because of weather conditions.

A complete assessment of the influence of the *initial flight condition*, when the pilot establishes visual contact, on the quality of the approach and landing would require a very extensive flight test programme in view of the great number of variables involved (e.g. horizontal and vertical deviation from the ideal flight path, angles of pitch and bank, heading and speed). In order to restrict the number of flights, 3 standardized initial positions have been chosen:

a. the ideal position: on the ILS glide path and on the runway centre line,
b. on the centre line and 2 dots ILS deflection above the glide path (i.e. about 50 feet above the glide path at the locator where the glide path height is 200 feet) and
c. on the glide path and 1 dot ILS deflection left of the centre line (i.e. about 100 feet left of the glide path at the locator).

These 3 positions were furthermore characterized by:

— a 10-degree flap setting,
— an airspeed of 100 kts IAS,
— wings level,
— a power setting consistent with an approach on the ILS glide path (initial positions *a* and *c*) or with a somewhat steeper trajectory corresponding to a 2-dots ILS deflection above the glide path (initial position *b*),
— a heading equal to the runway heading corrected for drift (initial positions *a* and *b*) with — in case of the lateral displaced approaches (initial position *c*) — an additional minor correction for a trajectory corresponding to a 1-dot ILS deflection left of the centre line.

It was decided to have each pilot carry out 1 approach from each of the 3 initial positions on each of the 3 light configurations. With the number of test flights per pilot thus obtained, no appreciable familiarization with local conditions could occur to cause the differences in the systems under examination to be largely levelled out. As 16 pilots performed a complete set of approaches, the total number of test flights amounted to $16 \times 3 \times 3 = 144$. Of course all these flights could not be made in one night. It was decided, therefore, to have each pilot do 9 flights per night. The actual order of flights has been given in Appendix II. The order of the light systems and the order of the flights with a specific light system has been chosen at random in view of unavoidable influences such as fatigue, variations in direction and speed of the wind etc.

On each test flight the safety pilot in the right hand seat carried out the first stage of the approach. For this purpose, this pilot had at his disposal all the available visual guidance without any limitation in addition to the information provided by the instruments. The aircraft was thus brought through a right hand circuit at 1000 feet to one of the 3 initial positions for the desired approach flight at about 500 feet height. The test pilot took over as soon as visual contact was established. Commands of power settings could be given by the test pilot. The landing lights were switched on by the safety pilot shortly before touch-down. The safety pilot took over control again as soon as the touch-down was definitely completed.

At the beginning of this chapter it has been mentioned that the basic idea underlying the recordings carried out during each approach and landing is that the effectiveness of the guidance of a configuration of lights can be examined from the quality of the approach and landing and from the pilot's effort to carry them out.

It was considered feasible to obtain a fairly good assessment of the *quality of an approach and landing* from data on:

— the actual flight path in horizontal and vertical projection until touch-down,
— the height at the moment of passing the runway threshold,
— the distance between the threshold and the actual touch-down point,
— the vertical deceleration of impact at touch-down.

The *pilot's effort* was assessed from information on:

— the deflections of elevator, rudder and ailerons and
— the frequency of the pilot's heart beat.

The data required for the assessment of approach and landing quality and of the pilot's effort were obtained by recording the indications of the relevant aircraft instruments and of special instruments installed for this purpose in the aircraft and on the ground. The determination of the flight-path of the approaches before passing the runway threshold was based upon the deflections from the ideal ILS flight-path. For this purpose the outputs of the ILS glide path and localizer receivers were recorded, this being a typical in-flight measurement. The landing flight-path (beyond the threshold), on the other hand, was recorded by ground cameras. A detailed description of the recording equipment with some samples of recordings has been given in chapter 5.

The *pilot's judgement* on the guidance obtained from a certain system was derived from the answers collected by systematically and carefully questioning the pilot shortly after the performance of each test flight. Details on this information are given in chapter 8.

4. Method of fog simulation

4.1 Basic principles

The National Aeronautical and Astronautical Research Institute (NLR) was requested to design and build a device, capable of simulating a constant visual range as prevailing in fog of homogeneous density. This visual range should be kept constant irrespective of the longitudinal attitude and the height of the aircraft during the approach and the landing manoeuvre. The desired simulation is obtained by limiting the pilot's visual field by an opaque movable screen attached to the cockpit window. As illustrated in fig. 4 the upper limitation of the visual sector is determined by the lower edge of the movable screen and the lower limitation is defined by the shape of the cockpit cut-off. To avoid a reduction of the visual range with decreasing height, the screen has to be raised slowly during the approach at a rate dependent on the rate of descent of the aircraft. When the aircraft is flying at high altitude, the cockpit window is completely masked by the screen. When the aircraft has descended to the height where the distance from the ground – measured in the direction of the cockpit cut-off – is equal to the visual range to be simulated (the visual sector and segment thus still being zero), the driving gear of the screen is switched on so that the bottom edge of the cockpit window begins to clear. Provision to ensure that the visual range is not affected by alterations in the longitudinal attitude of the aircraft is made by gyroscopic stabilisation. A constant value of the visual range is obtained with the screen moving according to the principles just described, provided that the pilot's eyes have a fixed position relative to the aircraft. This has been obtained by means of a head-support firmly attached to the screen frame. The head-support also carries a combination of filters which, together with a convenient setting of the luminous intensity of the lights, simulates seeing conditions in fog.

Fig. 5 shows which part of the 3 light configurations is visible beneath the screen when the aircraft is at heights of 160, 130, 100 and 70 feet respectively for a visual range of 1000 feet. Fig. 6 gives an impression of what is really seen by the test pilot of the configurations at these heights.

4.2 Construction and operation of cockpit screen

The following gives an explanation of the design principles of the screen system. If (see fig. 4):

- z denotes the constant visual range to be simulated,
- θ the longitudinal attitude of the aircraft,
- φ the sight angle, i.e. the inclination of the upper limitation of the visual sector,
- h the height of the pilot's eyes above the ground,
- w the rate of descent of the aircraft,
- s the displacement of the movable screen measured from the intersection of the screen with a line through the pilot's eye parallel to the longitudinal axis of the aircraft,
- a the distance of the pilot's eye to the screen measured in the direction of the longitudinal axis,
- α the angle between the screen and the longitudinal axis,

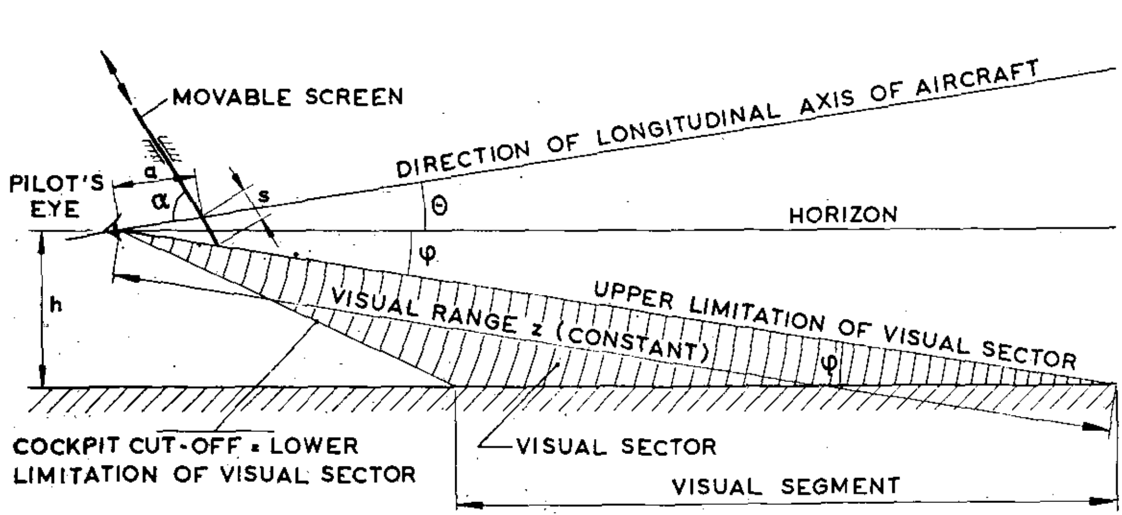

Fig. 4. Relation between screen position s, longitudinal attitude θ, height h and sight angle φ for a given visual range z.

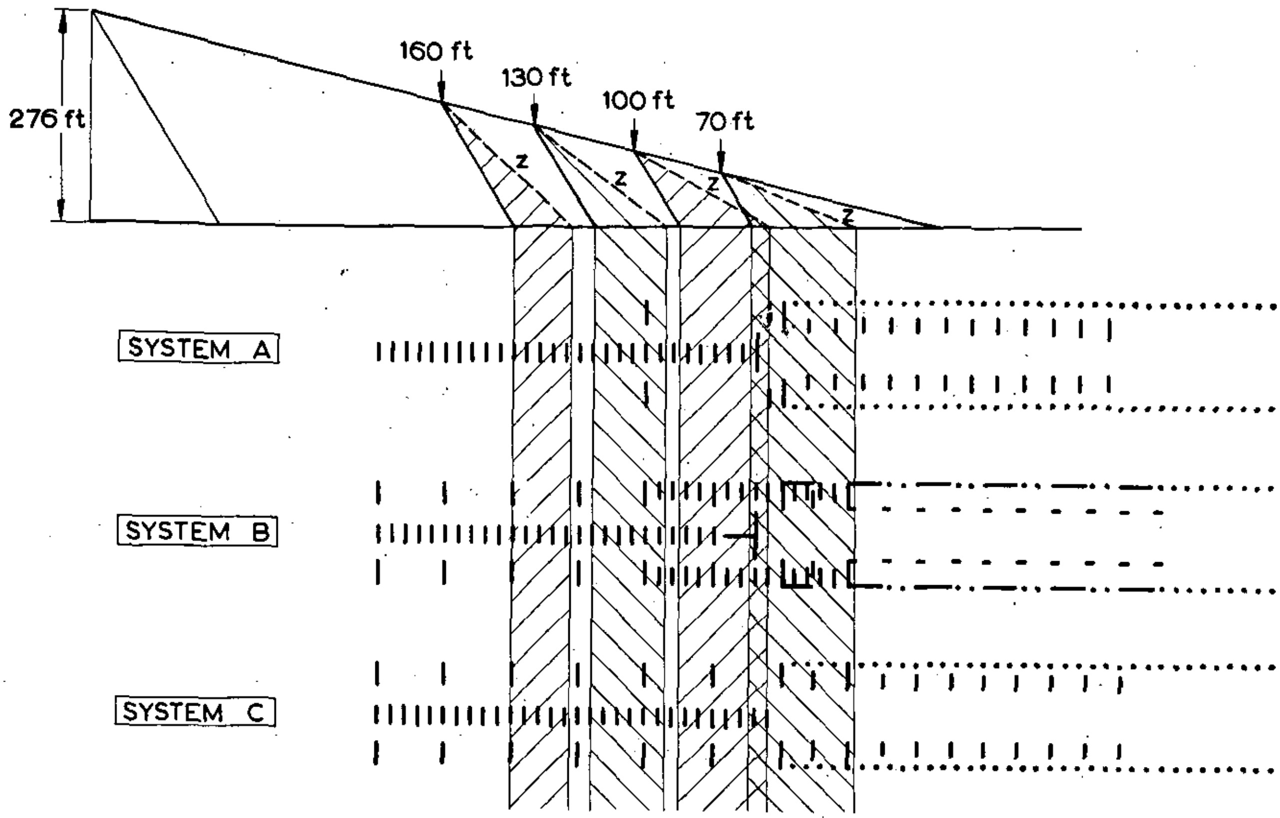

Fig. 5. Visual segments as determined by screen position at heights of 160, 130, 100 and 70 feet for a visual range z of 1000 feet.

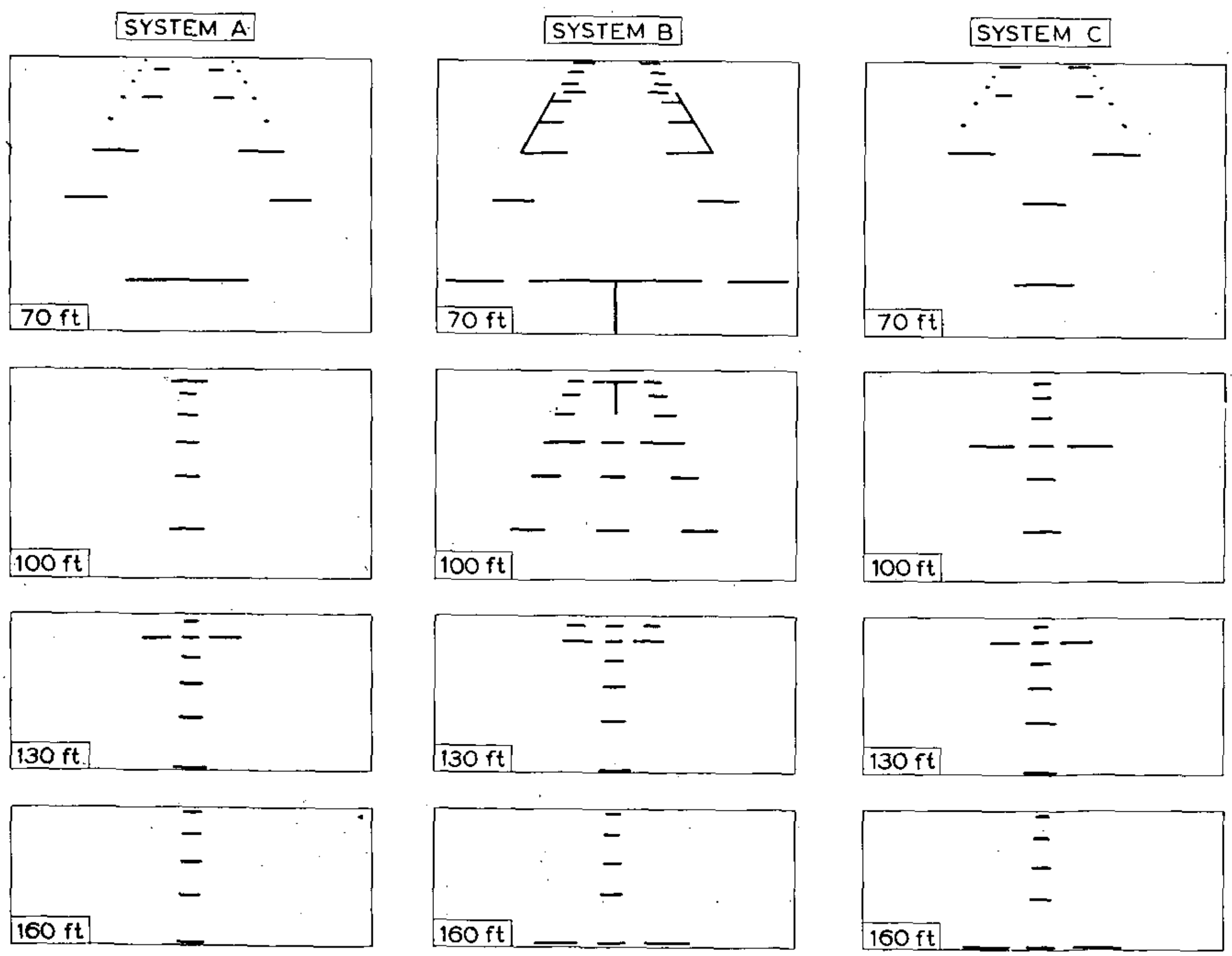

Fig. 6. Visual segments as seen by test pilot at heights of 160, 130, 100 and 70 feet.

then it appears from fig. 4:

$$\frac{s}{\sin(\theta+\varphi)} = \frac{a}{\sin[\alpha-(\theta+\varphi)]} \quad \text{or}$$

$$s = a\,\frac{\sin(\theta+\varphi)}{\sin[\alpha-(\theta+\varphi)]} \tag{1}$$

As stated before, the device has to satisfy the basic requirement:

$$z = \frac{h}{\sin\varphi} = \text{constant} \tag{2}$$

From (1) and (2) it follows that s must be controlled by θ and h in order to obtain a constant visual range z. For practical reasons not h but the rate of descent w is used as the second controlling variable.

The relation between h and w is given by

$$h = h_o - \int_o^t w\,dt \tag{3}$$

A device has been developed which performs the integration according to (3) mechanically. A description of this device – denoted by 'height-control unit' – is given below.

The controlling variable θ is obtained from a vertical gyro.

The device developed to carry out the screen control according to the principles just mentioned is diagrammatically illustrated in fig. 7. Its main part consists of the elevator channel of a Bendix PB-10 autopilot, containing the following basic elements, forming a servo system:

1. a vertical gyro measuring the longitudinal attitude θ by means of a rotating differential transformer A, coupled to the lateral gimbal axis,
2. a rotating differential transformer B, giving an output signal proportional to h_o-h. The transformer is controlled by the height-control unit mentioned above. This device (see lower part of fig. 7) consists of a dc constant speed motor, driving the differential transformer by means of a variable cone-cylinder transmission. During the approach the gear ratio is manually controlled by turning a transparent disc over an angle equal to the deflection w of a quick-response rate-of-descent indicator which is placed below the disc. The remainder of this apparatus is described below. The signal obtained in this way from the differential transformer B and the signal θ from the differential transformer A determine the screen positions s in accordance with equations (1) and (2).
3. a servo amplifier and a servo motor which drives the screen. The rotating differential transformer C is coupled to the axis of the servo motor.

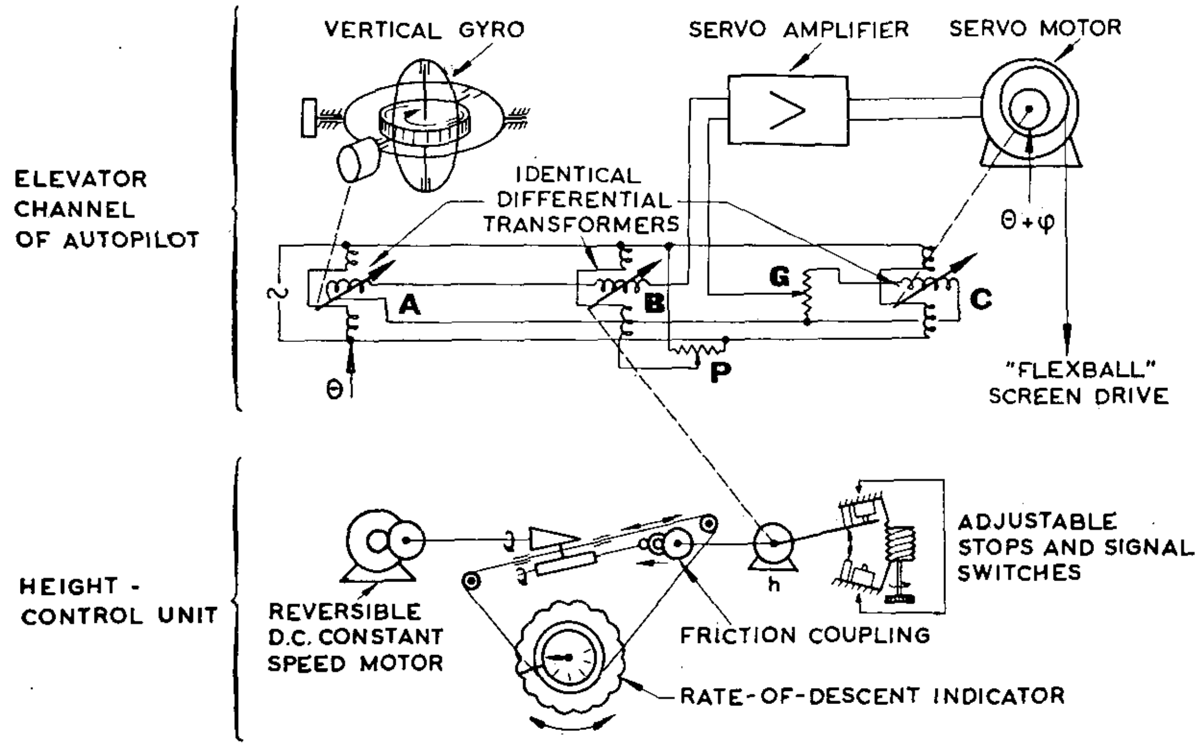

Fig. 7. Schematic diagram of screen control system.

The practical application of the screen control apparatus requires the adjustment of an initial screen position s_o at a given altitude h_o and a given longitudinal attitude θ_o; the value of s_o is determined by substitution of h_o and θ_o in equations (2) and (1).

The outputs of the 3 identical differential transformers A, B and C, having a common electrical supply, are connected in series; the sense of the output of C is opposite to that of A and B. The resultant voltage is fed to the servo amplifier, driving the servo motor which comes to

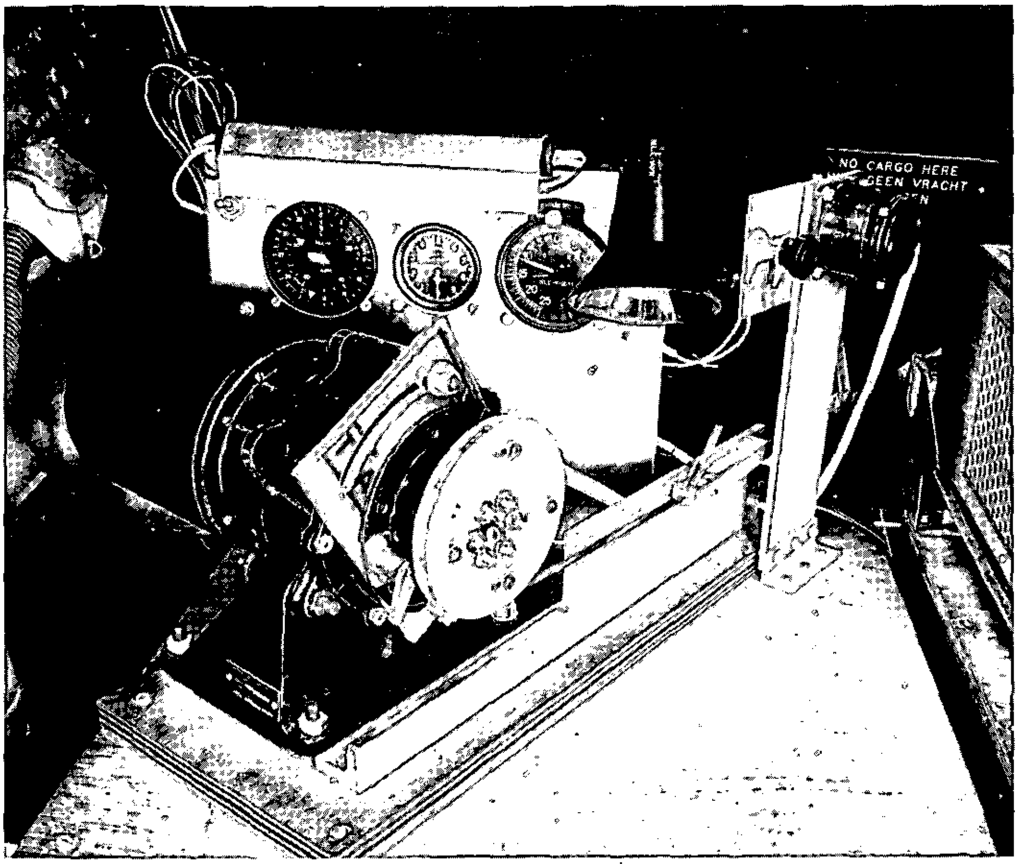

Fig. 8. Screen driving mechanism with instruments for checking proper functioning.

rest when the resultant input voltage of the amplifier becomes zero.

A potentiometer G is used to adjust the input-to-output ratio of this servo system. The potentiometer P controlling the supply voltage of B provides adjustment for equal output voltages of A and B per degree of rotation.

The servo motor is provided with an adjustable eccentric disc driving a steel tape, which is coupled to a 'flexball' driving cable to the end of which the moving screen is attached under spring load. The shape of the eccentric disc is determined by the equation (1), i.e. the tape moves over a distance s for an input angle $\theta + \varphi$ according to (1).

In the height-control unit a second transmission (with constant gear ratio) incorporates a friction coupling, enabling the differential transformer B to be at rest in both its limit positions, defined by 2 adjustable stops, without stopping the driving motor. Small in-flight correc-

Fig. 9. Manual operation of height-control unit during test flights.

Table 1. *General data of screen installation in C-47 aircraft*

Visual range = 1000 ft		
θ = + 1.0°.	Approach	α = 57°.
φ at 276 ft = 16.0°.		a = 15 inch.
IAS = 100 kts.		Screen movement
w = 445 ft/min (2.3 m/sec)		initiated at 295 ft.
at zero wind.		Screen opens at 276 ft.
Slope of glide path = 2.5°.		Nominal duration of
θ = + 6.0°.	Touch-down	upward screen movement
φ = 0.8°.		34.3 sec.
Height of pilot's eyes		Overall accuracy of φ
above runway = 14 ft.		better than ± 0.25°.

tions of the screen position and, consequently, of the actual visual range can be applied if this should deviate from the prescribed nominal value due to a possible error of the PB-10 vertical gyro or to other circumstances. This is done by rotating the mounting plate carrying the stops by means of a hand-operated gear (see fig. 7, below right). The correction is checked by means of a graph of s vs θ for the minimum sight angle φ when the differential transformer B is turned to its stop for 'screen upward'. In this case according to (1) the position of the screen s is only controlled by the longitudinal attitude θ. The check may thus be performed at any convenient altitude, e.g. during the flight preceding the test approaches.

In order to move the screen downward to the initial condition for a new approach, the motor driving the differential transformer B is of the reversible type.

Fig. 8 shows the servo motor and eccentric-disc assembly as well as the instrument panel for checking the proper functioning of the installation. On the left side of this panel is a precision instrument indicating the longitudinal attitude θ, which is sensed by a Sperry A 12 vertical gyro. A pendulum inclinometer, intended as a stand-by instrument, is situated at the right side. At the centre of the panel a desynn indicator measuring the screen position s is mounted.

Fig. 9 shows the operator of the height-control unit turning the perspex disc on the rate-of-descent indicator. To the right of this indicator the correction device for small deviations from the nominal visual range can be seen. The instrument panel in the background is provided with:

- a turn and bank indicator (left) to avoid untimely corrective action of the operator when the aircraft is turning,
- an altimeter (centre) used to determine the moment when the upward screen motion has to be started,
- 2 signal lights for the screen-position limits and
- a switch for moving the screen up- and downward.

Before the flight tests the position error of the aircraft's static-pressure system in the approach configuration has been measured. It appeared that with the altimeter adjusted to zero at the moment of touch-down, the readings during the approach were in very good agreement with the true height of the aircraft.

A sketch of the screen itself is given in fig. 10. The screen is moved by 2 pivoting rods in such a way as to obtain a displacement which is a combination of a rotational and a rectilinear motion, ensuring that the plane through the pilot's eyes and the lower edge of the screen is always perpendicular to the aircraft's plane of symmetry. The screen is made of a light-weight and rigid sandwich construction and is guided by ball bearings moving in slits mounted on a flexible base plate, thus ensuring a smooth motion even in case of slight distortion of the base plate when secured to the cockpit-window frame. Fig. 11 shows the screen device as installed in the aircraft.

For the installation in the C-47 aircraft some important data are given in table 1.

4.3 Adjustment and calibration of screen mechanism

In its original form the PB-10 servo motor is equipped with an electrically operated coupling to the elevator control system. This coupling can be activated in any desired combination of longitudinal attitude, screen position and height, obeying the basic equations (1) and (2). However, it is most practical to accomplish the coupling during the pre-flight check (see below), so that during flight the screen position needs only to be checked by means of the s vs θ-graph as mentioned before.

For the adjustment and calibration of the installation on the ground a board provided with a $(\theta + \varphi)$-scale is mounted on the cockpit nose perpendicular to the longitudinal axis of the aircraft; the intersection of this axis with the board is the point for which $\theta + \varphi = 0$ (see fig. 4). The scale on the board is observed from the test pilot's eye position. Increasing or decreasing the longitudinal attitude of the aircraft (or only of the case containing the PB-10 vertical gyro) by a known angle should result in a variation of $\theta + \varphi$ by the same angle.

The calibration board also provides the possibility of accurate and efficient coupling of the eccentric-disc and screen-drive assembly in the required position relative to the servo motor on the ground. For this purpose the screen, with the differential transformer B in its limit position for 'screen upward', is placed in a position so that on the $(\theta + \varphi)$-scale of the board the sum of the actual attitude angle θ and the minimum value of φ is read. Then the coupling is energized directly from the aircraft battery in order to avoid inadvertent uncoupling.

The height-control unit is calibrated separately by applying increasing static pressure to the rate-of-descent indicator and altimeter, and determining the time to 'descend' from a known altitude with the disc manually operated to follow the pointer of the rate-of-descent indicator.

4.4 Filter assembly

As mentioned before, seeing conditions in fog were simulated in the first place by adjusting the luminous intensity of the lights on the ground to a low value and, moreover, by applying a combination of filters, adapted to this value, in the pilot's head-support. The luminous intensity of the lights was turned down to 50 cd, a value at which no intolerable color distortion or non-uniformity of luminous intensity occurred. The combination of filters, placed 4 inches in front of the pilot's eyes in the head-support, consisted of a clear neutral filter with a transmission of 10 % and a slightly diffusing sheet of perspex with a transmission of 80 %. The shape of the

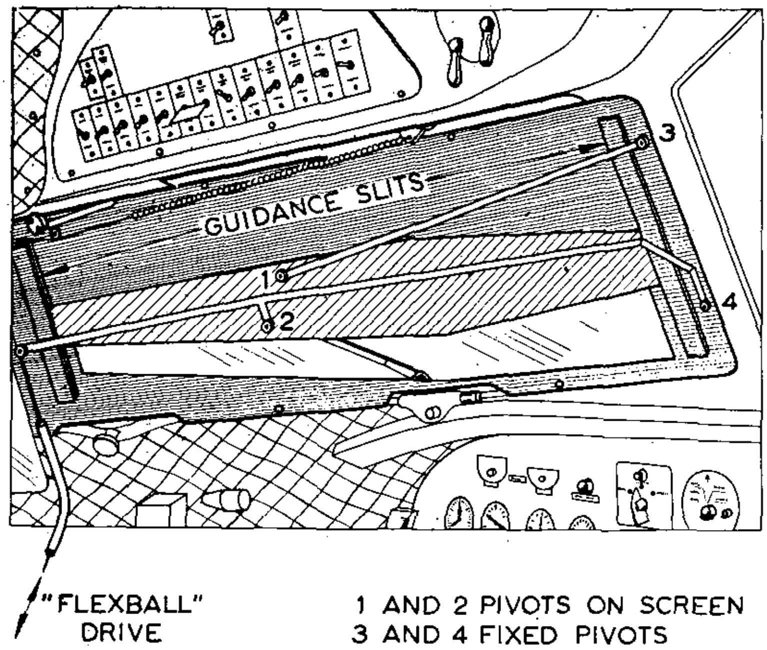

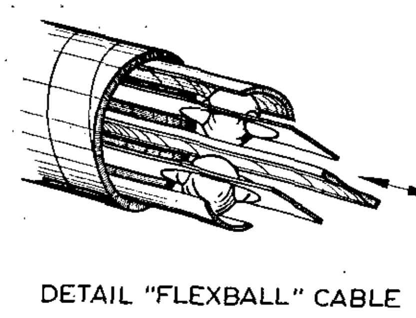

Fig. 10. Sketch of cockpit screen.

filter and the perspex sheet allowed the pilot an unobstructed view of his flight instrument panel.

An impression of the diffusing properties of the perspex sheet can be obtained from results of measurements which have been carried out in an arrangement shown schematically in fig. 12. A light source L with a diameter of 1 cm has been placed at a distance of 10 m from the perspex sheet PS. From the point P at a distance of 0.5 m on the opposite side of PS, the bright spot visible through PS is viewed through a microphotometer. Fig. 13 gives the relative luminance of the bright spot as a function of the radius r indicated in fig. 12. These measurements have been done at a distance of 0.5 m between the photometer and PS as the diffusing perspex sheet was placed originally on the cockpit window, thus roughly at a distance of 0.5 m from the pilot's eyes.

Fig. 11. Cockpit screen installation.

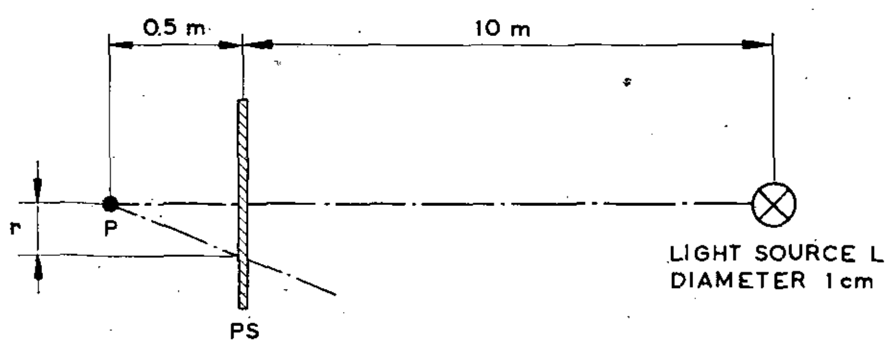

Fig. 12. Measuring arrangement for determining diffusing characteristics of perspex sheet.

In real homogeneous fog, lights at distances near to the visual range will be attenuated more than in the simulating device just described. This can be seen from fig. 14 giving the illumination on the pilot's eyes from a light source with a luminous intensity of 50 cd as a function of the distance from the pilot to this light source. The curved line A shows the eye illumination when the light source is seen through a homogeneous fog with a meteorological visibility of 1000 feet. The straight lines B and C apply to a clear atmosphere when the source is seen directly (B) and through a filter with a transmission of 8 % (C) (i.e. the transmission of the combination of the neutral and the diffusing filter). The figure shows that in the latter case the lights at a distance from the pilot almost equal to the visual range simulated by the movable screen (1000 feet) are seen brighter than in real homogeneous fog, while at short distance the lights are seen more dimly.

There is another reason why visibility conditions in homogeneous fog have not been simulated exactly by the device described in this chapter. When the aircraft banks, the plane through the pilot's eyes and the lower edge of the movable screen does not intersect the ground plane along a line which is seen parallel to the horizon by the pilot. Consequently, instead of a limitation of the visual segment of the light pattern according to a line perpendicular to the centre line, as would occur in homogeneous fog, the far limit of this visible segment is determined by a tilted line, the amount of tilt depending on the angle of bank of the aircraft. The number and the pattern of lights visible to the pilot at each moment may, therefore, differ slightly from what can be seen under conditions of real homogeneous fog with the simulated meteorological visibility. At a certain moment, e.g. the extreme end of a long crossbar may become visible, the remainder of it still being obscured, whereas in homogeneous fog all the lights of the crossbar enter the visual field simultaneously. However, as the angle of bank was always small during the test flights, some influence of the movable screen, following the roll of the aircraft, in favour of one of the light patterns is hardly imaginable.

As the test flights have been carried out by night, the

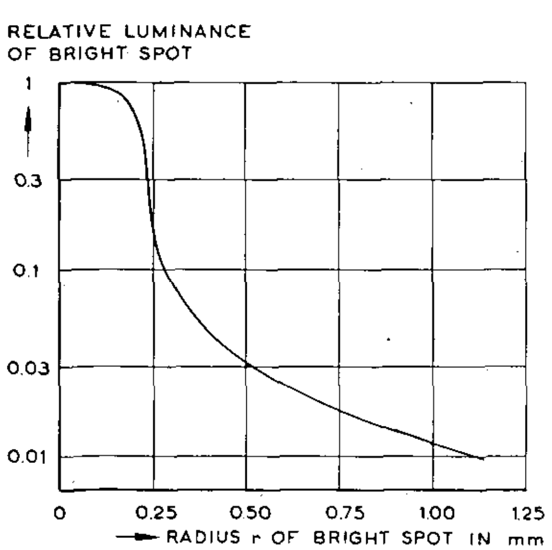

Fig. 13. Results of diffusion measurements on perspex sheet.

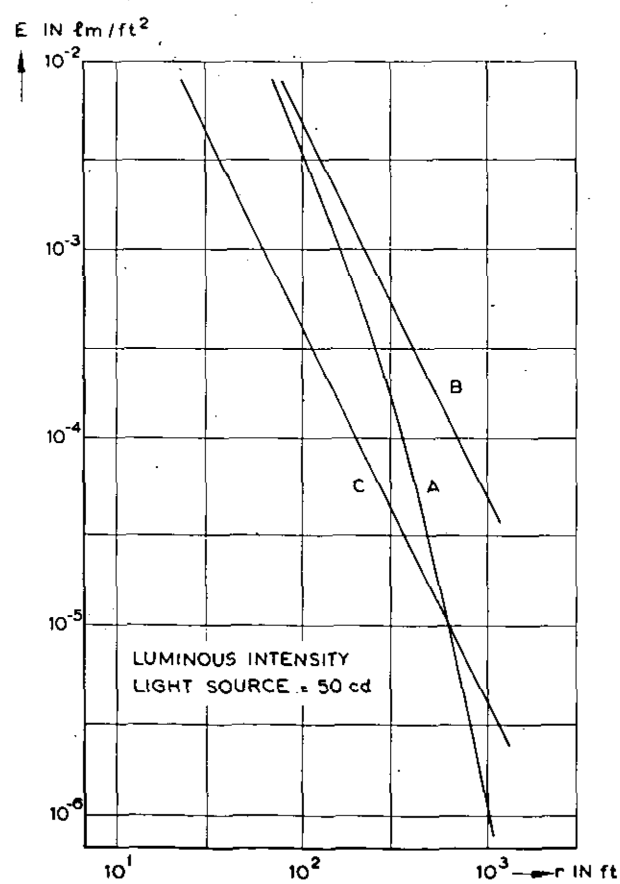

Fig. 14. Illumination E on the pilot's eye in homogeneous fog with a meteorological visibility of 1000 feet (A), clear atmosphere (B) and through neutral filter (C) as a function of distance *r* between pilot's eye and observed light source.

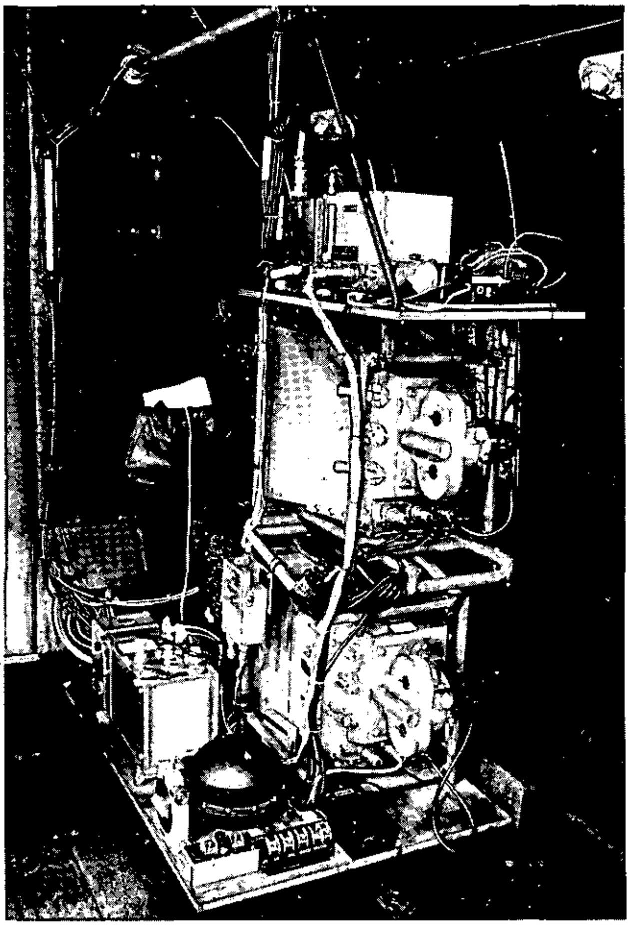

Fig. 15. Measuring equipment.

luminance of the movable screen and that of its immediate surroundings in the cockpit, as well as that of the ground outside as seen by the test pilot (through the filter combination with a transmission of 8 %) were so low, that the lower edge of the movable screen could hardly be discerned. This is an important circumstance, as the permanent presence of a line under a fixed angle to the aircraft frame in the most important part of the pilot's visual field would provide him with some information on the bank of the aircraft when comparing this line with the horizon information obtained from the crossbars in the light pattern.

Finally, the filter set before the pilot's eyes does not simulate exactly the luminance distribution in a field consisting of a pattern of lights in fog. The immediate surroundings of the lights obtain a certain luminance depending on the total luminous flux and on the beam spread of the individual lights. The more lights a pattern contains, the higher the average luminance of the fog through which the lights are seen, and the shorter the range at which lights of a certain luminous intensity are revealed. The same is true for the average luminance of the diffusing sheet of perspex before the pilot's eyes. However, in a homogeneous fog of the simulated density the effect will be more pronounced. At first sight, therefore, it seems that the chosen simulation of fog favours the system with the largest number of lights. If such an effect should exist, however, it has nothing to do with the comparison of light configurations. It would only affect the optical design of the lights which must be chosen such that the required visual range of the lights is obtained in the configuration considered, taking into account the atmospheric absorption and the scattering of the light corresponding to the simulated fog density.

As a whole, there is a good agreement between simulated and real seeing conditions and this was confirmed by the test pilots and by many other pilots who have inspected this test installation. In their opinion it provides a realistic simulation of what is generally observed in fog.

5. Measuring equipment

Measuring equipment has been installed in the C-47 test aircraft for continuous recording of the quantities mentioned in chapter 3 necessary to assess the quality of the approach and landing and the pilot's effort. A multiple trace recorder and a photographic observer have been used for this purpose. A second automatic observer used

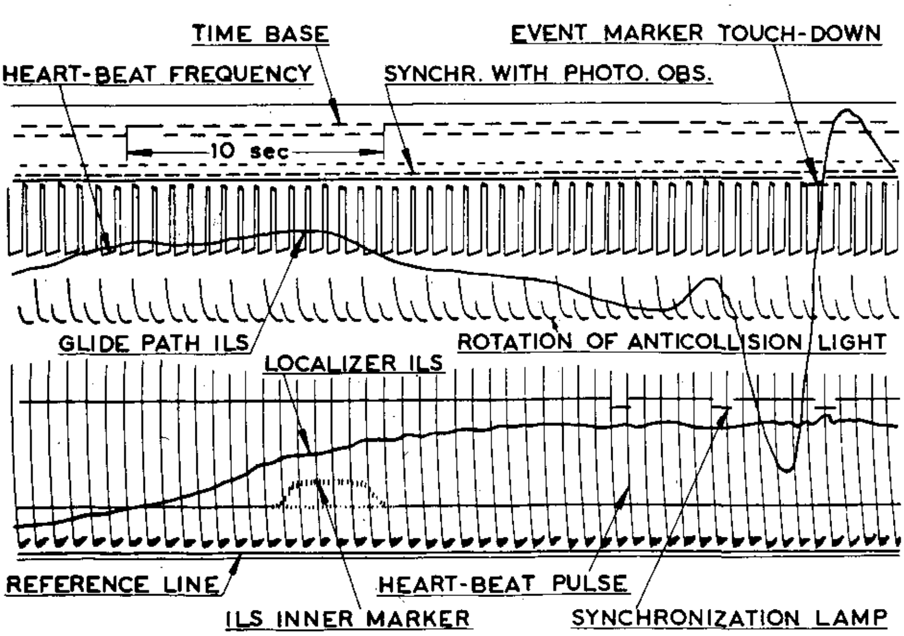

Fig. 16. Typical multiple trace recording.

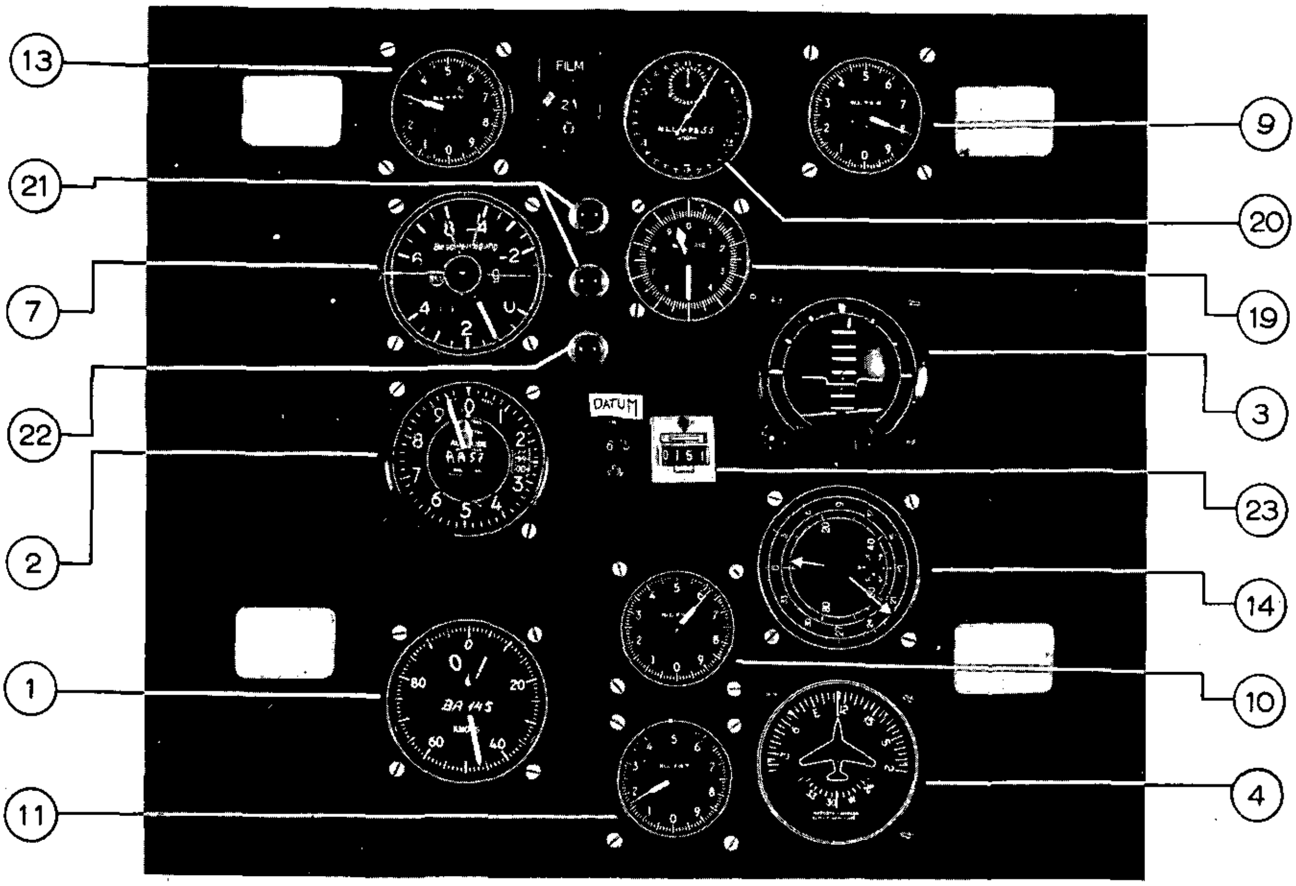

Fig. 17. Typical picture of photographic observer (1. airspeed indicator, 2. altimeter, 3. artificial horizon (pitch and bank), 4. gyrosyn slave indicator (magnetic heading), 7. top-axis accelerometer, 9. elevator deflection indicator, 10. rudder deflection indicator, 11. aileron deflection indicator, 13. screen position indicator, 14. precision gyroscopic longitudinal attitude indicator, 19. synchronizer (one rev. long pointer in 0.75 sec, closing contact in 12 o'clock position exactly), 20. split second watch (one rev. every 6 sec), 21. light signals for 'up' and 'down' position of height-control unit, 22. event marker, 23. counter).

in preparative tests did not contain instruments of essential importance for the underlying investigation. In addition, some instruments for checking the proper functioning of the screen installation were installed.

The equipment is shown in fig. 15. On top of the upper photographic observer, the heart-beat frequency measuring equipment may be seen in front of a servo-amplifier and supply box of the attitude indicator belonging to a Sperry A 12 vertical gyro, the latter being mounted on the base plate in front of the trace recorder.

In the *trace recorder* (type Beaudouin A-1320) light spots create traces on photographic paper – moving with a speed of 0.22 inch/sec – by means of galvanometers installed in the recorder. A typical recording is reproduced in fig. 16, showing 2 types of traces. First, there are the continuous traces produced by the galvanometers. The deviation of these traces, measured against a constant reference line at the bottom of the film, are proportional to the current through the galvanometers. The relation between trace deviation and input signal must be determined by calibration. Secondly, marker traces are produced consisting of parallel straight lines off-set slightly by an instantaneous 'on-off' signal. These traces, in fact, only mark the exact moment at which an event takes place. For instance, the time base is formed by a marker trace connected to an electrical chronometer producing an 'on-off' signal every second and omitting an 'off' signal every 10 seconds.

The *photographic observer* equipped with a modified 16-mm cine camera running at a speed of 4 frames/sec, was used to record indications of the instruments shown in fig. 17 (numbers of instruments agree with those of parameters, etc. mentioned below).

On the airfield 2 *Leica cameras* were placed beside the runway and perpendicular to it for the purpose of recording the landing flight-path.

The following parameters, events and signals were recorded by the trace recorder (referred to below as *tr. rec.*), the photographic observer (ph. obs.) or the ground cameras:

a. *parameters describing general flight condition:*

1. airspeed: indicator connected to the co-pilot's pitot-static system (ph. obs.);
2. altitude: altimeter connected to the co-pilot's static system (ph. obs.);
3. longitudinal attitude (angle of pitch) and lateral inclination (angle of bank) (ph. obs.);
4. magnetic heading (ph. obs.);

b. *parameters determining quality of approach and landing:*

5. ILS localizer deflection: the input current of the localizer indicator, giving sideways angular deviation from the centre line (tr. rec.);

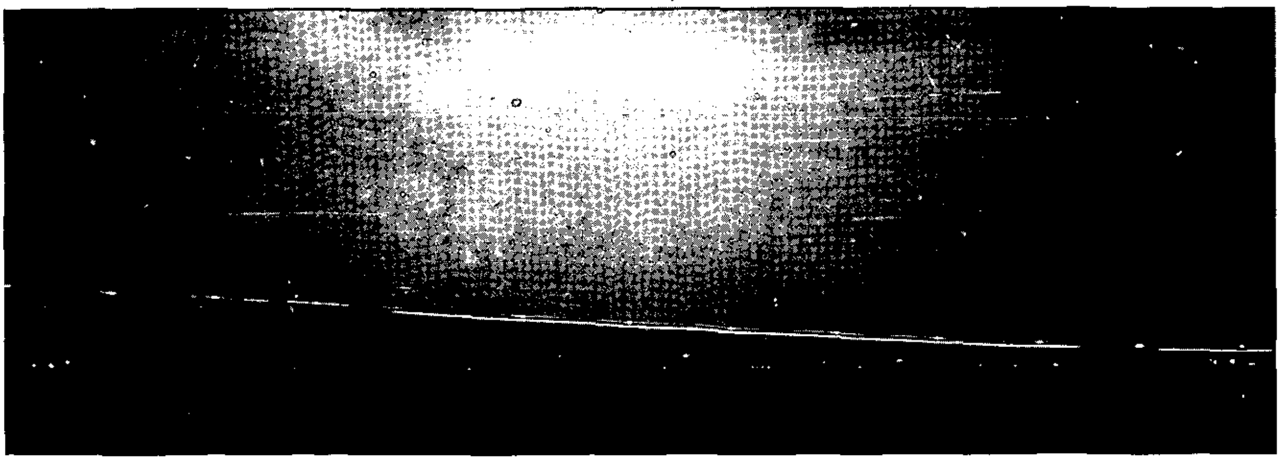

Fig. 18. Typical recording of ground camera.

6. ILS glide path deflection: the input current of the glide path indicator, giving vertical angular deviation from the ILS glide path (tr. rec.);
7. top-axis acceleration (deceleration of impact at touch-down) (ph. obs.);
8. actual flight path from threshold until touch-down: the recordings are made by the ground cameras with the shutters continuously open during the landing. The successive images of the aircraft's anticollision light (the timing of which is recorded as described in item 16) together with the images of fixed reference lights on the ground and of a synchronization lamp behind the cabin window make it possible to determine the flight path in the landing region in correlation with the test data recorded in the aircraft. A typical recording of a ground camera is given in fig. 18;

c. *parameters determining pilot's effort:*

9, 10 and 11. elevator, rudder and aileron deflections (ph. obs.);

12. heart-beat frequency: this signal is derived from a small unit incorporating a miniature light bulb and a photo-electric cell, which is clipped to the ear-lobe of the test pilot. Blood pulses through the arteries vary the amount of light received by the photo-electric cell. Two types of traces are recorded. Both show deviations for each blood pulse, but in one of them the height of the pulse is proportional to the blood pulse frequency also (tr. rec.) [7];

d. *parameters determining the visual range actually attained:*

13. position of cockpit screen (ph. obs.);
14. longitudinal attitude (precision measurement) (ph. obs) (For the calculation of the actual visual range the true height must also be known (see 2 and 8));

e. *event marks and other signals:*

15. moment of ignition of the synchronization light behind a cabin window. The recording is needed for establishing the correlation between the flight path recordings on the ground and the recordings of the airborne equipment (tr. rec.);
16. the rotations of the aircraft's anti-collision light by means of a photo resistor in the (perspex) navigation dome (tr. rec.);
17. moment of touch-down. The event marker was controlled manually (tr. rec.);
18. ILS inner-marker beacon signals, facilitating the identification of the recordings (tr. rec.);
19. correlation between the recordings of photographic observer and trace recorder: an instrument with 2 pointers rotating at a constant speed of 1.3 and 0.13 revolutions per sec respectively, is mounted in the photographic observer. Each time the fast pointer passes the zero mark of the dial a contact is closed resulting in an 'on' signal of a marker trace in the trace recorder;
20. time: 'on-off' signals every second (tr. rec.) and split second watch (ph. obs.);
21. light signals, indicating 'up' and 'down' positions of the screen (ph. obs.);
22. event marker for the indication of other important moments (ph. obs.);
23. counter number of every shot (ph. obs.).

A normal *tape recorder* and a *miniature wire recorder* (as stand-by) were used to record all remarks made by the test pilot or the test personnel during the test flights in order to facilitate an explanation of irregularities in the approaches and landings afterwards. It turned out, however, that there was no need for these recordings.

The stability of the ILS system was frequently checked by carrying out a perfect cross needle approach and recording the actual flight path by means of a ground tracking cine-camera, the latter being synchronized with the trace recorder in the aircraft.

Calibration of the ILS signals was achieved by determining the relation between the difference in depth of modulation (DDM) of the ILS transmitters for various deviations from the ILS glide path in azimuth and elevation, followed by the calibration of the trace recorder for various signals applied to the input of the ILS localizer and glide path receivers.

The actual visual range obtained during the flight tests could be calculated from the recorded values of longitudinal attitude θ and height h by applying equations (1) and (2) of chapter 4; the value of h was taken from the

[7]) For further details, see:
'A transmission cardiotachometer for continuous measurements on working persons' by G. A. Harten and A. K. Koroncai, Philips Technical Review **21**, p. 304, 1959/60.

ground-camera pictures and, for larger altitudes, from the altimeter recordings. These calculations showed that a deviation of ± 100 feet from the nominal visual range – which was 1000 feet for all tests – was generally not exceeded, except during the final part of the flare-out. This agrees with the overall accuracy of the sight angle φ governed by the cockpit screen installation which, as stated in table 1, was found to be better than ±0.25°.

To ensure the deviations of the visual range to be small also at very low heights just prior to touch-down, a much higher accuracy of the sight angle and, consequently, a better class of vertical gyro for the attitude stabilization of the cockpit screen would be required.

Generally, the simulated visual range in the touch-down region exceeded to some extent the nominal value due to deceleration effects on the vertical gyro.

6. Interpretation of test data

From the recordings obtained with the equipment described in the preceding chapter the following data have been derived:

a. on the quality of the approach:
- approach height (actual flight path projected on a vertical plane parallel to the runway centre line) until threshold,
- approach ground-track (actual flight path projected on a horizontal plane) until threshold,

b. on the quality of the landing flight path and the touch-down:
- height (as a function of distance) from threshold until touch-down,
- distance of touch-down point from runway threshold,
- vertical deceleration of impact at touch-down,

c. on the pilot's effort:
- control movements,
- pilot's heart-beat frequency during approach and landing.

The data on the actual flight path derived from the recordings, if not stated otherwise, are related to the lowest point of the main undercarriage, projected to the aircraft's plane of symmetry.

Some of the data on the quality of the landing and on the pilot's effort can be analysed and compared between light patterns in a rather simple way. Others, specially those determining the flight path and the data on the control movements, do not easily lend themselves to direct comparison and to statistical analysis. In view of this, a special evaluation procedure [8]) has been applied in order to be able to express the quality of the flight path during approach and landing in one or two figures of merit.

The quality of the approaches and landings has been expressed in marks based on the shape and the location of the actual flight path. The marks varied linearly from 0 to 10 between unacceptable and ideal performance respectively.

For the *approach quality* the actual flight path is considered from a point 3000 feet before the threshold, when the pilot should establish visual contact, until the threshold. The assessment of the quality of the approach has been based on the 'relative ease' with which the pilot can bring the aircraft into an 'entrance portal' at the runway threshold. This portal is of a rectangular shape and has a height of 16 feet and a width of 30 feet (see fig. 19 and 20). The centre of the portal is chosen at 37 feet above the runway, equal to the average height above the threshold of all flights made during the preliminary investigation referred to in chapter 3. The relative ease is in the first place determined by the minimum size of a straight tapered channel by which the actual flight path can be enclosed. The channels corresponding to the quality marks 1 to 10 have a rectangular cross section with horizontal and vertical sides. The linear dimensions of the entrance cross sections of the channels are 3.6 times those of their exit sections (located at the runway threshold), permitting a certain channel to be defined completely by its exit section only. Additionally, the axis of an approach channel should run through the above mentioned entrance portal at the threshold. Two marks for the quality of the approach have been determined, one for *approach height* with the aid of fig. 19 and one for *approach ground-track* with the aid of fig. 20.

[8]) This procedure has been proposed by ir. F. E. Douwes Dekker of the National Aeronautical and Astronautical Research Institute (NLR), Amsterdam.

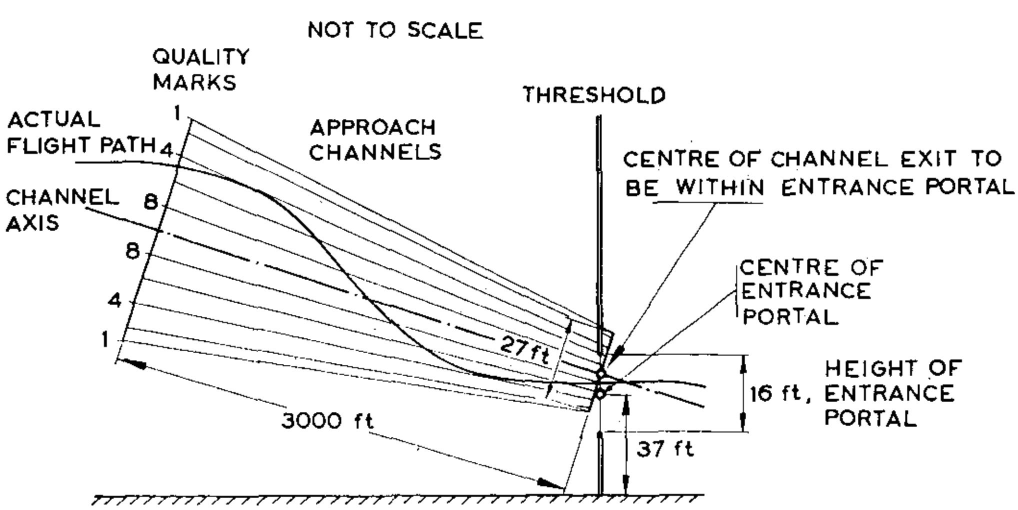

Fig. 19. Principle of assessment of approach height quality.

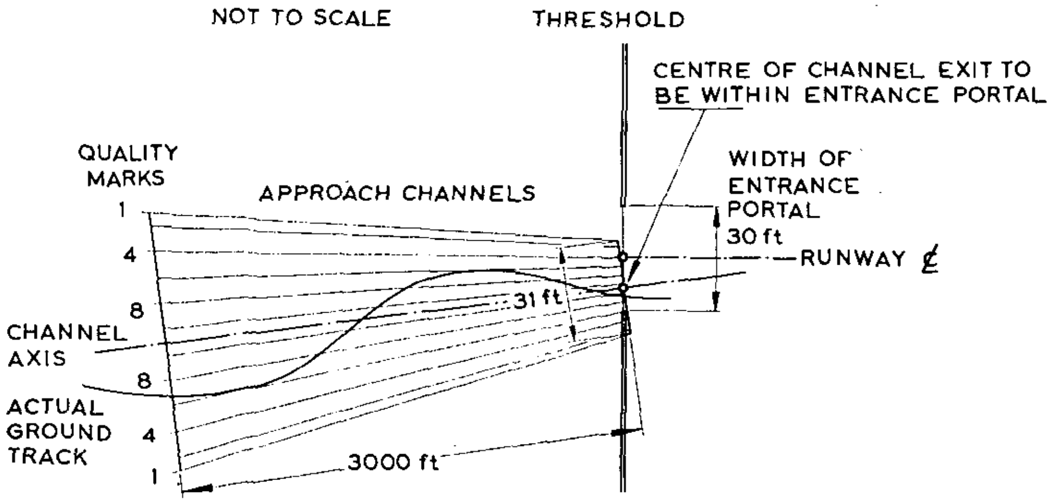

Fig. 20. Principle of assessment of approach ground-track quality.

To obtain full marks (10) for approach height the actual flight path slope should be constant, in other words, the vertical dimensions of the enclosing channel must be zero (see fig. 19). To obtain full marks (10) for approach ground-track it must be possible for the actual flight path to be enclosed by a channel with an initial width of 11 feet tapering to 3 feet at the threshold (see fig. 20). All approach channels with an exit height of more than 27 feet or an exit width of more than 31 feet are judged unacceptable, giving no marks (0) for approach height and approach ground-track respectively. It follows from what has been stated before that no marks (0) are given also in case the axis of an approach channel does not intersect the entrance portal. It ought to be remembered that the slope of the approach channel was not prescribed, because the actual initial position, 3000 feet before the runway threshold, could not be influenced by the test pilot.

The process of judgment of the approach quality was amended, in so far as ground-track is concerned, in case the initial approach position of the aircraft was purposely deviated sideways from the centre line by the safety pilot. The tapering ratio of the channel was than doubled to 7.2, while its axis was curved gradually from the initial direction on to the centre line at the threshold.

The *quality of the landing flight path and the touch-down* has only been evaluated in height from the threshold over a length of 2700 feet down the runway, when the touch-down should have been completed, and in the location of the touch-down point. Here also 2 quality marks, one for *height from threshold until touch-down* and the other for *distance of touch-down from threshold,* have been determined. The quality mark for height from threshold until touch-down is again considered to be determined by the minimum size of a tapering channel by which the actual flight path can be enclosed.

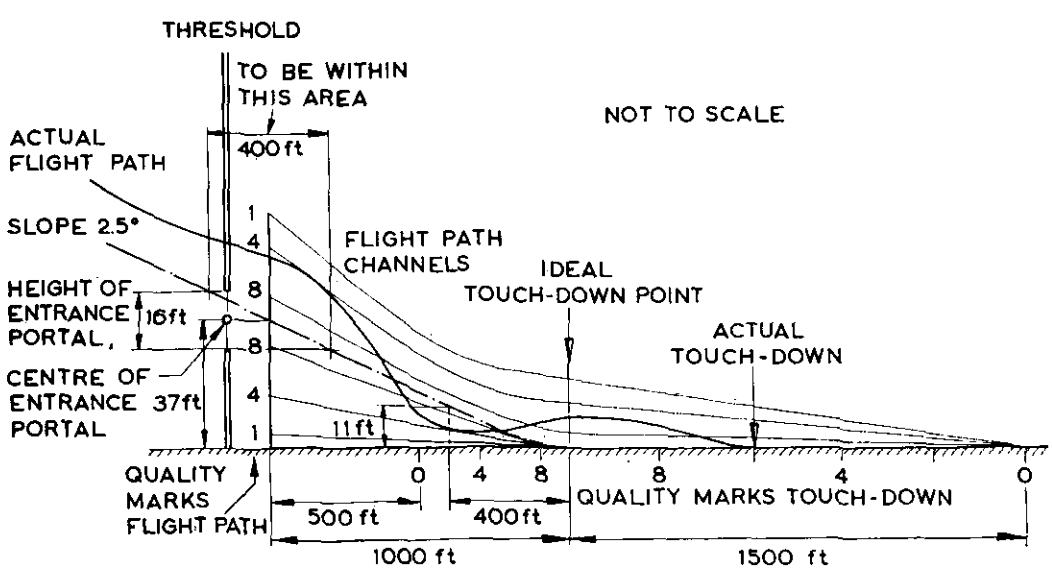

Fig. 21. Principle of assessment of quality of landing flight-path and touch-down.

The shape and the dimensions of the channels are chosen on the basis of the following considerations (see fig. 21).

For a landing flight path and a touch-down judged with the highest quality mark (10), the aircraft should pass the threshold at some height within the entrance portal and descend with a constant slope of 2.5° until flare-out. Moreover, the landing should be continued by following a flight path parallel to the one corresponding to a height at threshold of 37 feet and a distance of touch-down from threshold of 1000 feet, the flare-out starting at a height of 11 feet and covering a distance of 400 feet. This defines the channel of zero thickness of fig. 21, to which the highest quality mark for height from threshold until touch-down and for the touch-down itself (10) is attached. To allow for passing the threshold at an arbitrary height within the entrance portal, the channels may be displaced 200 feet forward or backward which also means that a touch-down qualified with mark 10 may occur at a distance between 800 and 1200 feet.

No marks (0) are given for height from threshold until touch-down, when the touch-down takes place at a distance of 1000 feet from the threshold after having passed the threshold at a height of less than 1 foot. The vertical distance between this height of 1 foot and the height of the centre of the entrance portal (37 feet) is divided equally over the channels belonging to the marks 1 to 9. The vertical position of the upper and lower boundaries of the channels near the threshold is symmetrical with respect to the channel with mark 10. The upper boundary of the channel with mark 1 is further determined by the requirement that the point of touch-down is not allowed to be more than 2700 feet beyond the threshold. This means that the height above the runway is considered unacceptable (quality mark 0) when it surpasses a value varying from 89 feet at threshold to zero at 2700 feet beyond threshold. The height of 89 feet corresponds with the point of intersection of the upper boundary of the channel, carrying quality mark 1, with the vertical line through the extreme left threshold position, when the grid of fig. 21 is displaced 200 feet in the landing direction.

The second quality mark (for the distance of touch-down from the threshold) is read off from the scale along the horizontal axis of fig. 21. It has already been stated that full marks (10) are obtained when the touch-down occurs between 800 and 1200 feet. The scale shows that, when making allowance for passing the threshold at an arbitrary height within the entrance portal, no quality mark (0) for touch-down distance is obtained when the distance from the threshold is less than 300 or more than 2700 feet.

Some corrections had to be applied to the several quality marks determined according to the procedures just described. The quality marks for approach height and approach ground-track have been corrected for deviations in actual runway visual range from the intended 1000 feet. One point was added to or subtracted from both marks in a few cases, where this deviation was more than 100 feet shorter or longer than the nominal one respectively. The quality mark for touch-down was corrected for rough landings by subtracting one point for every 0.5 g vertical deceleration at the impact.

For the appraisal of the *pilot's effort* based on the recordings of the control movements and of the pilot's heart-beat frequency, a 'travel index' and a 'heart-beat factor' have been introduced respectively. For the travel index a figure proportional to the total travel of elevator, rudder and ailerons over a certain period has been deduced from the recordings. This period was taken from 5 seconds before until 10 seconds after passing the inner marker. The heart-beat factor is the ratio of the heart-beat frequency of the test pilot at touch-down and that just prior to the approach, when the test pilot was already in his cockpit seat but not yet flying the aircraft.

7. Result and their statistical analysis [9])

7.1 Results

Appendix III contains a complete survey of the results, obtained with the 16 pilots who carried out the whole test programme. These results contain the quality marks for approach height, approach ground-track, height from threshold until touch-down, touch-down and furthermore the travel indices for the control movements as well as the heart-beat factors. These marks, indices and factors have been deduced from the recorded results as described in the foregoing chapter. The appendix contains moreover the heights above the threshold and data on the wind speed and wind direction.

7.2 Quality of approach

7.2.1 Quality of approach height, travel index for elevator and height of the aircraft at the moment of crossing the runway threshold

Table 2 shows the average of the quality marks of the approach height and the average of the travel indices of the elevator for each combination of initial position and light system.

Table 2. *Average of approach height quality marks and of elevator travel indices*

Initial position ⟶			Ideal	High	Left	Average
Approach height quality mark	System	A	3.4	3.9	3.7	3.7
		B	3.6	4.4	3.8	3.9
		C	2.8	4.2	2.6	3.2
Elevator travel index	System	A	18.8	19.6	18.0	18.8
		B	20.4	21.9	16.0	19.5
		C	19.4	17.6	20.8	19.3

The standard deviation of the averages per system is 0.32 for the approach height quality mark and 1.04 for the elevator travel index. This means that it can be concluded with a confidence of 95 % that there is a real difference in approach height between the systems B and C.

Naturally, the scaling of the quality marks given in chapter 6 may be criticized and therefore it may be

[9]) The statistical analysis has been carried out under the supervision of Prof. ir. J. W. Sieben of the Technological University, Delft.

declared inadmissible to attach technical verdicts to the differences between the averages mentioned above. However, if one is convinced that the (unknown) score which ought to be used is a monotoneously increasing function of the score used here, the conclusion stated in this paragraph may still be reached by slightly different reasoning, and these conclusions will then depend to a much lesser extent on the appraisal scale.

As already marked, 16 pilots each made 3 flights with each of the 3 systems. The sequence of the systems was chosen at random. For each pilot the average quality marks for approach height of the 3 systems can be ranked according to magnitude with rank 1 for the system with the lowest average, 3 for the system with the highest average and 2 for the third system. If the average marks for 2 systems are equal, each system is given the average of the corresponding ranking numbers. The same can be done for the elevator travel indices. In this way the ranking numbers of table 3 will be obtained.

If there were no difference between the 3 systems, the same total for each system would be expected at the bottom of the table. If that is not the case, it may be due to chance or to a real difference between the systems. The latter can only be decided upon when the differences between the totals are large. A yardstick for this is provided by the Friedman's test for m rankings. It can be concluded from this with almost 97.5 % confidence that on average system C gets a really lower appraisal of approach height than systems A and B. The data on elevator movement, however, do not show significant differences between the light patterns.

Table 3. *Ranking numbers of test flights according to magnitude of approach height quality marks and of elevator travel indices*

Pilot	Approach height quality mark			Elevator travel index		
	A	B	C	A	B	C
1	3	1	2	1	2	3
2	2½	2½	1	1	2	3
3	3	2	1	3	2	1
4	1	3	2	1	3	2
5	1	3	2	3	2	1
6	3	1	2	2	1	3
7	2½	2½	1	3	2	1
8	1½	3	1½	1	3	2
9	2	1	3	3	2	1
10	3	2	1	3	2	1
11	1	3	2	2	3	1
12	2	3	1	3	2	1
13	3	2	1	1	3	2
14	2½	2½	1	2	1	3
15	2	3	1	3	1½	1½
16	2	3	1	1	2½	2½
Total	35	37½	23½	33	34	29

Appraisal of the height of the aircraft at the moment of passing the threshold [10]) is difficult because, as may be seen from Appendix III, quite a lot of test data are lacking. However, from this appendix the average difference in height for the 3 systems for each pilot, shown in table 4 can be derived.

Table 4. *Average difference in height above threshold*

Pilot	System B — System A	System B — System C
1	—11.3	— 5.3
2	—19.5	—30.5
3	— 4.5	—25.7
4	—29.5	—15.0
5	—11.0	— 2.3
6	—13.0	—20.7
7	+ 9.7	— 7.3
8	—13.0	+ 1.0
9	+10.0	+15.0
10	— 3.0	—20.0
11	— 2.7	—34.0
12	+ 4.0	+22.0
13	— 5.2	+ 5.5
14	+ 4.7	—10.7
15	—12.0	—10.0
16	— 9.7	—14.5

From these figures, with the aid of the 'Wilcoxon symmetry test' it can be concluded with 95 % to 97.5 % confidence that the average height above the runway threshold for the systems A and C is greater than for system B. There is not much difference between A and C.

The average height above threshold with system C (54 ft) proves with great confidence (more than 99 %) to be really greater than with system B (44 ft), whilst with system A this height (51 ft) is also really greater than in the case of system B but now to a level of confidence of 98 %. The test used here is commonly referred to as 'T-test'. Its use is in fact not entirely justified for this kind of experimental data. It can be argued, however, that this unjustified application of the T-test results in a decrease of the level of confidence. Therefore, the values of 99 % and 98 % can be considered as conservative. The standard deviation of the height at the individual flights with the systems A, B and C is 17.3, 14.8 and 15.3 respectively. The differences in this standard deviation are of no importance.

From the date in this paragraph the following general conclusions can be drawn:

The quality of the approach, as demonstrated in the approach height is worse for light system C than for A and B. With the light systems A and C the runway threshold is generally crossed at a greater height than in the case of system B.

As will be indicated in paragraph 7.3, this has no

[10]) The heights above the runway threshold mentioned in Appendix III are related to the aircrafts anti-collision light. The distance between this light and the lowest point of the main undercarriage (being the reference point of the flight path interpretation of chapter 6) is 14 feet in the approach attitude. If the aircraft follows the ILS glide path exactly, the height of the lowest point of the undercarriage at the runway threshold is 30 feet.

influence on the quality of the landing and moreover, the average height for B is roughly equal to the height of the ILS glide path at the threshold.

7.2.2 Quality of approach ground-track and of travel indices for rudder and aileron

Table 5 shows the averages of all pilots with respect to the approach ground-track quality marks and to the rudder and aileron travel indices for each combination of system and initial position.

Table 5. *Average of approach ground-track quality marks and of rudder and aileron travel indices*

Initial position ⟶			Ideal	High	Left	Average
Approach ground-track quality mark	System	A	6.6	6.9	4.4	5.9
		B	7.8	8.2	5.4	7.2
		C	7.2	7.3	5.0	6.5
Rudder travel index	System	A	25.7	17.1	21.9	21.5
		B	17.8	13.7	20.4	17.3
		C	18.4	16.2	21.2	18.6
Aileron travel index	System	A	46.7	37.7	51.7	45.2
		B	40.0	31.9	47.2	39.7
		C	43.6	41.5	60.1	48.4

The standard deviations of the average per system are 0.21 for approach ground-track quality mark, 1.59 for rudder travel index and 3.35 for aileron travel index.

From the average values in table 5 and from their standard deviations it is evident that there is a difference between the systems, and also between the initial positions, in the average approach ground-track quality. With at least 95 % confidence it can be established that the differences between the 3 systems in average score are significant, in the sense that B is better than C and C is better than A. There are differences in control movements too. However, the only significant difference in this respect is that the rudder is used more with A than with B. This difference is significant on the 90 %-confidence level only.

Using the method of m rankings as in paragraph 7.2.1 the results of table 6 are obtained.

Two real differences are now found:

a. the quality of the approach ground-track for system B is really better than for system A,

b. the travel index for rudder in system A may be regarded as really higher than in system B.

The difference between B and C in quality of approach ground-track and those in the aileron or in the rudder travel index, other than between A and B, are not significant.

The foregoing gives rise to the following conclusion:

With respect to keeping the aircraft on the extended centre line of the runway, system B is better than system A and C: the adherence to the centre line with system B is significantly better than in the case of system A and this better result is achieved with less total movement of the rudder.

Table 6. *Ranking numbers of test flights according to magnitude of approach ground-track quality marks and rudder and aileron travel indices*

Pilot	Approach ground-track quality mark			Travel index of rudder			Travel index of aileron		
	A	B	C	A	B	C	A	B	C
1	2	2	2	3	1	2	1	2	3
2	1	2½	2½	3	1	2	2	1	3
3	1	2½	2½	2	3	1	1	2	3
4	2	3	1	3	1½	1½	2	1	3
5	1	3	2	1	3	2	1	2	3
6	1	2	3	1	2	3	2	1	3
7	1	3	2	3	2	1	1	3	2
8	2	3	1	1	3	2	2	3	1
9	1	2	3	3	2	1	3	2	1
10	1½	3	1½	3	2	1	3	2	1
11	1	3	2	3	1	2	3	2	1
12	1	2	3	3	1	2	3	1	2
13	2	3	1	3	2	1	2	1	3
14	1½	3	1½	3	1	2	2	1	3
15	1	2½	2½	3	2	1	3	1	2
16	2	3	1	2	1	3	1	2	3
Total	22	42½	31½	40	28½	27½	32	27	37

7.3 Quality of landing

There is a considerable lack of data in the case of the quality marks for the landing, so that an exact statistical treatment would be very laborious.

However, the method of m rankings, introduced in paragraph 7.2, can be applied with the aid of the cases in which a direct comparison of all 3 systems is possible. This gives the results of table 7.

Table 7. *Ranking numbers of quality marks for height from threshold until touch-down and for touch-down*

Pilot	Quality mark for height from threshold until touch-down			Quality mark for touch-down		
	A	B	C	A	B	C
1	2½	2½	1	1	3	2
2	3	2	1	3	1	2
3	2	1	3	2	1	3
4	1	2½	2½	1	2	3
5	2	2	2	2½	1	2½
6	3	1	2	3	1	2
7	1	3	2	3	1	2
8	1½	1½	3	1	2	3
9	3	1½	1½	1	2	3
10	3	2	1	1½	3	1½
11	2	1	3	1	2	3
12	2	3	1	2	3	1
13	1	3	2	3	2	1
14	1	3	2	2	1	3
15	2	1	3	3	1	2
16	1	3	2	2	3	1
Total	31	33	32	32	29	35

From the totals in the bottom line of the table, which differ very little, it is evident that from a point of view of landing quality there is no real difference between the 3 systems. Nor is there any real difference between the systems with regard to the number of overshoots: with system A there were 5, with system B 7 and with system C 6 overshoots.

The conclusion must therefore be:

From the figures based on the data recorded between the threshold and the touch-down point it cannot be concluded with any certainty that there is a real difference between the 3 light systems as far as the possibilities of executing a correct landing are concerned. It should be kept in mind, however, that the landings have been carried out with landing lights switched on immediately after passing the threshold. This conclusion, therefore, may not hold for landings made with the visual guidance of the different light patterns only.

7.4 Heart-beat factor

In table 8 the average heart-beat factor is given for each combination of initial position and light system.

Allowing for the fact that the standard deviation of the average per system can be estimated as 0.018, it may be stated from this table that:

With system C the heart-beat factor is higher on the average (95 % confidence) than in the case of system A. The heart-beat factor for system B is also higher than for system A (confidence lower than 95 %).

Table 8. *Average heart-beat factor*

Initial position ⟶		Ideal	High	Left	Average
System	A	1.36	1.33	1.35	1.35
	B	1.39	1.40	1.39	1.39
	C	1.41	1.46	1.40	1.42

This result does not comply with the general tendency of the conclusions stated in the foregoing paragraphs of this chapter.

7.5 Wind speed and wind direction

The wind speed and wind direction are shown in Appendix III for every flight. For none of the scores and data analysed in the paragraphs 7.2 to 7.4 could a difference between the results achieved with the 3 light patterns be attributed to variations in wind speed and/or wind direction.

8. Verbal comments

Immediately after completion of each approach and landing, the test pilot was questioned by an engineering test pilot of the National Aero- and Astronautical Research Institute. The questions were roughly similar for all concerned and were designed to encourage the test pilots to comment frankly on the various aspects of the light systems involved. Generally, pilots went into great detail describing their respective experiences and seemed to have firm opinions. Unfortunately, all comments were rather different and sometimes even contradicting. E.g.: the intensity of the green threshold lights was considered to be 'poor', 'too bright' or 'satisfactory' by different pilots; appreciation of the red T varied between 'very useful', 'useless', 'much too bright' and 'not noticed at all'. This may illustrate the doubtful value of subjective appraisal based on verbal comments only. It also proves the necessity of quantitative evaluation. However, different opinions could in some cases be related to the same basic judgement. In the following an attempt has been made to give a survey of general opinions.

Most pilots did rely on the intervention of the safety pilot in case of emergency and would therefore refuse to do the same tests without a safety pilot. The use of landing lights from about 50 ft height until the touch-down was completed, impeded a clear judgement of the runway lighting. Many pilots focussed their attention on the lighted texture and painted markings of the runway instead of the runway lights, to perform flare-out and touch-down.

With regard to system A there was a general complaint of severe lack of height information in the manoeuvring zone, until the 1000-ft crossbar. This crossbar, however, was appreciated as a clear indication of the 1000-ft warning. The 60-ft gauge of the runway lights was considered too narrow.

The isolated crossbars of system B supplied sufficient initial information to start corrective action for alignment or height. The area between the 1000-ft bar and the threshold, however, seemed to be the main source of information to complete the corrective action, especially in case of a very late contact. The too wide gauge (138 feet) of the double row of lights between the threshold and the aiming point created a black gap with respect to the bright pre-threshold area. Therefore, the aiming point lighting was rather appreciated. The 150-ft wide gauge runway lights were considered useless compared with the 75-ft narrow gauge runway lights. Roll guidance was considered unsatisfactory in the landing zone.

The centre line with crossbars of system C was generally considered satisfactory. The 1000-ft warning in the form of a red crossbar was found insufficient. The 250-ft longitudinal spacing of the narrow gauge system was considered too large; height information for flare-out and touch-down became therefore unsatisfactory.

It may be concluded that system A was practically unanimously rejected. A majority of the test pilots was willing to accept system B, provided that specific, rather controversial modifications were applied. These modifications seemed to have the common aim of creating a compromise between the basic ideas underlying the systems B and C, keeping the overall pattern simple and having a clear configuration change at the threshold, adequate 1000-ft warning and aiming point lighting, and adding centre line lights on the runway.

Generally, the fog simulating system was appreciated as being basically sound, there being no errors introduced by altitude or attitude variations. The system was also considered a very useful training device.

9. Conclusions

9.1 Test procedure and interpretation of results

The test procedure applied in this investigation is characterized by

a. the use of airborne recording equipment for collecting quantitative data determining the quality of the actual flight path from the beginning of the final approach until touch-down as well as data on the pilot's effort (control movements, heart-beat frequency) to establish approach and landing,

b. the application of a movable screen before the pilot's eyes which, in combination with suitable filters and a convenient adjustment of the luminous intensity of the lights on the ground, simulates weather conditions in homogeneous fog,

c. the elimination of the influence of personal characteristics in the test results by means of a flight test programme to be carried out by a minimum number of test pilots and comprising a minimum of flying hours. This programme was set up on a strict statistical basis in order to obtain sufficient test data and to avoid appreciable familiarization with the light configurations and with local circumstances.

The data collected when applying the simulating device mentioned under b) present a reliable basis of comparison of the effectiveness of the guidance obtained from visual aids during approach and landing.

The amount of data obtained in this procedure is so large and is produced in such a form that a special interpretation method had to be developed to reduce the test results to a form suitable for statistical analysis. This interpretation method yields consistent figures of merit for the quality of the actual flight path and the touch-down.

9.2 Verbal comments

The survey of the answers to a carefully selected set of questions put to the pilots in the present investigation shows that such answers in themselves can not present a reliable basis for comparison of the quality of guidance of different light patterns. Too much variance of subjective impressions is brought forward in the answers. An exception to this was the almost unanimously expressed opinion that system A should be rejected.

Keeping in mind the restricted reliability of verbal comments, a further conclusion might be that the majority of pilots is willing to accept system B, if adequately modified. The desired modifications point to a compromise between the systems B and C, incorporating a configuration change at the threshold, adequate 1000-feet-warning, aiming point and centre line lighting on the runway.

The movable screen and filter assembly was judged by many pilots to give a realistic simulation of seeing conditions in fog. This equipment was therefore considered to be very useful for training purposes also.

9.3 Flight operational conclusions of results

The lowest quality marks for approach ground-track as found for system A is most probably caused by insufficient roll and alignment information. It is interesting to note that more use of rudder has been made with this system, which may indicate difficulties for the pilot with respect to track-heading correlation.

The quality of the ground-track of the approaches with system B (the Netherlands proposal) was better than with system A and system C, which indicates better roll guidance and orientation capabilities. This better result has been achieved with less total movement of rudder than in the case of system A.

It appears furthermore that the height over the threshold with the systems A and C was above the ILS glide path whereas with system B this height was very close to the ILS glide path. These differences may have been caused by a better height information from system B as compared to that obtained from the systems A and C.

No significant differences in the qualities of landing between the different systems have been found. This is probably due to the use of landing lights after crossing the threshold, which enabled the pilots to pick up other information (tyre marks, paintings, timber boards of the experimental light installation, etc.) than from the landing mat only. This extra information levelled out possible differences in guidance from the light patterns compared.

9.4 Future work

In view of the last sentence of the foregoing paragraph and the unsatisfactory height guidance provided by all 3 systems (see table 2) it is very desirable to have the investigations continued, especially with the aim of studying details of the light pattern on the first 2000 or 3000 feet of the runway as:

— the desirability of a configuration change at the threshold,
— single or double gauge systems consisting of lateral or longitudinal barrettes or both,
— the addition of centre-line lights and
— the conspicuity of the light pattern at the ideal aiming point.

Other subjects which demand investigation are:

— the weather limits for the application of visual approach slope indicators and
— the possibilities of simplification of light patterns in general.

It would be of the greatest importance to repeat a part of the present investigations in aircraft of recent design.

Acknowledgements

The experimental investigation described in this paper required a vast amount of work of all kinds. Although several organizations, represented in the study group in charge of this investigation, very generously made man power and financial means available, the experiments could not have been carried out in such an efficient way without the enthusiasm and the application of very many of those participating directly in the preparation and the performance of the tests. The authors are therefore greatly indebted to the whole team involved in this work and especially to the KLM captains acting as safety pilots, to the pilots mentioned in Appendix I and to others who have flown the sometimes very strenuous preliminary test flights, to staff members of NLR, of KLM and of Philips' Lighting Laboratory and to employees of Eelde Airport Inc.

APPENDIX I

TEST PILOTS PARTICIPATING IN THE FLIGHT TEST PROGRAMME

Name	Qualification and affiliation	Main flying experience
P. Both	Chief Pilot, Martin's Air Charter	DC-3
R. W. Bray	Sqn. Ldr., Blind landing Experimental Unit, Royal Aircraft Establishment	Varsity
P. E. Bressey	Captain, IFALPA	Viscount
M. L. H. Carter	Captain, IFALPA	Viscount
C. D. Crogan	Flt. lt., Blind landing Experimental Unit, Royal Aircraft Establishment	Varsity
H. J. P. Dijkema	Pilot, Dutch Pilots Association	Convair
J. H. Eilders	Captain, Dutch Pilots Association	DC-8
H. A. Hooper	Captain, BEA	Viscount
J. Koedam	Captain, Dutch Pilots Association	DC-7
H. R. Leutwiler	Captain, Swissair	DC-3
S. E. C. Martynse	Pilot, Dutch Pilots Association	DC-6
C. Mattern	Captain, Dutch Pilots Association	Electra
B. M. Orange	Captain, Dutch Pilots Association	Electra
C. G. J. Reyers	Inspector, Neth. Dep. Civ. Aviation	Beechcraft
H. D. Savage	Cdr., Ops. Specialist, FAA	Carrier-acft
L. W. F. Stark	Flt. lt., Blind Landing Experimental Unit, Royal Aircraft Establishment	Varsity
J. C. P. Stuy	Pilot, KLM	Convair
R. Walker	Dep. Chief Test Pilot, Fokker	Friendship

APPENDIX II

FLIGHT TEST PROGRAMME

Series	Date													
1	7-13-1960	System							A					
		Pilot nr.	1	2	3	4	3	2	3	4	1	2	1	4
		Initial position [1]	I	I	L	I	I	H	H	H	H	L	L	L
2	7-15-1960	System							A					
		Pilot nr.	5	7	5	6	6	7	5	7	6			
		Initial position	I	L	L	L	H	I	H	H	I			
3	7-21-1960	System							C					
		Pilot nr.	8	8	10	9	10	8	10	9	9			
		Initial position	L	I	H	L	I	H	L	I	H			
4	7-27-1960	System							B					
		Pilot nr.	11	12	11	13	13	12	11	12	13			
		Initial position	I	L	L	L	H	I	H	H	I			
5	7-29-1960	System							A					
		Pilot nr.	15	16	15	14	14	14	15	16	16			
		Initial position	H	I	L	I	L	H	I	H	L			

Series	Date													
1	7-13-1960	System							C					
		Pilot nr.	2	3	2	4	1	1	3	4	2	3	1	4
		Initial position [1]	I	I	H	H	I	L	L	L	L	H	H	I
2	7-15-1960	System							B					
		Pilot nr.	6	5	7	7	5	6	7	6	5			
		Initial position	L	H	H	I	I	H	L	I	L			
3	7-21-1960	System							B					
		Pilot nr.	10	9	8	8	9	8	9	10	10			
		Initial position	H	L	L	I	I	H	H	L	I			
4	7-27-1960	System							C					
		Pilot nr.	13	11	12	12	11	13	12	13	11			
		Initial position	L	H	H	I	I	H	L	I	L			
5	7-29-1960	System							C					
		Pilot nr.	14	16	15	14	15	16	15	16	14			
		Initial position	L	L	L	H	I	I	H	H	I			

Series	Date													
1	7-13-1960	System							B					
		Pilot nr.	3	2	1	4	3	2	3	4	2	1	1	4
		Initial position [1]	H	L	L	L	L	I	I	I	H	I	H	H
2	7-15-1960	System							C					
		Pilot nr.	6	6	7	5	6	5	5	7	7			
		Initial position	H	I	I	I	L	L	H	L	H			
3	7-21-1960	System							A					
		Pilot nr.	10	9	8	8	9	8	10	9	10			
		Initial position	I	H	I	L	L	H	L	I	H			
4	7-27-1960	System							A					
		Pilot nr.	13	13	12	11	13	11	11	12	12			
		Initial position	H	I	I	I	L	L	H	L	H			
5	7-29-1960	System							B					
		Pilot nr.	15	15	16	14	15	16	14	14	16			
		Initial position	H	L	I	H	I	L	I	L	H			

[1] I = Ideal (on glide path and on centre line); H = High (above glide path); L = Left (left of centre line).

APPENDIX III RESULTS

Series	Pilot	System	Initial position [1] →	Approach height quality mark			Elevator travel index			Height above threshold [2] in ft			Approach ground-track-quality mark			Rudder travel index			Aileron travel index			Quality mark for: Height from threshold until touch-down			Quality mark for: Touch-down			Heart-beat factor			Wind speed and wind direction (runway direction 237 °M)		
				I	H	L	I	H	L	I	H	L	I	H	L	I	H	L	I	H	L	I	H	L	I	H	L	I	H	L	I	H	L
1	1	A		2	8	10	14.5	14.5	9.5	88-92	58	58	7	10	2	27	9	16.5	32	11.5	29	4	5	6*	5	3	0*	1.32	1.24	1.19	170/5	170/7	170/6
		B		3	1	3	23	15	5.5	26	80-85	62-65	9	8	2	4	3.5	31	27.5	36	48	3*	5*	7*	6*	5*	5*	1.30	1.27	1.32	170/6	170/7	170/7
		C		4	6	2	15	22.5	16.5	55	55-65	73	10	8	1	17	14.5	14	32	48.5	66.5	7	6*	0*	8	5*	0*	1.26	1.30	1.20	170/8	170/8	170/8
	2	A		4	6	8	14	10.5	11	44	52	—	7	8	3	11	7.5	12	51.5	18	34.5	8	3	–	7	5	–	1.10	1.08	1.23	160/4	170/8	160/5
		B		6	6	6	29	12.5	8.5	23	34	—	8	9	5	3	3.5	3	17	32.5	22.5	3*	7*	–	5*	1*	–	1.15	1.24	1.14	180/8	170/5	170/7
		C		3	3	3	10	9.5	32.5	68	50	—	10	10	2	6.5	4.5	11.5	37.5	34	73	2	5*	–	5	5*	–	1.08	1.17	1.08	170/5	170/7	180/9
	3	A		4	5	7	9.5	16	12.5	58	35	—	7	7	1	17	9	11	32.5	29.5	29.5	8	6	0*	6	5	0*	1.55	1.56	1.49	160/8	160/7	160/5
		B		5	5	4	14.5	10	13	48	36	29	9	8	6	21	12.5	20.5	59	35.5	42.5	7	4	1	2	4	1	1.54	1.50	1.60	180/8	170/6	180/7
		C		3	7	2	12	10.5	4	63	57	70	10	8	5	6.5	13.5	12.5	29.5	58.5	59	7	8*	6	7	3*	8	1.65	1.78	1.33	170/8	170/8	180/9
	4	A		1	3	2	6.5	14	10	81	84	68-72	6	8	5	47	31.5	57.5	106	66.5	95.5	5	4	0*	2	1	0*	1.27	1.50	1.21	170/7	160/7	170/4
		B		6	–	7	12.5	—	25.5	47	—	45	8	–	5	44	—	15.5	111.5	—	46	4	–	4*	5	–	3*	1.37	—	1.71	170/7	—	170/8
		C		5	5	5	15.5	10.5	24	62	63	60	9	9	1	35	19	23	113	93.5	73.5	8	8	0	7	5	3	1.43	1.45	1.62	170/8	170/7	170/7
2	5	A		1	2	1	21	9	14	—	71	—	9	8	2	6	2.5	6.5	7	16	15.5	–	8	–	8□	6	–	1.31	1.17	1.21	None	None	None
		B		1	6	6	11.5	11	15	72	60	47	9	9	7	16.5	9	14.5	33.5	13	17	4	8	8	0	4	7	1.40	1.41	1.41	60/4	170/1	180/6
		C		3	6	3	10	10	16	65	57	62-66	8	9	6	13	11.5	12.5	23	22	30.5	8	8	7	7	7	8	1.36	1.25	1.37	150/5	160/4	150/4
	6	A		5	6	5	24	21.5	9.5	42	36	—	9	9	2	20.5	25.5	19.5	24	29.5	58.5	8	5	–	8	6	7□	1.26	1.14	1.43	None	None	None
		B		3	1	3	20.5	19	9.5	29	23	38	9	9	4	28	46.5	16	22.5	47.5	26.5	1	3	6	5	6	7	1.21	1.19	1.24	10/2	170/1	190/3
		C		7	5	3	45	21.5	31	42	40	58-62	8	9	8	34	50.5	57.5	55	67.5	104.5	5	6	9	6	6	7	1.24	1.41	1.33	150/5	180/6	160/4
	7	A		8	1	7	11	19.5	13.5	39	36	44-54	7	7	6	23.5	16	29.5	27.5	30.5	44.5	5	7	7*	9	8	3*	1.44	1.38	1.42	None	None	None
		B		6	5	5	12	21.5	9.5	53	53	47	9	9	8	27.5	8	28.5	54	26	97.5	9	8	8	4	4	6	1.29	1.43	1.56	180/3	190/4	140/1
		C		6	6	3	9	10	11	61	51	63	9	8	7	8.5	18	28.5	31	30.5	73.5	7	7	7	4	5	8	1.42	1.34	1.33	160/4	170/6	140/4
3	8	A		1	1	3	13	15.5	11.5	66	—	57	8	7	7	34	41	21.5	50	76	53	7	–	6	0	3□	6	1.32	1.28	1.42	190/6	180/4	200/7
		B		2	7	1	19.5	16.5	10	52	38	45	7	8	8	46	31	38	78.5	48	61	7	5	6	3	5	5	1.42	1.36	1.44	190/4	200/6	180/6
		C		2	3	0	13	13	17.5	43	41	48	7	3	6	39	33	40	32.5	44.5	72	8*	5	6	3*	6	6	1.34	1.64	1.41	200/4	180/5	200/6
	9	A		2	4	1	29.5	35.5	15	—	53	—	7	4	4	20	16.5	34	63	63	99	–	8	–	4□	0	7□	1.21	1.28	1.39	200/7	190/6	200/7
		B		1	2	1	21	16	16	37	63	59	6	8	5	15	11	16.5	34	63	65	2	7	8	9	4	6	1.18	1.14	1.20	160/5	180/6	190/5
		C		0	6	2	22	10.5	14.5	32	43	39	7	9	6	21	5	15.5	52	21	58.5	2	7	6	9	6	7	1.40	1.23	—	200/7	200/7	200/4
	10	A		4	6	6	20.5	11	15	45	45	57	4	8	8	40.5	17.5	23	79	46.5	50	7	7	8	7	3	3	1.23	1.21	1.29	190/6	200/7	200/6
		B		5	6	4	16.5	11.5	15.5	34	55	49	7	7	7	13.5	14	20.5	21.5	15.5	36	5	6	9	8	0	7	1.13	1.28	1.15	160/5	180/7	200/6
		C		0	6	2	8	15	16.5	74	—	49	6	7	7	6	11	18	15.5	19	32.5	8	–	3	9	–	1	1.21	1.23	1.24	180/5	200/4	170/4
4	11	A		2	5	4	19.5	14.5	14	21	39	43	6	7	4	6.5	7.5	8	51.5	53.5	53	2*	5	7	0*	8	6	1.42	1.54	1.51	None	None	None
		B		3	4	6	23	36.5	17.5	30	30	35	7	7	6	5	6	6.5	35.5	47	72	4	1	5	8	0	8	1.39	1.48	1.39	None	None	None
		C		4	3	5	19	9.5	17.5	—	64	—	6	8	5	8.5	6	5.5	23	33.5	52	–	8	–	9□	6	7□	1.50	1.50	1.71	240/0	240/0	240/0
	12	A		7	0	2	28	42.5	25.5	33	29	29	6	7	6	42	22.5	25.5	51.5	19	31	3	3	3	0	5	7	1.79	1.51	1.51	None	None	None
		B		6	6	4	32.5	31	29	29	31	43	7	9	4	17.5	15.5	36	25.5	20	49.5	2	3	5	9	7	3	1.77	1.60	1.37	None	None	None
		C		1	5	1	32	33	16.5	—	—	21	7	7	7	15	19	39.5	18.5	28.0	52	–	–	1	4□	6□	1	1.65	1.69	1.64	240/0	240/0	240/0
	13	A		2	5	3	27	31	36.5	30-45	—	25	4	7	9	52	5.5	26.5	52	22	63.5	4	–	0	9	9□	0	1.42	1.43	1.33	None	None	None
		B		2	2	4	33	47.5	24	18	24	34	8	8	7	7.5	6	19	24.5	25	45	1	1*	2	0	1*	0	1.65	1.45	1.45	None	None	None
		C		–	0	5	—	37.5	38	—	20	27	–	7	8	—	5	7	—	30.5	57.5	–	1	1	–	0	0	—	1.54	1.39	240/0	240/0	240/0
5	14	A		7	1	0	16	27.5	37.5	47	39	31	7	4	7	39	40	41	35	41.5	53.5	6	6	5	2	7	4	1.34	1.23	1.23	None	None	None
		B		4	2	2	22	30.5	18.5	52	38	41	6	7	7	27	23.5	44	38.5	11.5	38.5	8	8	8	1	5	3	1.09	1.24	1.20	None	None	None
		C		1	1	4	27.5	35	35	36	70	57	4	7	7	38.5	28	28.5	69.5	29.5	46.5	7	4	7	5	4	5	1.32	1.67	1.20	240/0	240/0	240/0
	15	A		3	7	0	24.5	12	34	56	46	54	7	6	2	11	7.5	11.5	49	52.5	100.5	6	4	8	9	6	7	1.44	1.48	1.38	None	None	330/3
		B		4	5	5	19	18.5	12	27	37	55-57	8	7	1	3.5	4	4	23	27.5	51.5	1	5	5	4	2	1	1.54	1.45	1.46	None	None	None
		C		2	5	2	22.5	14	13	54	45	61	7	8	1	3	1.5	4.5	58	49.5	36	8	9	7	4	8	4	1.42	1.55	1.60	240/0	240/0	240/0
	16	A		1	3	0	22.5	18.5	18.5	81	63	77	5	4	2	13.5	14	6.5	35	27	17	2	2	3	2	4	2	1.37	1.34	1.35	None	None	None
		B		0	6	0	17.5	34.5	27.5	72	56	64	7	8	5	6.5	7.5	13.5	33.5	23.5	37	7	5	7	3	5	4	1.69	1.77	1.69	None	None	None
		C		2	1	0	30.5	19	30	60	97	—	1	0	3	24	20	22	59.5	54	74.5	9	0*	–	5	0*	2□	1.67	1.54	1.55	240/0	240/0	330/3

[1]) I = Ideal (on glide path and on centre line); H = High (above glide path); L = Left (left of centre line). * Overshoot. □ No ground-camera shot.
[2]) Heights above threshold are related to the aircrafts anti-collision light.

REPORT NLR-MP. 222

Flight Operational Evaluation of Approach and Runway Lighting (Second Test Series)

by

Ir. F. E. Douwes Dekker

Summary. The present report deals with the results of comparative flight testing of 3 configurations for approach and runway lighting under simulated conditions of 1000 ft slant visual range. As such, this investigation is a continuation of earlier work of this kind. The flight tests have been carried out at Köln-Bonn International Airport in December 1962 with a Lockheed Super-Constellation aircraft. The 3 light configurations consisted essentially of:

- an existing layout at the above airport,
- the reference pattern, suggested during the 2nd meeting (1962) of the ICAO Visual Aids Panel,
- an installation similar to that at New York Idlewild International Airport.

The evaluation of the flight test results, based on analysis of measured data obtained during 144 landings executed by 24 pilots, shows the best overall landing performance for the second configuration. The present results confirm the most important conclusions from the earlier experimental studies on those items which were common to both investigations. Generally, pilots' opinions contributed effectively in reaching pertinent conclusions.

The investigation was sponsored by the Netherlands Department of Civil Aviation and guided by a study group composed of experts representing interested organizations in the Netherlands.

Contents

1 Introduction

During the last few years considerable effort has been devoted in the Netherlands to the development of visual aids for approach and landing. In particular, attention has been focussed on the flight operational evaluation of existing and proposed light patterns under conditions of reduced visibility as prevailing in phase two operations[1].

After initial flight tests in 1959 at Eelde Airport (Groningen, the Netherlands) a complete test programme was carried out at the same airfield in 1960. A detailed account of the latter test series has been published in a paper, entitled "Flight Operational Evaluation of Approach and Runway Lighting" by J. B. de Boer and T. van Oosterom ("De Ingenieur", nrs. 49 and 51, 1961).

The present series of tests may therefore be regarded as a natural sequel to previous investigations in this field and to the recommendations for future work ensuing from them. These new investigations were especially aimed at studying details of light patterns from 1000 ft before until 3000 ft beyond the threshold, using a much heavier aircraft, viz. a Lockheed L-1049G Super-Constellation, made available by KLM-Royal Dutch Airlines (see fig. 1).

Full-scale tests on runway light patterns do not allow much variation in pattern without serious financial and practical consequences. The use of many experimental lights, even of very light weight, on an active runway was considered unacceptable. Therefore, it was preferred to carry out the test flights on a runway with existing flush type narrow gauge and centre line lighting. Such a runway was found at Köln-Bonn International Airport and kindly made available by the authorities of this airport. The flight tests were performed in December 1962 at this airport, with the experimental light patterns laid out on runway 32-right.

The test procedure followed in the "Eelde trials" has been applied, except for certain details. As to the basic procedure, reference may be made to the paper mentioned above; alterations will be dealt with in this report.

Adaptation of the NLR fog simulator, described in the above mentioned paper, to the Super-Constellation required extensive redesign and allowed some mechanical improvements towards full automatic operation. The basic principle of operation (i.e. maintaining constant slant visual range regardless of height and pitch attitude throughout approach and landing), however, has not been changed. It may be reminded that with this device the outside view for the safety pilot in the right-hand seat remains unaffected.

The required absence of additional visible texture on the ground necessitated the tests to be flown without daylight or aircraft landing lights.

[1]) According to IATA-ICAO terminology, a "phase two operation" is characterized by 100 feet cloud base and ¼ mile visibility.

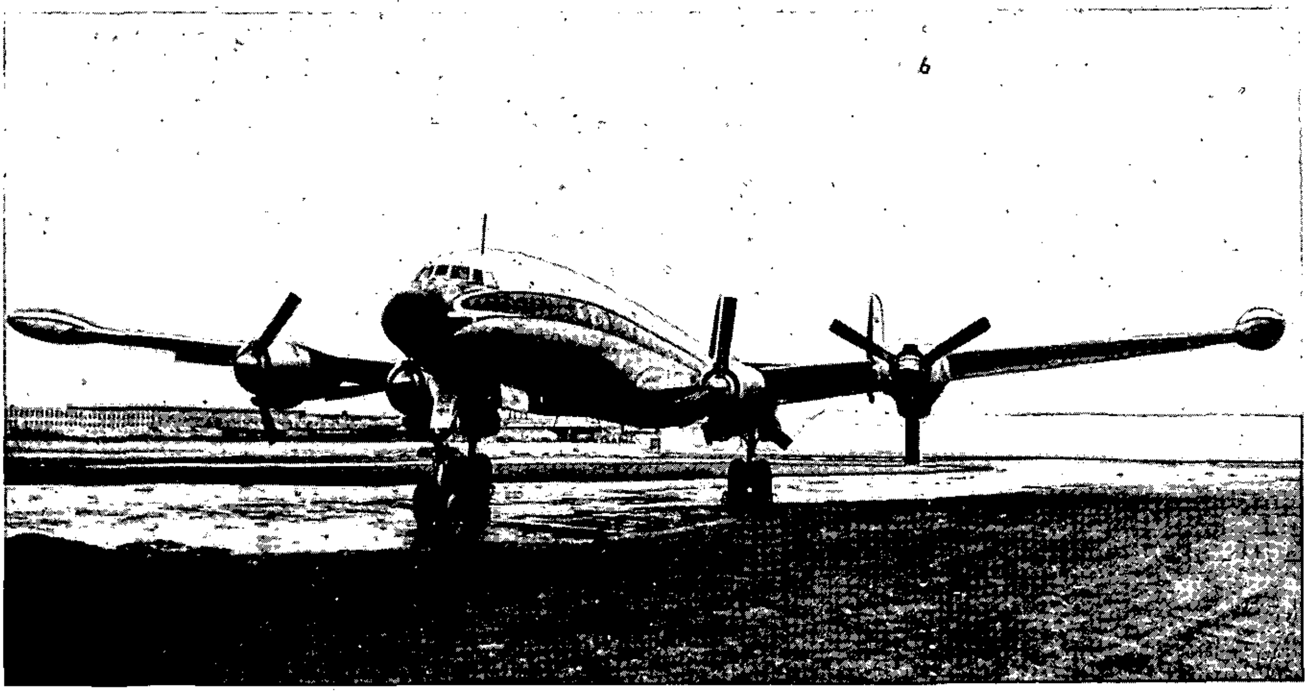

Fig. 1. Test aircraft Lockheed L-1049 G, Super-Constellation, PH-LKA.

2 Light configurations

The 3 light configurations illustrated in fig. 2 have been evaluated. They have 2 basic components in common, viz. a standard Calvert approach light pattern with 6 crossbars, having 500 ft longitudinal spacing, and a 60-ft narrow gauge of lateral arrays on the runway with 200 ft longitudinal spacing, extending 4000 ft from the threshold along the runway. All systems are equipped with a 200-ft wide green threshold marking provided with a 60-ft central gap.

Configuration 1, representing the standard pattern actually laid out on runway 32–right of Köln-Bonn Airport, had, in addition to the basic system described above, a centre line with 100 ft spacing, extending all along the runway, as well as two 15-ft long wing-bars, 200 ft apart, at the ILS reference point located 1000 ft from the threshold.

Configuration 2 contained the so-called ICAO reference pattern, recommended by some members of the ICAO Visual Aids Panel in its 2nd meeting (summer 1962) as a standard reference in comparative trials and as such adopted by a working group of this panel. This pattern is composed of configuration 1 without the wing-bars and with the addition of a 120-ft wide red gauge between the 1000-ft crossbar and the threshold, a reinforced white centre line in the same area (barrettes of 5 lights instead of single lights) 2 green longitudinal barrettes with 150-ft gauge, connected with the threshold marking, and 2 T-shaped markers at the ILS reference point.

Configuration 3, representing essentially the originial installation at runway 04–right of New York Idlewild Airport, consisted of the basic system described above, completed by the reinforced centre line as applied in configuration 2, and a runway centre line commencing at 4000 ft from the threshold.

All lights in addition to the permanent installation were of the same construction as the experimental lights previously used during the "Eelde trials". Change of light configuration from one system to another could be accomplished in a few minutes. The luminous intensity of various groups of light sources could be adjusted independently, ensuring a correct balance of each complete configuration [3]).

3 Flight test procedure [4])

A total of 24 subject pilots participated in the tests, each one performing 2 landings on each of the 3 light configurations, bringing the total number of test landings at 144. Names and particulars of the subject pilots are listed in table 1. Earlier experience indicated that a number of 24 subjects is large enough to prevent intolerable influence from individual characteristics in the test results.

The whole test programme has been carried out during 8 test nights, designed A to H inclusive (see table 4). During each test night a flight programme was carried out, consisting of 18 landing trials for 3 subject pilots, requiring about 3 hours total block time. Each night, the first landing, marked SP in table 4, was made by the safety pilot without the fog simulator.

The landing sequence with regard to pilot and light pattern

[3]) The lighting installation and the relevant electrical equipment was built and maintained under supervision of Mr. H. Aarts, Philips' Lighting Laboratory.

[4]) Capt. F. J. Lodeizen, KLM flight instructor, acted as safety pilot during all test flights. Flight engineering duties were performed by Mr. F. N. Beudeker or Mr. C. H. O. Meyer, both of KLM. All other duties in the aircraft with regard to recording equipment, fog simulator, pilots' comments and general management were attended to by staff of the NLR. All duties on the ground with respect to photographic equipment, light installation and liaison were taken care of by staff of RLD, Philips, and Köln-Bonn Airport.

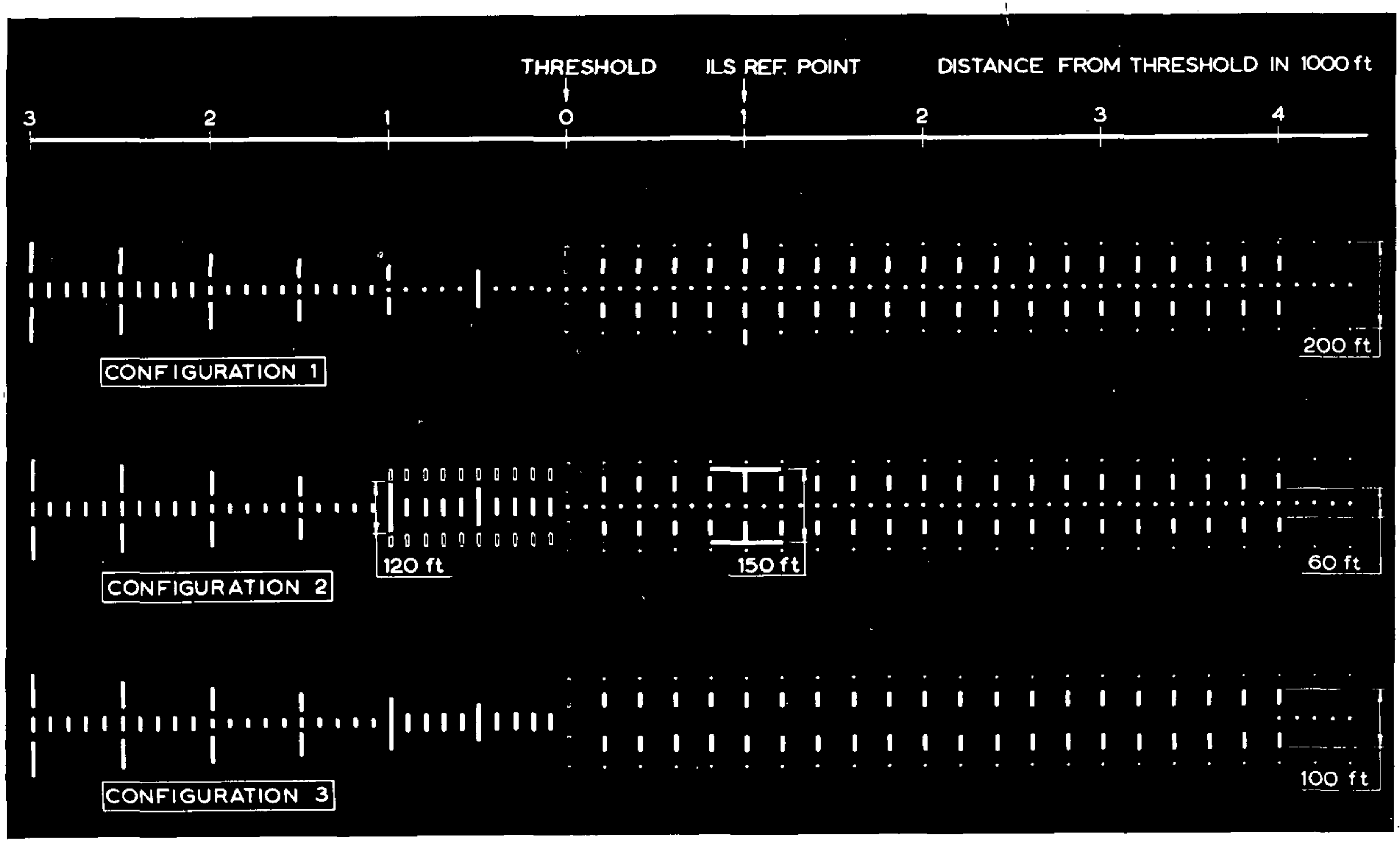

Fig. 2. *Investigated light configurations.*

(see table 4) varied from night to night and was carefully chosen in order to cancel out as much as possible the influence of variations in wind speed, wind direction and turbulence, occurring during the individual test nights. In addition, this choice should exclude the influence of fatigue as well as the familiarization of the pilots with the light configurations.

Similar to the procedure followed in the previous test series, the visual range of the lights as seen by the subject pilot has been kept constant throughout the approach and landing to 1000 ft slant visual range by means of a modified version of the NLR fog simulator. This simulator is only applied to the visual field of the subject pilot, whereas the safety pilot has unrestricted view.

The safety pilot brought the aircraft in a stabilized position on the ILS glide path at about 900 ft height in the following configuration: 80% flaps, landing gear extended, 130 kts IAS, 2400 RPM and about 28 inch MAP; the aircraft weight was 100,000 lbs (nearly maximum landing weight). Then the subject pilot took over control of the aircraft on instruments, continued the approach and performed the landing. Wave-off procedure, if necessary, was usually initiated and always performed by the safety pilot.

Immediately after nose-wheel touch-down, the safety pilot proceeded with a rolling take-off and brought the aircraft, via a visual circuit, again on the initial position described above. The 80%-flap setting remained unchanged during approach and landing. The subject pilot knew in advance which light configuration to expect.

The procedure outlined above differed from the one applied in the previous test series. It had been the intention to have the subject pilot take over control, as usual, only when visual contact was established. He should have been brought by the safety pilot in a specified off-centre position at the middle marker. The initial deviation was either 100 ft left of the centre line or 30 ft above the glide path but unknown to the subject pilot. Therefore, zero reader and ILS cross pointer ought to be blanked-off. This procedure was followed during the first 6 landings of the first test night. It then became clear that, due to the high speed of the less manoeuvrable aircraft used in these tests, the initial lateral deviation necessitated unacceptable corrective manoeuvres, while the initial height deviation not being corrected, resulted only in a greater air distance. Even reduction of the initial deviations to about half their original values mentioned above, proved that it was rather unrealistic to take over control of this type of aircraft at this late stage of the approach, and depriving the subject pilot of apparently vital information contained in zero reader and ILS cross pointer indications. It was therefore decided to adopt the modified procedure described above, from the second test night onwards. The initial position deviation just prior to establishing contact, when following this procedure, can be considered to be of a random nature, still providing sufficient scatter in the initial test conditions.

Power settings, demanded by the subject pilot, were accomplished by the flight engineer. The subject pilot's altimeter was set at sea-level pressure (QNH). Due to a threshold elevation of 300 ft, pitot-static position error and instrument error, touch-down usually took place at about 250 ft indicated altitude and at normal touch-down speed (100 kts).

Details on weather conditions are given in table 2.

4 Fog simulation

The NLR fog simulator has been adapted to the Super-Constellation cockpit. The original device, as applied in the C-47 aircraft (see paper mentioned in the introduction), has been modified but basic operation remained the same. The height control unit was removed and replaced by a Bendix altitude sensor in the control loop, which resulted in automatic height control and a better performance in the case of large variations in rate of descent. The pitch attitude sensor of the elevator channel of the PB-10 autopilot, used for servo-control of the screen, was replaced by a Sperry A-12

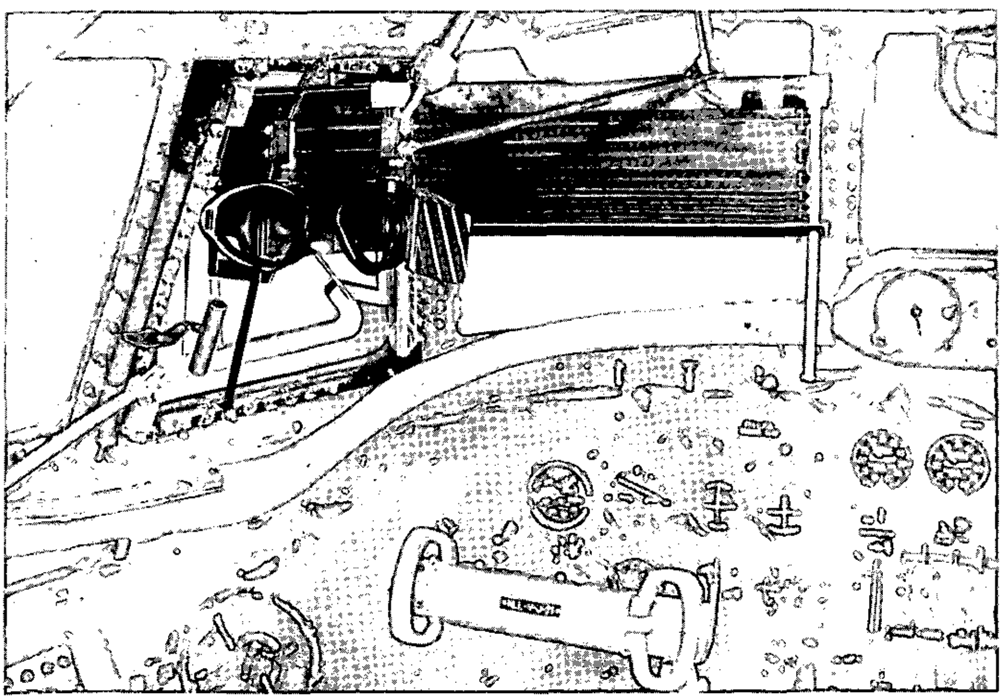

Fig. 3. NLR fog simulator.

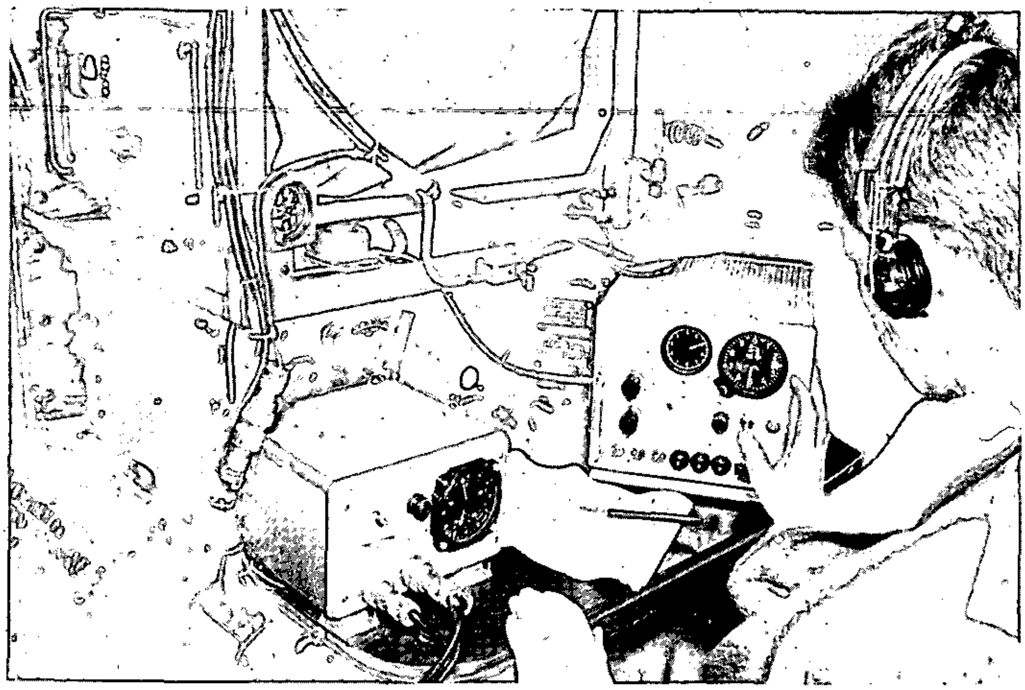

Fig. 4. Control and checking equipment of fog simulator.

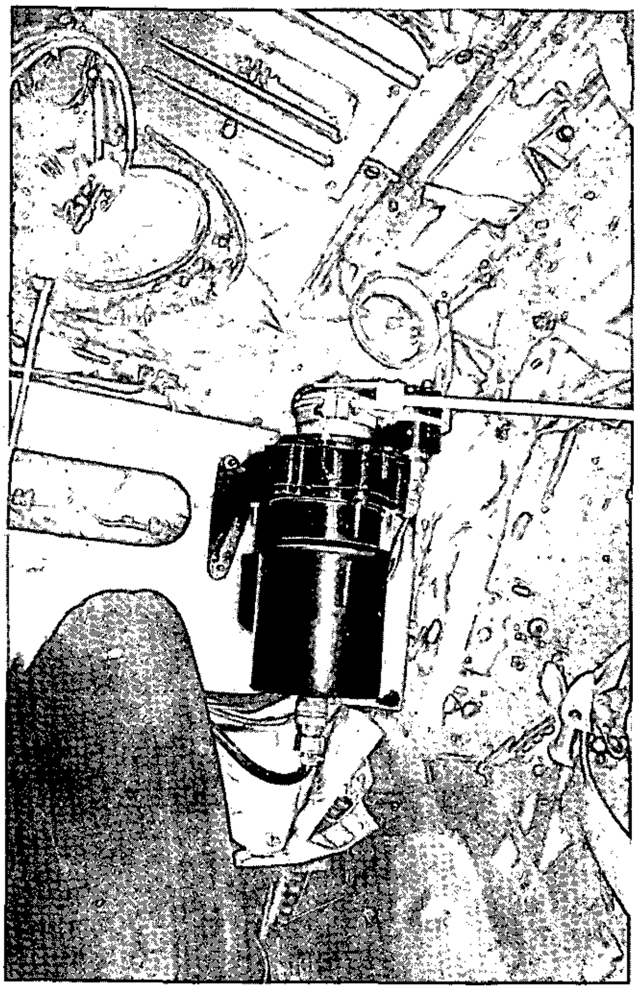

Fig. 5. Screen drive.

vertical gyro, which increased the total accuracy of the system. In-flight adjustment of the screen position with respect to pitch attitude was accomplished by a Bendix trim synchro in the same control loop.

The screen itself, in front of the subject pilot, was moving in a plane perpendicular to the aircraft's longitudinal axis, ensuring a linear relationship between servo motor- and screen position and simplifying the screen drive [5]).

The total transmission of the filter assembly mounted in the fixed head support [6]) remained at 8%. The visibility below ceiling was always better than 5 miles during all test landings. These conditions together with the adjustment of the luminous intensity of all lights at approximately 50 cd assured rather homogeneous visibility of the lights well above threshold visibility without creating distraction by glare.

The aircraft's landing lights have never been used. The fog simulator as mounted in the test aircraft is illustrated in figs. 3, 4 and 5.

The fog simulator was always adjusted for a slant visual range of 1000 ft except during the first 6 landings of test night C, when the visual range was estimated to decrease gradually from 2500 ft to 1000 ft. During landing no. 17 of this particular night, the fog simulator was switched on too late, so that the visual range suddenly changed from 0 to 1000 ft at a position 1000 ft in front of the threshold. The influence of these and other minor deviations mentioned in table 4 – occurring in a small number of tests only – on the total results proved to be negligible.

[5]) The modified fog simulator has been designed by Messrs. H. A. Mensink and K. Wams of the NLR.

[6]) The head support was located 15 ft above and 43 ft in front of the main wheels' lowest point, measured along the aircraft's reference axes. The cockpit cut-off angle amounted to 15° with respect to the aircraft's longitudinal reference axis.

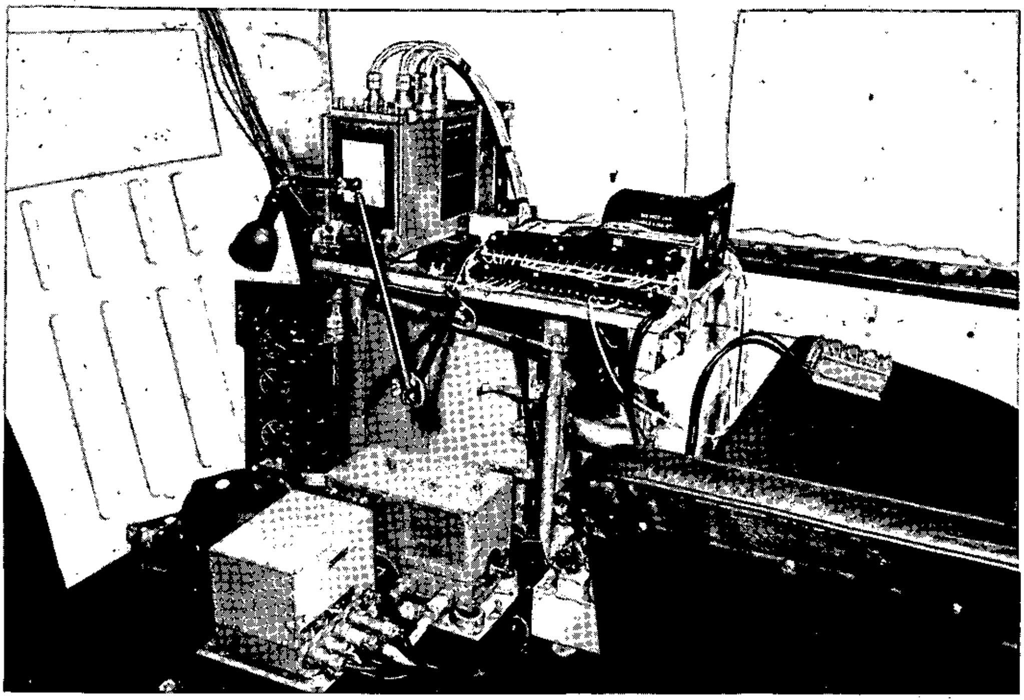

Fig. 6. Recording equipment in the aircraft.

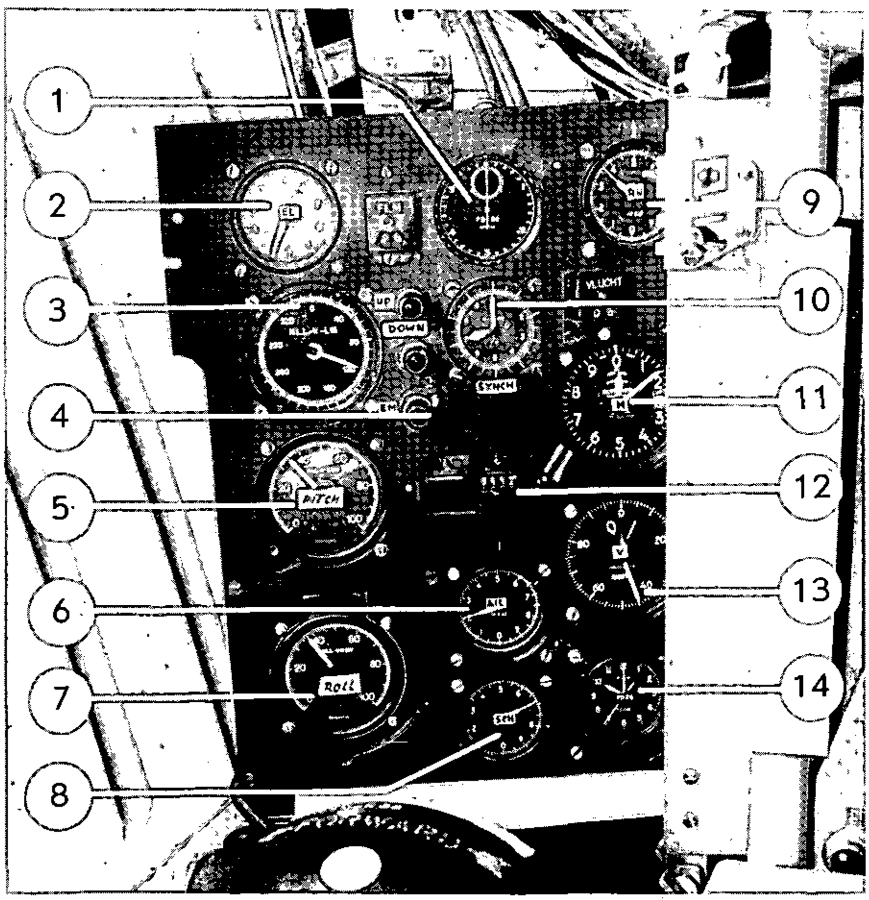

Fig. 7. Instrument panel of automatic observer (1. split second watch, 2. elevator position indicator, 3. top-axis accelerometer, 4. event marker, 5. pitch attitude indicator, 6. aileron position indicator, 7. angle of roll indicator, 8. screen position indicator, 9. rudder position indicator, 10. synchronizer, 11. altimeter, 12. counter, 13. airspeed indicator, 14. watch).

5 Recording equipment

The basic idea underlying this comparative evaluation of approach and runway light configurations is to exclude the influence of subjective judgement by statistical analysis of measured performance data. This requires the choice of certain parameters obtained from recorded data which may be considered to represent the quality of different aspects of the whole approach and landing manoeuvre and of the pilot's effort to carry it out. This choice will be dealt with in detail in chapter 6.

The recording equipment in the aircraft and on the ground did not differ essentially from what was used during the "Eelde trials"; for details of this equipment reference may be made to the paper mentioned in the introduction. It may be reminded, however, that the following quantities were recorded:

- indicated airspeed,
- altitude,
- pitch attitude,
- angle of roll,
- ILS localizer deflection,
- ILS glide-path deflection,
- vertical acceleration,
- control surface deflections,
- flight path from threshold until touch-down.

The airborne recording equipment is shown in figs. 6 and 7.

Calibration of the ILS signals was carried out by the local authorities. This resulted in the following basic characteristics:

- localizer transmitter, located 13,353 ft from threshold,
- ILS reference point, located 960 ft from threshold,
- localizer beam width 3.3° (no bends),
- glide path slope 2.7° (no bends),
- glide path beam width 1.1° (symmetrical beam type).

The ILS receiver antenna was located 13 ft above and 51 ft in front of the main wheels' lowest point, measured along the aircraft's axes.

Instead of the aircraft's anti-collision light a constant-rate flash light, mounted behind the starboard most aft cabin window, was used for flight path recording by means of ground camera's as applied in the first test series. The ground camera's covered the flight path profile over a length of 2400 ft beyond the threshold.

This time no physiological data (such as the heart-beat frequency) have been used in the evaluation procedure.

The opinion of the subject pilot himself might add to a better understanding of the quantitative conclusions. Therefore, care has been taken to record pilots' opinions during the execution of the tests. A general survey of these comments is given in capter 8.

6 Evaluation system

From the various recordings, graphs have been composed of pitch attitude, angle of roll, aircraft height and lateral deviation (ground track) as a function of distance from threshold for all test landings as well as for the landings (marked SP in table 4) performed by the safety pilot. Aircraft height was defined as the distance between the lowest point of the main wheels and the average plane through the first 3000 ft of the runway surface, having an average slope of .5%. A typical graph is given in fig. 8. Values for travel of elevator, rudder and aileron, according to the definition given below, appear in the legend of this graph.

Quality marks have been assigned to various aspects of the complete manoeuvre with essentially the same evaluation procedure as the one applied to the "Eelde trials". This procedure has slightly been modified and adapted to the present circumstances, the latter being different in type of aircraft landing technique, approach speed etc. The various aspects of the performance are:

approach height deviation, height (measured vertically) of a conical channel as described below, enclosing the flight path until threshold,

approach ground track, width (measured laterally) of a conical channel as described below, enclosing the flight path until threshold,

threshold height,

threshold speed,

flare-out:

- *height deviation*, height of a channel shaped as described below, enclosing the flight path from threshold until touch-down,
- *ground track*, width of a prismatic channel, enclosing the flight path from threshold until touch-down,
- *touch-down distance*, distance from threshold until touch-down,

roll wave-length, average distance covered for one roll oscillation,

roll amplitude, maximum change of angle of roll for one roll oscillation,

pitch wave-length, average distance covered for one pitch oscillation,

pitch amplitude, maximum change of pitch attitude for one pitch oscillation,

elevator, rudder and aileron travel, the average of all differences (absolute values) between successive control deflections, measured at 1 sec interval over the period of 15 sec preceding the crossing of the threshold.

Pitch- and roll characteristics have been considered near the threshold only.

Unlike the evaluation of the previous tests, the vertical deceleration of impact at touch-down has not been used for evaluation of the touch-down quality because heavy landings were prevented by the safety pilot.

Some of the quantities mentioned above, have been evaluated by means of a grid system as shown in fig. 9.

Four of these grids, each being related to a part of the total flight path, represent channels of rectangular cross section enclosing the flight path. The application of these grids is as follows:

- grid 1, approach height deviation,
- grid 2, approach ground track,
- grid 3, flare-out height deviation, touch-down distance (horizontal scale only), threshold height (vertical scale only),
- grid 4, flare-out ground track.

The use of an "entrance portal", as in the previous test series, has been replaced by the more realistic requirement, that the approach flight path should be directed towards an "ideal" aiming point (see points A and B in fig. 9), around which the relevant grids 1 and 2 may be pivoted in order to find the smallest channel able to enclose the actual flight path.

Grid 3 has been fitted to the scales of threshold height and touch-down distance by channels tapering towards point A and gradually merging into parallel channels with 1% slope.

The way in which grid 4 is applied, is clear from fig. 9.

Grid 5 is used to evaluate wave-length as well as amplitude of roll and pitch oscillations.

The numerical values of the quality marks for the various performance aspects are defined in table 3. Generally, higher marks represent better performances. It should be kept in mind, that higher quality marks for control travel, correspond to greater pilot's effort in performing the landing manoeuvre.

The results of the application of the evaluation procedure described and defined above, have been collected in table 4. A few mistakes made during the tests are noted in

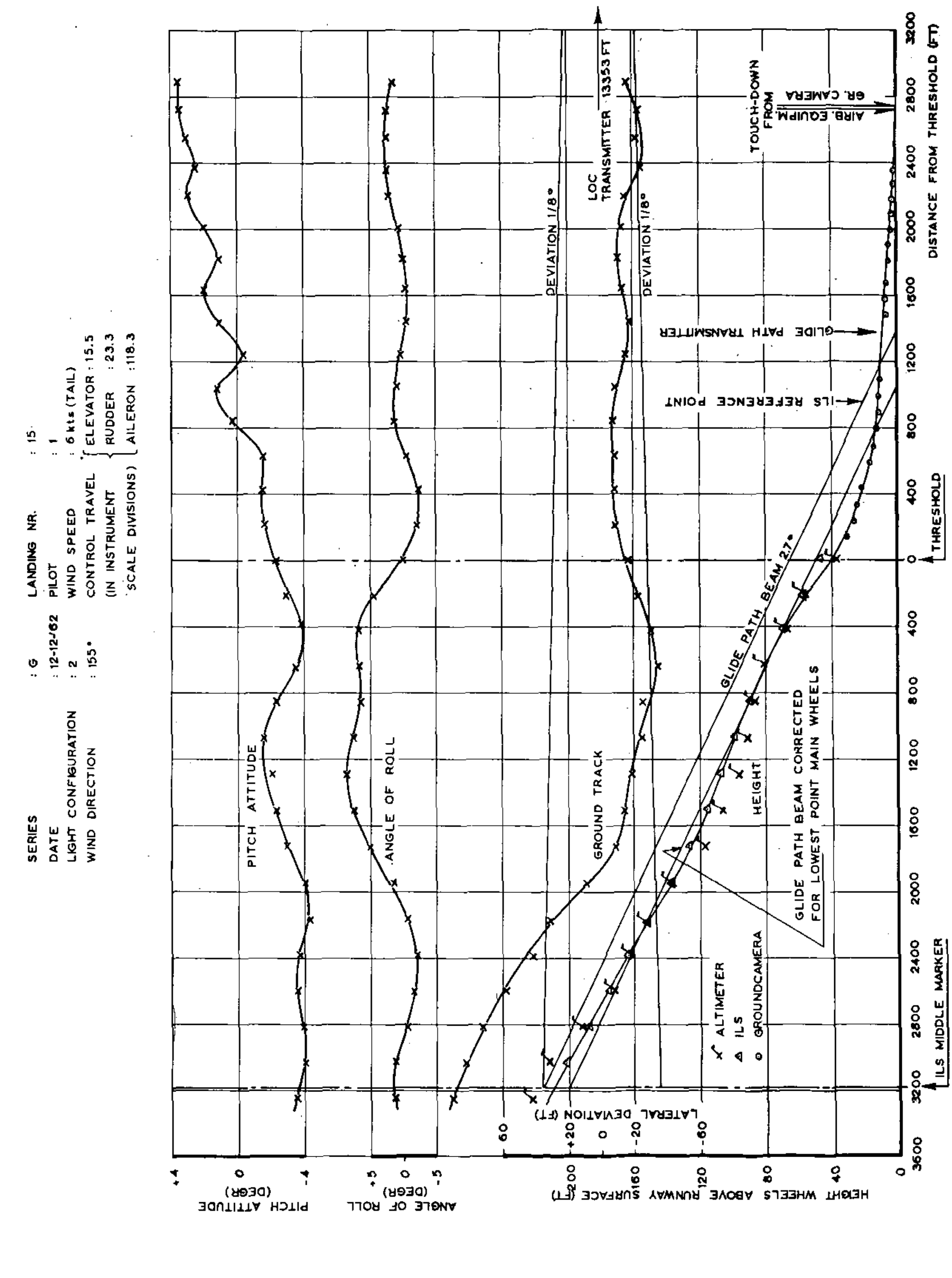

Fig. 8. Typical graph of flight performance.

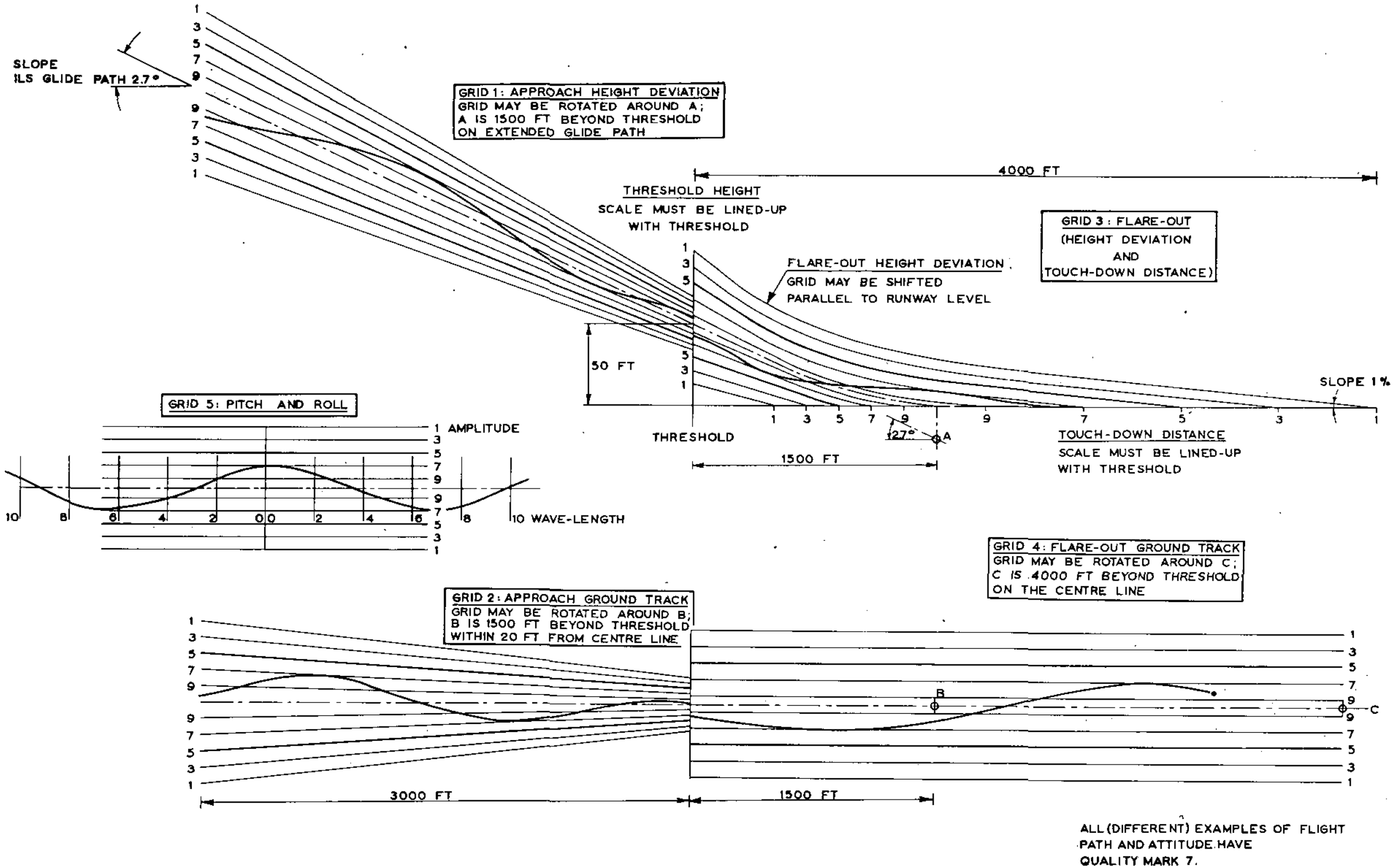

Fig. 9. Principle of assessment of quality marks.

this table. In some cases, marked "overshoot", the landing had to be aborted due to unacceptable flight conditions near the threshold. In other cases, marked "corrected", the safety pilot had to intervene during flare-out, in order to avoid damage to the undercarriage of the aircraft.

It may be noted from table 2 that some tailwind component was generally experienced except during the test series F and H, having an average headwind component of 8 and 3 kts respectively. Therefore, all quality marks for threshold height, threshold speed and touch-down distance for the test series F and H have been reduced by 2 and 1 point respectively in order to make these results comparable to other ones.

The large choice of aspects, representative for the quality of the performance achieved by the pilot and for the pilot's effort, together with the satisfactory spread in quality marks as shown in table 4, are believed to offer the best possible basis for statistical analysis of the recorded test data.

7 Results and their statistical analysis [7])

In table 5, for each light configuration, the total average values – i.e. the values averaged over all test nights – of the quality marks for the various aspects of the landing manoeuvre are given. In order to determine whether the difference between 2 total average values for the same aspect should be considered "significant", a statistical analysis of the experimental results has been made.

Firstly, the standard deviation of the total average values has been calculated. By statistical reasoning, it can be found that the ratio of the difference between 2 total average values and their standard deviation ought to be at least 2.56 in order to reach a 90% "confidence" that a real difference between the light configurations does exist. If the ratio exceeds 3.15, the confidence level reaches 95%. It is customary to accept this level as a sufficient proof of a real difference.

Secondly, to check the conclusions from the differences in average values and their standard deviations, ranking methods have been used. To this end, for each night and each performance aspect, a ranking number has been given to each light configuration: 1 to the configuration with the lowest average value, 3 to the configuration with the highest and 2 to the configuration with the intermediate value. For each light configuration and each performance aspect the sum of the eight ranking numbers has been calculated. From statistical considerations it results that if this sum equals 21 or more, real quality differences exist between light configurations for that performance aspect.

The statististical treatment of the quality marks described above, resulted in significant differences with respect to the following aspects: approach height deviation, elevator travel, pitch amplitude, flare-out ground track and threshold height. For all other aspects, the natural scatter of the quality marks was too great to draw definite conclusions.

In the tables 6 to 10 inclusive, the average values of quality marks, the ranking numbers and their totals are given for each test night with respect to the 5 aspects referred to above. These tables also contain the standard deviation of the total averages.

The results of the statistical analysis are summarized in the following table. In this table the differences between the light configurations and the confidence levels of these differences for the 5 aspects referred to above are shown. The meaning of the symbols is:

$\gg$ "greater than" with a confidence level of at least 95%,
$>$ "greater than" with a confidence level of 90–95%,
$=$ the confidence level is smaller than 90%.

Light configuration	1		2		3		1
Quality mark for:							
approach height deviation	1	$\ll$	2	$>$	3	$=$	1
elevator travel *)	1	$=$	2	$<$	3	$\gg$	1
pitch amplitude	1	$>$	2	$=$	3	$=$	1
flare-out ground track	1	$\ll$	2	$\gg$	3	$=$	1
threshold height	1	$\ll$	2	$>$	3	$>$	1

*) High quality mark corresponds to low performance.

From this table the following conclusions, based on 95% confidence, may be drawn:

a. configuration 2 gives better height guidance during approach, better tracking during flare-out and better threshold height than configuration 1,
b. configuration 2 allows better tracking performance during flare-out than configuration 3,
c. configuration 3 requires more elevator movement than configuration 1.

In addition, the following tendencies seem to exist (confidence level 90–95%):

a. configuration 2 gives better height guidance during approach and better threshold height than configuration 3,
b. configuration 3 requires more elevator movement than configuration 2,
c. configuration 1 shows less pitch attitude variation than configuration 2 or 3,
d. configuration 3 shows better threshold height than configuration 1.

The ranking numbers give a satisfactory confirmation of the above conclusions.

The total average threshold height for the light configurations 1, 2 and 3 was found to be 73, 61 and 65 ft respectively, while the ideal threshold height is 50 ft. This confirms the relevant conclusions based on average quality marks and also shows that the threshold height scale below 50 ft has practically not been used. Pilots appear therefore to fly high over the threshold, particularly with configuration 1, less with configuration 3 and closest to the ideal height with configuration 2.

The 24 subject pilots can be divided into 3 groups: 6 KLM captains, 12 KLM co-pilots, and a group consisting of 2 captains of Air France, 2 captains of Deutsche Lufthansa and 2 pilots of the Blind Landing Experimental Unit (U.K.). It has been argued that this does not represent a random distribution, resulting in certain influences (e.g. of training, experience, age, etc.) on the test results. Therefore, table 11 has been composed to show the average values of quality marks for these 3 groups separately. In this table, ranking numbers have been assigned with respect to light configurations for each aspect under consideration and for each group of pilots, as well as for all pilots together.

It is shown that the results for the different groups of pilots were consistent, except in the case of pitch amplitude, which is in accordance with the fact that "significant" differences appeared to be relatively poor in the foregoing analysis for this performance aspect.

[7]) The statistical analysis has been performed by Prof. ir. J. W. Sieben of the Technological University, Delft.

There have been 22 overshoots out of 144 tests. Besides, the flare-out has been corrected 12 times by the safety pilot to avoid damage to the aircraft. No significant conclusions could be reached in this connection with regard to the light configuration used.

The reduction of the number of test results due to these overshoots appears only in the flare-out performance data, which may have contributed to the fact that no significant differences have been found in this respect.

8 Pilots' comments

Before entering into detail as regards the various comments of the subject pilots, the following general remarks should be made.

It has been observed that pilots' comments went far less into detail as compared to the previous "Eelde trials". Pilots were relatively more busy in controlling the aircraft and had less time to appreciate the individual features of the visual aids. This was probably due to the much higher ground speed during approach of about 130 kts with respect to 95 kts during the previous tests. Furthermore, the much higher aircraft weight allowed less manoeuvering in the approach area.

The total time required to correct a lateral position deviation amounted to about 15 sec, which corresponds to about 3000 ft distance covered. This means that in order to reach an acceptable flight condition at the ILS reference point [8]), an immediate, well judged corrective action was imperative as soon as visual contact was established. During the tests, it became quite clear that carrying out such corrective action, based on visual outside cues alone, was more difficult than relying upon the information available from the instrument panel and using the outside cues merely as a confirmation of the latter information. From the foregoing it appears that the operational flight technique for low-visibility landing affects the appreciation of visual aids. For instance, the importance of a 1000-ft pre-threshold warning bar depends on whether or not pilot's action on power-setting or configuration is related to it. It has been understood that some pilots prefer to maintain strictly one flight condition i.e. pitch, airspeed, power setting and configuration, until a flare-out at the minimum acceptable height. In such a case a stabilized instrument approach will guarantee a safe height of about 125 ft when the 1000-ft bar is well visible and no action will be required. The same applies to the perception of the threshold. Both observations then merely confirm the progress of the approach. Other pilots are used to carry out a gradual change of configuration, power-setting, airspeed and pitch during the last 3000 ft distance before touch-down. Such flight technique definitely requires distance-to-go information as well as some sort of height and pitch guidance.

With respect to pilots' comments, the 24 subject pilots can be divided into 5 different groups:

a. 2 Lufthansa captains,
b. 12 KLM co-pilots,
c. 6 KLM captains,
d. 2 Air France captains,
e. 2 BLEU research pilots.

[8]) *ILS reference point, as described in ICAO Annex 10, Attachment C, para. 2.4.*

Pilots' opinions will be related to these groups in the text below.

It was rather surprising to note that the first 4 crossbars of the Calvert approach light pattern were not much appreciated. They were even considered confusing (group *a*) with regard to finding the location and the direction of the centre line. During this stage of the approach, the visual segment is still so short that these lights can hardly supply useful information, especially when some lateral deviation or crab angle prevails. It was suggested to delete these crossbars (group *a* and *d*).

Those pilots willing to rely completely on outside visual cues (group *b*) found themselves often misled after their first corrective action upon initial visual contact, while those continuing mainly on instruments until visual information was considered to be complete (group *c*), generally reached a better position near the threshold. A perfect instrument approach could be spoiled by trying to use relatively poor outside information.

The 1000-ft bar was considered to be inconspicuous in the configurations 1 and 3. In this respect the red wide gauge lighting of configuration 2 was welcomed by all pilots. These red lights were found to be very useful as a bracket or gate by which the acceptability of the lateral position deviation could well be judged (group *e*). A few pilots considered the red double row to be confusing (group *a*, some of group *b*) especially when a corrective manoeuvre was already initiated; the direction of the centre line seemed to be lost in such a case.

The end of the area with red lights of configuration 2 meant distinctly and obviously that the threshold was in sight. This was the main reason for all pilots, except group *a* and some of group *b*, to prefer configuration 2 above 1 and 3. Those criticizing the red lights favoured a simple light pattern but insisted upon a good threshold indication which they found insufficient in configurations 1 and 3; it was generally not realized or too late, that the beginning of the narrow gauge runway lighting was the beginning of the runway as well.

The pilots of group *b* showed a tendency to swing between the narrow gauge or to be attracted to either side. Some thought this oscillation to be caused by the existence, others by the absence of a runway centre line. Generally, however, there was no doubt about the necessity of a runway centre line, provided that these lights should not be brighter than the narrow gauge lights.

No complaints or suggestions with regard to gauge width or longitudinal spacing of the runway lights were expressed.

The length of the visual segment was generally too small to enable the pilots to perform a clear-cut flare-out. Many pilots showed a tendency to misjudge the flare-out or to feel their way down to a touch-down 3000 ft from the threshold.

The ILS reference point wing-bars of configuration 1 were hardly ever noticed. Pilots did not seem to appreciate any indication of the ILS reference point because no decision or action was related to it.

A total length of 4000 ft narrow gauge lighting was generally favoured.

A distance marker at about 2500 ft from the threshold was thought to be useful as a warning when landing on a runway of critical length.

The following conclusions based on the opinions of the majority of subject pilots, may be derived:

a. the first 1500 ft approach lights were not considered of much importance,
b. an unmistakable distance warning, located 1000 ft in front of the threshold, was considered either useful or essential,
c. all pilots required a clear and very distinctive indication of the threshold,
d. the red wide gauge pre-threshold lighting of configuration 2 was considered as to meet the desire mentioned in *b* and the requirement stated in *c*,
e. no pilot insisted upon an indication of the ILS reference point, although some would like a distance marker at about 2500 ft from the threshold for a runway of critical length,
f. all pilots, except a few in group *b*, required a centre line throughout the complete light configuration,
g. all pilots seemed satisfied with the narrow gauge runway lights, although many of them had difficulties in assessing their flare-out.

9 Conclusions

9.1 *General*

When reviewing the results of the present investigation, it should be kept in mind that this is a continuation of the "Eelde trials" executed in 1960. In order to emphasize the value of the complete investigation, the conclusions resulting from the present tests, therefore, should also be considered as far as possible in relation to those of the previous trials.

Generally, it can be concluded that the application of a large four-engine nosewheel aircraft of more modern design to these tests does not affect the trend of the results obtained from the "Eelde trials", but rather strengthens the conclusions and views based on these trials.

In the following conclusions the main items of approach and runway lighting are treated separately.

9.2 *Approach lighting*

With respect to the approach lighting the following conclusions can be drawn:

a. from the statistical analysis of the present test data it appears that the red wide gauge pre-threshold lighting of configuration 2 is responsible for its better guidance in height before and over the threshold. Threshold heights closest to the ILS glide path were also found for the similar light configuration in the "Eelde trials". The latter, moreover, proved to offer better tracking qualities before crossing the threshold, which is confirmed in the present tests by pilots' judgement only but is not "significantly" shown by the test results as such,
b. the reinforced pre-threshold centre line of configuration 3, apparently, improves the height guidance in the pre-threshold region as well. However, this improvement is of less importance than the one obtained by the double row of red lights in configuration 2,
c. configuration 2 allows better tracking performance during flare-out than configurations 1 and 3. In this respect, the latter configurations do not show a "significant" difference, proving that the uninterrupted centre line of configuration 2 cannot be responsible for the better flare-out tracking capability of this configuration. Therefore, it seems justified to state that the better flare-out tracking guidance as proved by the test results must result from the red pre-threshold lights, allowing better stabilization and judgement of lateral deviation as stated by some pilots. This points to better tracking guidance before the threshold which was proved by the "Eelde trials".

9.3 *Threshold identification*

Apparently, pilots find in the red lights of configuration 2 an unmistakable distance warning of conspicuous repetitive character, beginning at 1000 ft before the threshold, as well as a distinctive threshold marking.

The main criticism on configurations 1 and 3 was directed towards poor threshold lighting and insufficient pre-threshold warning. In this respect the pre-threshold centre line of configuration 1 was considered too weak.

9.4 *Aiming point*

The indication of the aiming point as applied in the runway light patterns does not seem to improve flare-out.

A distance marking at 2500 ft from the threshold, however, should according to pilots' comments, be considered as a useful warning in case of a landing on a runway of critical length.

9.5 *Runway centre line*

Elevator movement has been applied to a higher degree with configuration 3 as compared with configuration 1 and also (at a smaller confidence level) with configuration 2. This may be attributed to the interruption of the centre line in the first part of the runway of configuration 3, presenting a less complete ground plane picture to the pilot.

According to pilots' opinions an uninterrupted centre line lighting, preferably of slightly less intensity than the narrow gauge runway lighting, is generally appreciated. The test results, however, do not show the centre line to be of help in reducing lateral deviations.

9.6 *Additional conclusion*

No significant differences in the light configurations could be found with respect to approach ground track, threshold speed, flare-out height deviation, touch-down distance, lateral and directional control.

Remark:
It should be realized that these conclusions are closely related to the short visual range (1000 ft) applied in these trials.

10 Future work

From the tests executed so far, no guidelines can be derived for obtaining the highest effectiveness of *runway* light patterns. In the "Eelde trials" the application of landing lights prevented any conclusion in this respect, while in the present tests no comparison of systems could be made because only one type of narrow gauge system with lateral elements could be presented on the runway.

Moreover, the aiming point indication in the present trials was not similar to that applied in the previous test series and was less conspicuous in character.

It is considered necessary to investigate this item separately by flight operational evaluation after a pre-selection of patterns by simulated landing trials.

Acknowledgements

The co-operation of the German authorities, which greatly facilitated the execution of this investigation, is highly appreciated.

Similar to the "Eelde trials", once more a vast amount of work has been done in a joint effort of interested parties in the Netherlands to evaluate certain aspects of approach and runway lighting problems. Next to financial support, such a mission requires just as well enthusiasm and perseverance of the men on the spot. In this respect, the Working Group has expressed its high appreciation of the work done by the safety pilot, who accomplished a most difficult task, the air- and ground crews, the subject pilots, and the local authorities, managers and technical employees of Köln-Bonn Airport and the KLM field office.

The complete absence of accidents or incidents may prove the high standard of safety with which the operation has been carried out.

The author is greatly indebted to Mr. J. B. de Boer and Prof. ir. T. van Oosterom for their most valuable assistance in preparing this report.

Table 1. List of subject pilots.

Name	*Grade*	*Affiliation*	*Flying hours total approx.*	*Age*
J. N. van der Ben	Co-pilot	KLM	3500	27
R. K. van der Bijl	Co-pilot	KLM	4000	29
C. D. Crogan	Flt. Lt.	BLEU	3600	39
C. R. Dierdorp	Captain	KLM	12000	41
O. Ferwerda	Co-pilot	KLM	4000	30
J. Förster	Captain	Lufthansa	12000	41
R. Gaurand	Captain	Air France	10000	42
R. Goedkoop	Co-pilot	KLM	4200	31
C. Groenendijk	Co-pilot	KLM	5000	33
D. C. Hovingh	Co-pilot	KLM	4000	29
G. H. de Jong	Captain	KLM	7500	33
B. G. Koning	Captain	KLM	12000	41
K. de Lange	Co-pilot	KLM	4000	27
J. Londaïts	Captain	Air France	12000	40
B. Lyklema	Co-pilot	KLM	3600	27
A. Mulder	Co-pilot	KLM	4000	27
J. M. Nieuwenhuyse	Co-pilot	KLM	3500	29
J. Ohm	Captain	Lufthansa	10000	41
F. J. de Regt	Co-pilot	KLM	7000	31
J. J. M. van Rijn	Co-pilot	KLM	3500	32
J. Sprong	Captain	KLM	12000	40
N. van der Stroom	Captain	KLM	10000	39
E. C. Turner	Flt. Lt.	BLEU	2800	32
Y. H. Wiarda	Captain	KLM	14000	42

Table 2. Average weather conditions.

Date 1962	*Test night*	*Block-time (hrs. min)*	*Average wind speed components (kts)* head	tail	stbd	port	*Gusts*	*Cloud base (ft)*
20 nov.[1]	A	3.34		2		6	slight	2500
4 dec.[1]	B	3.14		6	3		none	none
5 dec.	C	2.42		4	2		none	none
6 dec.	D	2.24		7	2		none	none
7 dec.	E	3.14		6	1		none	misty
10 dec.	F	2.52	8			4	some	800
12 dec.	G	2.40		6	0	0	slight	1200
13 dec.	H	2.47	3			3	slight	1500

[1]) Unfavourable weather conditions (natural fog) prevented test flying during the period between test nights A en B.

Table 3. Numerical values of quality marks for various performance aspects.

Quality mark	0	1	2	3	4	5	6	7	8	9	10
Approach height deviation / Approach gnd. track	55	50	45	40	35	30	25	20	15	10	5
Threshold height	100	95	90	85	80	75	70	65	60	55	50
	10	14	18	22	26	30	34	38	42	46	50
Threshold speed	137	135	133	131	129	127	125	123	121	119	117
Flare-out ground track	50	45	40	35	30	25	20	15	10	5	0
Touch-down distance	4	5	6	7	8	9	10	11	12	13	14
	45	42	39	36	33	30	27	24	21	18	15
Roll-and pitch wave-length	0	3	6	9	12	15	18	21	24	27	30
Roll amplitude	21	19	17	15	13	11	9	7	5	3	1
Pitch amplitude	8.4	7.6	6.8	6.0	5.2	4.4	3.6	2.8	2.0	1.2	0.4
Elevator- and rudder travel	0	0.24	0.48	0.72	0.96	1.20	1.44	1.68	1.92	2.16	2.40
Aileron travel	0	2.6	5.2	7.8	10.4	13.0	15.6	18.2	20.8	23.4	26.0

The figures in this table corresponding with the quality marks 1–10, represent for:

approach height deviation, half of channel height in ft, measured 3000 ft in front of threshold (fig. 10, grid 1),

approach ground track, half of channel width in ft, measured 3000 ft in front of threshold (fig. 10, grid 2),

threshold height, range in ft (fig. 10, grid 3),

threshold speed, kts IAS,

flare-out:
- *ground track*, half of channel width in ft (fig. 10, grid 4),
- *touch-down distance*, range of distance from threshold in 100 ft (fig. 10, grid 3),
- (*height deviation*, not mentioned in table, combination of scales for *threshold height* and *touch-down distance* (fig. 10, grid 3)),

roll- and pitch wave-length, distance covered for one oscillation in 100 ft (fig. 10, grid 5),

roll amplitude, maximum angle of roll in degrees (fig. 10, grid 5),

pitch amplitude, maximum change of pitch attitude in degrees (fig. 10, grid 5),

control travel:
- *elevator and rudder*, average control surface movement in degrees, according to definition given in chapter 6,
- *aileron*, average control wheel rotation in degrees, according to definition given in chapter 6.

Table 4. Quantitative results of performance evaluation.

0	1	2	3	4	5	6	7	8	9	10	11	12	13	14	15	16	17	18	19	20	21
Test night	Landing number	Pilot number	Light configuration	Headwind component (kts)	S.B. crosswind comp. (kts)	Approach height deviation	Approach ground track	Threshold height	Threshold speed	Flare-out height deviation	Flare-out ground track	Touch-down distance	Roll amplitude	Roll wave-length	Pitch amplitude	Pitch wave-length	Elevator travel	Rudder travel	Aileron travel	True threshold height (ft)	Remarks
A	0	SP	2	+1	—6	—	—	—	7	—	—	—	9	—	7	—	2	1	3	—	
	1	1	2	+1	—6	—	—	—	6	—	—	—	0	—	3	—	10	10	10	—	overshoot
	2	3	2	0	—6	5	9	9	4	7	8	7	8	4	7	5	2	0	8	57	
	3	1	3	0	—6	—	—	—	4	—	—	—	—	—	—	—	10	10	10	—	overshoot
	4	2	3	0	—6	2	1	4	7	—	7	—	4	10	6	3	5	1	4	77	overshoot
	5	3	1	—1	—6	5	5	4	3	8	2	3	2	4	7	4	4	1	5	77	
	6	2	1	—1	—6	5	1	6	3	—	1	—	1	9	5	2	6	7	4	72	overshoot
	7	3	1	—4	—4	0	9	0	5	9	7	5	7	5	6	4	2	0	3	117	
	8	1	1	+1	—6	6	8	7	5	6	7	4	6	6	6	3	5	4	3	65	
	9	2	3	—2	—5	3	2	3	4	7	5	5	3	9	6	3	6	4	3	84	
	10	3	3	—2	—5	1	8	2	5	9	5	7	6	4	8	10	1	0	5	87	
	11	1	2	—3	—5	7	7	7	4	7	6	6	4	8	7	3	5	3	5	66	
	12	2	2	—2	—5	9	7	7	5	6	7	3	9	8	7	3	7	1	3	64	
	13	3	2	—3	—5	2	5	3	6	8	8	7	4	4	5	3	3	0	5	86	
	14	2	2	—3	—5	5	7	4	3	6	6	6	5	9	7	8	2	4	3	77	
	15	1	3	—4	—4	3	8	4	7	8	8	6	5	3	8	3	3	3	5	78	
	16	3	3	—4	—4	3	1	3	3	9	8	5	4	5	8	4	2	0	5	82	
	17	2	1	—4	—4	5	2	6	4	7	7	5	5	9	4	2	6	4	3	71	
	18	1	1	—4	—4	5	10	4	2	7	8	5	9	3	9	7	3	1	2	80	
B	0	SP	0	—6	+1	9	9	9	7	6	8	6	9	6	8	—	4	1	3	43	
	1	1	1	—6	+1	4	5	4	5	—	6	—	6	10	8	4	3	1	3	78	overshoot
	2	2	1	—6	+1	0	0	0	4	—	4	—	3	5	4	9[1]	4	3	7	117	overshoot
	3	3	2	—8	0	6	2	5	5	7	7	3	1	6	5	3	9	1	10	77	
	4	1	2	—6	0	9	0	9	8	7	8	7	6	10	6	8	2	1	2	56	
	5	3	3	—5	+1	0	3	0	6	8	0	4	3	5	5	2	3	2	8	126	
	6	2	3	—4	+2	9	9	9	3	6	7	6	6	7	6	2	3	1	5	55	
	7	3	3	—5	+2	0	1	0	5	6	4	4	3	5	4	3	6	1	8	102	
	8	1	3	—4	+1	2	0	4	7	9	6	6	2	6	5	3[1]	4	0	5	79	corrected
	9	2	2	—7	+1	4	0	9	6	8	7	8	5	10	4	3	5	1	5	45	
	10	1	2	—8	+1	2	1	4	5	6	8	3	7	8	6	8	2	0	3	80	
	11	2	1	—7	0	7	2	7	6	9	9	8	4	4	6	3[1]	1	2	4	66	
	12	3	1	—6	0	4	5	4	4	6	7	4	2	5	5	4	3	1	7	80	
	13	1	1	—6	+1	4	3	4	5	8	8	5	6	7	8	8	2	0	4	79	
	14	3	1	—5	+2	2	5	2	6	8	8	7	2	4	5	—	2	1	8	88	
	15	2	2	—4	+4	7	1	9	4	6	8	8	6	8	4	3	2	1	5	42	
	16	3	2	—3	+4	5	7	5	5	7	8	6	6	4	5	2	3	1	8	73	corrected
	17	1	3	—4	+4	5	1	6	4	9	7	7	4	10	7	3	2	6	5	69	
	18	2	3	—5	+2	8	7	7	5	7	9	6	6	5	7	5	4	3	6	65	
C	0	SP	2	—5	+1	10	8	10	6	7	8	5	8	6	8	5	2	2	3	51	
	1	2	3	—5	+1	9	0	9	5	4	5	1	0	7	8	3	8	10	10	46	[2]
	2	3	3	—5	+2	3	3	4	4	5	7	1	6	10	5	—	7	10	10	80	[2]
	3	2	1	—4	+3	4	1	5	5	7	7	5	6	3	5	3[1]	3	4	5	32	[2]
	4	1	1	—4	+4	3	3	4	7	6	5	4	3	6	7	2	6	2	7	77	[2]
	5	1	2	—4	+4	8	3	8	6	7	8	7	5	5	5	10	2	2	5	61	[2]
	6	3	2	—1	+1	8	6	8	6	8	7	7	5	7	5	9[1]	3	3	5	60	[2]
	7	2	2	—1	+1	8	8	8	7	9	9	10	7	6	5	—	4	0	4	58	[2]
	8	3	2	—3	+3	5	0	5	3	4	8	0	0	10	7	3	8	10	10	74	
	9	1	1	—5	+1	1	0	1	8	7	8	7	8	5	2	4	3	0	4	92	corrected
	10	3	1	—5	+1	4	9	4	5	9	7	7	6	7	8	4	1	0	3	78	
	11	2	3	—5	+1	9	0	8	5	6	9	5	4	5	5	4	2	7	9	59	
	12	1	3	—3	0	2	2	3	5	8	6	5	5	5	6	3	3	4	8	85	corrected
	13	3	3	—2	0	4	1	4	7	6	8	3	5	10	7	4	2	3	4	79	
	14	1	3	—2	0	7	1	8	8	7	7	7	5	5	6	2	5	0	10	61	
	15	2	1	—2	0	7	0	7	6	7	8	5	4	10	7	6	1	6	5	64	
	16	3	1	—2	0	3	8	4	6	6	8	3	6	5	4	3	2	4	5	79	
	17	2	2	—2	0	10	6	9	3	7	5	5	7	5	8	5	3	0	2	53	[4]
	18	1	2	—2	0	4	5	4	6	7	9	6	6	6	2	—	2	0	6	80	
D	0	SP	2	—8	+1	10	8	9	3	7	5	6	10	5	8	2	4	0	2	52	
	1	2	1	—8	+1	0	0	0	1	—	0	—	4	10	9	10	0	0	2	152	corrected
	2	1	1	—8	+2	1	1	3	5	8	2	5	6	7	3	3	5	1	2	82	
	3	3	3	—8	+3	8	7	7	5	8	4	6	6	7	6	6	3	1	2	67	
	4	1	3	—6	+2	7	1	9	0	7	2	3	6	7	3	3	3	1	3	53	
	5	3	2	—6	+1	8	9	7	5	8	6	5	6	9	7	3	3	6	4	66	
	6	2	2	—6	+2	9	6	10	5	7	6	5	5	9	8	3	3	4	3	50	
	7	1	2	—6	+2	9	4	9	2	5	8	5	7	9	7	3	2	1	3	56	
	8	2	2	—3	0	9	1	10	6	7	8	7	2	10	7	2	2	7	4	51	
	9	2	3	—4	+1	9	6	10	5	9	6	10	7	10	8	2	5	2	3	49	corrected
	10	3	3	—6	+1	9	8	10	8	8	5	8	6	9	6	6	4	5	3	51	
	11	3	1	—6	+1	8	5	9	7	8	8	9	7	7	7	2	4	4	3	47	
	12	1	1	—7	+2	5	7	6	5	8	9	7	8	6	4	2	5	0	4	71	
	13	2	1	—7	+2	8	8	8	4	8	6	6	8	6	6	3	6	1	3	57	
	14	3	1	—6	+1	3	8	5	7	6	7	8	6	8	5	3	4	6	2	29	
	15	1	3	—7	+1	9	8	9	6	9	8	9	9	4	7	4	5	0	3	53	
	16	2	3	—7	+1	9	5	9	4	9	6	8	6	10	4	2	5	2	4	55	
	17	1	2	—6	+1	9	7	8	3	10	9	9	8	5	6	3	5	0	3	58	
	18	3	2	—6	+1	9	0	6	6	8	2	6	4	6	5	2	4	4	4	69	corrected[3]

[1] Unreliable; [2] SVR about 2500 ft, decreasing to 1000 ft; [3] Landed by safety pilot, to be considered as overshoot; [4] Sudden change of SVR from 0 to 1000 ft at 1000 ft before threshold; [5] Pilot expected configuration 3; [6] Pilot expected configuration 2; [7] R. H. red barrette nearest to threshold unserviceable; [8] Port aiming point lighting unserviceable.

Table 4. Quantitative results of performance evaluation *(cont'd).*

0	1	2	3	4	5	6	7	8	9	10	11	12	13	14	15	16	17	18	19	20	21
Test night	Landing number	Pilot number	Light configuration	Headwind component (kts)	S.B. crosswind comp. (kts)	Approach height deviation	Approach ground track	*Threshold height*	Threshold speed	Flare-out height deviation	Flare-out ground track	Touch-down distance	*Roll amplitude*	Roll wave-length	Pitch amplitude	Pitch wave-length	Elevator travel	Rudder travel	Aileron travel	True threshold height (ft)	Remarks
E	0	SP	2	—4	0	10	7	9	7	7	6	6	7	5	8	5	3	8	2	47	
	1	2	3	—4	0	7	7	10	4	—	7	—	6	7	6	7	3	0	4	48	overshoot
	2	3	3	—4	0	5	7	5	3	—	8	—	7	8	8	3	2	1	3	72	overshoot
	3	1	2	—4	0	7	6	9	5	6	0	7	9	6	9	5	2	0	2	44	corrected 5)
	4	3	2	—6	+1	5	7	6	8	10	7	9	7	10	6	5	3	1	3	69	
	5	1	1	—4	0	8	5	7	5	—	1	—	3	9	8	4	1	7	3	64	overshoot
	6	2	1	—4	0	5	9	6	3	—	6	—	9	2	7	10	2	2	4	70	overshoot
	7	3	1	—4	0	0	8	0	6	—	7	—	9	7	7	10	2	10	4	104	overshoot 6)
	8	1	1	—4	0	8	0	8	7	8	8	9	7	10	10	—	2	7	4	45	
	9	2	2	—7	+1	9	5	10	3	5	9	4	9	6	7	4	3	1	4	50	
	10	3	2	—5	+1	1	5	2	9	—	6	—	9	6	3	10	4	10	3	90	overshoot
	11	2	3	—6	+2	8	7	9	2	5	8	5	6	6	7	6	1	0	6	45	
	12	1	3	—7	+2	7	5	8	6	7	3	8	7	8	8	3	2	2	2	40	corrected
	13	1	3	—6	+2	9	0	10	6	7	1	7	2	10	8	2	1	7	4	49	corrected 3)
	14	3	3	—8	+3	0	3	0	8	—	7	—	4	7	4	6	2	8	3	101	overshoot
	15	1	2	—8	+3	10	0	9	6	7	3	6	4	8	6	3	2	4	2	54	corrected
	16	2	2	—8	+3	10	0	9	3	4	7	3	7	2	8	3	2	0	7	53	
	17	2	1	—8	+3	9	3	8	2	7	7	4	8	3	9	—	0	0	6	59	
	18	3	1	—6	+1	0	9	0	5	6	7	4	9	7	1	8	2	1	3	117	corrected 3)
F 7)	0	SP	2	+7	—4	—	—	—	—	—	—	6	8	4	8	5	5	6	5		
	1	3	2	+4	—3	5	10	5	6	7	8	7	9	3	3	4	7	0	4	37	corrected
	2	1	2	+9	—3	9	7	8	4	8	8	6	6	6	7	6	3	0	4	52	corrected
	3	2	1	+7	—7	8	1	7	6	—	6	—	0	10	3	6	5	4	10	54	overshoot
	4	3	1	+8	—5	7	5	5	7	—	7	—	5	7	5	7	5	1	7	62	overshoot
	5	1	3	+10	—6	3	8	3	7	7	8	3	7	5	5	3	6	4	8	77	corrected
	6	2	3	+6	—5	9	8	7	3	5	4	0	4	8	7	5	10	10	10	55	
	7	3	3	+8	—6	2	9	2	5	—	6	—	6	7	5	3 1)	3	4	4	77	overshoot
	8	2	3	+6	—5	7	3	6	5	9	8	8	8	3	3	4	4	0	5	60	
	9	3	1	+7	—6	9	9	6	5	5	4	0	3	7	6	5	10	10	10	60	
	10	1	1	+7	—4	7	8	4	6	7	8	4	6	4	7	2	4	2	8	68	
	11	1	2	+6	—5	9	9	8	6	6	8	4	8	5	5	3 1)	3	1	8	51	8)
	12	2	2	+6	—5	—	—	—	—	—	—	—	—	—	—	—	—	—	—	—	8)
	13	2	2	+8	—6	7	0	7	7	6	8	4	4	3	5	8	3	0	7	56	8)
	14	3	2	+7	—4	9	8	8	7	7	7	6	6	6	6	4 1)	7	1	5	49	8)
	15	1	1	+7	—4	10	0	7	5	6	7	4	2	10	5	8	5	2	5	55	
	16	2	1	+6	—5	9	2	6	6	5	4	1	7	3	5	4	4	0	4	57	
	17	3	3	+7	—4	9	9	7	8	9	6	8	6	9	7	2	5	1	4	52	
	18	1	3	+6	—5	10	8	7	6	6	8	4	5	6	3	—	3	4	8	54	
G	0	SP	2	+1	—1	9	8	9	7	6	8	5	8	4	6	4	4	7	3	52	
	1	3	2	+1	—1	6	1	8	9	7	6	8	6	4	5	2	4	3	6	44	
	2	2	2	0	0	7	5	8	4	7	7	8	6	4	2	—	3	3	3	55	
	3	2	3	+1	—1	7	0	8	4	3	8	1	4	6	3	—	10	4	5	54	
	4	1	3	+3	—2	2	1	2	6	7	6	2	3	4	7	2	4	7	6	85	
	5	3	1	+1	—1	0	8	0	8	9	1	6	8	3	5	3	3	4	3	110	
	6	1	1	+3	—2	3	0	2	5	7	7	2	2	10	6	2	2	6	6	80	
	7	2	1	—5	+2	7	4	5	2	7	8	4	4	9	5	6	3	2	5	70	
	8	1	1	—6	+2	0	0	0	6	—	0	—	0	—	4	3	2	9	5	105	overshoot
	9	1	2	—6	+2	3	4	2	5	5	2	2	3	5	5	2	2	7	6	82	
	10	3	2	—7	+1	9	6	6	4	7	4	5	7	8	6	2	4	4	4	63	
	11	2	3	—6	+1	8	0	5	1	7	8	5	6	10	5	4	10	2	2	70	
	12	3	3	—6	+1	3	4	2	7	8	0	5	6	5	7	3	4	2	3	82	
	13	3	3	—6	+1	5	9	7	9	6	1	7	9	3	3	3	4	1	3	40	
	14	1	3	—5	—1	10	6	8	6	8	8	7	4	5	7	3	3	7	8	55	
	15	1	2	—6	—1	7	0	7	5	6	7	5	5	4	6	2	3	4	6	40	
	16	2	2	—6	—1	7	5	4	2	7	7	6	5	7	2	6	2	2	3	73	
	17	2	1	—6	—3	2	0	1	3	6	7	4	5	5	3	—	2	2	5	90	
	18	3	1	—5	—3	0	0	0	9	8	0	4	1	10	6	2	4	8	5	109	
H	0	SP	2	0	0	9	9	9	7	7	8	6	9	3	7	5	8	3	3	53	
	1	1	1	0	0	9	9	9	6	6	6	5	8	4	5	2	2	0	4	55	
	2	3	1	0	0	8	4	10	9	6	1	6	6	10	8	7	2	1	5	48	
	3	2	2	0	0	5	0	6	3	7	5	3	4	4	7	6	—	—	—	67	
	4	1	2	0	0	10	9	10	5	10	7	10	8	2	6	4	4	0	5	51	
	5	3	3	0	0	0	1	0	10	—	0	—	1	10	8	3	1	2	4	100	overshoot
	6	2	3	+2	—1	9	0	9	9	6	5	4	6	4	5	5	4	1	3	55	
	7	2	3	+3	—2	0	0	0	9	—	5	—	6	7	1	—	4	2	2	112	overshoot
	8	1	3	+3	—3	9	3	10	7	9	9	9	5	3	5	3	5	1	7	50	
	9	3	1	+4	—4	3	2	4	8	8	7	5	6	3	7	4	3	1	4	80	
	10	2	1	+3	—4	7	4	6	8	7	9	7	5	3	6	3	3	1	2	70	
	11	3	2	+1	—3	0	0	0	9	9	6	4	3	10	6	8	2	1	2	105	
	12	1	2	+2	—3	8	0	10	8	8	9	9	7	4	3	5 1)	4	1	4	49	
	13	3	2	+2	—3	4	0	5	10	8	9	10	5	10	5	3	3	1	3	76	
	14	2	2	+3	—2	9	6	9	9	7	7	7	8	4	5	5	2	0	2	56	
	15	1	1	+3	—3	6	4	7	6	9	8	9	5	4	6	3	6	1	5	66	
	16	2	1	+5	—3	7	1	8	10	7	7	7	6	3	5	4	5	1	2	58	
	17	1	3	+3	—2	9	9	9	7	6	8	6	8	4	5	2	3	1	5	46	
	18	3	3	0	0	10	9	9	8	9	6	9	8	9	5	4	3	1	3	53	

Table 5. Totale average values of quality marks.

	Light configuration		
	1	2	3
Approach height deviation	4.7	6.8	5.7
Elevator travel	3.3	3.7	4.4
Pitch amplitude	6.0	5.45	5.6
Pitch period	3.3	3.5	4.4
Approach groundtrack	4.2	4.5	4.3
Flare-out ,,	5.9	6.9	5.8
Rudder travel	2.8	2.2	3.1
Aileron travel	4.5	4.6	5.2
Roll amplitude	5.2	5.7	5.2
Roll period	6.3	6.3	6.6
Threshold height	4.6	6.8	5.8
Threshold speed	5.4	5.3	5.6
Flare-out height deviation	7.5	6.9	6.9
Touch-down distance	3.9	4.8	3.8

Table 6. Average quality marks and ranking numbers for "approach height deviation".

Light	*Average marks*			*Ranking numbers*		
configuration	1	2	3	1	2	3
Test night						
A	4.3	5.6	2.4	2	3	1
B	3.5	5.5	4.0	1	3	2
C	3.7	7.2	5.7	1	3	2
D	4.2	8.7	8.5	1	3	2
E	5.0	7.0	6.0	1	3	2
F	8.4	7.8	6.7	3	2	1
G	2.0	6.5	5.8	1	3	2
H	6.7	6.0	6.2	3	1	2
Total	4.7	6.8	5.7	13	21	14

Standard deviation of total average: 0.41.
90% significant difference on total average: 1.05.
95% significant difference on total average: 1.29.

Table 7. Average quality marks and ranking numbers for "elevator travel".

Light	*Average marks*			*Ranking numbers*		
configuration	1	2	3	1	2	3
Test night						
A	4.3	4.9	4.5	1	3	2
B	2.5	3.9	3.7	1	3	2
C	2.7	3.7	4.5	2	2	3
D	4.0	3.2	4.2	2	1	3
E	1.5	3.2	4.2	1	2	3
F	5.5	4.6	5.2	3	1	2
G	2.7	3.0	5.9	1	2	3
H	3.5	3.0	3.3	3	1	2
Total	3.3	3.7	4.4	13	15	20

Standard deviation of total average: 0.28.
90% significant difference on total average: 0.72.
95% significant difference on total average: 0.88.

Table 8. Average quality marks and ranking numbers for "pitch amplitude".

Light	*Average marks*			*Ranking numbers*		
configuration	1	2	3	1	2	3
Test night						
A	6.2	6.0	6.0	3	1½	1½
B	6.0	5.0	5.7	3	1	2
C	6.5	5.4	6.2	3	1	2
D	5.7	6.7	5.7	1½	3	1½
E	7.0	6.5	6.9	3	1	2
F	5.2	4.3	5.0	3	1	2
G	4.9	4.3	5.3	2	1	3
H	6.3	5.2	4.2	3	2	1
Total	6.0	5.45	5.6	21½	11½	15

Standard deviation of total average: 0.23.
90% significant difference on total average: 0.59.
95% significant difference on total average: 0.73.

Table 9. Average quality marks and ranking numbers for "flare-out ground track".

Light	*Average marks*			*Ranking numbers*		
configuration	1	2	3	1	2	3
Test night						
A	5.3	7.0	5.5	1	3	2
B	7.0	7.7	5.5	2	3	1
C	7.2	7.7	7.0	2	3	1
D	5.3	6.5	5.2	2	3	1
E	6.0	5.3	5.7	3	1	2
F	6.0	8.0	6.7	1	3	2
G	3.8	5.5	5.2	1	3	2
H	6.3	7.2	5.5	2	3	1
Total	5.9	6.9	5.8	14	22	12

Standard deviation of total average: 0.22.
90% significant difference on total average: 0.56.
95% significant difference on total average: 0.69.

Table 10. Average quality marks and ranking numbers for "threshold height".

Light	*Average marks*			*Ranking numbers*		
configuration	1	2	3	1	2	3
Test night						
A	4.5	6.0	3.2	2	3	1
B	3.5	6.8	4.3	1	3	2
C	4.2	7.0	6.0	1	3	2
D	5.2	8.3	9.0	1	2	3
E	4.9	7.5	7.0	1	3	2
F	5.9	6.2	5.3	2	3	1
G	1.3	5.9	5.3	1	3	2
H	7.3	6.7	6.1	3	2	1
Total	4.6	6.8	5.8	12	22	14

Standard deviation of total average: 0.41.
90% significant difference on total average: 1.05.
95% significant difference on total average: 1.29

Table 11. Average quality marks and ranking numbers for 3 groups of subject pilots.

Aspect	*Light configuration*	*Average quality marks and ranking numbers*						*Total average*	
		KLM captains		*KLM co-pilots*		*Foreign captains*			
Approach height deviation	1	5.4	(2) [1]	4.1	(1)	4.8	(1)	4.7	(1)
	2	6.5	(3)	7.1	(3)	5.7	(3)	6.8	(3)
	3	5.3	(1)	6.0	(2)	4.9	(2)	5.7	(2)
Elevator travel	1	4.0	(2)	2.7	(1)	3.5	(1)	3.3	(1)
	2	3.9	(1)	3.5	(2)	3.7	(2)	3.5	(2)
	3	4.7	(3)	4.2	(3)	5.2	(3)	4.4	(3)
Pitch amplitude	1	5.6	(3)	6.3	(3)	5.8	(2)	6.0	(3)
	2	5.0	(1)	5.9	(1)	5.9	(3)	5.45	(1)
	3	5.1	(2)	6.1	(2)	5.5	(1)	5.6	(2)
Flare-out ground track	1	5.3	(1)	6.4	(2)	5.8	(1)	5.9	(2)
	2	6.9	(3)	6.8	(3)	6.3	(3)	6.9	(3)
	3	5.7	(2)	5.8	(1)	6.0	(2)	5.8	(1)
Threshold height	1	4.8	(1)	4.5	(1)	4.2	(1)	4.6	(1)
	2	6.2	(3)	7.4	(3)	6.0	(3)	6.8	(3)
	3	5.0	(2)	6.6	(2)	5.6	(2)	5.8	(2)

[1]) Figures in parentheses are ranking numbers.

C.C.L. Class. D 401

REPORT NLR-TR T. 83

The computation by Lighthill's method of transonic potential flow around a family of quasi-elliptical aerofoils

by

G. Y. Nieuwland

Summary

This report contains a number of numerically worked out solutions of the potential equations for compressible air flow, representing examples of continuous transonic flow around a 3-parameter family of aerofoils.

As these flows have been the subject of a long standing debate as to their mathematical and physical existence, material has been included to enable an interpretation of the results in both respects.

In the second section, Lighthill's method is used to construct a 3-parameter family of solutions derived from the symmetrical incompressible flow around an ellipse; some of the properties exhibited by this family are of interest in the design problem for the shock free profile flows of the "peaky pressure distribution" type, which have recently been experimentally obtained by Pearcey.

The third section contains some details of the numerical work, which has been designed to overcome the severe convergence problems associated with the computation of thin shapes. These difficulties have been partially solved by a formal application of Wynn's ε-algorithm.

In an Appendix, a general discussion is given on the physical interpretability of the results of this report (the "transonic controversy"), in view of recent mathematical and experimental evidence.

In a second Appendix, some elementary algebraic aspects of the hodograph transformation are discussed, giving the key to some of the mathematical and physical properties particular to plane potential flows. In particular, the feasibility of the hodograph transformation is considered, and shown to depend on the metrical properties and dimensionality of physical space. Some of the relations derived are used in the analysis of the results of this report.

This investigation has been performed under contract with the Netherlands Aircraft Development Board. (N.I.V.)

Contents

2 tables
8 figures

List of symbols

a_i	— acceleration vector
c	— velocity of sound
C_m	— def. (A7)
c_n, d_n, e_n, f_n	— def. (2.2.4)
$e_k(S_m)$	— Shanks' transform (3.2.2)
F_i	— external force vector
g_n	— def. (2.3.7)
H	— velocity divergence (2 dim.)

J — det. $(u_{i,j})$
M — Mach number
p — static pressure
q, q_{max} — velocity magnitude; def. (C.2.7)
R_0 — radius of nose curvature
s — velocity parameter, def. (A3)
s, n — arc length along streamline, equi-potential-line
u_i — velocity vector
(u, v) — 2-dim. velocity vector
x_i — position vector
x, y — 2 dim. position vector
z — $x+iy$
α — acceleration angle (C.4.7d)
β — Mach angle
γ — specific heat ratio
δ_{ij} — unit matrix
ε — ellipticity
$\varepsilon_k^{(m)}$ — Wynn's transform def. (3.2.6)
ζ — complex velocity $qe^{-i\theta}$
θ — flow angle
$\left.\begin{matrix}\lambda_n\\ \mu_n\end{matrix}\right\}$ — def. (2.2.4)
ξ, η — arc length along characteristics
$\rho; \rho_0$ — flow density; stagnation value of —
σ — sonic value of s, def. (A3)
τ — $(q/q_{max})^2$
$\tau_{1/\varepsilon}$ — $\left\{\tau : s(\tau) = s_\infty + \log \frac{1}{\varepsilon}\right\}$
Φ, φ — (complex) potential function
ψ — stream function
ψ_n — Chaplygin's function
ω — mass divergence

1 Introduction

This report is to be the first in a series on the general subject of the development of practical computational methods for transonic flow fields. The motivation for this programme is not only in the more direct engineering applications, but also in the fact that in many respects, the problems encountered in the transonic field are of a much more general aerodynamic interest.

More specifically, this report is concerned with the computation of transonic plane potential (shock free) flows. This class of flow fields has been the subject of a long standing discussion as to its mathematical and physical existence. As is well known, examples of transonic potential flows can be constructed by analytical hodograph methods, as have been developed by Cherry (ref. 6), Lighthill (ref. 13) and Bergman, cf. ref. 11. From the mathematical point of view, these solutions have for a long time been suspected to be singular in some sense. This conjecture has been made precise by Morawetz (refs. 18, 19, 20), in a series of papers which have become a standard reference in the field.

The possibility of a physical realization of these flows has always been regarded to be rather questionable, in view of the occurrence of viscous effects (boundary layer separation, shock phenomena). Thus, Morawetz's results are often interpreted to indicate that in the real flow a shock wave, terminating the supersonic region, must be present. However, Pearcey (private communication), cf. ref. 23, has recently conclusively demonstrated that transonic profile flows, exhibiting a to all practical standards shock free supersonic region, can experimentally be realized.

With these two fundamental results as reference points, a considerable part of this report is concerned with matters pertaining to the mathematical and physical interpretation of the practical results obtained.

The actual solutions, which can be obtained by the methods of this report are intended as a basis for comparison with approximate methods in the high subsonic and transonic field, and as a reference base for an experimental programme on the genesis of shock waves in transonic flows.

In the first section, Lighthill's integral operator technique is used to construct a three-parameter family of "quasi-elliptical" aerofoils, representing subsonic and transonic profile flows. These are derived from the incompressible doubly symmetrical flow around an ellipse. This represents analytically a straightforward generalization of the corresponding solution related to the incompressible flow around a circle, solved by Goldstein, Lighthill and Craggs (ref. 9) and Cherry (ref. 6), and numerically worked out by Cherry (ref. 7). The analytical problem has been previously solved by Levey (ref. 12) using Cherry's theory, which report came to the author's attention when the work of this section was nearly completed. The analysis is, using Lighthill's theory, almost completely equivalent. (For a treatment of the subsonic problem on the basis of Bergman's integral operator theory, see ref. 2.)

Five numerically worked out examples are presented, having one or two symmetry axes, depending on the choice of parameters, and showing various interesting properties. The most important fact, however, is that aerofoils can be exhibited within the family, having the geometric features and "peaky pressure distributions" of the sections shown by Pearcey (ref. 23) to be conducive to physically shock free flows. It is suggested that the method presented here could be the basis for a theoretical design method for these sections, which as yet does not exist.

The second section of the report discusses the numerical analysis, which represents the crux of the work.

Numerically, the goal of constructing thin shapes presented a problem of a magnitude completely unsurmountable at the time the analytical methods were developed, and which even now, using automatic computing equipment and sophisticated numerical methods cannot be solved without restrictions on the combinations of parameters representing thickness and asymptotic Mach numbers. The numerical convergence problems have been solved to an appreciable extent by formal application of Wynn's ε-algorithm.

Appendix A contains, for convenient reference, a survey of the main analytical results of Lighthill's work, which is extensively reported upon in the literature (refs. 13, 14, 17).

Appendix B presents a somewhat philosophic contribution to the discussion in the much disputed "transonic controversy". The physical interpretability of the results presented is discussed and some consequences of Morawetz's theorems and Pearcey's experimental results for the design problem in the transonic field are suggested.

Appendix C is a study of some algebraic aspects of the theory of plane potential flows. The conditions, under which the hodograph transformation is feasible, are analysed, exhibiting the significance of the metrical properties and dimensionality of physical space. This leads to a number of invariant relations, which are basic for the local aspects of the theory of this report and are used in the analysis of the results. Many of the results presented are implicit in Busemann's original work on characteristics methods; the discussion has been partly inspired by Birkhoff's study (ref. 14) of group properties in aerodynamics, in particular by his question as to the reason for the linearity of the hodograph equation. Most of the algebraic relations and their physical interpretation have also been given by Reyn (refs. 24, 25) from a slightly different point of view.

The collaboration of M. J. M. G. van Gennip, who has been in charge of the crucial numerical work (ref. 8) for this report, is gratefully acknowledged.

We thank professor dr. E. van Spiegel for a discussion of the material of this report; and professor dr. ir. A. I. van de Vooren for first drawing our attention to the ε-algorithm, which eventually turned out to be the conditio sine qua non in the computational work.

2 Computation of transonic potential flow around a family of quasi-elliptical aerofoils

2.1 *Lighthill's integral operator*

In this section, a three parameter family of transonic potential flows around aerofoils will be constructed, using Lighthill's integral operator technique.

This paragraph presents a discussion of Lighthill's operator in very general terms; for the analytical work reference is made to the original paper (refs. 13, 14) and to the very clear introduction in von Mises' book (ref. 17), where also the connection with Bergman's methods is expounded. A compact survey of the main results of the theory is given in Appendix A, where also the definition of the symbols used in this section can be found.

The hodograph equation is written in the form (cf. Appendix A):

$$\tau(1-\tau)\psi_{\tau\tau} + \frac{1-\dfrac{\gamma+1}{\gamma-1}\tau}{4\tau}\psi_{\theta\theta} = -\left(1+\frac{2-\gamma}{\gamma+1}\tau\right)\psi_\tau \tag{2.1.1}$$

with $\tau = (q/q_{max})^2$, implying use of the isentropic gas law.

The problem is, then, to construct singularities in some solution space of this equation, generating a hodograph manifold of the type required for an aerofoil flow; this is essentially a topological problem. A considerable insight into just these problems lies at the core of the classical theory of functions of a complex variable, and the basic idea in all of the function theoretic methods mentioned is to derive the hodograph of the compressible flow from the analytic function describing an incompressible hodograph of the type required, by a continuous transformation.

In Lighthill's method the basic property of linearity and rotational invariance of solutions of eq.(2.1.1) are used to obtain Chaplygin's particular solutions of the first kind* by separation of variables:

$$\psi_n(\tau)\, e^{\pm\, in\,\theta} \tag{2.1.2}$$

where

$$\psi_n = \tau^{\frac{1}{2}n} F(a_n, b_n, n+1; \tau) \quad \text{for} \quad n \neq -2, -3, \ldots$$

This implies an essential restriction of the solution space of eq. (2.1.1) to functions analytic on the hodograph except for a finite number of isolated singularities.

The fundamental fact in Lighthill's theory is that for subsonic τ, the set of ψ_n's, for n generally complex, can be expressed in a series of the functions ψ_m, for m integral positive, cf. (A8), implying that the Chaplygin particular solutions of positive integral index provide in the subsonic case a base in the restricted space of rotationally invariant analytic solutions of eq. (2.1.1).

Now, when a reference speed q_∞ is chosen (which will be taken equal to unity in this report), the parameter q_{max} (vide Appendix C.2) governs compressibility in the flow. It is then possible to define a continuous limiting process

$$\lim_{q_{max}\to\infty} f(n, \tau_\infty)\,\psi_n(\tau) = (q/q_\infty)^n.$$

* There is a Chaplygin function of the second kind, singular at the origin, cf. Note, par. 2.5.

involving a suitable function $f(n, \tau_\infty)$, giving correspondence between the set (2.1.2) and the particular solutions $\zeta^n = q^n e^{-in\theta}$ in incompressible flow. The decomposition (A8), and the relation (A3a):

$$\lim_{q_{\max}\to\infty} e^{s-s_\infty} = q/q_\infty$$

suggest the feasibility of choosing $f(n, \tau_\infty) \equiv e^{-ns_\infty}$.

The simplest form of integral operator given by Lighthill, valid for circulation free flow fields and defined in the subsonic part of the compressible hodograph reads:

$$\psi = \operatorname{Im}\left\{\sum_{m=0}^{\infty} C_m \psi_m(\tau) e^{m(s_\infty + i\theta)} \int_{\zeta_0}^{e^{s-s_\infty - i\theta}} \zeta^m \,\mathrm{d}\Phi(\zeta)\right\} \tag{2.1.3}$$

where by definition $C_0 = 1$, $C_1 = 0$.

The formal properties of this operator are listed in Appendix A, but a rough indication of its meaning can be given on the basis of the above discussion. The integral part of the operator takes suitable moments of the incompressible hodograph function $\Phi(\zeta)$, involving the subsonic compressible velocity parameter e^{s-s_∞}. These are projected on to the (conjugate) base vectors $\psi_m e^{im\theta}$, this operation involving the weight functions $C_m e^{ms_\infty}$. The parameter s_∞ governs compressibility, and for $s_\infty \to -\infty$ the incompressible hodograph is recovered. The integral in eq. (2.1.3) depends in principle on the path chosen in the incompressible hodograph manifold, but should be single valued at least in the hodograph image of the external flow field of the transformed profile. Inspection of the example given in the next section will clarify the way in which the topology of the hodograph manifold depends on the conditions at infinity in physical space for a circulation free incompressible flow. In this case the operator form (2.1.3), involving the particularly simple function $f(n, \tau_\infty) \equiv e^{-ns_\infty}$ to control the continuous transformation, can be shown to be single valued. The significance of the operator will become more obvious in par. 2.2. where it will be developed in series form.

The case of circulatory flow, also given by Lighthill, is of course much more complicated.

2.2 *Hodograph of the symmetrical, incompressible flow around an ellipse*

The complex potential $\Phi(\zeta)$ associated with the incompressible circulation free flow around an ellipse of excentricity ε is found from that for the circle by Zhukovskii's transformation:

$$\Phi(z) = z_1 + \frac{1}{z_1} \tag{2.2.1a}$$

$$z = z_1 + \frac{\varepsilon}{z_1} \tag{2.2.1b}$$

Eliminating z_1 between (2.2.1) and the complex velocity

$$\zeta = \frac{\mathrm{d}\Phi}{\mathrm{d}z} = \frac{\mathrm{d}\Phi}{\mathrm{d}z_1}\frac{\mathrm{d}z_1}{\mathrm{d}z} = \frac{z_1^2 - 1}{z_1^2 - \varepsilon} \tag{2.2.2}$$

the hodograph flow is obtained

$$\Phi(\zeta) = \left(\frac{1-\varepsilon\zeta}{1-\zeta}\right)^{\frac{1}{2}} + \left(\frac{1-\zeta}{1-\varepsilon\zeta}\right)^{\frac{1}{2}}. \tag{2.2.3}$$

The pair (2.2.1), (2.2.3) defines the hodograph transformation, which is obviously conformal in the incompressible case. The physical and hodograph manifolds are sketched in fig. 1, which may clarify the way in which the topology of these manifolds is generated by the singularities of the analytic functions describing the flows. One notes, that circles around the origin in the z_1-plane, including the boundary streamline, are mapped on double traversed circles in the hodograph manifold (2.2.2), the circle $|z_1| = \varepsilon$ degenerating.

The mapping $\zeta \to \dfrac{\zeta}{(1+\varepsilon)\zeta - 1}$ expresses the symmetry with respect to the circle $|z_1| = \varepsilon$, between the "physical plane" and the "generating flow" situated in the second sheet of the Riemann surface. Together, the two sheets make up the complete "physical manifold".

Furthermore, fig. 1 indicates how curves of constant speed and flow angle (the analytic function $\log\zeta = \log q + i\theta$) are generated in the physical plane by the stagnation points and the singularities at the focal points of the ellipse. The latter map on the infinite point of the hodograph.

Now, writing down series expansions of (2.2.3) valid for $|\zeta| < 1$, $1 < |\zeta| < \frac{1}{\varepsilon}$ and $|\zeta| > \frac{1}{\varepsilon}$ respectively, one obtains:

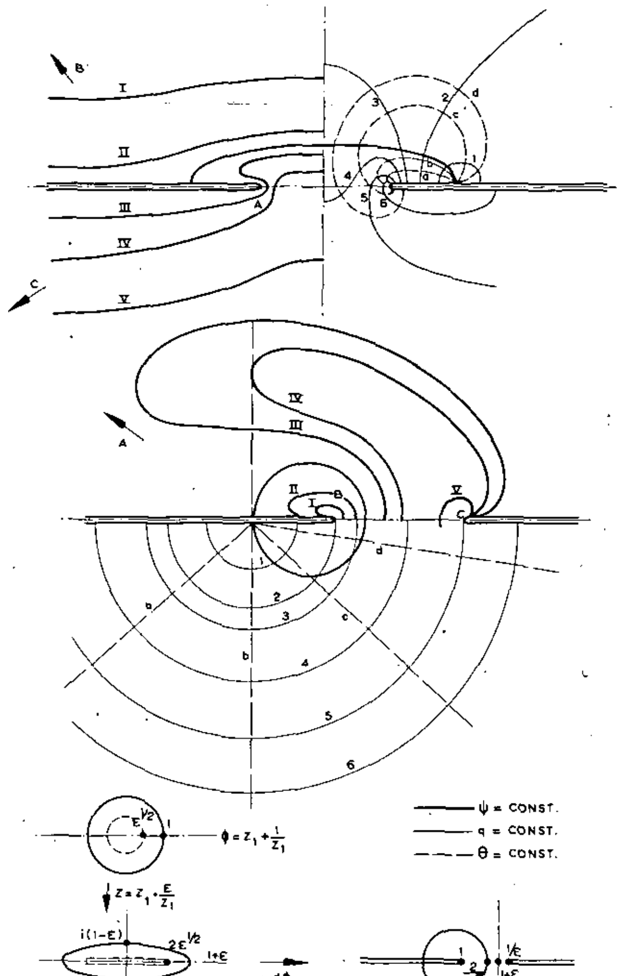

Fig. 1. Physical and hodograph manifold for incompressible symmetrical flow around an ellipse.

for $|\zeta| < 1$

$$\Phi(\zeta) = \sum_{n=0}^{\infty} c_n \zeta^n \tag{2.2.4a}$$

$$c_n = 2\lambda_n - (1+\varepsilon)\lambda_{n-1}$$

$$c_0 = 2$$

$$\lambda_n = \frac{(n-\frac{1}{2})!}{n!\sqrt{\pi}} F(\tfrac{1}{2}, -n, \tfrac{1}{2}-n; \varepsilon)$$

for $1 < |\zeta| < \dfrac{1}{\varepsilon}$

$$\Phi(\zeta) = i \sum_{n=0}^{\infty} (d_n \varepsilon^n \zeta^{n+\frac{1}{2}} + e_n \zeta^{-n-\frac{1}{2}}) \tag{2.2.4b}$$

$$d_n = 2\varepsilon\mu_{n+1} - (1+\varepsilon)\mu_n$$

$$e_n = 2\mu_n - (1+\varepsilon)\mu_{n+1}$$

$$\mu_n = \frac{(n-\frac{1}{2})!}{n!\sqrt{\pi}} F(\tfrac{1}{2}, n+\tfrac{1}{2}, n+1, \varepsilon)$$

for $|\zeta| > \dfrac{1}{\varepsilon}$

$$\Phi(\zeta) = -\sum_{n=0}^{\infty} f_n \varepsilon^{-n-\frac{1}{2}} \zeta^{-n} \tag{2.2.4c}$$

$$f_n = 2\varepsilon\lambda_{n-1} - (1+\varepsilon)\lambda_n$$

$$f_0 = -(1+\varepsilon)$$

where F denotes the ordinary hypergeometric function (λ_n is a nth degree polynomial).

Both hypergeometric functions can be shown to be $(1-\varepsilon)^{-\frac{1}{2}}\left\{1+0\left(\frac{1}{n}\right)\right\}$ for $|\varepsilon| \leqq 1-\delta$ by transformation to Steiner's form, the associated series having the required asymptotic properties. This observation verifies the regions of convergence as stated.

2.3 *Construction of compressible solutions*

Following Lighthill, series solutions of (2.1.1), representing the compressible hodograph flow, can now be derived from (2.2.4), using the operator (2.1.3). These series immediately provide the analytic continuation of the solution into the supersonic region $|\zeta| > e^{\sigma - s_\infty}$.

Referring to fig. 2a, in region I the series (2.2.4a) can be inserted into the operator, and, performing the integration, one obtains:

$$\psi = \operatorname{Im} \sum_{m=0}^{\infty} C_m \psi_m e^{m(s_\infty + i\theta)} \sum_{n=0}^{\infty} \frac{nc_n}{m+n} e^{(n+m)(s-s_\infty - i\theta)}$$

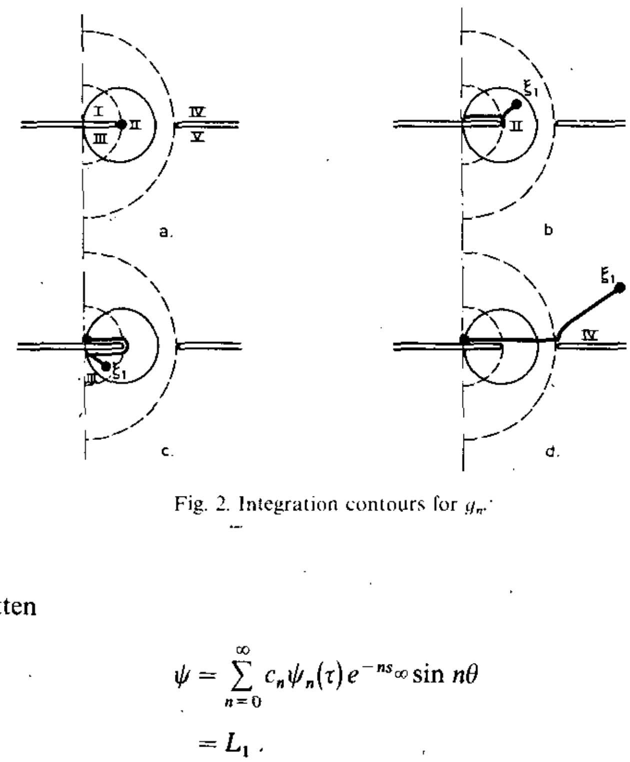

Fig. 2. Integration contours for g_n.

Using (A8), this can be written

$$\psi = \sum_{n=0}^{\infty} c_n \psi_n(\tau) e^{-ns_\infty} \sin n\theta \tag{2.3.1}$$

$$= L_1 .$$

To continue this solution into region II, an arbitrary fixed parameter point ζ_1 is chosen in II, subject to the condition $|\zeta_1| < e^{\sigma - s_\infty}$. Writing symbolically

$$\Phi(\zeta) = \sum d_{n'} \zeta^{n'}$$

as a shorthand for the expression (2.2.4b), it follows:

$$\psi = \operatorname{Im} \sum_{m=0}^{\infty} C_m \psi_m e^{m(s_\infty + i\theta)} \left[\int_0^{\zeta_1} \zeta^m \, \mathrm{d}\Phi(\zeta) + \sum \frac{n' d_{n'}}{m+n'} \left(e^{(n'+m)(s-s_\infty - i\theta)} - \zeta_1^{n'+m}\right) \right]. \tag{2.3.2}$$

Evaluating the integral along a path shown in fig. 2b, circumventing the point $\zeta = 1$ with a circle of radius δ, it follows, using one partial integration:

$$\int_0^{\zeta_1} \zeta^m \, \mathrm{d}\Phi = \zeta^m \Phi \Big|_0^{\zeta_1} - m \int_0^{1-\delta} \Phi \zeta^{m-1} \, \mathrm{d}\zeta - m \int_{1-\delta}^{1+\delta} \Phi \zeta^{m-1} \, \mathrm{d}\zeta - m \int_{1+\delta}^{\zeta_1} \Phi \zeta^{m-1} \, \mathrm{d}\zeta \tag{2.3.3}$$

Now, for $\delta \to 0$ the third term vanishes, and the fourth at the lower bound. Collecting terms in ζ_1 from (2.3.3), these cancel those in the series in (2.3.2) as they should; and only the second term in (2.3.3) remains. This can be written, using (2.2.3) and the integral representation for the hypergeometric function (ref. 10, p. 196):

$$g_n = -\frac{\sqrt{\pi}(n+1)!}{(n+\frac{1}{2})!} F\left(-\tfrac{1}{2}, n, n+\tfrac{3}{2}; \varepsilon\right).$$

Then, in II

$$\psi = \sum_{n=0}^{\infty} \left\{ d_n \varepsilon^n \psi_{n+\frac{1}{2}}(\tau) e^{-(n+\frac{1}{2})s_\infty} + e_n \psi_{-n-\frac{1}{2}}(\tau) e^{(n+\frac{1}{2})s_\infty} \right\} \cos(n+\tfrac{1}{2})\theta - \sum_{n=0}^{\infty} g_n C_n e^{ns_\infty} \psi_n(\tau) \sin n\theta \tag{2.3.4}$$

$$= L_2 - G_2 .$$

L_2 obviously represents the direct counterpart of the incompressible series (2.2.4b), the series G_2 is induced by the operator to give analytic continuity of the compressible hodograph.

Similarly, in region III, the point ζ_1 is chosen in this region, and the solution is written

$$\psi = L_3 - G_3 \tag{2.3.5}$$

The integration contours chosen as shown (fig. 2c), it follows immediately by symmetry:

$$\begin{aligned} L_3 &= -L_1 \\ G_3 &= 2G_2 . \end{aligned} \tag{2.3.6}$$

Continuing in the lower sheet of the hodograph manifold, the symmetrical solution is obtained.

Now considering convergence of these series, their d'Alembert ratio $\mu = \lim_{n\to\infty} |t_{n+1}/t_n|$ can be estimated using the asymptotic expansions (A7a), (A9) and (A11). For L_1: $\mu = e^{s-s_\infty}$ and for the two series constituting L_2: $\mu = \varepsilon e^{s-s_\infty} < \varepsilon e^{\sigma - s_\infty}$ and $\mu = e^{-s+s_\infty} < e^{-\sigma+s_\infty}$ respectively. It follows that L_1 converges absolutely for $0 < \tau < \tau_\infty$ and L_2 for $\tau_\infty < \tau < \tau_{1/\varepsilon}$ (where $\tau_{1/\varepsilon}$ is implicitly defined as $\{\tau : s(\tau) = s_\infty - \log \varepsilon\}$) when $\frac{1}{\varepsilon} < e^{\sigma - s_\infty}$; when this last inequality is reversed L_2 converges for $\tau > \tau_\infty$, including the supersonic region. On the other hand for G_2 $\mu < e^{s_\infty - \sigma}$, and thus G_2 converges on the whole hodograph disc $0 \leq \tau < 1$.

By linearity then, a multiple of the solution G may be added, thus obtaining a 3-parameter family of solutions of (2.1.1), with continuous parameters $\tau_\infty = \frac{1}{q^2_{max}}$, ε and λ, reducing to the incompressible flow around an ellipse for $q_{max} \to \infty$.

Summarizing, one obtains

$$\begin{aligned} \psi &= L_1 - (\lambda - 1)G \quad \text{in I} \\ &= L_2 - \lambda G \quad\quad\;\; \text{in II} \\ &= -L_1 - (\lambda + 1)G \quad \text{in III} \end{aligned} \tag{2.3.7}$$

$$L_1 = \sum_{n=0}^{\infty} c_n \psi_n(\tau) e^{-ns_\infty} \sin n\theta$$

$$L_2 = \sum_{n=0}^{\infty} \{ d_n \varepsilon^n \psi_{n+\frac{1}{2}}(\tau) e^{-(n+\frac{1}{2})s_\infty} + e_n \psi_{-n-\frac{1}{2}}(\tau) e^{(n+\frac{1}{2})s_\infty} \} \cos(n+\tfrac{1}{2})\theta$$

$$G = \sum_{n=0}^{\infty} g_n C_n e^{ns_\infty} \psi_n(\tau) \sin n\theta$$

$$g_n = -\frac{\sqrt{\pi}(n+1)!}{(n+\frac{1}{2})!} F(-\tfrac{1}{2}, n, n+\tfrac{3}{2}; \varepsilon)$$

c_n, d_n, e_n given by (2.2.4)

C_n, s_∞ defined by (A7), (A3).

The family has in general a horizontal symmetry axis only, a doubly symmetrical aerofoil is obtained by choosing $\lambda = 0$.

2.4 *Transformation into the physical plane*

The transformation of (2.3.7) into the physical plane is obtained from the definition of potential and streamfunction:

$$dz = \frac{e^{i\theta}}{q} \left(d\varphi + \frac{i}{\rho} d\psi \right).$$

Differentiating and using Chaplygin's equation (A2a):

$$z_\theta = \frac{e^{i\theta}}{\rho q} (q\psi_q + i\psi_\theta)$$

$$z_q = \frac{e^{i\theta}}{\rho q}\left(-\frac{1-M^2}{q}\psi_0 + i\psi_q\right).$$

Now, when (2.3.7) is represented by

$$\psi = \sum_n A_n \psi_n \sin\left(n\theta + \mu\frac{\pi}{2}\right) \qquad \mu=0.1$$

by integration it is found, using (AI):

$$z = x+iy = \tfrac{1}{2}\left(\frac{\tau_0}{\tau}\right)^{\frac{1}{2}} \frac{2\tau}{(1-\tau)^{\frac{1}{\gamma-1}}} \sum_n A_n \left[\frac{e^{i\{(n+1)\theta+\mu\frac{\pi}{2}\}}}{n+1}\left(\frac{n}{2\tau}\psi_n - \psi_n'\right) - \frac{e^{i\{(1-n)\theta+\mu\frac{\pi}{2}\}}}{n-1}\left(\frac{n}{2\tau}\psi_n + \psi_n'\right)\right]$$

where

$$\psi_n' = \frac{d\psi_n}{d\tau}.$$

2.5 *Note*

It is illustrative for the technique of Lighthill's continuation process to consider what happens to the part $|\zeta| > \frac{1}{\varepsilon}$ of the incompressible hodograph plane under the transformation. For the present work, this is only of academic interest; however, as pointed out by Levey (ref. 12), when complex values for ε are taken to obtain the circulation free flow around an ellipse with incidence, part of the external flow field may be described by this continuation.

The incompressible series (2.2.4c) has negative integral exponents; in this case it is necessary to use a second solution ψ_n, involving logarithmic terms, defined for n an integer $\geqq 2$. This independent solution has been defined by Lighthill to be:

$$\psi_n^*(\tau) = \lim_{\nu\to -n}\left(\psi_\nu - \frac{\nu C_n \psi_{-\nu}}{\nu+n}\right). \tag{2.5.1}$$

For the formal details of Lighthill's technique in this case, reference is made to the original paper, the results only being given below. A more immediate interpretation of the analytical situation is obtained by working out the "Barnes contour integral representation" for the operator (2.1.3) corresponding to the series (2.2.4), cf. ref. 9. This leads to the equivalent result in a somewhat different form. This technique will be amply demonstrated for the circulatory flow case to be studied in a following report.

Using the present formalism, the analysis is similar to that in the foregoing cases, however, one has to consider a contribution of the lower bound at $\zeta = \frac{1}{\varepsilon}$ of the integral corresponding to the fourth term in (2.3.3), when integrating along the contour shown in fig. 2d. It follows:

$$\begin{aligned} &\text{in IV} \qquad \psi = L_4 + H - (\lambda-1)\,G \\ &\text{in V} \qquad \psi = -L_4 - H - (\lambda+1)\,G \end{aligned} \tag{2.5.2}$$

$$L_4 = -\operatorname{Im}\sum_{n=0}^{\infty} f_n \varepsilon^{-n-\frac{1}{2}}\left[\psi_n^* e^{n(s_\infty+i\theta)} + nC_n\frac{d}{dn}\{\psi_n e^{n(s_\infty+i\theta)}\}\right]$$

$$H = -\operatorname{Im}\sum_{n=2}^{\infty} h_n C_n \psi_n e^{n(s_\infty+i\theta)}$$

where

$$h_n = n\varepsilon^{-n-\frac{1}{2}}\sum_{m=0}^{n-1} + \sum_{m=n+1}^{\infty}\frac{f_m}{n-m} + \varepsilon^{-n-\frac{1}{2}} f_n\left(1+n\log\frac{1}{\varepsilon}\right) + \frac{\sqrt{\pi}(n+1)!}{(n+\frac{1}{2})!\,\varepsilon^n}\,F\left(-\tfrac{1}{2}, n, n+\tfrac{3}{2}; \frac{1}{\varepsilon}\right)$$

and by definition,

$$C_0 = 1 \qquad \psi_0^* = 1$$
$$C_1 = 0 \qquad \psi_1^* = \psi_{-1}$$

Again, using Lighthill's asymptotic estimate for ψ_m^* it follows that L_4 converges for $\tau > \tau_{1/\varepsilon}$ when $\frac{1}{\varepsilon} < e^{\sigma - s_\infty}$ and the series H converges on the whole hodograph.

These series define implicitly the "internal generating singularities" as analytic continuations of the external compressible flow field, for $\tau = 1$ and $\tau = \tau_{1/\varepsilon}$. The incompressible physical and hodograph manifolds can be closed by addition of the points at infinity, this property is lost by the finite compressible hodograph obtained by the transformation: This fact gives the possibility of defining solutions representing profiles without fore and aft symmetry, associated with a doubly symmetrical incompressible generating flow.

2.6 *Discussion of results*

2.6.1 The series (2.3.7), (2.4.1) have been evaluated for a number of combinations (τ_∞, ε, λ), to give closed profiles with a neighbourhood of the field in the physical plane.

When transonic flows around thin shapes are aimed for, convergence of the series becomes very slow, especially on the circle $|\zeta| = 1$ and in the high speed regions of the flow field. These difficulties have been partly overcome through the use of a numerical scheme described in detail in section 3; one is left, however, with a rather severe restriction on the possible combinations of τ_∞ and ε for the flow fields that can be fully worked out.

This restriction depends on the number of significant figures available in the computation of the Chaplygin functions ψ_n, and in the present case it turned out that profilesin the range up to $t/c \sim 0.15$–0.20 exhibiting a local maximum speed of approximately $\tau = 0.18$ ($M \sim 1.1$) could be computed.

To prevent overcrowding this report by a deluge of tabulatory material, only tables for co-ordinates and velocity distribution along the profiles, which have been interpolated from the results, are given in table 1. All points

TABLE 1. NUMERICAL PROFILE DATA

TABLE 1A

$M_\infty = 0.673$ $\tau_\infty = 0.083$
$\varepsilon = 0.6$ $\lambda = 0$

x	y	M	θ
−1.562	0.021	0.319	0.744
−1.547	0.034	0.393	0.680
−1.527	0.049	0.456	0.623
−1.502	0.066	0.513	0.571
−1.474	0.083	0.565	0.521
−1.437	0.103	0.613	0.476
−1.393	0.125	0.659	0.431
−1.381	0.130	0.673	0.418
−1.342	0.147	0.703	0.386
−1.276	0.174	0.745	0.343
−1.203	0.196	0.786	0.302
−1.108	0.223	0.826	0.260
−0.991	0.251	0.864	0.217
−0.839	0.281	0.902	0.171
−0.629	0.312	0.939	0.120
−0.216	0.343	0.976	0.038

TABLE 1B

$\tau_\infty = 0.09$ $M_\infty = 0.704$
$\varepsilon = 0.6$ $\lambda = 0$

x	y	M	θ
−1.578	0.006	0.225	0.724
−1.567	0.016	0.319	0.690
−1.552	0.028	0.393	0.645
−1.533	0.041	0.456	0.598
−1.510	0.056	0.513	0.555
−1.483	0.072	0.565	0.512
−1.450	0.090	0.613	0.471
−1.411	0.109	0.659	0.432
−1.311	0.151	0.745	0.354
−1.253	0.169	0.786	0.321
−1.175	0.195	0.826	0.278
−1.092	0.216	0.864	0.245
−0.991	0.239	0.902	0.210
−0.869	0.263	0.939	0.171
−0.720	0.286	0.976	0.133
−0.595	0.301	1.000	0.104
−0.514	0.308	1.012	0.088
−0.338	0.321	1.030	0.055
−0.105	0.329	1.041	0.016

TABLE 1C

$\tau_\infty = 0.10$ $M_\infty = 0.745$
$\varepsilon = 0.7$ $\lambda = 0$

x	y	M	θ
−1.690	0.001	0.319	0.241
−1.684	0.002	0.351	0.315
−1.675	0.006	0.393	0.362
−1.635	0.022	0.513	0.390
−1.574	0.046	0.613	0.354
−1.431	0.093	0.745	0.273
−1.361	0.113	0.786	0.241
−1.277	0.132	0.826	0.210
−1.180	0.150	0.864	0.186
−0.888	0.195	0.939	0.121
−0.658	0.218	0.976	0.082
−0.386	0.235	1.000	0.044
−0.099	0.243	1.012	0.011

TABLE 1D

$\tau_\infty = 0.09$ $\quad M_\infty = 0.704$

$\varepsilon = 0.6$ $\quad \lambda = 1$

x	y	M	θ
−1.587	0.000	0.000	$\pi/2$
−1.575	0.051	0.319	1.1402
−1.560	0.077	0.456	0.957
−1.541	0.100	0.565	0.814
−1.516	0.123	0.659	0.676
−1.501	0.135	0.703	0.629
−1.463	0.160	0.786	0.532
−1.439	0.173	0.826	0.484
−1.411	0.187	0.864	0.436
−1.379	0.201	0.902	0.401
−1.340	0.217	0.939	0.346
−1.296	0.232	0.976	0.303
−1.262	0.242	1.000	0.274
−1.133	0.272	1.065	0.190
−1.061	0.284	1.083	0.156
−0.768	0.315	1.083	0.070
−0.581	0.326	1.065	0.035
−0.057	0.322	1.000	−0.049
0.109	0.312	0.976	−0.074
0.336	0.291	0.939	−0.110
0.535	0.265	0.902	−0.144
0.708	0.238	0.864	−0.176
0.856	0.209	0.826	−0.208
0.983	0.180	0.786	−0.238
1.261	0.102	0.659	−0.323
1.387	0.056	0.565	−0.366
1.474	0.022	0.456	−0.380
1.506	0.009	0.393	−0.349
1.521	0.004	0.358	−0.305
1.533	0.001	0.319	−0.206
1.540	0.000	0.276	−0.000

TABLE 1E

$\tau_\infty = 0.08$ $\quad M_\infty = 0.659$

$\varepsilon = 0.6$ $\quad \lambda = 2$

x	y	M	θ
−1.581	0.000	0.000	$\pi/2$
−1.573	0.069	0.225	1.346
−1.565	0.097	0.319	1.253
−1.551	0.133	0.456	1.122
−1.537	0.158	0.565	1.023
−1.525	0.176	0.659	0.940
−1.514	0.190	0.745	0.868
−1.504	0.201	0.826	0.804
−1.499	0.206	0.864	0.773
−1.495	0.210	0.902	0.742
−1.491	0.214	0.939	0.713
−1.487	0.217	0.976	0.684
−1.483	0.220	1.012	0.655
−1.479	0.223	1.048	0.624
−1.474	0.227	1.083	0.591
−1.468	0.231	1.118	0.552
−1.464	0.232	1.118	0.543
−1.327	0.277	1.083	0.313
−1.151	0.318	1.048	0.144
−0.983	0.340	1.012	0.083
−0.752	0.353	0.976	0.028
−0.459	0.352	0.939	−0.019
−0.136	0.338	0.902	−0.067
0.166	0.311	0.864	−0.112
0.427	0.276	0.826	−0.152
0.839	0.197	0.745	−0.231
1.193	0.102	0.613	−0.304
1.287	0.070	0.565	−0.333
1.415	0.025	0.456	−0.342
1.500	0.000	0.319	0.000

computed have been drawn in into the figures 3a through 3e, corresponding to the following combinations of parameters

fig.	τ_∞	ε	λ	M_∞	M_{max}	$\frac{1-\varepsilon}{1+\varepsilon}$	t/c
3a	0.083	0.6	0	0.673	0.983	0.250	0.217
b	0.090	0.6	0	0.704	1.046	0.250	0.208
c	0.100	0.7	0	0.745	1.012	0.176	0.141
d	0.090	0.6	1	0.704	1.090	0.250	0.212
e	0.080	0.6	2	0.659	1.118	0.250	0.230

Hodographs of the boundary streamlines are given for the last three cases in fig. 4.

2.6.2 The most striking phenomenon exhibited by the examples computed is the considerable sharpening of the profile ends by addition of series G and the corresponding blunting under substraction. This means, that when λ is chosen >0 and τ_∞ sufficiently high, profiles are obtained having a rounded leading edge, and a cusped trailing edge.

An analysis of this phenomenon provides an application of the relations obtained in Appendix C.

From C.4.6 and C.4.7a it follows:

$$\theta_s^2 = \frac{1}{R^2} = \frac{-J}{\{1+(1-M^2)\operatorname{cotg}^2\alpha\}q^2}$$

In hodograph plane variables one has

$$\operatorname{tg}\alpha = \left.\frac{-2\tau\psi_\tau}{\psi_\theta}\right|_{\psi=c}$$

$$J = \frac{-\rho^2\tau^2}{4\tau^2\psi_\tau^2+(1-M^2)\psi_\theta^2}\cdot\frac{1}{\tau_\infty^2}.$$

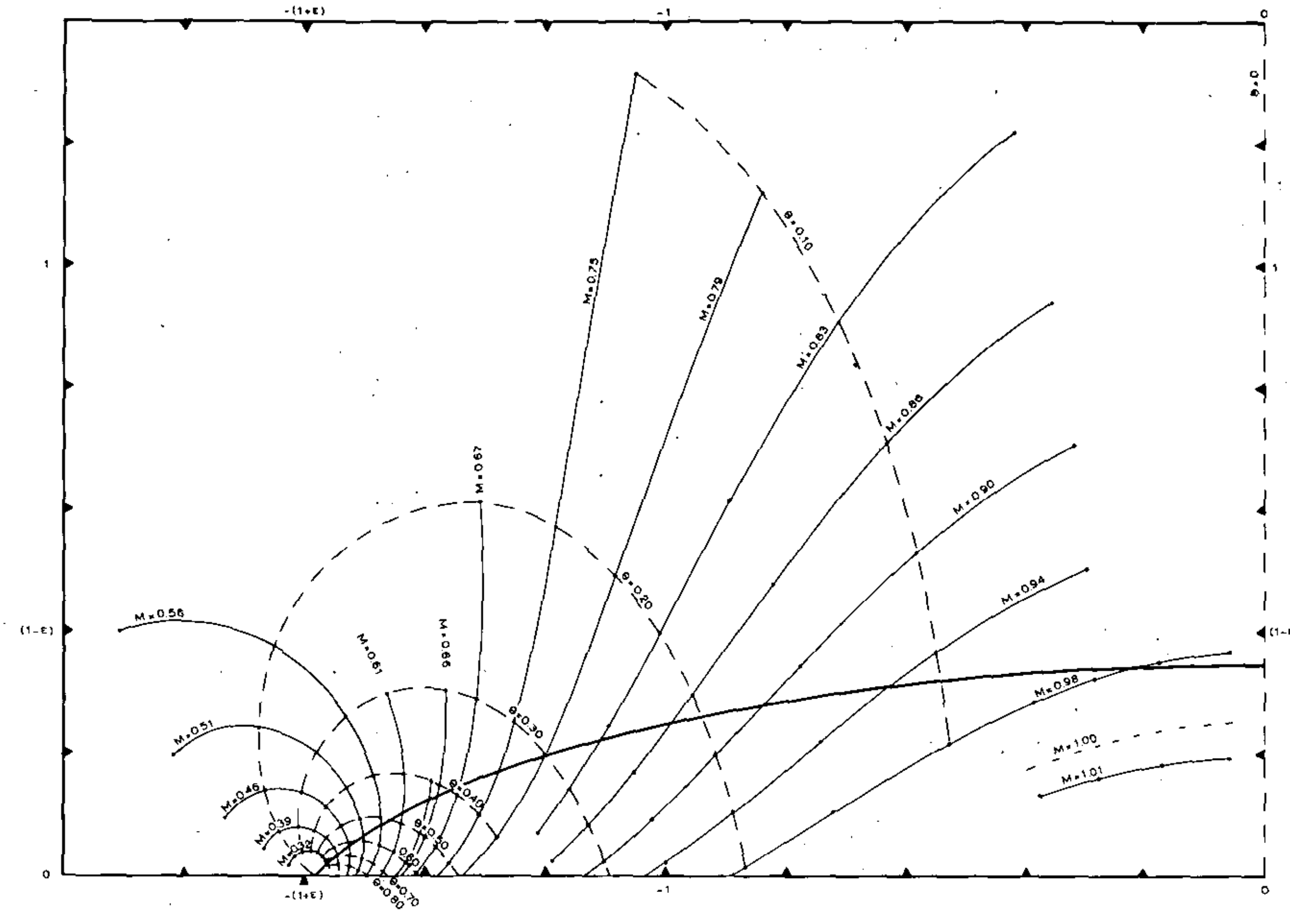

Fig. 3a. Transonic potential flow around quasi-ellipse $M_\infty = 0.673$; $\varepsilon = 0.6$; $\lambda = 0$.

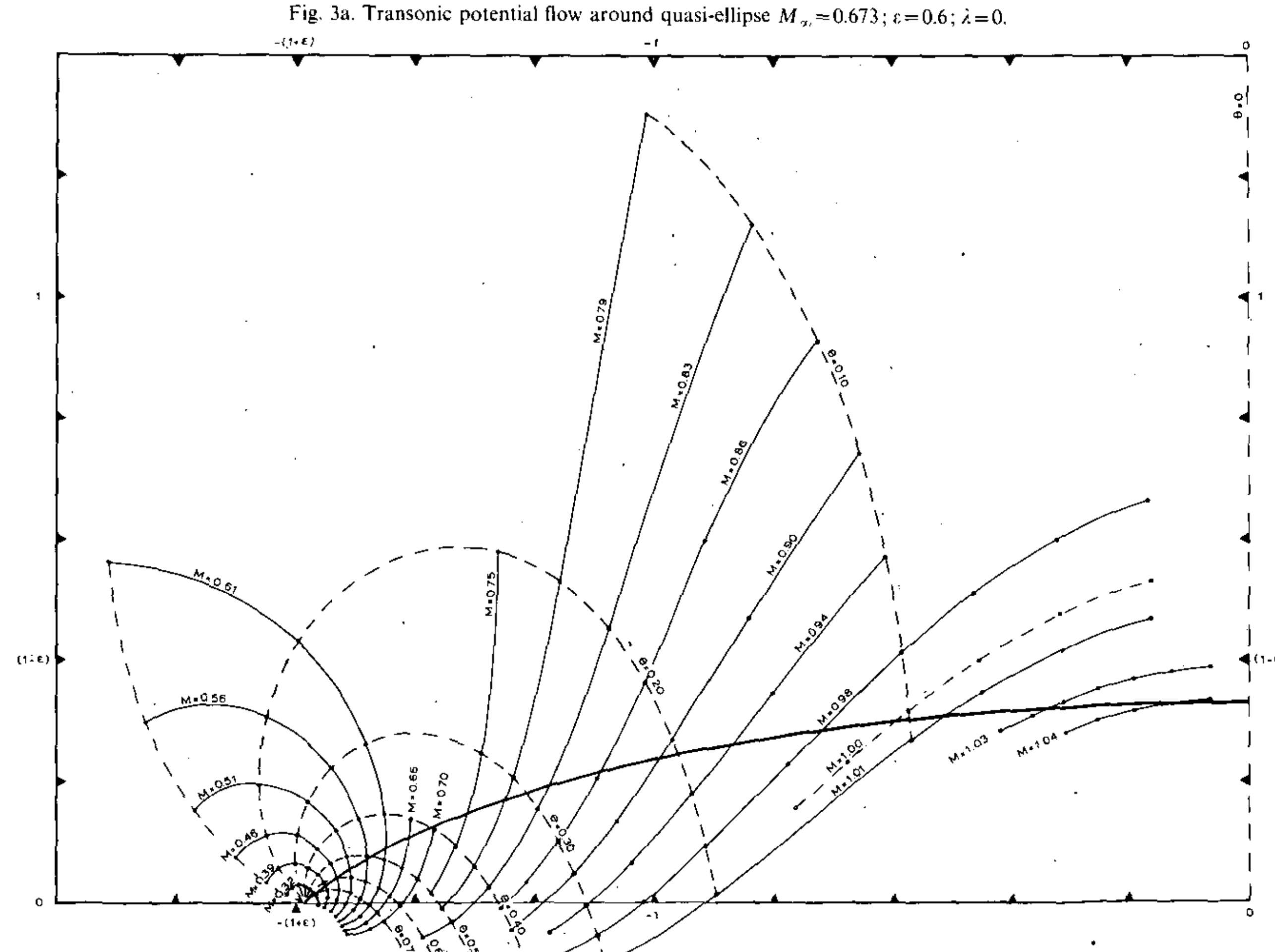

Fig. 3b. Transonic potential flow around quasi-ellipse $M_\infty = 0.704$; $\varepsilon = 0.6$; $\lambda = 0$.

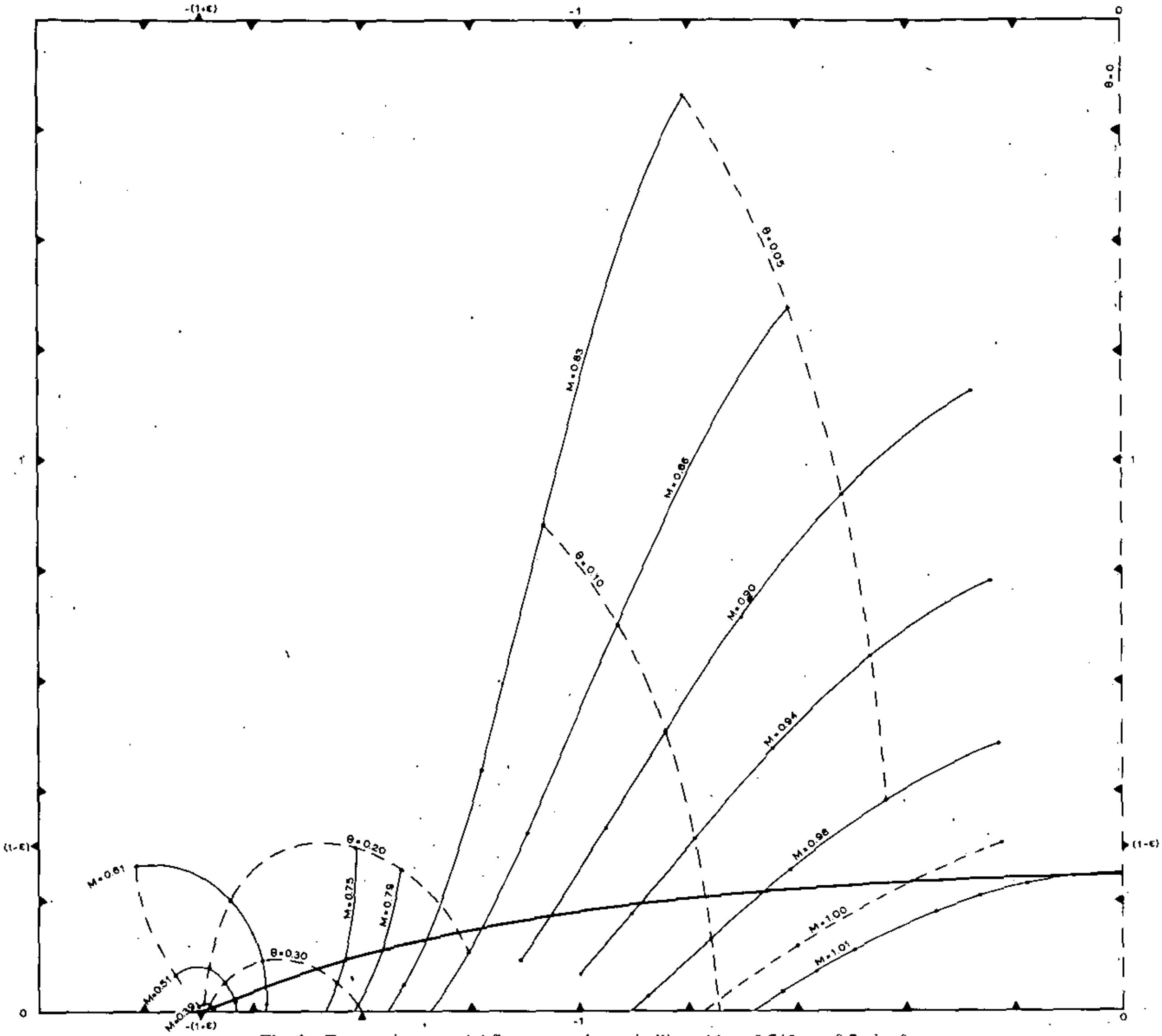

Fig. 3c. Transonic potential flow around quasi-ellipse $M_{\infty}=0.745$; $\varepsilon=0.7$; $\lambda=0$.

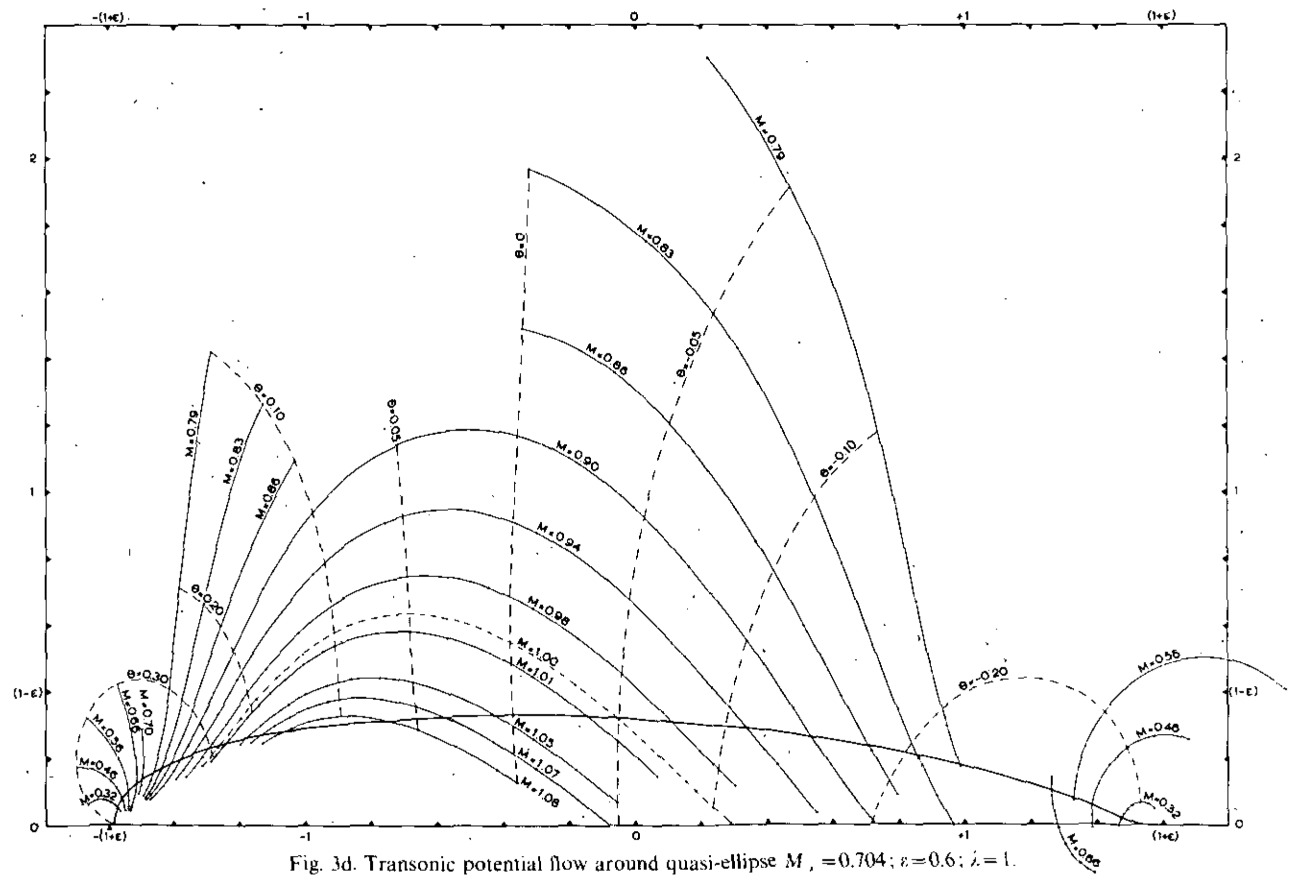

Fig. 3d. Transonic potential flow around quasi-ellipse $M_{\infty}=0.704$; $\varepsilon=0.6$; $\lambda=1$.

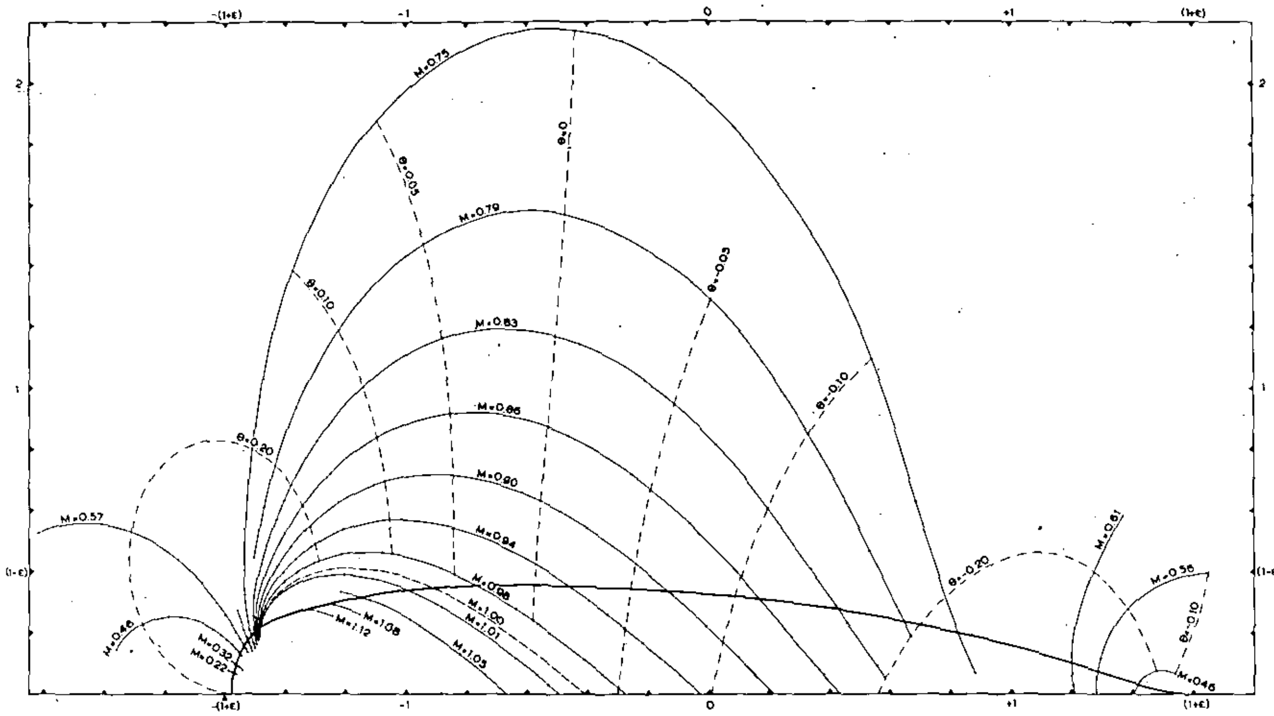

Fig. 3e. Transonic potential flow around quasi-ellipse $M_\infty = 0.659$; $\varepsilon = 0.6$; $\lambda = 2$.

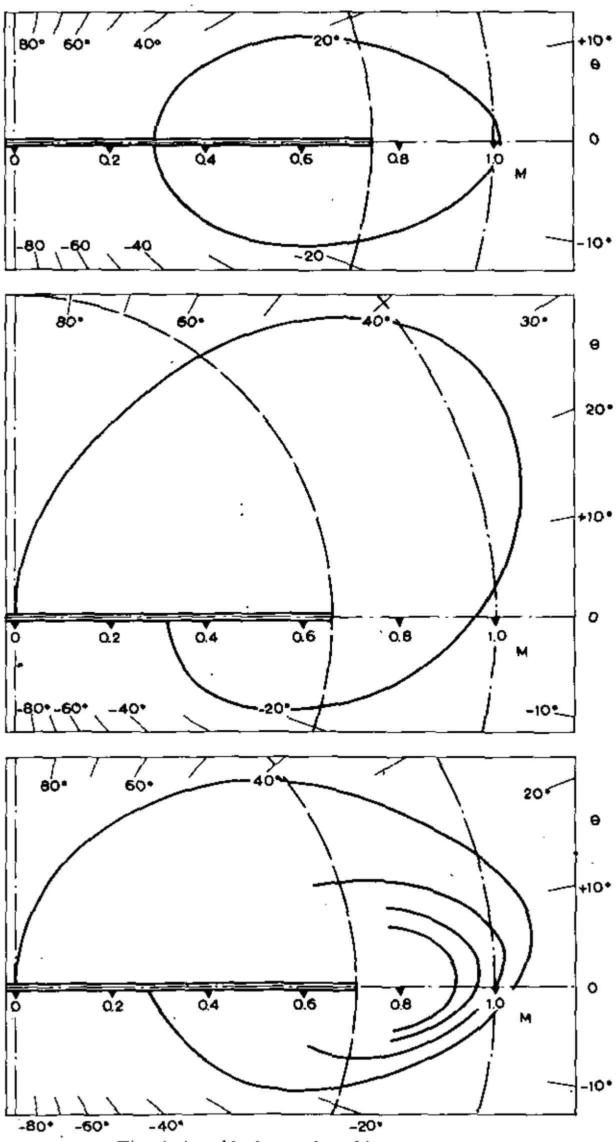

Fig. 4a,b,c. Hodographs of body contours.

where, as in previous results, q_∞ has been chosen equal to unity. At a front stagnation point the first of the series (2.3.7) should be used for

$$\tau=0, \quad \theta=\frac{\pi}{2}, \quad \psi=0 \quad \text{and it follows}$$

$$\frac{1}{R_0} = -\frac{c_3 e^{-3s_\infty} - (\lambda-1) g_3 C_3 e^{3s_\infty}}{4\{c_2 e^{-2s_\infty} - (\lambda-1) g_2 C_2 e^{2s_\infty}\}^2} \cdot \frac{1}{\sqrt{\tau_\infty}} \tag{2.6.1}$$

As $c_2=\frac{1}{4}(1-\varepsilon)^2$; $c_3=\frac{1}{4}(1+\varepsilon)(1-\varepsilon)^2$, this reduces to the value

$$\frac{1}{R_0} = -\frac{1+\varepsilon}{(1-\varepsilon)^2}$$

in incompressible flow. (At a rear stagnation point, use $\lambda^* = -\lambda$ and the opposite sign).

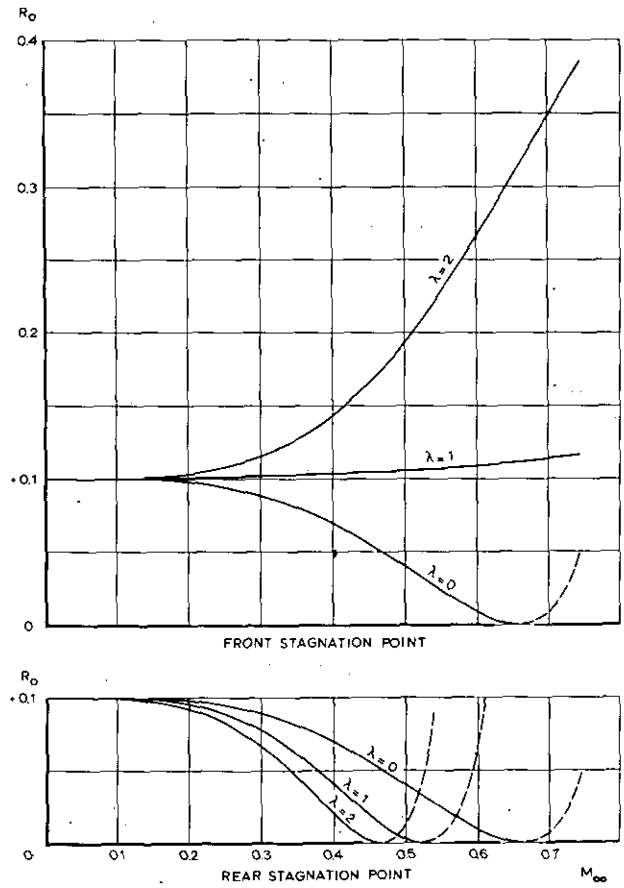

Fig. 5 a,b. Radius of nose curvature $\varepsilon=0.6$.

A graph of R_0 as a function of $M_\infty(\equiv\tau_\infty)$ is presented for $\begin{cases}\varepsilon=0,6\\ \lambda=0,1,2\end{cases}$ in fig. 5.

Starting from the incompressible value, for $\lambda>0$ $\dfrac{1}{R_0}$ increases to infinity corresponding to a zero in the denominator in (2.6.1), for a certain value of M_∞. From this point on, the stagnation point is "pushed" by the G-series into the sheet of the physical manifold forming the analytic continuation of the interior of the body, leaving a cusped profile. (cf. the hodographs fig. 4). This phenomenon is exhibited by all of the examples computed, detailed illustrations of the cusps for two cases are given in figs. 7a, 7b.

A remark should be made on the (relative) unit of length the expression (2.6.1) refers to. The lengths of the major and minor semi-axes of the incompressible ellipse are $1+\varepsilon$ and $1-\varepsilon$ respectively. The corresponding lengths in the compressible physical plane are found as a result of the integration process, and no explicit expressions exist for them. The examples computed show, that the profile chord does not differ much from the value $2(1+\varepsilon)$, the discrepancies becoming larger when a cusp is present at one or both profile ends. The reduction in the resulting profile thickness as compared with the value $2(1-\varepsilon)$ can become appreciable with increasing M_∞.

2.6.3 All of the examples computed are continuous solutions in the physical plane, i.e. no limit lines occur in the external flow field (cf. Appendix C 4,5).

For the cases presented in figs. 3d, 3e, the graphs of the quantities q_s, θ_s and J versus arc length parameter along the profile contour are given in figs. 6a, b. It should be remarked, that these curves have been obtained by numerically differentiating and smoothing interpolated data, and thus have not much more than qualitative significance.

For the profile fig. 3d, J does not show any tendency towards large values in the supersonic region; however, the behaviour of J for the more asymmetric profile fig. 3e suggests the presence of the cusp of a limit line in the interior of the profile quite near the contour. The limit line, in Reyn's terminology (ref. 26), "generates" the strong expansion over the nose, the profile contour exhibiting very nearly a curvature discontinuity there. Further increasing λ and/or τ_∞ would lead to a point of infinite curvature on the profile, i.e. a discontinuous junction of a blunt nose into a weakly curved profile. For still higher values of the parameters no physical profile would be defined, as the limit line would pierce into the external flow field. (A brief discussion of the "limit lines" is presented in Appendix C5).

By manipulating λ, clearly a family of profiles exhibiting rapid expansions of varying strength over the nose region followed by gradual recompression, may be generated; a point of fundamental interest in connection with the design problem for profiles having a "peaky pressure distribution" (ref. 23, par. 7 ff; Appendix B 3, 4).

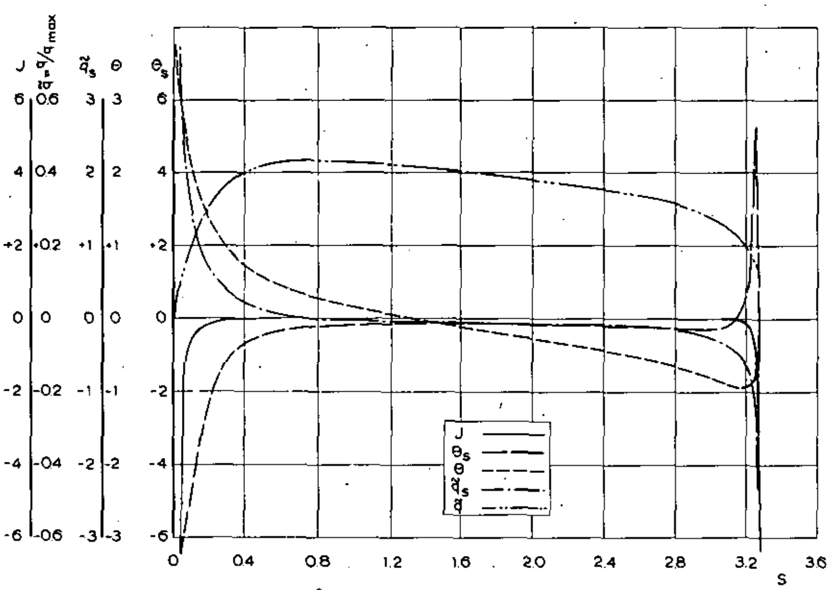

Fig. 6a. Graph of J, $\tilde{q}$, $\tilde{q}_s$, θ and θ_s versus arc length s along body contour $M_\infty=0.704$; $\varepsilon=0.6$; $\lambda=1$.

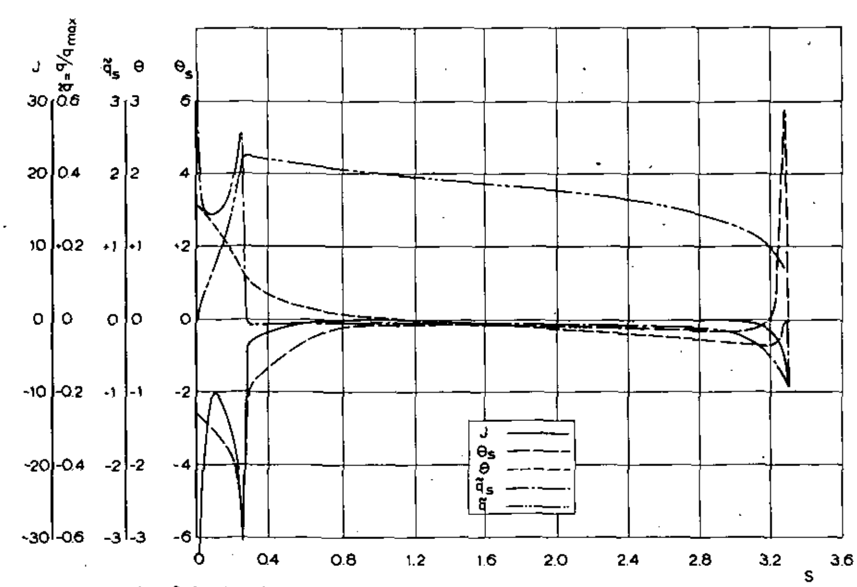

Fig. 6b. Graph of J, $\tilde{q}$, $\tilde{q}_s$, θ and θ_s versus arc length s along body contour $M_\infty=0.659$; $\varepsilon=0.6$; $\lambda=2$.

2.6.4 It is in particular this possibility of identifying profiles of the "peaky pressure distribution" type within the family considered, that makes an extension of the present procedure to more general classes of profiles, including cases of practical significance, interesting.

A discussion of the physical interpretability of these solutions is presented in Appendix B. It is suggested there, that in general, a transonic potential flow solution has no a priori bearing on physical reality at all. On the other hand, practically shock free flows of the "peaky pressure distribution" type have experimentally been shown to exist, and the present method might provide a basis for a systematic exploration of the physical limits of this concept. This would necessitate the development of the present work to a practical design method, involving a set of parameters giving profiles of the required physical characteristics, in a range that has to be defined by experimental verification.

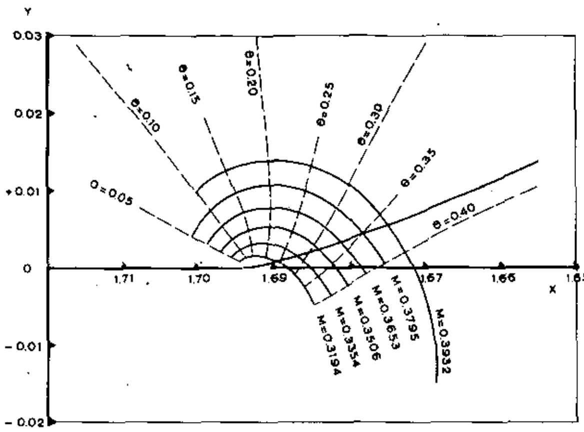

Fig. 7a. Detail of cusped profile nose of quasi-ellipse, Fig. 3c.

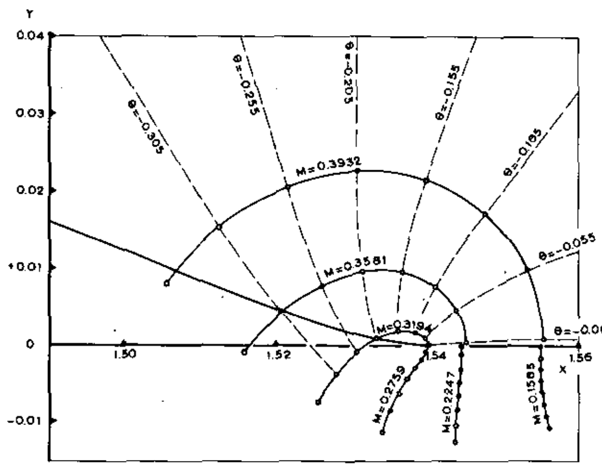

Fig. 7b. Detail of cusped trailing edge of quasi-ellipse, Fig. 3d.

It would seem to be more profitable to explore the practical possibilities of extending the present family by adding further solutions $\psi_n \cos n\theta$, $\psi_n \sin n\theta$ to the hodograph solutions to give camber etc., than to try and find the series representations for more general profiles in the incompressible physical plane, as these profiles are strongly distorted anyway. The most urgent problems would then be the further extension of the numerical scheme to make higher local Mach numbers and thinner profiles admissable, and an attack on the case involving circulation. When these problems could be solved, it is probable that sufficient parameters are available to make the procedure of some practical interest.

3 Some details of the numerical work*

3.1 *Computation of ψ_n; significance control*

From the computational point of view, the series representation (2.3.7), (2.4.1) presents considerable difficulties: in the high speed regions of the flow field, the series are to be evaluated for relatively high values of the argument τ;

* Parts of this section have been written in collaboration with M. J. M. G. van Gennip, who has been in charge of the actual numerical and programming work, cf. ref. 8.

for thin shapes (large values of ε), the approach of the second branch point at $\zeta = \frac{1}{\varepsilon}$ to that at $\zeta = 1$ makes itself felt in a very slow convergence of the series. This behaviour is serious in that in the series (2.3.7), (2.4.1) high order ψ_n are then required, which are extremely difficult to compute.

The qualitative behaviour of $F_n(\tau)$ for increasing n can be seen from the asymptotic forms (A11), and is illustrated in fig. 8. $F_n(\tau)$ is positive for $\tau < \frac{\gamma - 1}{\gamma + 1}$ (sonic value) and shows oscillatory behaviour for supersonic τ, the first

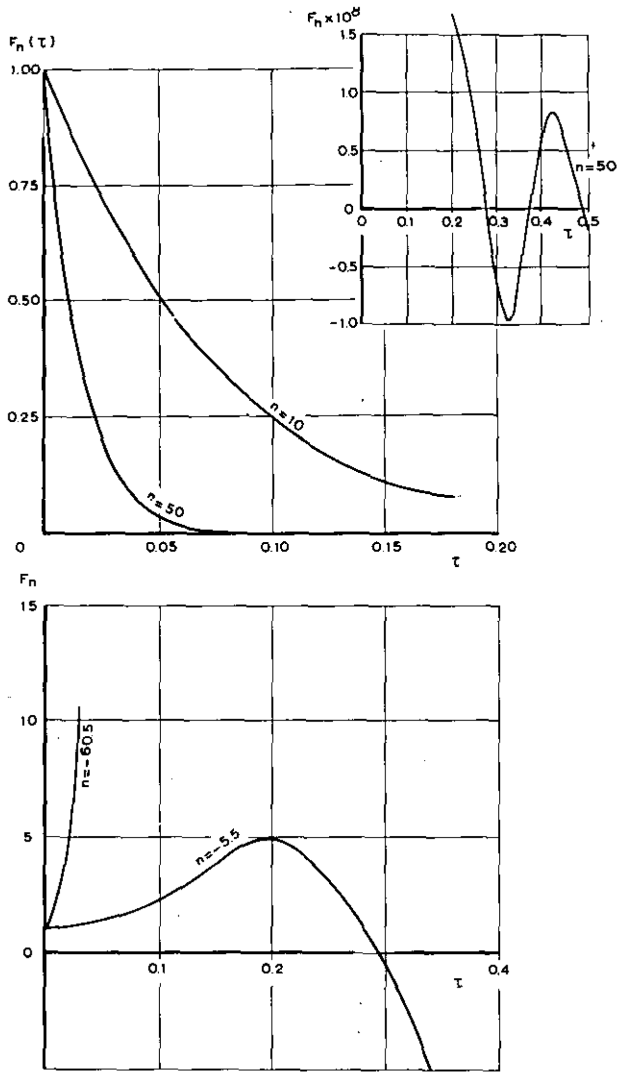

Fig. 8. Graphs of hypergeometric function $F_n(a_n, b_n, n+1 : \tau)$.

zero approaching the sonic value with increasing n. For positive large n, $F_n(\tau)$ shows a very steep gradient at $\tau = 0$; for negative n around the sonic value.

These large gradients in the graph are reflected in a severe cancellation between terms in the series representation (A6), and essentially the same difficulty occurs in some form or another in alternative ways of computing ψ_n. Significance control in the computation of ψ_n is then the critical problem in a computer using floating point arithmetic.

It will be clear, that this problem is quite different from the problems posed by any slow convergence of the series for $F_n(\tau)$ for large n. Actually, the hypergeometric series converges in the range of τ of interest to a practical answer using a few times n, say $2n$, terms, and should thus be considered as a fairly efficient means of generating ψ_n. The point is, that a rather exceptional accuracy in the numerical representation is required in order to handle the wide range of values and steep gradients in the graphs. The asymptotic forms (A 11) for large n are, in fact, of little use from the computational point of view, as n has to be very large before ψ_n is represented by the main term with any accuracy. Higher order terms are difficult to find in the supersonic case, but can be found easily from (A 8) in the subsonic case and prove then also to converge very slowly. Cherry's method (ref. 7) of applying empirical corrections to the asymptotic main term is in the present case obviously unsuitable.

As the convergence properties of the series (A 6) do not become in itself prohibitive in the present case, the series representation appears to be the most efficient method of generating ψ_n. Significance control in the computation of ψ_n was done in the crude but effective way of a priori restriction of the range of pairs (τ, n).

Setting as a goal q significant figures in the νth partial sum $F_n^{(\nu)}$ of the hypergeometric series, and using p-figure floating point arithmetic, the admissable range of τ is restricted for given n by the inequality

$$p-q \geqq {}^{10}\log\left|\frac{t(n,\tau)}{F_n^{(\nu)}}\right| + {}^{10}\log\sqrt{\nu} \tag{3.1.1}$$

where $t(n,\tau)$ is the largest individual term of the hypergeometric series, and the last term in the inequality is an estimate for rounding error. In this estimate of cancellation effects, the index ν is given by the bound for the truncation error $t_\nu/F_n^{(\nu)}$ in F_n, as the hypergeometric series is ultimately alternating (for $\nu > n$). For $F_n^{(\nu)}$ the estimates (A 9, A 11) can be used with advantage.

In the present computational work, 13 figure arithmetic was available in the computer, and choosing $q=6$, one may choose

$$\left|\frac{t_\nu}{F_n^{(\nu)}}\right| < 5\cdot 10^{-6}$$

n was chosen to be restricted by

$$|n| < 50\tfrac{1}{2}$$

By (3.1.1), $F_n(\tau)$ can then be computed to within the above accuracy for

$$\tau < \sim 0.18$$

for every n within this range, the restriction of course being given by the value $n = -50\frac{1}{2}$.

In this way, a very severe restriction is obtained on combinations (τ_*, ε) for which explicit solutions can be computed. In the first place, these combinations should be so that the maximum velocity in the external flow field does not exceed $\tau=0.18(M=1.1)$, (see, however, a remark in par. 3.3). Secondly, for a given truncation error on the series (2.3.7), (2.4.1), these series should sum within this bound for $|n|<50$. Whether these criteria are met, can unfortunately only be verified a posteriori. The maximum value of ε that gives a full neighbourhood of a profile in the physical plane with any accuracy by direct summation, is very roughly estimated to be in the order of 0.3, giving a profile being very far from thin indeed. The range of admissable ε's can, however, appreciably be extended by formal application of Wynn's ε-algorithm (ref. 29) to the available sequence of partial sums (2.3.7), (2.4.1), as a procedure essentially attacking the slow convergence of the hodograph series. In view of the interest of this method, a somewhat discursive discussion may follow in the next paragraphs.

3.2 *Shanks' e_k-transforms; ε-algorithm*

3.2.1 Given a sequence of, say, partial sums

$$S_1, \ldots, S_m, \ldots \tag{3.2.1}$$

a sequence to sequence transform is formally defined (Shanks; ref. 27):

$$e_k(S_m) = \frac{\begin{vmatrix} S_{m-k} & \cdots & S_m \\ \Delta S_{m-k} & & \Delta S_m \\ \vdots & & \\ \Delta S_{m-1} & \cdots & \Delta S_{m+k-1} \end{vmatrix}}{\begin{vmatrix} 1 & \cdots & 1 \\ \Delta S_{m-k} & & \Delta S_m \\ \vdots & & \\ \Delta S_{m-1} & \cdots & \Delta S_{m+k-1} \end{vmatrix}} \tag{3.2.2}$$

where

$$\Delta S_m = S_{m+1} - S_m$$

$e_k(S_m)$ appears as a weighted combination of $S_{m-k}, \ldots, S_m$ with non-linear weights depending on $S_{m-k+1}, \ldots, S_{m+k}$, and the sequence $e_k(S_m)$ is hoped to converge faster than S_m does, or even in some cases to sum diverging sequences S_m.

In fact, when for $m-k \leq r \leq m+k$ S_r can be written

$$S_r = a_{k,m} + \sum_{i=1}^{k} \alpha_{i,m} \lambda_{i,m}^r , \tag{3.2.3}$$

application of (3.2.2) gives $e_k(S_m) = a_{k,m}$ irrespective of convergence or divergence of the sequence S_m.

An important application is the case where (3.2.1) is the sequence of partial sums of the power series development of an analytic function

$$\Phi = \sum_{i=0}^{\infty} c_i \zeta^i \tag{3.2.4}$$

$$S_m = \sum_{i=0}^{m} c_i \zeta^i .$$

In this case (3.2.2) can be written:

$$e_k(S_m) = \frac{\begin{vmatrix} \zeta^k S_{m-k} & \dots & \zeta^0 S_m \\ c_{m-k+1} & & c_{m+1} \\ \vdots & & \\ c_m & \dots & c_{m+k} \end{vmatrix}}{\begin{vmatrix} \zeta^k & \dots & \zeta^0 \\ c_{m-k+1} & & c_{m+1} \\ \vdots & & \\ c_m & \dots & c_{m+k} \end{vmatrix}} = \frac{A_k^{(m)}}{B_m^{(k)}} \tag{3.2.5}$$

and $e_k(S_m)$ is the quotient of two polynomials of degree m and k respectively, which can be identified to be the rational fraction approximation to the function Φ of order (k, m) having the property that the series obtained by dividing out the fraction agrees with the series development (3.2.4) up to the term ζ^{m+k}.

In this case, the theory of the $e_k(S_m)$ transforms is equivalent to rational fraction approximation, or continued fraction expansion (ref. 27, 29).

The way in which the $e_k(S_m)$ operates is then clearly illustrated by one of the interesting examples given by Shanks (ref. 27): if Φ is an analytic function having p poles in a circle $|\zeta| = R$, being otherwise regular in this circle, $e_p(S_m)$ approximates Φ uniformly in this region (with small circles around the poles cut out) for $m \to \infty$. This means that the zero's of $B_m^{(p)}$ in (3.2.5) are eventually situated in any neighbourhood of the poles of Φ. The convergence or divergence of the sequences, ..., S_m, ... are clearly irrelevant: the power series expansion around the origin can be used in the whole circle $|\zeta| = R$, and the transforms supply the analytic continuation automatically; contrariwise, the transforms applied to a Laurent series expansion do not provide the rational fraction approximation.

The situation is not so clear, however, for functions involving branch type singularities like (2.2.3). Cutting the hodograph plane between $\zeta = 1$, ∞ one would by analogy and symmetry, be tempted to expect uniform convergence of $e_n(S_n)$ for $n \to \infty$ in a finite region of the hodograph plane excluding a rectangular strip around the cut, i.e. the branch points to be approximated by sources lying eventually within this rectangle. This would, however, be very difficult to prove, the non-formal aspects of the approximation technique being as yet not very extensively developed.

When, as is the case in the present application, the e_k-transforms are applied to the partial sums of the series (2.3.7), (2.4.1), representing the compressible hodograph solution, no such functional representation of the approximation exists even in the formal sense. The resulting process is a purely local "filtering out of higher order components" from the sequence (cf. (3.2.3)), in the sense of Shanks' original intuitive motivation, with no more justification than the plausibility of the answer obtained. The transforms have only been used on convergent sequences, i.e. analytic continuation has been done by using Laurent series, in the expectation that application will at any rate not worsen convergence.

3.2.2 Application of the e_k-transforms in the form (3.2.2) is prohibitively laborious. They have been rewritten, however, in the form of a recursive algorithm by Wynn (ref. 29). His technique, the ε-algorithm, is defined by:

$$\begin{aligned} &\varepsilon_{-1}^{(m)} = 0 \qquad \varepsilon_0^{(m)} = S_m \\ &\varepsilon_{k+1}^{(m)} = \varepsilon_{k-1}^{(m+1)} + \frac{1}{\varepsilon_k^{(m+1)} - \varepsilon_k^{(m)}} \end{aligned} \qquad m = 0, 1, \dots \tag{3.2.6}$$

and Wynn proves

$$\varepsilon_{2k}^{(m)} = e_k(S_m)$$

The algorithm has been used in the form (3.2.6) to sum the series (2.3.7) and (2.4.1).

3.3 *Application to evaluation of series* (2.3.7), (2.4.1)

The concept of "convergence" used in summing these series by formal use of the ε-algorithm is of necessity intrinsically numerical; that is depends essentially on a criterion involving a subjective degree of confidence in the result ultimately chosen after inspection of the output of the process.

As a definition of "convergence" of the ε-algorithm, it was decided to test for two subsequent numbers in an even numbered column of the ε-array to agree within 4 rounded significant figures, and to repeat this test in the next even numbered column to give the same result. This last test was only sampled, however, in the most critical parts of the field.

The ε-array was based on a sequence $\varepsilon_0^{(m)}$ of at most 50 partial sums, as discussed in the preceding paragraph. An example of the output of the process in the computation of the series (2.3.7 I) for $\tau=0.09$; $\varepsilon=0.6$; $\lambda=1$ for $\tau=0.07$, $\theta=0.9$ is given in table 2, where odd numbered columns have been deleted. Application of the ε-algorithm

TABLE 2. EXAMPLE OF ε-ALGORITHM

Series (2.3.7) I; $\varepsilon=0.6$; $\tau_\infty=0.099$; $\lambda=1$; $\tau=0.07$; $\theta=0.9$

m	$\varepsilon_0^{(m)} \equiv S_m$	$\varepsilon_2^{(m)} \equiv e_1(S_m)$	$\varepsilon_4^{(m)} \equiv e_2(S_m)$	$\varepsilon_6^{(m)} \equiv e_3(S_m)$	$\varepsilon_8^{(m)} \equiv e_4(S_m)$	$\varepsilon_{10}^{(m)} \equiv e_5(S_m)$	$\varepsilon_{12}^{(m)} \equiv e_6(S_m)$	$\varepsilon_{14}^{(m)} \equiv e_7(S_m)$
0		+0.42321						
1	+0.29472	+0.73302	−0.001718					
2	−0.023675	−0.18527	−0.14318	−0.18085				
3	−0.063669	−0.62880	−0.17170	−0.016273	−0.013517			
4	−0.062864	−0.63688	−0.015823	−0.021267	−0.013543	−0.013529		
5	−0.028245	−0.40258	−0.013963	−0.012410	−0.01351	−0.013577	−0.013471	
6	+0.0099013	+0.033370	−0.013115	−0.013106	−0.013462	−0.013348	<u>−0.013468</u>	<u>−0.013468</u>
7	+0.024431	+0.017196	−0.013106	−0.013429	−0.013429	−0.013426	<u>−0.013468</u>	
8	+0.010021	+0.010021	+0.040241	−0.013338	−0.013646	−0.013429		
9	−0.017522	−0.079359	−0.013471	−0.013477	−0.013447			
10	−0.036578	−0.035857	−0.013477	−0.013472				
11	−0.035829	−0.036614	−0.013454					
12	−0.019897	−0.26397						
13	−0.002852							

proves to be almost spectacularly successful. As discussed before, the reason for this success cannot really be explained, apart from the somewhat lame observation that apparently, the oscillatory character of the sequence of partial sums is well suited to application of the transformations (cf. 3.2.3).

The restriction of the basis of the algorithm to 50 partial sums means that only combinations of $(\tau_\infty, \varepsilon)$ are admissable, which provide "convergence" of the process in the above sense for the points of interest on the profile and in the external flow field. When only part of this base is necessary to achieve convergence, it is possible to extend the range of admissable values of τ in the process slightly above the value given in par. 3.1, and thus the flow field fig. 3e, exhibiting a maximum speed $\tau_{max}= 0.20$ ($M_{max}= 1.12$) has been calculated. It will be clear, that increasing ε has a strongly adverse effect on the rate of convergence of the series representation, and thus on the performance of the process.

A very severe test of the process is taken on the circle of convergence $\tau=\tau_\infty$, where both series expansions (2.3.7) are conditionally, very slowly convergent, and should sum to give the same result. This computation is necessary to find the integration constant Δx in the series (2.4.1) to join the solutions from the two series representations. The process did not always converge on the line $\tau=\tau_\infty$ in the external flow field, in these cases a point in the interior has been computed to find Δx.

It will be clear, that the accuracy of the results obtained from the process cannot be guaranteed in any mathematical sense. Nevertheless, it is believed that the results obtained as shown in fig. 3, are correct to within at least 3 significant figures.

The gain in performance of the process, that can be obtained by computing F_n's using multiple length arithmetic in the computer will be a subject of further research. A second possibility of extending the range of admissable local maximum Mach numbers for thin profiles is the use of a model gas law, giving rise to particular solutions having somewhat more convenient numerical properties. This also, if useful, will be investigated.

4 Conclusions

1. A three parameter family of continuous transonic aerofoil flows is defined by means of Lighthill's integral operator. The computation of thin aerofoils is shown to be possible under some restrictions using automatic computing equipment and numerical methods that recently have been developed. Profiles that exhibit some of the characteristics of Pearcey's "peaky pressure distribution profiles" can be identified within this family.
2. In Appendix B, a discussion is presented on the "transonic controversy", in view of recent theoretical and experimental results. It is suggested, that while transonic potential flows cannot be said to "exist" in any physical sense, a practical method of calculating these flows might be a useful working tool in the experimental analysis of the process of shock formation in transonic flows. In particular, the physical limits of the "peaky pressure distribution" concept might thus be explored on a systematic basis.
3. The fact, that approximate methods cannot be expected to predict these flows with sufficient accuracy, justifies a renewed interest in the classical function theoretic hodograph methods, and an attempt at future development of finite difference methods for these flows. In particular, a further development of the present method would appear to be worthwhile, which would involve:
   a) extension of the numerical procedure to permit the computation of flows involving higher local Mach numbers over thinner profiles;
   b) application to circulatory flows and
   c) exploration of the possibility to extend the method to other flows of practical interest by adding further particular solutions in the hodograph plane.
4. In Appendix C, the feasibility of the hodograph transformation is discussed in terms of elementary algebraic considerations. This leads, in particular, to an insight into the significance of the dimensionality and metrical properties of physical space. A physical interpretation of the principal invariants of the rate of strain tensor in plane flow is given in this connection.

5 References

[1] Bergman, S., Integral operators in the theory of linear partial differential equations. Springer Verlag, Berlin, 1961.
[2] Bergman, S. and Epstein, B., Determination of a compressible flow past an oval shaped obstacle. J. Math. Phys., vol. 26 pp. 195–222, 1948.
[3] Bers, L., Mathematical aspects of subsonic and transonic gas dynamics. John Wiley, New York, 1958.
[4] Birkhoff, G., Hydrodynamics (2nd ed.) Princeton U.P.
[5] Chaplygin, On gas jets. Sci. Mem. Moscow Un. Math. Phys. no. 21, pp. 1–21, 1904. Transl. NACA Tech. Mem. 1063 (1944).
[6] Cherry, T. M., Flow of a compressible fluid about a cylinder. Proc., Royal Society A 196, pp. 1–31, 1949.
[7] Cherry, T. M., Numerical solutions for compressible flow past a cylinder. Counc. Sci. Ind. Res. (Austr.), Aer. Lab. Melbourne, Rep. A 48. Altern.: Proc. Roy. Soc., A 196, pp. 32–36 (1949).
[8] van Gennip, M. J. M. G., Numerical analysis and ALGOL programme for the computation of transonic potential flow around a family of quasi-elliptical aerofoils. NLR rep. W 27 (to be published).
[9] Goldstein, S., Lighthill, M. J. and Craggs, J. W., On the hodograph transformation for high speed flow. I. Quart. Journ. Mech. Appl. Math. vol. I, pp. 233–257, 1948.
[10] Ince, E. L., Ordinary differential equations. Dover Publ. Reprint (1956), 1926.
[11] Krzywoblocki, M. Z. E., Bergman's linear integral operator method in the theory of compressible fluid flow. Springer Verlag, Wien, 1960.
[12] Levey, H. C., High speed flow of a gas past an approximately elliptic cylinder. Proc. Cambr. Phil. Soc. vol. 46, 1950.
[13] Lighthill, M. J., The hodograph transformation in transsonic flow II, III. Proc. Royal Soc. A 191 pp. 341–369, 1947.
[14] Lighthill, M. J., The hodograph transformation; in: L. Howarth (ed.). Modern developments in fluid dynamics, High speed flow. Vol. I, Oxford C.P., 1953.
[15] Ludford, G. S. S., The boundary layer nature of shock transition in a real fluid, Quart. Appl. Math., vol. 10 pp. 1–16, 1952.
[16] Michel, R.; Marchaud, F. and le Gallo, J., Etude des écoulements transsoniques autour des profils lenticulaires, à incidence nulle. ONERA publ. no. 65, 1953.
[17] Mises, R. von, Mathematical theory of compressible fluid flow. Academic Press, New York, 1958.
[18] Morawetz, C. S., On the non-existence of continuous transonic flows past profiles I. Comm. Pure and Appl. Math. vol. 9 pp. 45–68, 1956.
[19] Morawetz, C. S., Idem II, Comm. Pure and Appl. Math., vol. 10 pp. 107–131, 1957.
[20] Morawetz, C. S., Idem III, Comm. Pure and Appl. Math., vol. 11 pp. 129–144, 1958.
[21] Morawetz, C. S. and Kolodner, I. I., On the non-existence of limiting lines in transonic flows. Comm. Pure and Appl. Math., vol. 6 no. 1, pp. 97–102, 1953.
[22] Nieuwland, G. Y., Enige opmerkingen over theorie en experiment in het transsone gebied. NLR-TM 57, (not published).
[23] Pearcey, H. H., The aerodynamic design of section shapes for swept wings; in: Advances in Aeronautical Sciences, Vol. 3, Proc. 2nd Int. Congr. Aer. Sci., Zürich 1960, Pergamon Press, 1962.
[24] Pearcey, H. H., Shock induced separation and its prevention by design and boundary layer control. in: Lachmann, G. V. (ed.) Boundary layer and flow control, Vol. I, Pergamon Press, 1961.
[25] Reyn, J. W., Differential-geometric considerations in the hodograph transformation for irrotational conical flow. Arch. Rat. Mech. An., vol. 6 no. 4 pp. 299–254, 1960.
[26] Reyn, J. W., Some remarks on the structure of compressible potential flow in connection with the hodograph transformation for plane flow. Proc. IUTAM Symposium Transsonicum, Aachen, September 1962 (to be published), 1962.
[27] Shanks, D., Non-linear transformations of divergent and slowly convergent sequences. Journ. Math. Phys., vol. 34 pp. 1–42, 1955.
[28] Tamaki, F., Experimental studies on the stability of the transonic flow past airfoils. Journ. Phys. Soc. Japan, vol. 12 no. 5 pp. 544–549, 1957.
[29] Wynn, P., The rational approximation of functions which are formally defined by a power series expansion. Mathematics of Computation, vol. 14 no. 70, pp. 147–186, 1960.

APPENDIX A

A summary of some of Lighthill's results (ref. 13)

In this appendix a number of results as obtained by Lighthill will be assembled for convenient reference.

The isentropic gas law

$$\frac{p}{\rho^{\gamma}} = C$$

is used, leading to the relations (cf. C 2.7):

$$\tau = \left(\frac{q}{q_{\max}}\right)^2 = \left(\frac{\gamma-1}{\gamma+1}\right)\left(\frac{q}{q^*}\right)^2 = \frac{1}{1+\dfrac{2}{\gamma-1}\dfrac{1}{M^2}} \tag{A 1}$$

$$\frac{\rho}{\rho_0} = (1-\tau)^{\frac{1}{\gamma-1}}$$

Introducing potential and streamfunction by the definitions

$$\varphi_{,i} = u_i$$

$$\psi_{,i} = \frac{\rho}{\rho_0}\eta_{ij}u_j \qquad (i, j = 1, 2)$$

where η_{ij} is the isotropic tensor $\begin{pmatrix} 0 & 1 \\ -1 & 0 \end{pmatrix}$, the *hodograph equations in Chaplygin's form* are immediately obtained by inversion of the forms (C.4.5)

$$\begin{aligned} \varphi_{\theta} &= \frac{q}{\rho}\psi_q \\ \varphi_q &= -\frac{1-M^2}{\rho q}\psi_{\theta}\,. \end{aligned} \tag{A 2a}$$

Eliminating φ it follows

$$q^2\psi_{qq} + (1-M^2)\psi_{\theta\theta} = -q(1+M^2)\psi_q \tag{A 2b}$$

or, introducing the relations (A 1)

$$\tau(1-\tau)\psi_{\tau\tau} + \frac{\dfrac{\gamma+1}{\gamma-1}\tau}{4\tau}\psi_{\theta\theta} = -\left(1+\frac{2-\gamma}{\gamma+1}\tau\right)\psi_{\tau}\,. \tag{A 2c}$$

The *subsonic normal form* of (A 2) is found, writing

$$\frac{\mathrm{d}s}{\mathrm{d}q} = \frac{1}{q}\sqrt{1-M^2}$$

where the integration constant σ can be fixed by the condition

$$\lim_{\tau\to 0}\frac{e^{2s}}{\tau} = 1\,, \tag{A 3a}$$

giving

$$\psi_{ss} + \psi_{\theta\theta} = T\psi_s \tag{A 3}$$

with

$$s = \sigma + \sqrt{\frac{\gamma+1}{\gamma-1}}\,\mathrm{artgh}\sqrt{\frac{\dfrac{\gamma-1}{\gamma+1}-\tau}{1-\tau}} - \mathrm{artgh}\sqrt{\frac{1-\dfrac{\gamma+1}{\gamma-1}\tau}{1-\tau}}$$

$$\sigma = -\sqrt{\frac{\gamma+1}{\gamma-1}}\,\mathrm{artgh}\sqrt{\frac{\gamma-1}{\gamma+1}} + \tfrac{1}{2}\log(2\gamma-2)$$

$$T(s) = -\frac{\rho}{\sqrt{1-M^2}}\frac{\mathrm{d}}{\mathrm{d}s}\left(\frac{\sqrt{1-M^2}}{\rho}\right) = \frac{\gamma+1}{1}\,\frac{M^4}{(1-M^2)^{\frac{3}{2}}}\,.$$

There is a similar *supersonic normal form*

$$\psi_{tt}-\psi_{00}=S\psi_t \tag{A 4}$$

with

$$\frac{dt}{dq}=\frac{1}{q}\sqrt{M^2-1}$$

which, however, will not be used explicitly.

Chaplygin's particular solutions are

$$\psi_n(\tau)e^{\pm in\theta}$$

with

$$\psi_n=\tau^{\frac{1}{2}n}F\ (a_n, b_n, n+1\,;\tau)$$

$$a_n, b_n=\tfrac{1}{2}\left[n-\frac{1}{\gamma-1}\pm\left\{\frac{\gamma+1}{\gamma-1}n^2+\left(\frac{1}{\gamma-1}\right)^2\right\}^{\frac{1}{2}}\right]$$

and F_n satisfies the hypergeometric differential equation

$$\tau(1-\tau)F''+[(n+1)-(a_n+b_n+1)\tau]F'-a_nb_nF=0\ . \tag{A 5}$$

Of the two independent solutions of (A 5) only the one denoted by $F_n(a_n, b_n, n+1\,;\tau)$, regular at the origin, will be used in the main body of the report (for the Chaplygin function of the second kind, mentioned in Note, par. 2.5, refer to the original paper):

$$F(\tau)=\frac{n!}{(a_n-1)!\,(b_n-1)!}\sum_{k=0}^{\infty}\frac{(a_n+k-1)!\,(b_n+k-1)!}{(n+k)!}\frac{\tau^k}{k!}. \tag{A 6}$$

From the series expansion it is seen that ψ_n as a function of the complex variable n, has poles at $n=-2,\ -3,\ -4,\ldots$ with residues

$$\lim_{n\to -m}(n+m)\psi_n(\tau)=-mC_m\psi_m(\tau)\qquad m=2, 3,\ldots \tag{A 7}$$

where

$$C_m=\frac{(a_m-1)!\,(m-b_m)!}{(a_m-m-1)!\,(-b_m)!}\frac{1}{(m!)^2}.$$

For large m one has

$$C_m=\frac{1}{2\pi m}e^{-2\sigma m}\ \ 1+0\left(\frac{1}{m}\right)\Big\}. \tag{A 7a}$$

Now the fundamental fact in Lighthill's method is, that for $\tau<\dfrac{\gamma-1}{\gamma+1}$ a development of $e^{-ns}\psi_n(\tau)$ can be given in terms of the residues (Mittag-Leffler's theorem):

$$e^{-ns}\psi_n(\tau)=1+n\cdot\sum_{m=2}^{\infty}\frac{C_me^{ms}\psi_m(\tau)}{m+n} \tag{A 8}$$

a result expressing ψ_n for arbitrary complex $n(\neq -1, -2,\ldots)$ in ψ_m's for positive integral m.

An *asymptotic form for subsonic* τ for large n can be found from (A 4):

$$\psi_n(\tau)=V(\tau)e^{ns}\left\{1+0\left(\frac{1}{n}\right)\right\} \tag{A 9}$$

where

$$V(\tau)=\left(\frac{\rho}{\sqrt{1-M^2}}\right)^{\frac{1}{2}}$$

$$\frac{2V'}{V}=T.$$

Comparing (A 8) and (A 9) it follows

$$V=1+\sum_{m=2}^{\infty}C_m\psi_me^{ms}. \tag{A 10}$$

The corresponding *asymptotic form for supersonic* τ is given as

$$\psi_n(\tau) = 2Ve^{n\sigma}\left[\sin(nt+\tfrac{1}{4}\pi) + 0\left\{\frac{e^{t|\mathrm{Im}\, n|}}{|n|}\right\}\right] \tag{A 11}$$

uniformly for

$$\frac{\gamma-1}{\gamma+1} + \varepsilon \leqq \tau \leqq 1-\varepsilon: \ |\arg\ n| \leqq \pi-\delta$$

$$\psi_n(\tau) = Ve^{n\sigma}\left[\sin(nt+\tfrac{1}{4}\pi) - \operatorname{cotg} n\pi \cos(nt+\tfrac{1}{4}\pi) + 0\left(\frac{e^{t|\mathrm{Im}\, n|}(1+|\operatorname{cotg} n\pi|)}{|n|}\right)\right]$$

uniformly for

$$\frac{\gamma-1}{\gamma+1} + \varepsilon \leqq \tau \leqq 1-\varepsilon\ ;\ |\arg(-n)| \leqq \pi-\delta$$

Lighthill's integral operator in its simplest form (for circulation free flow) defined in the subsonic region $|\zeta| < e^{\sigma - s_\infty}$ is given by

$$\psi = \mathrm{Im}\left[\sum_{m=0}^{\infty} C_m \psi_m(\tau) e^{m(s_\infty + i\theta)} \int_{\zeta_0}^{e^{s-s_\infty - i\theta}} \zeta^m \mathrm{d}\Phi(\zeta)\right] \tag{A 12}$$

$$C_0 = 1$$

$$C_1 = 0\,.$$

The properties of the operator can be seen from the results mentioned in this Appendix, to be:

a) (A 12) is regular in the subsonic part of the compressible hodograph plane, excluding the point $s=s_\infty$, $\theta=0$. This can be shown by majorization using the asymptotic estimates for C_m, ψ_m and the fact that the integral in (A 12) is regular in the part of the incompressible hodograph plane corresponding to the exterior of a body.

b) (A 12) satisfies (A 3), which follows immediately noting that

$$\mathrm{Im}\left[e^{-m(s-s_\infty - i\theta)} \int_{\zeta_0}^{e^{s-s_\infty - i\theta}} \zeta^m \mathrm{d}\Phi\right]$$

is a harmonic function of s, θ; (A 8), and the relation $T = \dfrac{2V'}{V}$.

c) for $q_{\max} \to \infty$, $\psi \to \mathrm{Im}\ \Phi$ as all terms except $m=0$ reduce to zero and $e^{s-s_\infty} \to \dfrac{q}{q_\infty}$.

d) By using a series expansion for $\Phi(\zeta)$ as (A 13), and the asymptotic properties of ψ_n, (A 9), it follows that the expansion of ψ for $\tau \to \tau_\infty$ is asymptotically similar to that of Im Φ for $q \to q_\infty$.
The development (A 14) shows that $f(n, \tau_\infty) \equiv e^{-ns_\infty}$ in this case.
The result can be given *in series form*, permitting extension to supersonic values of τ when a series development of $\Phi(\zeta)$ is available, which is written symbolically

$$\Phi = \sum_{n'} c_{n'} q^{n'} e^{-in'\theta} \tag{A 13}$$

implying the various analytic continuations.
Indeed, let ζ_1 be a point arbitrarily located in the subsonic region and an expansion of the form (A 13) given. Then,

$$\psi = \mathrm{Im} \sum_{m=0}^{\infty} C_m \psi_m e^{m(s_\infty + i\theta)}\left[\int_{\zeta_0}^{\zeta_1} \zeta^m \mathrm{d}\Phi + \int_{\zeta_1}^{e^{s-s_\infty - i\theta}} \zeta^m \sum n' c_n \zeta^{n'-1} \mathrm{d}\zeta\right].$$

Working out the second integral, assembling terms in ζ_1, in

$$g_m = \int_{\zeta_0}^{\zeta_1} \zeta^m \mathrm{d}\Phi - \sum_{n'} \frac{n' c_n'}{n'+m} \zeta_1^{n'+m}$$

it follows

$$\psi = \mathrm{Im}\left[\sum_{m=0}^{\infty} g_m C_m \psi_m e^{m(s_\infty + i\theta)} + \sum_{n'} c_{n'} \psi_{n'} e^{-n'(s_\infty + i\theta)}\right] \tag{A 14}$$

g_m obviously does not depend on ζ_1 as neither the second series nor ψ does. Using the asymptotic estimates, it can be shown that (A 14)converges in the whole supersonic region and in part of the adjacent subsonic region.

APPENDIX B

Mathematical model and experiment: the "transonic controversy"

B 1 *Introduction*

This Appendix presents a discussion on the mathematical and physical interpretation of the results of this report, in view of the current "transonic controversy"; cf. Bers' book (ref. 3) for a recent survey. 2) is an attempt at clarification of terminology and reviews the mathematical position; 3) refers to the experimental state of the art. In 4) some consequences for the design problem in the transonic field, in particular for "peaky pressure distribution" sections, are discussed.

B 2 *The transonic potential flow model*

Theoretical aerodynamics is concerned with the conception and analysis of mathematical models for flow phenomena. The aim is to study the interrelation between particular aspects of physical flows, which have been isolated in an aerodynamic theory, in a mathematically consistent system. The present discussion is concerned with the aerodynamic problems of flows around bodies at large Reynolds numbers, and the mathematical models can be thought as represented by, say, systems of partial differential equations with boundary or initial value conditions.

A useful model should meet conditions of mathematical consistency, and be, in some sense, physically adequate.

The classical conditions of mathematical consistency have been formulated by Hadamard: a solution to the mathematically "well posed" problem should exist, be unique and be stable against small perturbations of boundary or initial values.

The physical adequacy of the model is more difficult to define precisely: roughly, it is an assessment how well the model predicts the results of a particular set of experiments. This assessment often leads to an interpretation of the model in terms of a more general aerodynamic theory.

The main problem in the conception of models for the aerodynamic theories under discussion is to represent the effects of viscosity. These effects are only indirectly represented in linearized potential flow theories, for which the mathematical problems are in general well understood. Comparison with experiment shows these linearized models to be grossly inadequate however, necessitating the use of a more detailed, often non-linear, physical theory. The usual procedure is then to postulate the existence of a system of shock waves and vortex sheets as singular surfaces, carrying compatibility conditions, in the solution, and use the equations of inviscid compressible flow theory. In principle, again, the intrinsic mathematical consistency of the model should be analysed (which is unfortunately usually mathematically unfeasible), but this does of course still not verify the physical validity of the type of flow postulated. Moreover, as will be discussed in the next paragraph, in transonic flows experimental situations exist which do not seem to be analysable in terms of a stable mathematical model of this type. This is an essential difficulty in the conception of a consistent transonic theory, but not an exclusive feature of transonic flows only.

The physical basis of the above procedure is, that for large Reynolds number viscosity effects often take the form of boundary layer phenomena, and the resulting shock waves and vortex sheets can mathematically be shown to represent asymptotic solutions of the Navier-Stokes equations (ref. 15). It has been suggested by von Mises (ref. 17, V, 24, 6) that ideally, the physical validity of these models should be demonstrated by asymptotic analysis for $Re \to \infty$ of solutions of the full Navier-Stokes equations. This programme would undoubtedly remove any logical inconsistencies from the theory, but would seem to be somewhat beyond the present mathematical possibilities. This means, however, for the time being, that the physical validity of any mathematical model can only be established by a posteriori experimental verification.

The mathematical consistency problems have been rigorously analysed for physically the simplest model of compressible flow theory: the usual, Neumann-type external boundary value problem for the equations for plane potential flow. The existence of a solution under uniformly subsonic conditions has been proved by Bers (ref. 3). Thus, the mathematical model has been demonstrated to be stable in this case. The physical adequacy of this model, however, depends on boundary layer separation effects, for which at the moment, no satisfactory theory exists.

In the transonic case ($M_\infty < 1$), classes of potential flows can be defined by the methods discussed in this report. Morawetz (refs. 19, 20, 21) has proved that these do not possess neighbouring solutions when the boundary is perturbed in the supersonic region. This means that these solutions cannot be defined by boundary value problems: this mathematical model is unstable in Hadamard's sense. These results, which were preceded by mathematically somewhat less satisfactory discussions of related problems by Busemann and Guderley, (cf. ref. 3), have given rise to conflicting opinions on the so called "transonic controversy". It would appear, that most of the paradoxes advanced in this discussion vanish, when the modest status of mathematical theory as a model of physical reality is realised; somehow, experimenters have remained quite unruffled by the dispute.

Morawetz's results suggest immediately a host of interesting and extremely difficult mathematical questions as to the characterization of the class of profile contours that do admit transonic potential flow solutions: their analyticity properties, topological category, etc. However, again the physical relevance of this class of solutions is a quite different problem, which cannot be answered on the basis of potential theory. From the physical point of view, it would seem to be extremely doubtful whether these profiles, as a class, have any particular significance in one way or the other: the existence of a potential flow solution around a given contour does in no way indicate the possibility of shock free realization in a viscous flow; alternatively, it appears that a contour for which non-existence of a potential solution could be proved, would not necessarily generate a pronounced shock wave.

The mathematical position, then, would seem to be that the mathematical instability of this particular flow model has been proved; leaving, however, the decision on the physical relevance of any particular potential flow solution to experimental observation.

B 3 *Experiments in transonic profile flow*

A description of shock and shock-boundary layer interaction phenomena in transonic profile flows has been given by Pearcey (ref. 24). These phenomena usually accompany super-critical conditions; however, as discussed by Pearcey (ref. 23), by careful design it is often possible to reduce the shock strength appreciably, thereby alleviating the separation problems to a large extent. This is done by generating a carefully tailored expansion at the profile nose, which is reflected against the sonic line to give a gradual recompression in the supersonic region. In some cases (Pearcey, private communication) it is even possible to remove any stationary shock wave from the flow field in this way, resulting in a shock free supersonic recompression from a rather high local maximum Mach number on the profile contour. It is suggested by Pearcey, that this condition of "peaky pressure distribution" should be designed for, and these sections be used in the design of subsonic and supersonic swept wings. As transonic windtunnel conditions are generally far from perfect, the experimental evidence makes it probable that the stability of flow fields of this type is sufficiently uncritical for this concept to be a useful basis for engineering applications. However, a rational design method for these sections is as yet not available.

As suggested before these experimental results are, though perhaps somewhat unexpected, not at variance with Morawetz's results. Obviously the explanation of the physical stability of the flow with respect to the occurrence of shock waves would require a much deeper penetration into the properties of viscous flows than at present would seem to be possible. A further, detailed study of growth properties of instationary upstream travelling disturbances, building up to very weak instationary shock waves (refs. 22, 28) would be of interest, in particular for globally shock free flows. Apparently, for these flows the balance between the growth of the strength and speed of propagation of these disturbances is such as to prevent coalescence into a stationary shock wave. A theoretical solution to the physical stability problem as to the appearance or not of shock waves would require a mathematical analysis of this physical situation.

B 4 *The design problem*

The experimental results discussed clearly show the essential difficulty for a general theory for transonic flow around a given contour: the physical type of the flow is a priori unknown. In principle, it is possible to assume the existence of a shock wave and try to find an equilibrium position by iteration. This would present extremely difficult stability problems in the numerical analysis and will in many cases not necessarily represent the physically correct model.

The principal advantage of hodograph methods, as compared with the direct methods, is the possibility of a priori specification of the flow pattern, by virtue of the linearity of the hodograph equations. When the aim is to design flows of a prescribed physical type, the inverse nature of these methods presents no serious restrictions.

However, for a profile flow involving a local supersonic region closed by a shock wave, it is easily shown by qualitatively formulating the problem in the hodograph, that a doubly covered hodograph exists in the subsonic reexpansion region immediately behind the shock wave. From the considerations in Appendix C, this follows to be incompatible with the assumption of potential flow. Thus, the problem in the large cannot be formulated without taking vorticity effects into account. This again introduces a non-linearity in the description of such flows, which still awaits analysis.

At present perhaps the more important practical problem is, whether a rational design method can be found for shock free transonic flow fields of the type suggested by Pearcey, on the basis of potential theory, if at all. Such a design method would require a practical numerical method to construct continuous transonic solutions of the required type, permitting a systematic variation of the geometric parameters, and a criterion to designate the range of parameters leading to solutions having the required physical characteristics. As suggested in 2.6.4, such a design method could be developed on the basis of the methods used in this report. The physical criteria should be derived from a systematic experimental programme.

The alternative would be the development of methods allowing a direct definition of the "peaky pressure distribution" type of sections in the hodograph. This would require formulation of a correctly posed (Frankl-type) boundary value problem in the hodograph plane, combined with a singularity representing the far field conditions in the physical plane. The problem then, as the defining boundary cannot be closed, is to guarantee closure of the profile. If this problem could be solved, this method, using finite difference techniques in the numerical integration, would be the most flexible with respect to the boundary conditions that can be prescribed. Also, it would perhaps provide a basis for an extension to flow fields involving shock waves.

It will be clear from the foregoing discussion, that these theoretical solutions do not "exist" in any physical sense, or "explain" the possibility of a physically continuous flow. However, the possibility of characterising the "peaky pressure distribution" flow fields in this way, might make these solutions a useful tool in the further experimental analysis of this interesting physical situation.

APPENDIX C

Some elementary algebraic properties in the local theory of plane potential flows

C 1 *Introduction*

In this appendix, some of the algebraic properties for two dimensional flows are surveyed, of which some are basic for the whole theory, and others are used in the analysis of the practical results in the report. In 2) a somewhat leisurely review of the usual assumptions in the theory of compressible potential flow is presented. 3) gives a study of the general feasibility of the hodograph transformation, in which the linearity of the plane hodograph equations is clarified. 4) is a study of the algebraic invariants of the hodograph transformation, here represented by the rate of strain tensor, which are given a physical interpretation. 5) presents a brief discussion of the singularities of the hodograph transformation, in particular limit lines.

C 2 *Potential flow of a compressible medium*

A flow field is a continuous structure having interrelated kinematical, dynamical and thermodynamical aspects.

The flows to be considered will be stationary, and can then conveniently be described in Cartesian tensor notation, sufficient differentiability properties being assumed throughout.

The kinematical structure of the flow field is locally described by the rate of strain tensor:

$$\delta u_i = u_{i,j}\delta x_j \tag{C.2.1}$$

associating a velocity difference vector δu_i to a displacement vector δx_j in physical space.

For fluids without internal friction the dynamics of the flow field follow from the distributions of the flow density vector and momentum tensor:

$$h_i = \rho u_i$$
$$I_{ij} = p\delta_{ij} + \rho u_i u_j$$

the divergence operation on which measures the mass divergence and the external force field:

$$h_{i,i} = \omega \tag{C.2.2}$$

$$I_{ij,i} = F_j \tag{C.2.3}$$

Thirdly, the compressible flow field represents a thermodynamical process, relating locally the quantities p and ρ to the speed of propagation of small disturbances

$$c = \left(\frac{\mathrm{d}p}{\mathrm{d}\rho}\right)^{\frac{1}{2}} \tag{C.2.4}$$

The simplest possible structure of compressible fluid flow is considered, in which local thermodynamical variables p, ρ, c are functions of the velocity magnitude only.

This condition requires the absence of any spatially distributed dynamical influence; i.e. the case in which

$$\begin{aligned} F_j &\equiv 0 \\ \omega &\equiv 0 \end{aligned} \tag{C.2.5}$$

and a uniform relation

$$p = p(\rho) \tag{C.2.5a}$$

exists. Assuming uniform conditions asymptotically in the far field, this leads kinematically to symmetry of the rate of strain tensor

$$u_{i,j} = u_{j,i} \tag{C.2.6}$$

and the integrability of (C.2.3) to a uniform constant

$$\int \frac{\mathrm{d}p}{\rho} + \tfrac{1}{2}u_i u_i = \tfrac{1}{2}q_{\max}^2, \tag{C.2.7}$$

where the reference condition in the integral is taken at zero pressure.

When (C.2.5a) is of the form

$$p = k\rho^{\gamma} + C$$

(cf. ref. 4 for the necessity of this condition), the Mach number

$$M^2 = \frac{u_i u_i}{c^2} \tag{C.2.8}$$

expresses locally velocity similarity under changes of scale in physical space and of values of $q_{\max}$.

The physical properties of the fluid can then locally entirely be described by the continuity condition (C.2.2), which under the conditions (C.2.5) can be written:

$$\left(\delta_{ij} - \frac{1}{c^2} u_i u_j\right) u_{i,j} = 0 \,. \tag{C.2.9}$$

Together with the symmetry condition (C.2.6), this gives the usual equations for compressible potential flow.

C 3 *The hodograph transformation*

In this paragraph, the feasibility of the hodograph transformation for the equation (C.2.9) will be discussed, in which the role of the metrical properties and the dimensionality of the euclidean spaces considered will become apparent. These properties are of some basic interest, but seldom seem to have been made explicit; Birkhoff's discussion (ref. 4) of the group properties of the hodograph transformation would seem to be somewhat beside the real point.

In the previous paragraph, the flow field has been thought to be given as a vector distribution in physical space. However, it is also possible to define the flow field as a one to one mapping between physical space and a "velocity space" or hodograph, spanned by the physical components of the velocity vectors. One notes, that this point of view is only possible in euclidean space, as the aggregate of vectors defined on a general manifold do not form a vector space. Velocity space will be considered as an independent manifold, and the conditions, under which flow properties can invariantly be described by tensor (i.e. locally linear) operations defined on the hodograph manifold, are investigated. Under these conditions, the physical and hodograph manifold could be termed to be locally metrically equivalent.

Locally, the flow field defines a linear transformation

$$\delta\bar{u} = A\,\delta\bar{x} \tag{C.3.1}$$

between displacements vectors $\delta\bar{x}$ in physical space and displacement vectors $\delta\bar{u}$ in velocity space. This affine transformation is given as a matrix A defined in a local cartesian vector base (spanned in a tangent space to the physical manifold), which is simultaneously a local base on the hodograph manifold. Now, from the *affine* point of view, these manifolds are seen to be equivalent by virtue of the group property of the matrices considered: an inverse to the matrix A is immediately given and (C.3.1) can be written equivalently:

$$\delta\bar{x} = A^{-1}\,\delta\bar{u} \,. \tag{C.3.2}$$

However, the description of the flow properties by the divergence operation (C.2.2), (C.2.3) involves the *metrical* properties of space. In our case these have been implicitly used in the definition of the generalized divergence operation in (C.2.9), which is invariant with respect to the euclidean metric.

The use of the tensor notation

$$\delta u_i = u_{i,j}\,\delta x_j \tag{C.3.3}$$

for (C.3.1) expresses the metrical equivalence of the set of linear transformations

$$S_3 A S_3^{-1} \tag{C.3.4}$$

where S_3 are the 3 dim. orthonormal transformations, each one associated with a particular local reference frame. In algebraic terminology, the cartesian 2nd order tensors are thus obtained as equivalence classes in the 3-dim. real linear group by conjugation with the orthonormal sub-group. However, the equivalence relation (C.3.4) does not define sub-groups in the linear group: the inverse of a 2nd order tensor is in general not defined.

This means that in the three dimensional (and axi-symmetric) case, the hodograph manifold is not metrically equivalent, (C.2.9) is not invertible as a tensor expression, leading to a strongly non-linear (not quasi-linear) hodograph equation.

In two dimensions, the situation is different. The plane rotation group is commutative, giving a symmetry in the metrical conditions, which provides the possibility of the inversion operation.

Algebraically, this means that an automorphism of the plane orthonormal group

$$S_2 = \cos\varphi \begin{pmatrix} 1 & 0 \\ 0 & 1 \end{pmatrix} + \sin\varphi \begin{pmatrix} 0 & 1 \\ -1 & 0 \end{pmatrix}$$

is available, given by the translation

$$S_2(\varphi) \to \mathring{S}_2(\varphi) \equiv S_2\left(\varphi + \frac{\pi}{2}\right)$$

by which with every element from the set of 2×2 tensors an inverse can be invariantly associated:

$$\frac{1}{J}(S_2 A S_2^{-1})(\mathring{S}_2 A \mathring{S}_2^{-1})' = (S_2 A S_2^{-1})(S_2 A^{-1} S_2^{-1}) = I\,,$$

where $J = \det A$, and the prime denotes transposition.

Succinctly, this expression embodies the group theoretical interpretation of the hodograph transformations. Explicitly, this construction associates with every (2×2) tensor

$$\begin{pmatrix} u_x & u_y \\ v_x & v_y \end{pmatrix}$$

an inverse tensor, which can be identified as a tensor on the hodograph manifold:

$$\frac{1}{J}\begin{pmatrix} v_y & -u_y \\ -v_x & u_x \end{pmatrix} \equiv \begin{pmatrix} x_u & x_v \\ y_u & y_v \end{pmatrix}.$$

for $J = \det(u_{i,j}) \neq 0$.

The hodograph transformation, expressing the metrical equivalence between the physical and velocity space, is thus seen to be possible by virtue of the linearity of matrix inversion in the 2×2 case and the commutativity of the plane rotation group.

Two types of flow in physical space meet the condition giving a 2×2 rate of strain tensor: plane flows and conical flows (where in the latter case the tensor is defined in a tangent plane to a sphere $r = \text{const.}$), and from the local point of view they have completely analogous properties: locally, for these flows physical properties can be expressed in terms of invariants of the hodograph mapping.

From the global point of view, however, the difference is that the generalized divergence operator in (C.2.9) is *non-linear in velocity space for conical flow, leading to a quasi-linear formal partial differential operator.* For plane flow fields, however, this operator is linear in velocity space, giving the linear differential operator (in a notation which will be clear):

$$\begin{gathered} \left(\delta_{\alpha\beta} - \frac{1}{c_2} u_\alpha u_\beta\right) x_{\alpha,\beta} = 0 \\ x_{\alpha,\beta} = x_{\beta,\alpha}\,, \end{gathered} \tag{C.3.5}$$

the advantages of which in defining explicit solutions has of course been the motivation for the use of the hodograph transformation from Chaplygin (ref. 5) onwards.

It is immediately clear, that velocity space does not have all the invariance properties that physical space has: *the description of the physical properties of the flow field by (C.2.9) is invariant under translations, rotations and* scale transformations, while velocity space is obviously centred, and not invariant under scale transformations. The use of cartesian tensor notation in the hodograph space, while convenient in the present discussion, is thus perhaps open to some objection, which is removed in the formula C.4.5.

Finally, one might remark that the continuity condition can be transformed locally independent of the assumption of symmetry; the irrotationality condition does not involve the metrical properties of space.

C 4 *The principal invariants of the hodograph transformation*

In this paragraph, the algebraic invariants of the hodograph mapping are given a physical interpretation, which will prove useful in analysing the results, par. 2.6. The hodograph mapping will be taken to be represented by the rate of strain tensor (C.2.1), it will be clear that all representations are equivalent, and in fact in section 2 par. 6.2 these results are used expressed in hodograph plane variables. Reyn (ref. 25) has, for the analogous case of conical flow and later (ref. 26) for plane flow, interpreted some of these relations as curvature invariants in his analysis of the differential geometry of the Legendre potential surface in velocity space: the present interpretation is, perhaps, both more elementary and more direct.

The results obtained centre around the influence of compressibility on the acceleration vector, which is not surprising in view of the expression:

$$a_i = u_j u_{i,j}$$

Comparison with (C.2.1) shows the fundamental property of the hodograph transformation: in the hodograph, the tangent to the image of the streamline is in the direction of the acceleration vector in physical space.

Under the assumption of symmetry, the mapping properties (C.2.1) are equivalent to those of the quadratic form:

$$u_{i,j} x_i x_j = 1 \qquad (i, j = 1, 2) \tag{C.4.1}$$

the image of a vector δx_i as transformed by $u_{i,j}$ is normal to the conjugated vector of δx_i with respect to (C.4.1).

The eigenvalue problem for $u_{i,j}$ (which physically corresponds to the search for directions in which the fluid element is deformed without shear) leads to the characteristic equation

$$\lambda^2 - H\lambda + J = 0 \tag{C.4.2}$$

with the principal invariants

$$H = \mathrm{tr}(u_{i,j}) = u_{i,i}$$

$$J = \det u_{i,j} \qquad (i, j = 1, 2)$$

and the relations for the eigenvalues:

$$\lambda_{1,2} = \frac{H}{2} \pm \tfrac{1}{2}\sqrt{H^2 - 4J} \tag{C.4.3}$$

$$\lambda_1 \lambda_2 = J$$

$$\lambda_1 + \lambda_2 = H$$

$$\lambda_1 - \lambda_2 = \sqrt{H^2 - 4J} :$$

the discriminant is immediately seen to be non-negative by the symmetry condition, guaranteeing real λ's.

From (C.2.9) follows for the divergence expression:

$$H = \frac{1}{c^2} u_i u_j u_{i,j} \tag{C.4.4}$$

being $\frac{1}{c^2} \times$ the scalar product of velocity and acceleration vector, and reducing to zero in incompressible flow.

At this point it is convenient to leave tensor notation and consider the particular local reference frame chosen along and normal to the local velocity vector: compact and physically perspicuous results are then obtained because in this case the Mach number is exhibited explicitly.

Eq. (C.2.9) reduces to

$$(1 - M^2) q_s + q\theta_n = 0 \tag{C.4.5}$$

and

$$u_{i,j} \to \begin{pmatrix} q_s & q_n \\ q\theta_s & q\theta_n \end{pmatrix} = \begin{pmatrix} q_s & q\theta_s \\ q\theta_s & -(1 - M^2) q_s \end{pmatrix}$$

using (C.4.5) and the symmetry condition. $(qq_s, q^2\theta_s)$ are the components of the acceleration vector a_i in the resulting orthogonal curvilinear co-ordinates, formed by streamlines and equipotential lines.

Then

$$\left.\begin{aligned} J &= \lambda_1 \lambda_2 = -(1 - M^2) q_s^2 - q^2 \theta_s^2 \\ H &= \lambda_1 + \lambda_2 = M^2 q_s \end{aligned}\right\} \tag{C.4.6}$$

and

$$\lambda_{1,2} = \tfrac{1}{2} M^2 q_s \pm \sqrt{(1 - \tfrac{1}{2}M^2)^2 q_s^2 + q^2 \theta_s^2} .$$

Using these values one obtains for the directions of the eigenvectors the condition

$$\operatorname{cotg} 2\chi = (1 - \tfrac{1}{2}M^2) \operatorname{cotg} \alpha , \tag{C.4.7}$$

where

$$\alpha = \operatorname{arc\,tg} \frac{q\theta_s}{q_s} \tag{C.4.7a}$$

is the angle enclosed between acceleration vector and velocity vector, and the two roots of (C.4.7) give two perpendicular principal directions, in terms of the angles $\chi_{1,2}$ with respect to the direction of the velocity vector. One notes that in incompressible flow the eigenvectors bisect the angle between velocity and acceleration vectors, and that for $M=\sqrt{2}$ the eigenvectors have the characteristic directions, independent of the acceleration.

By the eigenvalue analysis, the quadratic form (C.4.1) has now been brought into standard form

$$\lambda_1 x_1^2 + \lambda_2 x_2^2 = 1 \tag{C.4.1a}$$

and can be classified as to type. For subsonic flow, by (C.4.6), $J<0$, so that λ_1, λ_2 always have opposite sign, (C.4.1) representing a system of conjugate hyperboles, orthogonal for $M=0$. For supersonic flow, however, J may go through zero and become positive, and the representation of the quadratic form goes through the degenerate case into an ellipse.

A direct physical interpretation of these facts is obtained by considering the structure of wave propagation in the flow. Introducing characteristic directions, which in this context are given by the displacement vectors mapping independent of the direction of the acceleration vector, one obtains

$$\operatorname{tg}^2 \beta = \frac{1}{M^2-1} \tag{C.4.8}$$

where β is the Mach angle. The pairwise orthogonality of these directions with their images in the hodograph plane, leading to the pair of linear ordinary differential equations

$$\frac{q\,\mathrm{d}\theta}{\mathrm{d}q} = \pm \operatorname{tg} \beta$$

for the fixed characteristics in the hodograph plane, is immediate.

Now, *choosing in the physical plane positive directions for the arc length on the two characteristic curves* ξ and η for $|\beta| < \frac{\pi}{2}$, the projections of the vector $(q_s, q\theta_s)$ on the two characteristic directions can be identified with the intrinsic derivatives q_ξ and q_η respectively. One obtains the decomposition

$$\begin{aligned} q_\xi + q_\eta &= 2\cos\beta\, q_s \\ q_\xi - q_\eta &= 2\sin\beta\, q\theta_s \end{aligned} \tag{C.4.9}$$

and the expression

$$J = M^2 q_\xi q_\eta \tag{C.4.10}$$

(C.4.9) expresses for locally supersonic flow the components of the acceleration vector in terms of the quantities q_ξ, q_η, the "strength" associated with the η and ξ-characteristic respectively, at the point in the physical plane considered. According to the sign of the associated strength, a characteristic may be termed expansive $(+)$ or compressive $(-)$. Also, (C.4.9) shows the reflection phenomena against the sonic line for $\beta = \frac{\pi}{2}$.

Clearly, in a supersonic flow $J<0$ means that characteristics of both types are present, $J>0$ indicates that both are of the same type.

These results can be conveniently summarized in vector notation:

$$J = M^2(\bar{q}_s \cdot \bar{\xi})(\bar{q}_s \cdot \bar{\eta}) \tag{C.4.11}$$

where $\bar{q}_s$ is the vector $(q_s, q\theta_s)$ and $\bar{\xi}$ and $\bar{\eta}$ are *unit vectors in the characteristic directions*. This shows sign J to indicate, whether the angle between acceleration vector and velocity vector be smaller or larger than $\frac{\pi}{2} - \beta$ or, in the hodograph plane, whether the tangent vector to the image of the streamline includes a smaller or larger than characteristic angle with the velocity vector. Also, of course, J measures the area ratio of elementary surface elements under the hodograph mapping, and sign J indicates the orientation of the mapping (circulation index).

Finally, one notes that the quantities q_ξ, q_η are a measure for the curvature of the ξ, η characteristic.

Explicitly, one has for, say, a ξ-characteristic:

$$\begin{aligned} \frac{1}{R} &= \frac{\partial}{\partial \xi}(\theta+\beta) \\ &= q_\xi\left(\beta_q + \frac{1}{q}\sqrt{M^2-1}\right) \\ &= \frac{1}{q} q_\xi \left[(M^2-1)^{-\frac{1}{2}}\left(\frac{3-\gamma}{2} M^2 - 2\right)\right] \end{aligned} \tag{C.4.12}$$

the last expression valid for the polytropic gas law. It is seen that a characteristic has an inflexion point on curves where $J=0$ (which are easily seen to be characteristic) and on the isobar for which

$$M = \left(\frac{4}{3-\gamma}\right)^{\frac{1}{2}} \qquad (=1.58 \quad \text{for} \quad \gamma=1.4),$$

a result first noted by Christianovitch (1941).

C 5 *Singularities of the hodograph transformation*

In the previous paragraph, the local physical and geometrical meaning of sign J has been discussed. Obviously, its main significance is as a local index for the topological properties of solutions in the large: in general, a change of sign in the functional determinant indicates the occurrence of a fold in either the physical or hodograph manifold.

The resulting singularities of the hodograph transformation for plane flows have been exhaustively investigated by Geiringer (in ref. 17) and their properties will here only be touched upon.

For a potential flow, $J<0$ in a subsonic region (C.4.6); thus a change in the sign of J can occur only in a supersonic region. However, a continuous transonic profile flow is by definition of the same type as a subsonic one, i.e. derivable from a continuous transformation, and this means $J<0$ *in the external flow field*. This is a basic inequality for these flows; the local physical consequences in the supersonic region have been discussed in C 4. (It may be remarked, that the definition $J=\det(u_{i,j})$ is used consistently in this discussion rather than its inverse, which would be perhaps the more natural when discussing properties in the physical plane of a solution defined in the hodograph).

A change of sign in J through a curve on which $J=0$ (branch line) indicates a fold in the hodograph manifold. It can immediately be read off from the formulae presented in par. C.4, that this curve in the (regular) physical plane is a characteristic, on which the other family of characteristics changes type (compressive $\leftrightarrow$ expansive). This type of hodograph plane singularity is physically realised in Laval nozzle flows. In the theory of this report, this type of singularity has been excluded by the fundamental postulate of regularity of the solution in the hodograph of the external flow, excepting the singularities representing conditions at infinity in physical space. However, for a regular solution defined in the hodograph plane, J can very well change sign through infinity on a curve in the supersonic region. This gives a fold in the physical manifold, the edges of which are the much discussed limit lines, forming a locus of cusps for characteristics of one family and for streamlines. When part of the boundary streamline $\psi=0$ is located on this fold, no regular profile is defined in the physical space, indicating the end to the usefulness of the theory.

It is known (ref. 21) that for a profile defined in the hodograph plane, when $J<0$ on the image of the boundary streamline, $J<0$ and regular in the entire image of the external flow field, i.e. the mapping in the physical plane is regular when the image of the boundary streamline is regular.

Apparently, "limit lines" have a long life in the "explanation" of shock phenomena. However, potential flow solutions, whether containing limit lines or not, are symmetric with respect to reversal of flow direction, while shock waves as viscous phenomena induce physically essentially asymmetrical effects. The physical justification of any attempt to characterise the genesis of shock waves in the flow around a given contour in terms of the singularities induced by a limit line, would seem to be extremely slight. In fact, as suggested before, limit lines appear in physical space as a consequence of the fundamental postulate of continuity of the solution in velocity space, and thus essentially result from the artifice of the hodograph transformation.

All the same, it would be interesting to know explicitly how limit lines are generated in an analytic hodograph under Lighthill's transformation (2.1.3), in order to study the connection with the "generating singularities" of the physical flow, and thus to visualise the complete compressible counterparts of the incompressible manifolds discussed in 2.2. Unfortunately, the series representations of solutions ψ are to awkward to elucidate these questions.

C.C.L. Class. D 304

REPORT NLR-TR W. 7

Tunnel wall corrections for a wing-flap system between two parallel walls.

by

E. M. de Jager and A. I. van de Vooren

Summary

A method is presented for the calculation of the corrections due to the tunnel walls, to be applied to the measured lift and moment of a two-dimensional wing-flap model between two parallel walls.

The theory developed here is non-linearized since the angle of flap deflection may be large. Calculations have been performed for three values of the ratio of wing to flap chord, for three values of the ratio of wing chord to tunnelheight and for angles of flap deflection up to 75°.

Contents

List of symbols.

a	wing chord
b	flap chord
a_i	coefficients of expansion of $\Delta p^*(x)-\Delta p(x)$
c_i	coefficients of expansion of $\gamma(x)$
c_i^*	coefficients of expansion of $\gamma^*(x)$
Δc_i	coefficients of expansion of $\Delta\gamma(x)$
h	semi-height of the tunnel
$p(x)$	pressure on aerofoil for wing-flap system in tunnel (positive in upward direction)
$p^*(x)$	pressure on aerofoil for wing-flap system in free flight (positive in upward direction)
$\Delta p(x)$	the difference $p^*(x)-p(x)$
s	distance along the flap
u	perturbation velocity component in x-direction
v	perturbation velocity component in y-direction
x,y	coordinates; y positive in downward direction
z	$x+iy$
C_L, C_M	lift resp. moment coefficient for wing-flap system in tunnel
C_L^*, C_M^*	lift resp. moment coefficient for wing-flap system in free flight
$\Delta C_L, \Delta C_M$,	$C_L^*-C_L, C_M^*-C_M$, tunnel wall corrections. These corrections are to be added to the tunnel values in order to obtain values in free flight
F	complex potential; $F=\Phi+i\psi$
$K^{(i)}(x,\xi)$	$i=1,2,3,4$; kernel of integral equation for vorticity distribution of wing-flap system in tunnel
$K^{(i)*}(x,\xi)$	$i=1,2,3,4$; ditto for free flight
$\Delta K^{(i)}(x,\xi)$	$i=1,2,3,4; K^{(i)*}(x,\xi)-K^{(i)}(x,\xi)$
U	velocity at infinity
$\gamma(x)$	vorticity distribution of wing-flap system in tunnel
$\gamma^*(x)$	vorticity distribution of wing-flap system in free flight
$\Delta\gamma(x)$	the difference $\gamma^*(x)-\gamma(x)$
δ	angle of flap deflection
ϑ	$\cos\vartheta = -\dfrac{2\xi+a}{a} \qquad 0<\vartheta<\pi$
ϑ'	$\cos\vartheta' = \dfrac{b\cos\delta-2\xi}{b\cos\delta} \qquad 0<\vartheta'<\pi$
ξ,η	integration variables; ξ corresponds with x-direction and η with y-direction
ρ	density

τ	ratio of flap to total wing-chord	Φ	velocity potential
Γ	vortex strength	ψ	stream function

1 Introduction.

The experimental investigation of high-lift devices in a wind tunnel requires the knowledge of tunnel wall corrections for such configurations; in order to reduce the results to free flow conditions.

At the National Aeronautical and Astronautical Research Institute an experimental program has been performed during which pressure distribution, lift-moment and drag have been measured for a two-dimensional wing-flap system at large angles of flap deflection. In order to retain smooth flow, air is blown along the upper side of the flap.

Tunnel wall corrections for this configuration, in comparison with those for a usual model, show the following complications:

(i) due to the large flap deflection it is not a priori certain, that linearization of the equations governing the flow is admissible;
(ii) even if the wing is placed in the middle of the tunnel, the points near the trailing edge are not and this leads to a more complicated reflection pattern of vortices;
(iii) the blown air can be schematized by a jet, which will influence the flow around the model, but this influence itself is also affected by tunnel wall corrections;
(iv) due to the larger lift an unfavorable pressure gradient will develop at the part of the lower wall, which is ahead of the model and which may induce boundary layer separation.

In the present report points (i) and (ii) are investigated. As long as the momentum of the jet is not too large, point (iii) will not be too important. It will form the subject of a further theoretical investigation. If boundary layer separation at the wall occurs, more or less important modifications of the tunnel wall corrections due to points (i) through (iii) can be expected. This, however, is probably more suited for experimental investigation. In any case it should be tried to prevent boundary layer separation at the wall.

The physical problem to be treated in this report has been schematized to a two-dimensional problem and therefore the influence of the sidewalls of the tunnel have not been taken into account.

2 General survey of the investigation.

The aerofoil is considered sufficiently thin to warrant its replacement by a single vortex sheet, coinciding with its mean camber line. As the aerofoil is symmetrical, this mean camber line consists of two straight line segments, the angle between them being equal to the flap deflection.

The local strength of the vortex sheet is determined by the condition of tangential flow at the aerofoil. This condition leads to an integral equation for the vortex distribution, containing the angle of flap deflection as a parameter, and which will be solved approximately.

Using the assumptions mentioned above, exact solutions for the case of a free aerofoil have been given by Keune (ref. 1). These exact solutions are used in the present investigation to check the approximate theory for the free aerofoil. Agreement turns out to be very satisfactory and therefore the approximate theory may be applied also for the aerofoil between tunnel walls, where no exact solution is available for an aerofoil with flap. It may be added that for a plain aerofoil between tunnel walls, an exact solution has been given by Tomotika (refs. 2, 3), but it did not seem feasible to extend this solution to an aerofoil with flap.

The approximation method itself consists in assuming for the vortex distribution a sum of six terms, each of them being the product of an unknown coefficient and a known function of the chordwise coordinate. Two of these functions contain a singularity, namely the square root singularity at the leading edge and the singularity corresponding to the flow at the angle between the two line segments. The four other functions are regular functions.

The six unknown coefficients are determined by a collocation method, which is well-known in lifting surface theory as the method of the pivotal points (see e.g. Multhopp, ref. 4).

In this way the vortex distribution for the free aerofoil and for the aerofoil between the walls can be determined, and the pressure distribution can be calculated by aid of formulae containing non-linear terms. After subtraction of the results for the cases without and with tunnel walls, the tunnel wall corrections could be obtained, unless so many digits disappear, that the corrections are of the same order of magnitude as the error introduced by the approximation method for solving the integral equation. Therefore it has been considered preferable to apply the approximation method to the determination of the difference between the vorticity distribution of the aerofoil in free flow and in the tunnel, instead of to the vorticity distribution itself. After this difference in vortex distribution has been determined, the corresponding difference in pressure distribution, i.e. the correction in the pressure distribution due to the tunnel walls, is obtained. Corrections for lift and moment are presented.

3 Analytical description of the method.

3.1 *The velocity field of a vortex placed asymmetrically between the tunnel walls.*

Due to the large flap deflection the vortices at the flap may no longer be assumed to have their position at the middle of the tunnel. We therefore shall investigate at first the flow field of a vortex which is placed at a distance η below the horizontal plane of symmetry of the tunnel. Let the tunnelheight be $2h$. The scheme of successive reflections of the vortex by the walls is shown in sketch a. If the original vortex at η has a positive strength Γ (clockwise rotation), it is seen that the complete pattern consists of vortices of strength $+\Gamma$ at $\eta+4nh$ and vortices of strength $-\Gamma$ at $2h-\eta+4nh$, where n assumes all positive and negative integer values including 0.

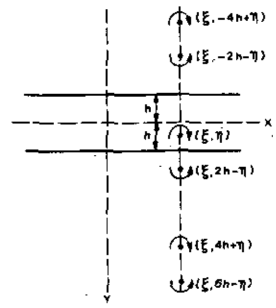

Sketch a: Reflection of vortices by tunnel walls.

The complex potential at a point $z=x+\mathrm{i}y$ (y-axis taken downward), due to a single vortex at the point z_1 is equal to

$$F = -\frac{\mathrm{i}\Gamma}{2\pi}\ln(z-z_1)$$

The complex velocity due to this vortex is

$$\frac{\mathrm{d}F}{\mathrm{d}z} = u-\mathrm{i}v = -\frac{\mathrm{i}\Gamma}{2\pi(z-z_1)}$$

where u and v are the velocity components in x-, and y-directions. Hence the complex velocity due to the complete vortex pattern is

$$-\frac{\mathrm{i}\Gamma}{2\pi}\sum_{n=-\infty}^{\infty}\left\{\frac{1}{z-\xi-\mathrm{i}(\eta+4nh)}-\frac{1}{z-\xi-\mathrm{i}(2h-\eta+4nh)}\right\}$$

Putting

$$z-\xi-\mathrm{i}\eta = \frac{4\mathrm{i}h\zeta}{\pi} \quad\text{and}\quad z-\xi-\mathrm{i}(2h-\eta) = \frac{4\mathrm{i}h\zeta'}{\pi}$$

this becomes

$$-\frac{\Gamma}{8h}\sum_{n=-\infty}^{\infty}\left(\frac{1}{\zeta-n\pi}-\frac{1}{\zeta'-n\pi}\right)$$

According to the theorem of Mittag-Leffler (ref. 5), one has

$$\operatorname{cotg}\zeta-\frac{1}{\zeta} = \sum_{\substack{n=-\infty\\ n\neq 0}}^{+\infty}\left\{\frac{1}{\zeta-n\pi}+\frac{1}{n\pi}\right\}$$

Hence $\operatorname{cotg}\zeta-\operatorname{cotg}\zeta' = \sum_{n=-\infty}^{+\infty}\left\{\frac{1}{\zeta-n\pi}-\frac{1}{\zeta'-n\pi}\right\}$ and thus

$$u-\mathrm{i}v = -\frac{\Gamma}{8h}\left[\cot\frac{\pi(z-\xi-\mathrm{i}\eta)}{4\mathrm{i}h}-\cot\frac{\pi\{z-\xi-\mathrm{i}(2h-\eta)\}}{4\mathrm{i}h}\right]$$

Using the formula

$$\cot(A+\mathrm{i}B) = \frac{\sin 2A-\mathrm{i}\sinh 2B}{\cosh 2B-\cos 2A}$$

the result for u and v becomes

$$u = -\frac{\Gamma}{8h}\left\{\frac{\sin\frac{\pi(y-\eta)}{2h}}{\cosh\frac{\pi(x-\xi)}{2h}-\cos\frac{\pi(y-\eta)}{2h}}+\frac{\sin\frac{\pi(y+\eta)}{2h}}{\cosh\frac{\pi(x-\xi)}{2h}+\cos\frac{\pi(y+\eta)}{2h}}\right\}$$

$$v = \frac{\Gamma}{8h}\left\{\frac{\sinh\frac{\pi(x-\xi)}{2h}}{\cosh\frac{\pi(x-\xi)}{2h}-\cos\frac{\pi(y-\eta)}{2h}}-\frac{\sinh\frac{\pi(x-\xi)}{2h}}{\cosh\frac{\pi(x-\xi)}{2h}+\cos\frac{\pi(y+\eta)}{2h}}\right\} \tag{3.1}$$

3.2 *The integral equation for the vortex distribution.*

For simplicity we shall assume that the wing is at zero incidence and at the middle of the tunnel. The chord of the wing (without flap) is a and the flap chord is b. The origin of coordinates is taken at the common point of wing and flap. The angle of flap deflection is δ. The complete scheme is shown in sketch b. The case that the wing angle of incidence is different from zero leads to more complicated formulae since then the wing vortices are not at the middle of the tunnel. However, there are no new fundamental difficulties and this case will be left out of discussion here.

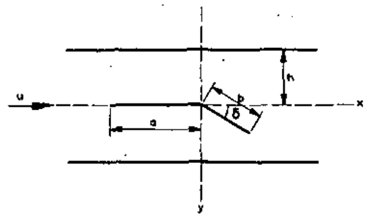

Sketch b: The position of the model in the tunnel.

The integral equation for the vortex distribution follows from the condition of vanishing normal velocity. This means

(i) at the wing $v=0$

(ii) at the flap $-(U+u)\sin\delta+v\cos\delta=0$. (3.2)

U is the speed of the undisturbed flow, while u and v denote the velocity components due to the vortex distribution. The vortex distribution will be denoted by $\gamma(\xi)$, which for the flap denotes the vorticity in that point of the flap which has ξ as its x-coordinate.

Consider first the normal velocity v_1 at the wing due to the wing vortices. Then $y=\eta=0$ and the normal velocity becomes by aid of eq. (3.1)

$$v_1(x,0) = \frac{1}{8h}\int_{-a}^{0}\gamma(\xi)\left\{\frac{\sinh\frac{\pi(x-\xi)}{2h}}{\cosh\frac{\pi(x-\xi)}{2h}-1}-\frac{\sinh\frac{\pi(x-\xi)}{2h}}{\cosh\frac{\pi(x-\xi)}{2h}+1}\right\}d\xi\,.$$

or

$$v_1(x,0) = \frac{1}{4h}\int_{-a}^{0}\frac{\gamma(\xi)}{\sinh\frac{\pi(x-\xi)}{2h}}\,d\xi \tag{3.3}$$

The normal velocity v_2 at the wing due to the flap vortices follows by taking $y=0$ and $\eta=\xi\tan\delta$. Hence

$$v_2(x,0) = \frac{1}{8h}\int_{0}^{b\cos\delta}\gamma(\xi)\left\{\frac{\sinh\frac{\pi(x-\xi)}{2h}}{\cosh\frac{\pi(x-\xi)}{2h}-\cos\frac{\pi\xi\tan\delta}{2h}}-\frac{\sinh\frac{\pi(x-\xi)}{2h}}{\cosh\frac{\pi(x-\xi)}{2h}+\cos\frac{\pi\xi\tan\delta}{2h}}\right\}\frac{d\xi}{\cos\delta}$$

or

$$v_2(x,0) = \frac{1}{4h\cos\delta}\int_{0}^{b\cos\delta}\gamma(\xi)\frac{\sinh\frac{\pi(x-\xi)}{2h}\cos\frac{\pi\xi\tan\delta}{2h}}{\cosh^2\frac{\pi(x-\xi)}{2h}-\cos^2\frac{\pi\xi\tan\delta}{2h}}\,d\xi \tag{3.4}$$

The normal velocity at the flap due to the wing vortices is obtained by taking $y=x\tan\delta$ and $\eta=0$

$$\{-u_1(x,y)\sin\delta+v_1(x,y)\cos\delta\}_{y=x\tan\delta}=$$

$$\frac{1}{8h}\int_{-a}^{0}\gamma(\xi)\left\{\frac{\sin\dfrac{\pi x\tan\delta}{2h}\sin\delta+\sinh\dfrac{\pi(x-\xi)}{2h}\cos\delta}{\cosh\dfrac{\pi(x-\xi)}{2h}-\cos\dfrac{\pi x\tan\delta}{2h}}+\frac{\sin\dfrac{\pi x\tan\delta}{2h}\sin\delta-\sinh\dfrac{\pi(x-\xi)}{2h}\cos\delta}{\cosh\dfrac{\pi(x-\xi)}{2h}+\cos\dfrac{\pi x\tan\delta}{2h}}\right\}d\xi$$

or

$$\{-u_1(x,y)\sin\delta+v_1(x,y)\cos\delta\}_{y=x\tan\delta}=$$

$$\frac{1}{4h}\int_{-a}^{0}\gamma(\xi)\frac{\sin\dfrac{\pi x\tan\delta}{2h}\sin\delta\cosh\dfrac{\pi(x-\xi)}{2h}+\cos\dfrac{\pi x\tan\delta}{2h}\cos\delta\sinh\dfrac{\pi(x-\xi)}{2h}}{\cosh^2\dfrac{\pi(x-\xi)}{2h}-\cos^2\dfrac{\pi x\tan\delta}{2h}}d\xi \tag{3.5}$$

Finally, the normal velocity at the flap due to the flap vortices is obtained by taking $y=x\tan\delta$ and $\eta=\xi\tan\delta$

$$\{-u_2(x,y)\sin\delta+v_2(x,y)\cos\delta\}_{y=x\tan\delta}=$$

$$\frac{1}{8h}\int_{0}^{b\cos\delta}\gamma(\xi)\left\{\frac{\sin\dfrac{\pi(x-\xi)\tan\delta}{2h}\sin\delta+\sinh\dfrac{\pi(x-\xi)}{2h}\cos\delta}{\cosh\dfrac{\pi(x-\xi)}{2h}-\cos\dfrac{\pi(x-\xi)\tan\delta}{2h}}+\frac{\sin\dfrac{\pi(x+\xi)\tan\delta}{2h}\sin\delta-\sinh\dfrac{\pi(x-\xi)}{2h}\cos\delta}{\cosh\dfrac{\pi(x-\xi)}{2h}+\cos\dfrac{\pi(x+\xi)\tan\delta}{2h}}\right\}\frac{d\xi}{\cos\delta} \tag{3.6}$$

The integral equations for the vorticity distribution can then be written as

$$\begin{aligned}&\int_{-a}^{0}\gamma(\xi)K^{(1)}(x,\xi)d\xi+\int_{0}^{b\cos\delta}\gamma(\xi)K^{(2)}(x,\xi)d\xi=0 \qquad -a\leqq x\leqq 0\\ &\int_{-a}^{0}\gamma(\xi)K^{(3)}(x,\xi)d\xi+\int_{0}^{b\cos\delta}\gamma(\xi)K^{(4)}(x,\xi)d\xi=U\sin\delta \qquad 0\leqq x\leqq b\cos\delta\end{aligned} \tag{3.7}$$

where

$$K^{(1)}(x,\xi)=\frac{1}{4h\sinh\dfrac{\pi(x-\xi)}{2h}}$$

$$K^{(2)}(x,\xi)=\frac{1}{4h\cos\delta}\frac{\sinh\left\{\dfrac{\pi(x-\xi)}{2h}\right\}\cos\left\{\dfrac{\pi\xi\tan\delta}{2h}\right\}}{\cosh^2\left\{\dfrac{\pi(x-\xi)}{2h}\right\}-\cos^2\left\{\dfrac{\pi\xi\tan\delta}{2h}\right\}}$$

$$K^{(3)}(x,\xi)=\frac{1}{4h}\frac{\sin\left\{\dfrac{\pi x\tan\delta}{2h}\right\}\sin\delta\cosh\left\{\dfrac{\pi(x-\xi)}{2h}\right\}+\cos\left\{\dfrac{\pi x\tan\delta}{2h}\right\}\cos\delta\sinh\left\{\dfrac{\pi(x-\xi)}{2h}\right\}}{\cosh^2\left\{\dfrac{\pi(x-\xi)}{2h}\right\}-\cos^2\left\{\dfrac{\pi x\tan\delta}{2h}\right\}}$$

$$\begin{aligned}K^{(4)}(x,\xi)=\frac{1}{8h\cos\delta}\Bigg[&\frac{\sin\left\{\dfrac{\pi(x-\xi)\tan\delta}{2h}\right\}\sin\delta+\sinh\left\{\dfrac{\pi(x-\xi)}{2h}\right\}\cos\delta}{\left\{\cosh\dfrac{\pi(x-\xi)}{2h}\right\}-\cos\left\{\dfrac{\pi(x-\xi)\tan\delta}{2h}\right\}}+\\ &+\frac{\sin\left\{\dfrac{\pi(x+\xi)\tan\delta}{2h}\right\}\sin\delta-\sinh\left\{\dfrac{\pi(x-\xi)}{2h}\right\}\cos\delta}{\cosh\left\{\dfrac{\pi(x-\xi)}{2h}\right\}+\cos\left\{\dfrac{\pi(x+\xi)\tan\delta}{2h}\right\}}\Bigg]\end{aligned} \tag{3.8}$$

Introducing asterisks to denote free flight conditions, one obtains for $h\to\infty$ the integral equations for the vorticity distribution for the wing in free flight, viz.:

$$\int_{-a}^{0} \gamma^*(\xi)K^{(1)*}(x,\xi)\mathrm{d}\xi + \int_{0}^{b\cos\delta} \gamma^*(\xi)K^{(2)*}(x,\xi)\mathrm{d}\xi = 0 \qquad -a \leqq x \leqq 0$$

$$\int_{-a}^{0} \gamma^*(\xi)K^{(3)*}(x,\xi)\mathrm{d}\xi + \int_{0}^{b\cos\delta} \gamma^*(\xi)K^{(4)*}(x,\xi)\mathrm{d}\xi = U \sin\delta \quad 0 \leqq x \leqq b\cos\delta \tag{3.9}$$

where

$$\begin{aligned} K^{(1)*}(x,\xi) &= \frac{1}{2\pi(x-\xi)} \\ K^{(2)*}(x,\xi) &= \frac{1}{2\pi\cos\delta}\,\frac{x-\xi}{(x-\xi)^2+\xi^2\tan^2\delta} \\ K^{(3)*}(x,\xi) &= \frac{1}{2\pi\cos\delta}\,\frac{x-\xi\cos^2\delta}{(x-\xi)^2+x^2\tan^2\delta} \\ K^{(4)*}(x,\xi) &= \frac{1}{2\pi(x-\xi)} \end{aligned} \tag{3.10}$$

Subtracting corresponding equations of (3.7) and (3.9) and introducing the quantities

$$\begin{aligned} \Delta\gamma(\xi) &= \gamma^*(\xi) - \gamma(\xi) \qquad \text{and} \\ \Delta K^{(i)}(x,\xi) &= K^{(i)*}(x,\xi) - K^{(i)}(x,\xi) \end{aligned} \tag{3.11}$$

one obtains for the corrections $\Delta\gamma(\xi)$ the integral equations

$$\int_{-a}^{0} \Delta\gamma(\xi)K^{(1)}(x,\xi)\mathrm{d}\xi + \int_{0}^{b\cos\delta} \Delta\gamma(\xi)K^{(2)}(x,\xi)\mathrm{d}\xi = -\int_{-a}^{0} \gamma^*(\xi)K^{(1)}(x,\xi)\mathrm{d}\xi - \int_{0}^{b\cos\delta} \gamma^*(\xi)\Delta K^{(2)}(x,\xi)\mathrm{d}\xi \qquad -a \leqq x \leqq 0$$

$$\int_{-a}^{0} \Delta\gamma(\xi)K^{(3)}(x,\xi)\mathrm{d}\xi + \int_{0}^{b\cos\delta} \Delta\gamma(\xi)K^{(4)}(x,\xi)\mathrm{d}\xi = -\int_{-a}^{0} \gamma^*(\xi)\Delta K^{(3)}(x,\xi)\mathrm{d}\xi - \int_{0}^{b\cos\delta} \gamma^*(\xi)\Delta K^{(4)}(x,\xi)\mathrm{d}\xi \qquad 0 \leqq x \leqq b\cos\delta \tag{3.12}$$

After solution of the integral equations (3.9) for $\gamma^*(\xi)$ and substituting the result into the right-hand sides of equations (3.12), one obtains a set of integral equations for the corrections $\Delta\gamma(\xi)$, which has the same kernels as the system (3.7).

For the solution of the integral equations a numerical method has been used which is described in Sec. 4.

3.3 *The pressure distribution at the aerofoil.*

The pressure in an arbitrary point of the field can be calculated from Bernouilli's equation

$$p + \tfrac{1}{2}\rho\{(U+u)^2 + v^2\} = \text{constant in the whole field.}$$

Hence, at the aerofoil

$$p^+(x) + \tfrac{1}{2}\rho v_{\mathrm{tang}}^{+2}(x) = p^-(x) + \tfrac{1}{2}\rho v_{\mathrm{tang}}^{-2}(x)$$

where the superscript + denotes the lower side of the aerofoil ($y=0^+$) and the superscript − denotes the upper side ($y=0^-$). The tangential velocity along the aerofoil is denoted by v_{tang}. Taking the pressure difference $\Delta p(x)$ positive in upward direction, one obtains

$$\Delta p(x) = p^+(x) - p^-(x) = \tfrac{1}{2}\rho\gamma(x)\,\{v_{\mathrm{tang}}^+(x) + v_{\mathrm{tang}}^-(x)\} \tag{3.13}$$

where $\gamma(x) = v_{\mathrm{tang}}^-(x) - v_{\mathrm{tang}}^+(x)$. In linearized theory the sum of the two tangential velocities may be replaced by $2U$, but this is not allowed here.

We must now calculate the tangential velocities due to the vortex distribution, and we shall do this by a similar splitting-up as was introduced when calculating the normal velocities.

The tangential velocity at the wing due to the wing vortices is given by

$$u_1(x,0^+) = -\tfrac{1}{2}\gamma(x) \quad \text{and} \quad u_1(x,0^-) = \tfrac{1}{2}\gamma(x) \tag{3.14}$$

This simple result is due to the fact that the tangential velocities of the reflected vortices at $2nh$ cancel out for each pair of positive and negative n. This result holds only if the wing is at the middle of the tunnel.

The tangential velocity at the wing due to the flap vortices is obtained from eq. (3.1) by substituting $y=0$, $\eta=\xi\tan\delta$. This velocity is equal for $y=0^+$ and $y=0^-$

$$u_2(x,0)=-\frac{1}{8h}\int_0^{b\cos\delta}\gamma(\xi)\left\{\frac{-\sin\dfrac{\pi\xi\tan\delta}{2h}}{\cosh\dfrac{\pi(x-\xi)}{2h}-\cos\dfrac{\pi\xi\tan\delta}{2h}}+\frac{\sin\dfrac{\pi\xi\tan\delta}{2h}}{\cosh\dfrac{\pi(x-\xi)}{2h}+\cos\dfrac{\pi\xi\tan\delta}{2h}}\right\}\frac{d\xi}{\cos\delta}$$

or

$$u_2(x,0)=\frac{1}{4h\cos\delta}\int_0^{b\cos\delta}\gamma(\xi)\frac{\sin\dfrac{\pi\xi\tan\delta}{h}}{\cosh\dfrac{\pi(x-\xi)}{h}-\cos\dfrac{\pi\xi\tan\delta}{h}}d\xi \tag{3.15}$$

The tangential velocity at the flap due to the wing vortices follows from (3.1) by taking $y=x\tan\delta$ and $\eta=0$. This part of the tangential velocity is equal at upper and lower side of the flap:

$\{u_1(x,y)\cos\delta+v_1(x,y)\sin\delta\}_{y=x\tan\delta}=$

$$\frac{1}{8h}\int_{-a}^{0}\gamma(\xi)\left\{\frac{-\sin\dfrac{\pi x\tan\delta}{2h}\cos\delta+\sinh\dfrac{\pi(x-\xi)}{2h}\sin\delta}{\cosh\dfrac{\pi(x-\xi)}{2h}-\cos\dfrac{\pi(x\tan\delta)}{2h}}+\frac{-\sin\dfrac{\pi x\tan\delta}{2h}\cos\delta-\sinh\dfrac{\pi(x-\xi)}{2h}\sin\delta}{\cosh\dfrac{\pi(x-\xi)}{2h}+\cos\dfrac{\pi x\tan\delta}{2h}}\right\}d\xi$$

or

$\{u_1(x,y)\cos\delta+v_1(x,y)\sin\delta\}_{y=x\tan\delta}=$

$$\frac{1}{4h}\int_{-a}^{0}\gamma(\xi)\frac{-\sin\dfrac{x\pi\tan\delta}{2h}\cos\delta\cosh\dfrac{\pi(x-\xi)}{2h}+\cos\dfrac{\pi x\tan\delta}{2h}\sin\delta\sinh\dfrac{\pi(x-\xi)}{2h}}{\cosh^2\dfrac{\pi(x-\xi)}{2h}-\cos^2\dfrac{\pi x\tan\delta}{2h}}d\xi \tag{3.16}$$

Finally, the tangential velocity at the flap due to the flap vortices must be considered. This tangential velocity however is discontinuous over the flap. Hence, this velocity must be calculated from eqs. (3.1) by substituting $y=x\tan\delta\pm\varepsilon$, $\eta=\xi\tan\delta$ and then, after having integrated over the whole flap, taking the limit $\varepsilon\to0$. Thus

$\{u_2(x,y)\cos\delta+v_2(x,y)\sin\delta\}_{y=x\tan\delta\pm\varepsilon}=$

$$\lim_{\varepsilon\to0}\frac{1}{8h}\int_0^{b\cos\delta}\gamma(\xi)\left\{\frac{-\sin\dfrac{\pi\{(x-\xi)\tan\delta\pm\varepsilon\}}{2h}\cos\delta+\sinh\dfrac{\pi(x-\xi)}{2h}\sin\delta}{\cosh\dfrac{\pi(x-\xi)}{2h}-\cos\dfrac{\pi\{(x-\xi)\tan\delta\pm\varepsilon\}}{2h}}+\right.$$
$$\left.-\frac{\sin\dfrac{\pi\{(x+\xi)\tan\delta\pm\varepsilon\}}{2h}\cos\delta+\sinh\dfrac{\pi(x-\xi)}{2h}\sin\delta}{\cosh\dfrac{\pi(x-\xi)}{2h}+\cos\dfrac{\pi\{(x+\xi)\tan\delta\pm\varepsilon\}}{2h}}\right\}\frac{d\xi}{\cos\delta}$$

For the second term of the integrand, the limit transition can be performed without difficulty. In the first term, however, taking $\varepsilon=0$ under the integral sign would lead to an integrand of which both the numerator and the denominator vanish for $\xi=x$. Therefore, the transition is not allowed in the first term.

The interval of integration of the first integral will be divided as

$$\int_0^{x-\Delta}+\int_{x-\Delta}^{x+\Delta}+\int_{x+\Delta}^{b\cos\delta}$$

In the first and the last of these three integrals ε can be taken equal to zero, but the second integral needs a more careful treatment. Since Δ will be assumed small, one may replace $\gamma(\xi)$ by $\gamma(x)$. It can be shown that this approximation produces no error in the final result. As, moreover, both $x-\xi$ and ε are small in this integral, we may write

$$\lim_{\varepsilon\to0}\frac{\gamma(x)}{8h}\int_{x-\Delta}^{x+\Delta}\frac{-\dfrac{\pi}{2h}\{(x-\xi)\tan\delta\pm\varepsilon\}\cos\delta+\dfrac{\pi(x-\xi)}{2h}\sin\delta}{\dfrac{\pi^2(x-\xi)^2}{8h^2}+\dfrac{\pi^2\{(x-\xi)\tan\delta\pm\varepsilon\}^2}{8h^2}}\frac{d\xi}{\cos\delta}=$$
$$=-\frac{\gamma(x)}{2\pi}\lim_{\varepsilon\to0}\int_{x-\Delta}^{x+\Delta}\frac{\pm\varepsilon}{(x-\xi)^2(1+\tan^2\delta)\pm2(x-\xi)\varepsilon\tan\delta+\varepsilon^2}d\xi=\mp\tfrac{1}{2}\gamma(x)$$

The first and the last of the three integrals may be written together in the form

$$\frac{1}{8h}\int_0^{b\cos\delta}\gamma(\xi)\left\{\frac{-\sin\dfrac{\pi(x-\xi)\tan\delta}{2h}\cos\delta+\sinh\dfrac{\pi(x-\xi)}{2h}\sin\delta}{\cosh\dfrac{\pi(x-\xi)}{2h}-\cos\dfrac{\pi(x-\xi)\tan\delta}{2h}}\right\}\frac{d\xi}{\cos\delta}$$

where the integral has to be conceived in the sense of Cauchy.

Therefore, the final expression for the tangential velocity at the flap due to the flap vortices is

$$\{u_2(x,y)\cos\delta+v_2(x,y)\sin\delta\}_{y=x\tan\delta\pm\varepsilon}=$$

$$\mp\tfrac{1}{2}\gamma(x)-\frac{1}{8h\cos\delta}\int_0^{b\cos\delta}\gamma(\xi)\left\{\frac{\sin\dfrac{\pi(x-\xi)\tan\delta}{2h}\cos\delta-\sinh\dfrac{\pi(x-\xi)}{2h}\sin\delta}{\cosh\dfrac{\pi(x-\xi)}{2h}-\cos\dfrac{\pi(x-\xi)\tan\delta}{2h}}+\right.$$

$$\left.+\frac{\sin\dfrac{\pi(x+\xi)\tan\delta}{2h}\cos\delta+\sinh\dfrac{\pi(x-\xi)}{2h}\sin\delta}{\cosh\dfrac{\pi(x-\xi)}{2h}+\cos\dfrac{\pi(x+\xi)\tan\delta}{2h}}\right\}d\xi \qquad (3.17)$$

At the lower side of the aerofoil ($y=0^+$), the tangential velocity should vanish near the angle between wing and flap if the flap is deflected downward ($\delta>0$). Hence

$$\lim_{x\to0^+}\left\{-\tfrac{1}{2}\gamma(x)+\frac{1}{4h\cos\delta}\int_0^{b\cos\delta}\gamma(\xi)\frac{\sin\dfrac{\pi\xi\tan\delta}{h}}{\cosh\dfrac{\pi(x-\xi)}{h}-\cos\dfrac{\pi\xi\tan\delta}{h}}d\xi\right\}+U=0 \quad \text{if} \quad \delta>0 \qquad (3.18)$$

$$\lim_{x\to0^+}\left\{-\tfrac{1}{2}\gamma(x)+\frac{1}{4h}\int_{-a}^{0}\gamma(\xi)\frac{-\sin\dfrac{\pi x\tan\delta}{2h}\cos\delta\cosh\dfrac{\pi(x-\xi)}{2h}+\cos\dfrac{\pi x\tan\delta}{2h}\sin\delta\sinh\dfrac{\pi(x-\xi)}{2h}}{\cosh^2\dfrac{\pi(x-\xi)}{2h}-\cos^2\dfrac{\pi x\tan\delta}{2h}}d\xi\right\}+$$

$$+\frac{1}{4h\cos\delta}\int_0^{b\cos\delta}\gamma(\xi)\cos\frac{\pi\xi\tan\delta}{2h}\,\frac{\sin\dfrac{\pi\xi\tan\delta}{2h}\cos\delta-\sinh\dfrac{\pi\xi}{2h}\sin\delta}{\cosh^2\dfrac{\pi\xi}{2h}-\cos^2\dfrac{\pi\xi\tan\delta}{2h}}d\xi+U\cos\delta=0 \quad \text{if} \quad \delta>0$$

All separate terms containing x become infinitely large for $x\to0$, but their sum remains finite. In the last term of the last equation, containing an integration over the flap vortices, the limit $x\to0$ could be performed, since only the reflections of these vortices by the tunnel walls contribute to the tangential velocity at the flap, once the local velocity $-\tfrac{1}{2}\gamma(x)$ has been taken into account.

Finally, we give the formula for the pressure difference, see eq. (3.13)

$$p(x)=\rho\gamma(x)\left\{U+\frac{1}{4h\cos\delta}\int_0^{b\cos\delta}\gamma(\xi)\frac{\sin\dfrac{\pi\xi\tan\delta}{h}}{\cosh\dfrac{\pi(x-\xi)}{h}-\cos\dfrac{\pi\xi\tan\delta}{h}}d\xi\right\} \qquad -a<x<0$$

$$p(x)=\rho\gamma(x)\left[U\cos\delta+\frac{1}{4h}\int_{-a}^{0}\gamma(\xi)\frac{-\sin\dfrac{\pi x\tan\delta}{2h}\cos\delta\cosh\dfrac{\pi(x-\xi)}{2h}+\cos\dfrac{\pi x\tan\delta}{2h}\sin\delta\sinh\dfrac{\pi(x-\xi)}{2h}}{\cosh^2\dfrac{\pi(x-\xi)}{2h}-\cos^2\dfrac{\pi x\tan\delta}{2h}}d\xi+\right.$$

$$\left.-\frac{1}{8h\cos\delta}\int_0^{b\cos\delta}\gamma(\xi)\left\{\frac{\sin\dfrac{\pi(x-\xi)\tan\delta}{2h}\cos\delta-\sinh\dfrac{\pi(x-\xi)}{2h}\sin\delta}{\cosh\dfrac{\pi(x-\xi)}{2h}-\cos\dfrac{\pi(x-\xi)\tan\delta}{2h}}+\frac{\sin\dfrac{\pi(x+\xi)\tan\delta}{2h}\cos\delta+\sinh\dfrac{\pi(x-\xi)}{2h}\sin\delta}{\cosh\dfrac{\pi(x-\xi)}{2h}+\cos\dfrac{\pi(x+\xi)\tan\delta}{2h}}\right\}d\xi\right] \qquad (3.19)$$

$$0<x<b\cos\delta$$

The formulae for the pressure difference in absence of the tunnel walls ($h \to \infty$) are

$$p^*(x) = \rho\gamma^*(x)\left\{U + \frac{1}{2\pi\cos\delta}\int_0^{b\cos\delta}\gamma^*(\xi)\frac{\xi\tan\delta}{(x-\xi)^2+\xi^2\tan^2\delta}\,d\xi\right\} \qquad -a<x<0 \tag{3.20}$$

$$p^*(x) = \rho\gamma^*(x)\left\{U\cos\delta - \frac{\sin\delta}{2\pi}\int_{-a}^{0}\gamma^*(\xi)\frac{\xi}{(x-\xi)^2+x^2\tan^2\delta}\,d\xi\right\} \qquad 0<x<b\cos\delta$$

Subtracting equations (3.19) from (3.20) yields the tunnel wall correction for the pressure distribution over the wing surface. In order to prevent unwanted inaccuracies, arising from this subtraction, it is better to express these corrections by formulae containing $\Delta\gamma(\xi)$, which can be calculated by aid of the formulae (3.12) with sufficient accuracy.

For convenience the equations (3.19) and (3.20) are written as:

$$p(x) = \rho U\gamma(x) + \rho\gamma(x)\int_0^{b\cos\delta}\gamma(\xi)H_1(x,\xi)\,d\xi \qquad -a\leqq x\leqq 0$$

$$p(x) = \rho U\cos\delta\,\gamma(x) + \rho\gamma(x)\int_{-a}^{0}\gamma(\xi)H_2(x,\xi)\,d\xi + \rho\gamma(x)\int_0^{b\cos\delta}\gamma(\xi)H_3(x,\xi)\,d\xi \qquad 0\leqq x\leqq b\cos\delta$$

$$p^*(x) = \rho U\gamma^*(x) + \rho\gamma^*(x)\int_0^{b\cos\delta}\gamma^*(\xi)H_1^*(x,\xi)\,d\xi \qquad -a\leqq x\leqq 0$$

$$p^*(x) = \rho U\cos\delta\,\gamma^*(x) + \rho\gamma^*(x)\int_{-a}^{0}\gamma^*(\xi)H_2^*(x,\xi)\,d\xi \qquad 0\leqq x\leqq b\cos\delta \tag{3.21}$$

where the functions H_1, H_2, H_3, H_1^* and H_2^* can easily be obtained from the equations (3.19) and (3.20).

Introducing again $\Delta p(x) = p^*(x) - p(x)$ and $\Delta H_i(x,\xi) = H_i^*(x,\xi) - H_i(x,\xi)\,(i=1,2)$ one gets after subtraction of corresponding formulae, the following expressions for the tunnel wall corrections $\Delta p(x)$:

$$\Delta p(x) = \rho U\Delta\gamma(x) + \rho\gamma^*(x)\int_0^{b\cos\delta}\gamma^*(\xi)\Delta H_1(x,\xi)\,d\xi + \rho\gamma^*(x)\int_0^{b\cos\delta}\Delta\gamma(\xi)H_1(x,\xi)\,d\xi + \rho\Delta\gamma(x)\int_0^{b\cos\delta}\gamma(\xi)H_1(x,\xi)\,d\xi \qquad -a\leqq x\leqq 0$$

$$\Delta p(x) = \rho U\cos\delta\,\Delta\gamma(x) + \rho\gamma^*(x)\int_{-a}^{0}\gamma^*(\xi)\Delta H_2(x,\xi)\,d\xi + \rho\gamma^*(x)\int_{-a}^{0}\Delta\gamma(\xi)H_2(x,\xi)\,d\xi +$$
$$+\rho\Delta\gamma(x)\int_{-a}^{0}\gamma(\xi)H_2(x,\xi)\,d\xi - \rho\gamma(x)\int_0^{b\cos\delta}\gamma(\xi)H_3(x,\xi)\,d\xi \qquad 0\leqq x\leqq b\cos\delta \tag{3.22}$$

3.4 *The singularity in the flow at the angle between wing and flap.*

In order to investigate this singularity we consider the flow along two straight half-lines making an angle δ with each other (sketch c). We perform a conformal transformation from the physical z-plane to the ζ-plane, where the two half-lines have been transformed into one single infinitely long straight line (ref. 6).

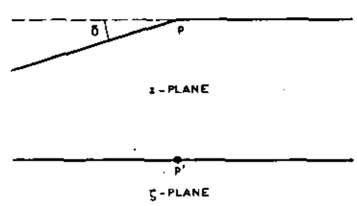

Sketch c: Conformal mapping of z-plane to ζ-plane.

The transformation which maps the part of the z-plane above the two half-lines into the upper half ζ-plane is

$$\zeta = z^{\pi/(\pi+\delta)}$$

Putting $z = re^{i\theta}$ one obtains $\zeta = r^{\pi/(\pi+\delta)}e^{(\pi/(\pi+\delta))\theta i}$. Hence the line $\theta=0$ in the z-plane becomes the line $\theta=0$ in the ζ-plane, while the line $\theta=\pi+\delta$ in the z-plane becomes the line $\theta=\pi$ in the ζ-plane. The flow in the ζ-plane is trivial, its complex potential being given by

$$F = A\zeta$$

In the z-plane

$$F = \Phi + i\psi = Az^{\pi/(\pi+\delta)}$$

which means that the velocity potential along the wall becomes $\Phi = \pm A r^{\pi/(\pi+\delta)}$, where the + sign corresponds with $\theta = 0$ and the − sign with $\theta = \pi + \delta$.

The tangential velocity along the wall is

$$v_{\text{tang}}(r) = \frac{\pi}{\pi+\delta} A r^{-\delta/(\pi+\delta)}$$

It is seen that if δ is positive (convex side of a corner) the velocity becomes infinitely large, while it vanishes for negative δ (concave side of the corner).

Considering now the flow at both sides of the half-lines, the boundary can be replaced by a vortex distribution of strength

$$\gamma(r) = A_1 r^{-\delta/(\pi+\delta)} + A_2 r^{\delta/(\pi-\delta)}$$

where A_1 and A_2 are still unknown constants and r denotes the distance toward the corner.

If we now consider the wing-flap system, where the wing and the flap are line segments of finite length, the flow at an infinitely small distance from the corner will be identical to that at a finite distance from the corner in the case of infinite half-lines. Hence, the singularity in the vortex distribution at the corner of the wing-flap system is of the type

$$\gamma(r) = A_1 r^{-\delta/(\pi+\delta)} \qquad \delta > 0 \tag{3.23}$$

The other terms in the vortex distribution all vanish for $r = 0$.

4 The solution of the integral equation for the vortex distribution.

4.1 *The numerical method.*

The vortex distribution for the wing in free flight is determined by the set of integral equations (3.9) and for the wing between two parallel walls by the set (3.7), while the correction $\Delta\gamma(x)$ of the vortex distribution $\gamma^*(x)$ due to the presence of the walls is determined by the integral equations (3.12).

These integral equations can be solved by a numerical method. The following exposition of this numerical method is confined to the case of the integral equations for the wing-flap system in free flight, but the method can also be applied to the equations for the wing-flap system between two parallel walls, and to the equations for the corrections of the vorticity distribution, after on the right-hand sides of the latter, the results of the vorticity-distribution in free flight have been substituted (see eqs. (3.12)). The basis of the method consists in assuming the following series expansion for the vortex distribution ($\delta > 0$)

at the wing: $-a < \xi < 0$, $0 < \vartheta < \pi$

$$\gamma^*(\xi) = c_0^* \cot\frac{\vartheta}{2} + 2\sum_{n=1}^{\infty} c_n^* \sin n\vartheta + c_s^* \left(\frac{-\xi}{a}\right)^{-\delta/(\pi+\delta)} \left(1 + \frac{\xi}{a}\right) \tag{4.1}$$

at the flap: $0 < \xi < b\cos\delta$, $0 < \vartheta' < \pi$

$$\gamma^*(\xi) = 2\sum_{n=1}^{\infty} c_n^{*\prime} \sin n\vartheta' + c_s^* \left(\frac{\xi}{a\cos\delta}\right)^{-\delta/(\pi+\delta)} \left(1 - \frac{\xi}{b\cos\delta}\right) \tag{4.2}$$

The relation between ξ, ϑ and ϑ' is

$$\left.\begin{aligned} &\text{at the wing: } \xi = -\tfrac{1}{2}a(1+\cos\vartheta) \qquad 0 < \vartheta < \pi \\ &\text{at the flap: } \xi = \tfrac{1}{2}b\cos\delta(1-\cos\vartheta') \qquad 0 < \vartheta' < \pi \end{aligned}\right\} \tag{4.3}$$

Hence $\vartheta = 0$ denotes the leading edge of the wing, $\vartheta = \pi$ or $\vartheta' = 0$ the common point of wing and flap, while $\vartheta' = \pi$ denotes the trailing edge.

The first term of the right-hand side of (4.1) gives the well-known leading edge singularity, while the last term agrees with the formula (3.23) except for an additional factor $1 + (\xi/a)$, which has been added to ensure that this term gives no contribution at the leading edge. Of course it does not change the character of the singularity. The remaining vortex distribution which vanishes both for $\vartheta = 0$ and $\vartheta = \pi$ has been expanded in a Fourier series.

At the flap the factor $1 - (\xi/b\cos\delta)$ in the last term ensures that the singularity at the corner does not disturb the Kutta-condition at the trailing edge.

The approximation which now will be introduced, is that all terms c_n^* and $c_n^{*\prime}$ for which n exceeds 2, will be neglected. We use a six-term approximation for the vortex distribution containing the unknown coefficients c_0^*, c_1^*, c_2^*, $c_1^{*\prime}$, $c_2^{*\prime}$ and c_s^*. Analogously six-term approximations can be used for $\gamma(x)$ and $\Delta\gamma(x)$.

With this approximation it is no longer possible to satisfy the integral equation (3.7) for any point x. It will be satisfied only in the so-called pivotal points. The most favourable positions of these points have been determined from arguments similar to those used by Multhopp in his lifting surface theory (ref. 4).

The positions are:

at the wing:

$$\vartheta_1=\tfrac{2}{7}\pi\ ;\quad x_1=-0.8118a$$
$$\vartheta_2=\tfrac{4}{7}\pi\ ;\quad x_2=-0.3888a$$
$$\vartheta_3=\tfrac{6}{7}\pi\ ;\quad x_3=-0.0495a$$

at the flap:

$$\vartheta'_1=\tfrac{2}{7}\pi\ ;\quad x'_1=+0.1888b\cos\delta$$
$$\vartheta'_2=\tfrac{4}{7}\pi\ ;\quad x'_2=+0.6113b\cos\delta$$
$$\vartheta'_3=\tfrac{6}{7}\pi\ ;\quad x'_3=+0.9505b\cos\delta$$

Hence eqs. (3.9) will be satisfied only for

$$\begin{aligned} &x_1=-0.8118a\,, \qquad x_2=-0.3888a\,, \qquad x_3=-0.0495a\,,\\ &x'_1=+0.1883b\cos\delta\,,\ x'_2=+0.6113b\cos\delta\,,\ x'_3=+0.9505b\cos\delta \end{aligned} \tag{4.4}$$

The expressions (4.1) and (4.2) must now be substituted into eqs. (3.9). This gives a number of integrations over ξ to be performed for the x-values given in (4.4). These integrals can be evaluated numerically after analytical isolation of the singularities in the integrands. The integrals containing in their integrands cot $\vartheta/2$, sin ϑ, sin 2ϑ, sin ϑ' or sin $2\vartheta'$ can be evaluated by a pivotal point method (ref. 7) as follows

$$\int_{-a}^{0} f(\xi)\,\mathrm{cotg}\,\frac{\vartheta}{2}\,d\xi=\tfrac{1}{2}a\{1.7063f(-0.9505a)+1.0973f(-0.6113a)+0.3380f(-0.1883a)\}$$

$$\int_{-a}^{0} f(\xi)\sin\vartheta\,d\xi=\tfrac{1}{2}a\{0.1690f(-0.9505a)+0.8532f(-0.6113a)+0.5487f(-0.1883a)\}$$

$$\int_{-a}^{0} f(\xi)\sin 2\vartheta\,d\xi=\tfrac{1}{2}a\{0.3045f(-0.9505a)+0.3797f(-0.6113a)-0.6842f(-0.1883a)\}$$

$$\int_{0}^{b\cos\delta} f(\xi)\sin\vartheta'\,d\xi=\tfrac{1}{2}b\cos\delta\{0.1690f(0.0495b\cos\delta)+0.8532f(0.3888b\cos\delta)+0.5487f(0.8118b\cos\delta)\}$$

$$\int_{0}^{b\cos\delta} f(\xi)\sin 2\vartheta'\,d\xi=\tfrac{1}{2}b\cos\delta\{0.3045f(0.0495b\cos\delta)+0.3797f(0.3888b\cos\delta)-0.6842f(0.8118b\cos\delta)\} \tag{4.5}$$

These formulae are valid even if $f(\xi)$ contains a singularity $1/(x-\xi)$ where x is at one of the positions (4.4). It can be shown that the error made by the approximations (4.5) is of the same order as the error made by neglecting the terms with c_n and c'_n in (4.1) and (4.2) for $n\geqq 3$.

After the integrals have been evaluated, a set of 6 algebraic equations for the unknowns c^*_0, c^*_1, c^*_2, $c^{*\prime}_1$, $c^{*\prime}_2$ and c^*_s results.

Solution of this system and substitution of the results into the equations (4.1) and (4.2) yields finally the vorticity distribution on the wing-flap system in free flight.

Inserting this vorticity distribution into the right-hand side of the equations (3.12), yields for the correction $\Delta\gamma(x)$ a similar set of integral equations as for the function $\gamma(x)$. The same method is applied in order to evaluate the coefficients Δc_0, Δc_1, Δc_2, $\Delta c'_1$, $\Delta c'_2$ and Δc_s of the series expansions for $\Delta\gamma(x)$, which read quite analogously to eqs. (4.1) and (4.2):

$$\Delta\gamma(\xi)=\Delta c_0\,\mathrm{cotg}\,\frac{\vartheta}{2}+2\Delta c_1\sin\vartheta+2\Delta c_2\sin 2\vartheta+\Delta c_s\left(\frac{-\xi}{a}\right)^{-\delta/(\pi+\delta)}\left(1+\frac{\xi}{a}\right) \qquad -a\leqq\xi\leqq 0$$

$$\Delta\gamma(\xi)=2\Delta c'_1\sin\vartheta'+2\Delta c'_2\sin 2\vartheta'+\Delta c_s\left(\frac{\xi}{a\cos\delta}\right)^{-\delta/(\pi+\delta)}\left(1-\frac{\xi}{b\cos\delta}\right) \qquad 0\leqq\xi\leqq b\cos\delta \tag{4.6}$$

4.2 *Check of the method.*

The numerical method described in the preceding section has been checked for the case of the wing-flap system placed in a free stream. The results for the vortex distribution obtained by this method have been compared with the exact results given by Keune (ref. 1): The comparison is shown in fig. 1, where the results of a calculation based on linear theory have also been inserted. It is seen that the present results agree very well with those obtained by Keune's method, while on the other hand the results from linear theory differ markedly.

Hence it may be concluded that the present method is well suited for accounting the non-linear effects due to the large angles of deflection.

In the example of fig. 1 the wing is in the direction of the undisturbed flow while the angle of deflection is 60°. The ratio of flap to total wing-chord is $b/(a+b)=\frac{1}{4}$.

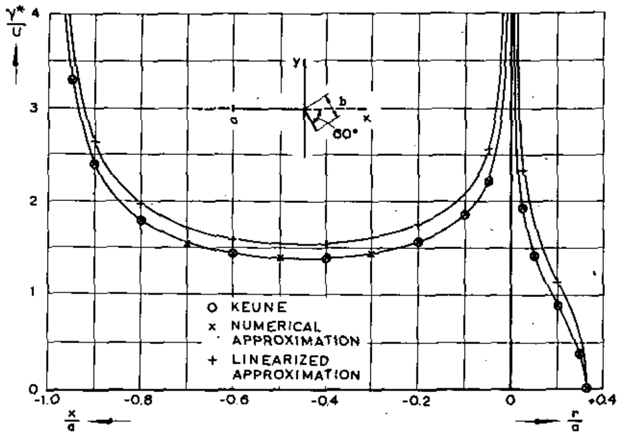

Fig. 1. Comparison between approximate and exact values of the vorticity on the wing in free flight. Angle of flap-deflection 60°, ratio of flap to total wing chord 25%.

5 Calculation of the aerodynamic coefficients.

Once the coefficients c_i^* and Δc_i have been determined, the coefficients c_i of the vortex distribution of the wing-flap system between two parallel walls can be obtained by $\Delta c_i = c_i^* - c_i$ and hence the series expansions of $\gamma^*(x)$, $\gamma(x)$ and $\Delta\gamma(x)$ are known.

Substitution of these expansions into the equations (3.20) and (3.22) yields the pressure distribution at the wing-flap system in free flight and its correction due to the presence of the walls.

The integrals occurring on the right-hand sides of (3.20) and (3.22) are again numerically calculated after analytical isolation of the singularities.

The pressure distribution and its correction have been calculated for 9 equidistant points at the wing and 9 equidistant points at the flap. The aerodynamic coefficients for the wing in free flight are defined as:

$$C_L^* = \frac{\int_{-a}^{0} p^*(x)\mathrm{d}x + \int_{0}^{b\cos\delta} p^*(x)\mathrm{d}x}{\frac{1}{2}\rho U^2(a+b)}$$

and

$$C_M^* = \frac{\int_{-a}^{0} xp^*(x)\mathrm{d}x + \frac{1}{\cos^2\delta}\int_{0}^{b\cos\delta} xp^*(x)\mathrm{d}x}{\frac{1}{2}\rho U^2(a+b)^2} + \frac{1}{4}\,\frac{3a-b}{a+b}\,C_L^* \tag{5.1}$$

where the moment has been taken about the quarter-chord point of the total wing.

For the tunnel wall corrections one obtains analogously:

$$\Delta C_L = C_L^* - C_L = \frac{\int_{-a}^{0} \Delta p(x)\mathrm{d}x + \int_{0}^{b\cos\delta} \Delta p(x)\mathrm{d}x}{\frac{1}{2}\rho U^2(a+b)}$$

and

$$\Delta C_M = C_M^* - C_M = \frac{\int_{-a}^{0} x\Delta p(x)\mathrm{d}x + \frac{1}{\cos^2\delta}\int_{0}^{b\cos\delta} x\Delta p(x)\mathrm{d}x}{\frac{1}{2}\rho U^2(a+b)^2} + \frac{1}{4}\,\frac{3a-b}{a+b}\,\Delta C_L \tag{5.2}$$

Having obtained values of the pressure distribution in a sufficiently large number of points at the wing and the flap, the coefficients C_L^*, C_M^* and their corrections can be calculated by numerical evaluation of the integrals occurring on the right-hand sides of equations (5.1) and (5.2).

For the numerical evaluation of the tunnel wall corrections it is necessary to isolate the singularities of $\Delta p(x)$. From the equations (3.22) it is clear, that the singularity of $\Delta p(x)$ at the leading edge of the wing, i.e. at $x=-a$, is of the same type as the singularity of $\Delta\gamma(x)$ in that point. This is, however, not the case for the singularity at the hinge point of the flap. Taking the limit for $x\to\pm 0$, it appears after some derivation that $\Delta p(x)$ has two singularities of the type $|x|^{-2\delta/(\pi+\delta)}$ and $|x|^{-\delta/(\pi+\delta)}$ at the hinge point, whereas the vorticity distribution has only one singularity of the type $|x|^{-\delta/(\pi+\delta)}$.

For the sake of interest the behaviour of $p^*(x)$ in the neighbourhood of the hinge point of the flap has been determined in the appendix. The singularities of $\Delta p(x)$ can be obtained in the same way. After isolation of the singularities in the integrands of equation (5.2), ΔC_L and ΔC_M can be calculated numerically.

The coefficients C_L^* and C_M^* for the free-flight case can be determined much easier by using the well-known momentum balance with respect to a closed contour around the aerofoil. The aerodynamic coefficients can be written as (compare ref. 8, chapter II)

$$C_L^* = 2\frac{\int_{-a}^{0} \frac{\gamma^*(x)}{U}\,dx + \frac{1}{\cos\delta}\int_0^{b\cos\delta}\frac{\gamma^*(x)}{U}\,dx}{a+b}$$

and

$$C_M^* = 2\frac{\int_{-a}^{0} x\frac{\gamma^*(x)}{U}\,dx + \frac{1}{\cos\delta}\int_0^{b\cos\delta} x\frac{\gamma^*(x)}{U}\,dx}{(a+b)^2} + \tfrac{1}{4}\frac{3a-b}{a+b}C_L^* \qquad (5.3)$$

Substituting the expansions (4.1) and (4.2) for $\gamma^*(x)$ into (5.3), one obtains after performing the integrations to x:

$$C_L^* = \frac{a\pi}{a+b}\left\{\frac{c_0^*}{U} + \frac{c_1^*}{U} + 2\frac{(\pi+\delta)^2}{\pi^2(2\pi+\delta)}\frac{c_s^*}{U}\right\} + \frac{b\pi}{a+b}\left\{\frac{c_1^{*\prime}}{U} + 2\frac{(\pi+\delta)^2}{\pi^2(2\pi+\delta)}\left(\frac{b}{a}\right)^{-\delta/(\pi+\delta)}\frac{c_s^*}{U}\right\}$$

and

$$C_M^* = -\left(\frac{a}{a+b}\right)^2\pi\left\{\tfrac{3}{4}\frac{c_0^*}{U} + \tfrac{1}{2}\frac{c_1^*}{U} + \tfrac{1}{4}\frac{c_2^*}{U} + 2\frac{(\pi+\delta)^2}{\pi(2\pi+\delta)(3\pi+2\delta)}\frac{c_s^*}{U}\right\} +$$

$$+\left(\frac{b}{a+b}\right)^2\pi\left\{\tfrac{1}{2}\frac{c_1^{*\prime}}{U} - \tfrac{1}{4}\frac{c_2^{*\prime}}{U} + 2\frac{(\pi+\delta)^2}{\pi(2\pi+\delta)(3\pi+2\delta)}\left(\frac{b}{a}\right)^{-\delta/(\pi+\delta)}\frac{c_s^*}{U}\right\}\cos\delta + \tfrac{1}{4}\frac{3a-b}{a+b}C_L^* \qquad (5.4)$$

Inserting in these equations the calculated values of c_i^*, the aerodynamic coefficients are obtained easily for the wing-flap system in free flight. The method of the momentum balance cannot be applied for the determination of lift and moment of the wing-flap system between the two parallel walls, since the contour enclosing the aerofoil but not the tunnel walls, does not contain in its interior all the vortices present in the field; the reflections of the vortex sheet representing the aerofoil are lying outside this contour.

6 Discussion of the numerical results.

The values of C_L^* and C_M^* for the wing in free flight have been calculated by aid of the formulae (5.4) for different values of the flap angle δ, ranging from 0 to 60 degrees, while the ratio $\tau = b/(a+b)$ of flap chord to total wing chord has been taken as $\frac{1}{3}$, $\frac{1}{4}$ and $\frac{1}{5}$.

The results are plotted as functions of the angle of deflection δ in figs. 2 and 3. The results of linearized theory are indicated by a dotted straight line which is the tangent at the origin to the curve corresponding to the results of non-linearized theory. It appears that the values of the aerodynamic coefficients C_L^* and C_M^* are somewhat overestimated by linearized theory. The derivative $(\partial C_M/\partial\delta)_{\delta=0}$ has a maximum for some value of τ in the neighbourhood of $\tau = \frac{1}{4}$. This agrees with the linearized theory of Glauert (ref. 9).

The tunnel wall corrections $\Delta C_L/C_L$ and $\Delta C_M/C_L$ have been calculated in the way described in the previous chapter. The ratio $(a+b)/2h$ of total wing-chord and tunnelheight has been chosen as 0.2, 0.3 and 0.4, and the same values as in the free flight case have been taken for the ratio τ of flap chord to total wing chord and for the angle of deflection δ. The results are plotted in figs. 4 through 9 as functions of the flap-angle δ, while the parameter τ is kept constant in each figure. The same results are given in figs. 10 through 15, where now, however, the parameter $(a+b)/2h$ is kept constant in each figure. For small values of the angle δ, the corrections completely agree with the values found by linear theory (compare ref. 10); the results of the latter are again indicated by a dotted straight horizontal line tangential to the curve for the values of non-linearized theory.

It appears that the tunnel wall corrections are overestimated by linearized theory, which is of no value for large angles of flap deflection. Their absolute values become larger when the height of the tunnel becomes smaller.

It is interesting to note, that the tunnel wall corrections become zero for some value of the angle of flap deflection, which is the same for all values of the ratio $(a+b)/2h$, but which decreases, when the flap chord increases.

The general conclusion can be made that the tunnel wall corrections for large angles of flap deflection are rather small. They amount at most to 5% for $(a+b)/2h = 0.4$; this maximum is attained for small values of the angle of flap deflection δ and they will be much smaller in the range of large values of δ.

7 References.

[1] Keune, F., Auftrieb einer geknickten ebenen Platte. Luftfahrtforschung, Band 13, No. 3, 1936.
[2] Tomotika, On the moment of the force acting on a flat plate in a stream between two parallel walls. Report No. 94, Proceedings of Aeronautical Research Institute of Tokyo, 1933.
[3] Tomotika, The lift on a flat plate placed in a stream between two parallel walls and some allied problems. Report No. 101, Proceedings of Aeronautical Research Institute of Tokyo, 1933.
[4] Multhopp, H., Methods for calculating the lift distribution of wings. (Subsonic lifting surface theory). R.A.E. Report Aero 2353, 1950.
[5] Whittaker-Watson, A course of modern analysis, second edition, 1915.
[6] Lamb, H., Hydrodynamics, Cambridge, 1924.
[7] van de Vooren, A. I., An approach to lifting surface theory. N.L.L. Report F. 129, National Aeronautical Research Institute, Amsterdam, 1953.
[8] Durand, W. F., Aerodynamic Theory, Vol. II, Springer, Berlin 1935.
[9] Glauert, H., Theoretical relationships for an aerofoil with a hinged flap. A.R.C. R. and M. 1095, 1927.
[10] de Jager, E. M., The aerodynamic forces and moments on an oscillating aerofoil with control-surface between two parallel walls. National Aeronautical Research Institute, Amsterdam, 1953.

Appendix: The pressure distribution in the neighbourhood of the intersection of wing and flap.

The pressure distribution on the wing and the flap for the free flight case is given by the formulae (3.20) of the text, viz.:

$$\Delta p^*(x)=\rho\gamma^*(x)\left\{U+\frac{1}{2\pi\cos\delta}\int_0^{b\cos\delta}\gamma^*(\xi)\frac{\xi\tan\delta}{(x-\xi)^2+\xi^2\tan^2\delta}\,\mathrm{d}\xi\right\}\qquad -a<x<0 \tag{A.1}$$

and

$$\Delta p^*(x)=\rho\gamma^*(x)\left\{U\cos\delta-\frac{\sin\delta}{2\pi}\int_{-a}^{0}\gamma^*(\xi)\frac{\xi\,\mathrm{d}\xi}{(x-\xi)^2+x^2\tan^2\delta}\right\}\qquad 0<x<b\cos\delta \tag{A.2}$$

Substitution of the formulae (4.2) and (4.1) into the integrals occurring in (A.1) and (A.2) yields

$$\int_0^{b\cos\delta}\gamma^*(\xi)\frac{\xi\tan\delta}{(x-\xi)^2+\xi^2\tan^2\delta}\,\mathrm{d}\xi=2c_1^*\int_0^{b\cos\delta}\sin\vartheta'\frac{\xi\tan\delta}{(x-\xi)^2+\xi^2\tan^2\delta}\,\mathrm{d}\xi+2c_2^*\int_0^{b\cos\delta}\sin 2\vartheta'\frac{\xi\tan\delta}{(x-\xi)^2+\xi^2\tan^2\delta}\,\mathrm{d}\xi+$$
$$+c_s^*\left(\frac{b}{a}\right)^{-\delta/(\pi+\delta)}\int_0^{b\cos\delta}\left(\frac{\xi}{b\cos\delta}\right)^{-\delta/(\pi+\delta)}\frac{\xi\tan\delta}{(x-\xi)^2+\xi^2\tan^2\delta}\,\mathrm{d}\xi-c_s^*\left(\frac{b}{a}\right)^{-\delta/(\pi+\delta)}\int_0^{b\cos\delta}\left(\frac{\xi}{b\cos\delta}\right)^{\pi/(\pi+\delta)}$$
$$\frac{\xi\tan\delta}{(x-\xi)^2+\xi^2\tan^2\delta}\,\mathrm{d}\xi \tag{A.3}$$

and

$$\int_{-a}^{0}\gamma^*(\xi)\frac{\xi\,\mathrm{d}\xi}{(x-\xi)^2+x^2\tan^2\delta}=c_0^*\int_{-a}^{0}\operatorname{cotg}\frac{\vartheta}{2}\frac{\xi\,\mathrm{d}\xi}{(x-\xi)^2+x^2\tan^2\delta}+2c_1^*\int_{-a}^{0}\sin\vartheta\frac{\xi\,\mathrm{d}\xi}{(x-\xi)^2+x^2\tan^2\delta}+$$
$$+2c_2^*\int_{-a}^{0}\sin 2\vartheta\frac{\xi\,\mathrm{d}\xi}{(x-\xi)^2+x^2\tan^2\delta}+c_s^*\int_{-a}^{0}\left(-\frac{\xi}{a}\right)^{-\delta/(\pi+\delta)}\frac{\xi\,\mathrm{d}\xi}{(x-\xi)^2+x^2\tan^2\delta}-c_s^*\int_{-a}^{0}\left(-\frac{\xi}{a}\right)^{+\pi/(\pi+\delta)}$$
$$\frac{\xi\,\mathrm{d}\xi}{(x-\xi)^2+x^2\tan^2\delta} \tag{A.4}$$

Putting $\xi=-xt$, one obtains after some calculations the following asymptotic approximations for $x\to-0$ for the integrals occurring on the right-hand side of eq. (A.3)

$$\int_0^{b\cos\delta}\sin\vartheta'\frac{\xi\tan\delta}{(x-\xi)^2+\xi^2\tan^2\delta}\,\mathrm{d}\xi=\pi\sin\delta\cos\delta+0\{(-x)^{\frac{1}{2}}\}$$
$$\int_0^{b\cos\delta}\sin 2\vartheta'\frac{\xi\tan\delta}{(x-\xi)^2+\xi^2\tan^2\delta}\,\mathrm{d}\xi=\pi\sin\delta\cos\delta+0\{(-x)^{\frac{1}{2}}\}$$
$$\int_0^{b\cos\delta}\left(\frac{\xi}{b\cos\delta}\right)^{-\delta/(\pi+\delta)}\frac{\xi\tan\delta}{(x-\xi)^2+\xi^2\tan^2\delta}\,\mathrm{d}\xi=\pi\cos\delta\left(\frac{b}{a}\right)^{\delta/(\pi+\delta)}\left(-\frac{x}{a}\right)^{-\delta/(\pi+\delta)}-\frac{\pi+\delta}{\delta}\sin\delta\cos\delta+0\{(-x)\}$$
$$\int_0^{b\cos\delta}\left(\frac{\xi}{b\cos\delta}\right)^{\pi/(\pi+\delta)}\frac{\xi\tan\delta}{(x-\xi)^2+\xi^2\tan^2\delta}\,\mathrm{d}\xi=\frac{\pi+\delta}{\pi}\sin\delta\cos\delta+0\{(-x)^{\pi/(\pi+\delta)}\}$$

In the same way the integrals occurring on the right-hand side of eqs. (A.4) can be approximated for $x\to+0$; one gets after some derivations:

$$\int_{-a}^{0}\operatorname{cotg}\frac{\vartheta}{2}\frac{\xi\,\mathrm{d}\xi}{(x-\xi)^2+x^2\tan^2\delta}=-\pi+0(x^{\frac{1}{2}})$$
$$\int_{-a}^{0}\sin\vartheta\frac{\xi\,\mathrm{d}\xi}{(x-\xi)^2+x^2\tan^2\delta}=-\pi+0(x^{\frac{1}{2}})$$
$$\int_{-a}^{0}\sin 2\vartheta\frac{\xi\,\mathrm{d}\xi}{(x-\xi)^2+x^2\tan^2\delta}=+\pi+0(x^{\frac{1}{2}})$$
$$\int_{-a}^{0}\left(-\frac{\xi}{a}\right)^{-\delta/(\pi+\delta)}\frac{\xi\,\mathrm{d}\xi}{(x-\xi)^2+x^2\tan^2\delta}=-\pi\frac{(\cos\delta)^{-\delta/(\pi+\delta)}}{\sin\delta}\left(\frac{x}{a}\right)^{-\delta/(\pi+\delta)}+\frac{\pi+\delta}{\delta}+0(x)$$
$$\int_{-a}^{0}\left(-\frac{\xi}{a}\right)^{\pi/(\pi+\delta)}\frac{\xi\,\mathrm{d}\xi}{(x-\xi)^2+x^2\tan^2\delta}=-\frac{\pi+\delta}{\pi}+0(x^{\pi/(\pi+\delta)})$$

Substituting all these results into the equations (A.3) resp. (A.4) the result is:

$$\int_0^{b\cos\delta} \gamma^*(\xi)\frac{\xi\tan\delta}{(x-\xi)^2+\xi^2\tan^2\delta}\,d\xi = 2\pi\sin\delta\cos\delta c_1^{*'}+2\pi\sin\delta\cos\delta c_2^{*'}+$$
$$-\frac{(\pi+\delta)^2}{\pi\delta}\sin\delta\cos\delta\left(\frac{b}{a}\right)^{-\delta/(\pi+\delta)}c_s^*+\pi\cos\delta c_s^*\left(-\frac{x}{a}\right)^{-\delta/(\pi+\delta)}+0\{(-x)^{\frac{1}{2}}\} \quad (A.5)$$

and

$$\int_{-a}^{0} \gamma^*(\xi)\frac{\xi\,d\xi}{(x-\xi)^2+x^2\tan^2\delta} = -\pi c_0^*-2\pi c_1^*+2\pi c_2^*+\frac{(\pi+\delta)^2}{\pi\delta}c_s^*-\pi\frac{(\cos\delta)^{\delta/(\pi+\delta)}}{\sin\delta}c_s^*\left(\frac{x}{a}\right)^{-\delta/(\pi+\delta)}+0(x^{\frac{1}{2}}) \quad (A.6)$$

Inserting finally (A.5) and (A.6) into (A.1) resp. (A.2) and replacing the vortex distributions $\gamma^*(x)$ by their series expansions (4.1) and (4.2), the pressure distribution in the neighbourhood of the point $x=0$ turns out to be

$$\Delta p^*(x)=\tfrac{1}{2}\rho(c_s^*)^2\left(-\frac{x}{a}\right)^{-2\delta/(\pi+\delta)}+\rho c_s^*\left\{U+c_1^{*'}\sin\delta+c_2^{*'}\sin\delta-c_s^*\frac{(\pi+\delta)^2}{2\pi^2\cdot\delta}\sin\delta\left(\frac{b}{a}\right)^{-\delta/(\pi+\delta)}\right\}\left(-\frac{x}{a}\right)^{-\delta/(\pi+\delta)}+$$
$$+0\left\{\left(-\frac{x}{a}\right)^{(\pi-\delta)/2(\pi+\delta)}\right\} \quad \text{for } x\to-0 \quad (A.7)$$

and

$$\Delta p^*(x)=\tfrac{1}{2}\rho(c_s^*)^2(\cos\delta)^{2\delta/(\pi+\delta)}\left(\frac{x}{a}\right)^{-2\delta/(\pi+\delta)}+\rho c_s^*(\cos\delta)^{(\pi+2\delta)/(\pi+\delta)}\left[U+\tan\delta\left\{\tfrac{1}{2}c_0^*+c_1^*-c_2^*+\right.\right.$$
$$\left.\left.-\frac{(\pi+\delta)^2}{2\pi^2\delta}c_s^*\right\}\right]\left(\frac{x}{a}\right)^{-\delta/(\pi+\delta)}+0\left\{(x)^{(\pi-\delta)/2(\pi+\delta)}\right\} \quad \text{for } x\to+0. \quad (A.8)$$

Hence it appears that the pressure distribution has two singularities at the point $x=0$; one of the type $|x|^{-2\delta/(\pi+\delta)}$ and the other of the type $|x|^{-\delta/(\pi+\delta)}$. The vorticity distribution however has only one singularity at the point $x=0$ viz. of the type $(x)^{-\delta/(\pi+\delta)}$. This difference in behaviour of vorticity- and pressure distribution is a typical feature of non-linearized theory. The pressure distribution in the neighbourhood of the intersection of wing and flap for the wing between the two parallel walls exhibits of course the same types of singularities as the wing in free flight.

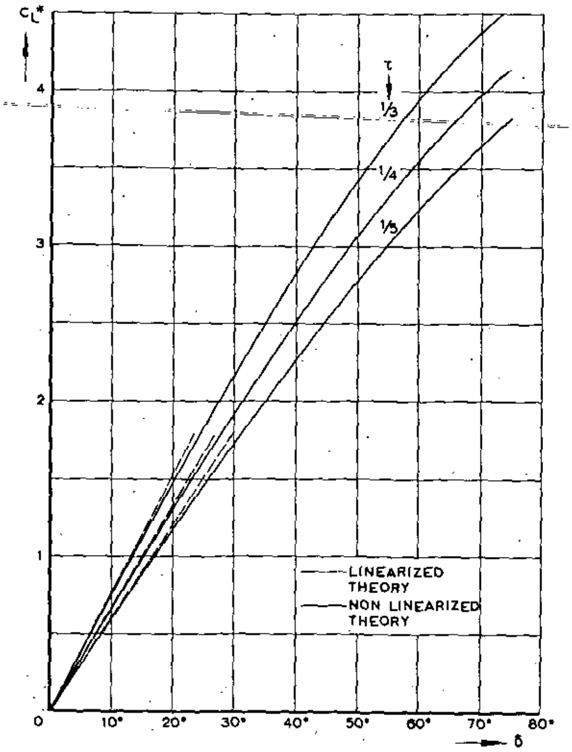

Fig. 2. Lift-coefficient of the wing in free flight as function of the angle of flap deflection for some values of the ratio τ of flap-to total wing-chord.

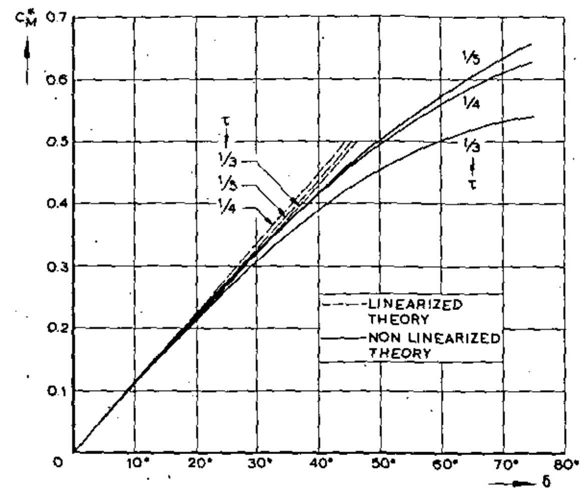

Fig. 3. Moment-coefficient of the wing in free flight as function of the angle of flap deflection for some values of the ratio τ of flap- to total wing-chord. The moment is taken about the quarter-chord point.

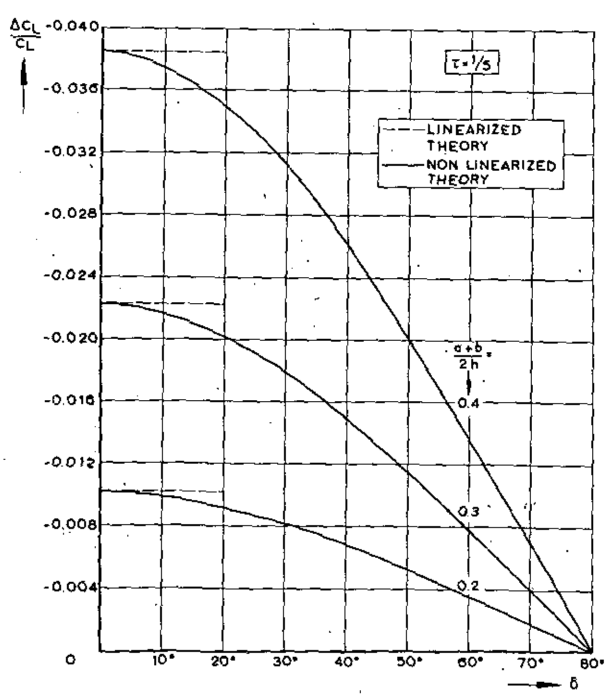

Fig. 4. Tunnel wall corrections for the lift coefficient as function of the angle of flap deflection for three values of $(a+b)/2h$; $\tau=\frac{1}{5}$.

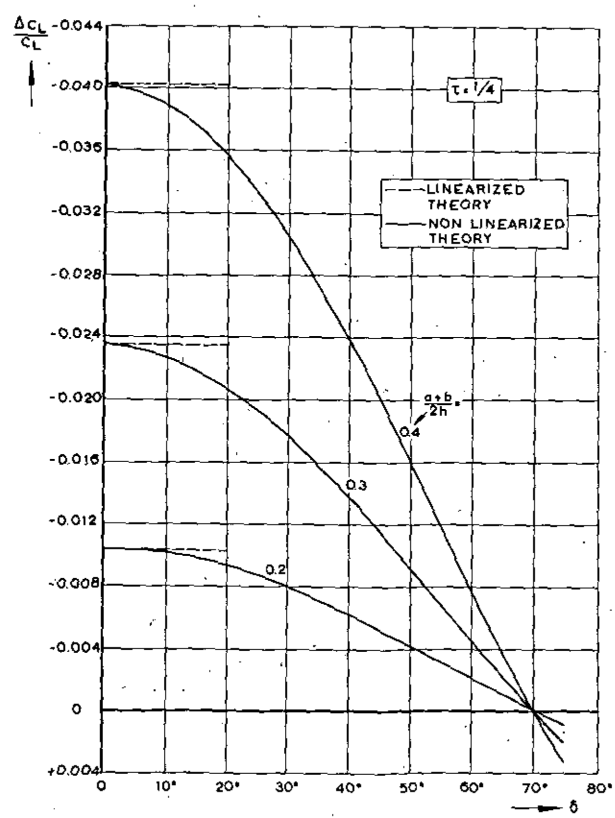

Fig. 5. Tunnel wall corrections for the lift coefficient as function of the angle of flap deflection for three values of $(a+b)/2h$; $\tau=\frac{1}{4}$.

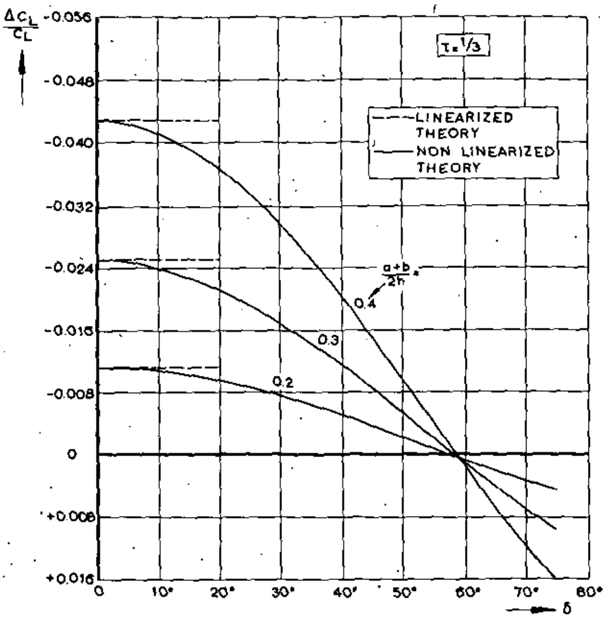

Fig. 6. Tunnel wall corrections for the lift coefficient as function of the angle of flap deflection for three values of $(a+b)/2h$; $\tau=\frac{1}{3}$.

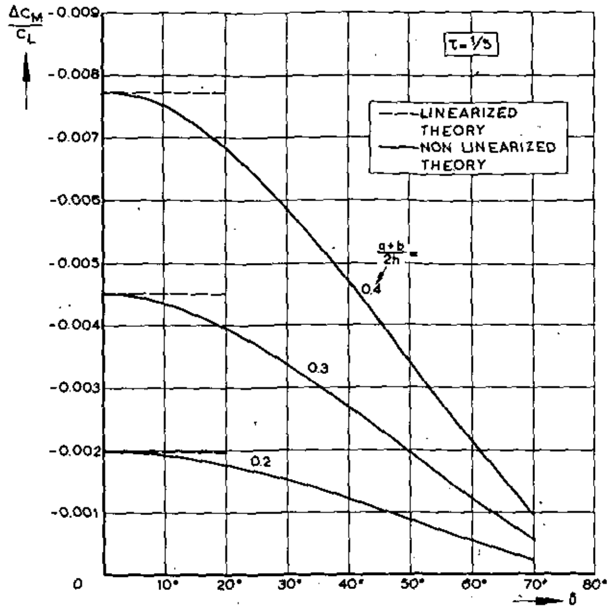

Fig. 7. Tunnel wall corrections for the lift coefficient as function of the angle of flap deflection for three values of $(a+b)/2h$; $\tau=\frac{1}{3}$. The moment is taken about the quarter-chord point.

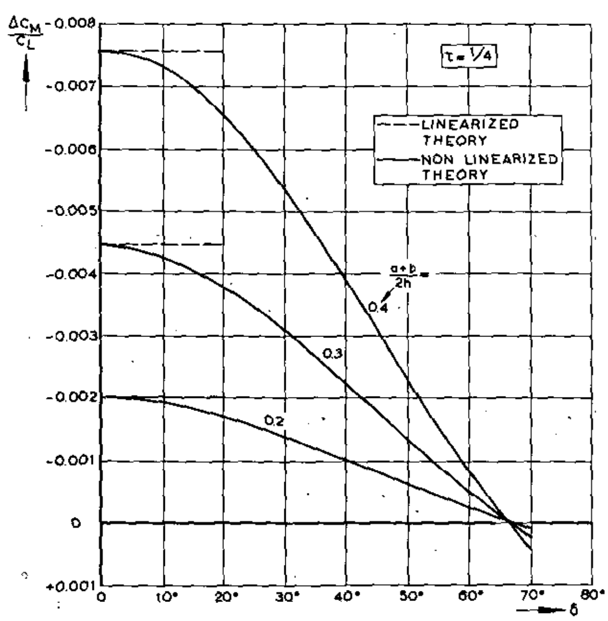

Fig. 8. Tunnel wall corrections for the moment coefficient as function of the angle of flap deflection for three values of $(a+b)/2h$: $\tau=\frac{1}{4}$. The moment is taken about the quarter-chord point.

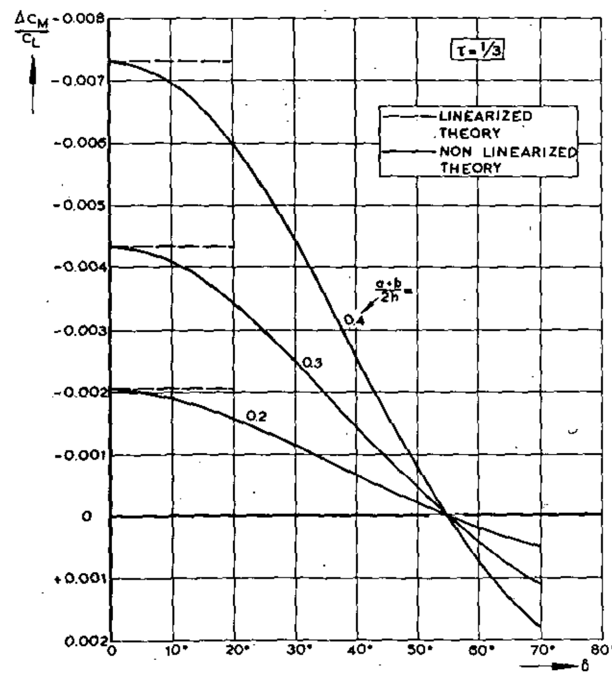

Fig. 9. Tunnel wall corrections for the moment coefficient as function of the angle of flap deflection for three values of $(a+b)/2h$; $\tau=\frac{1}{3}$. The moment is taken about the quarter-chord point.

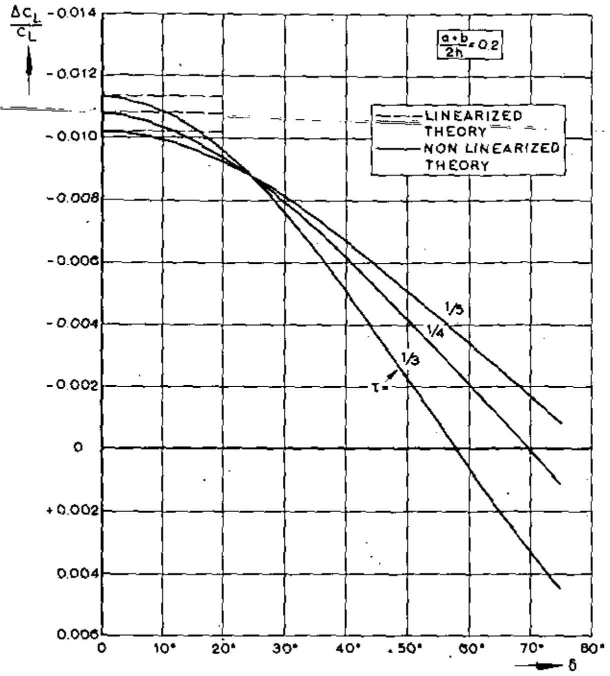

Fig. 10. Tunnel wall corrections for the lift coefficient as function of the angle of flap deflection for three values of τ; $(a+b)2h=0.2$.

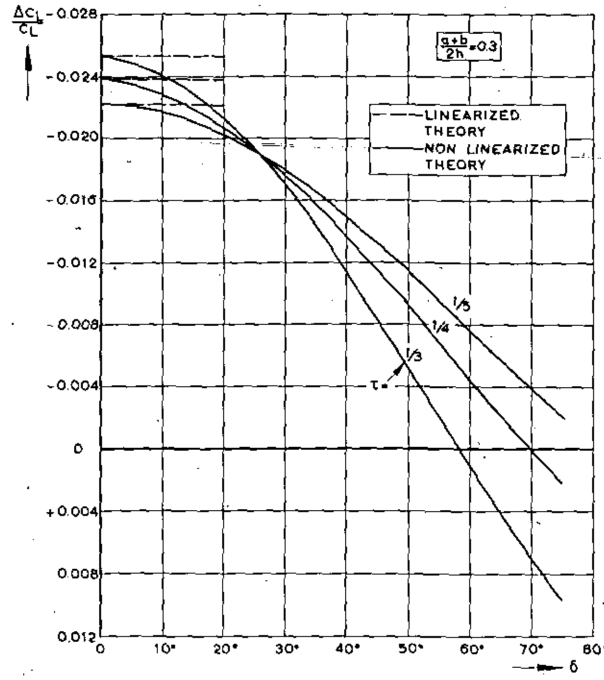

Fig. 11. Tunnel wall corrections for the lift coefficients as function of the angle of flap deflection for three values of τ; $(a+b)/2h=0.3$.

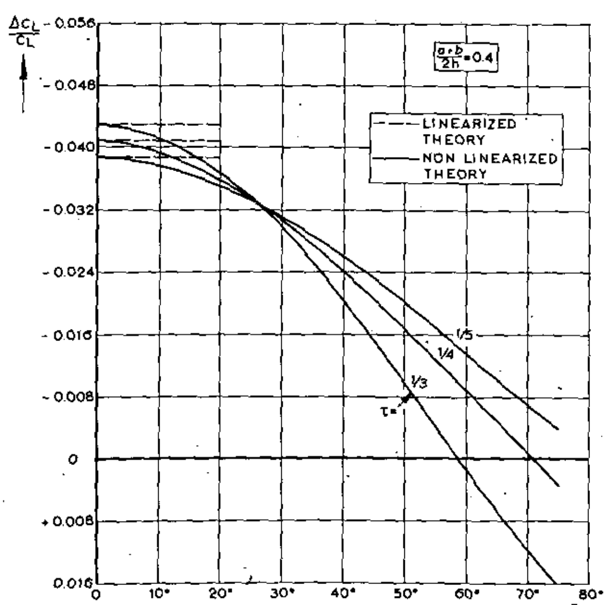

Fig. 12. Tunnel wall correction for the lift coefficient as function of the angle of flap deflection for three values of τ; $(a+b)/2h=0.4$.

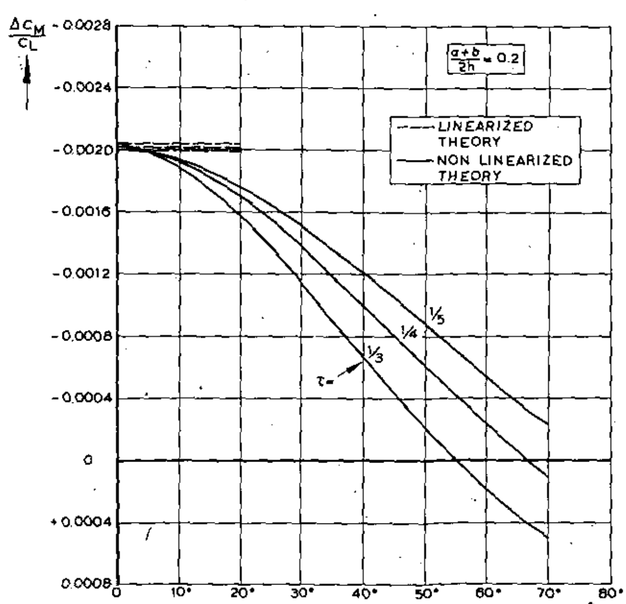

Fig. 13. Tunnel wall corrections for the moment coefficient as function of the angle of flap deflection for three values of τ; $(a+b)/2h=0.2$. The moment is taken about the quarter-chord point.

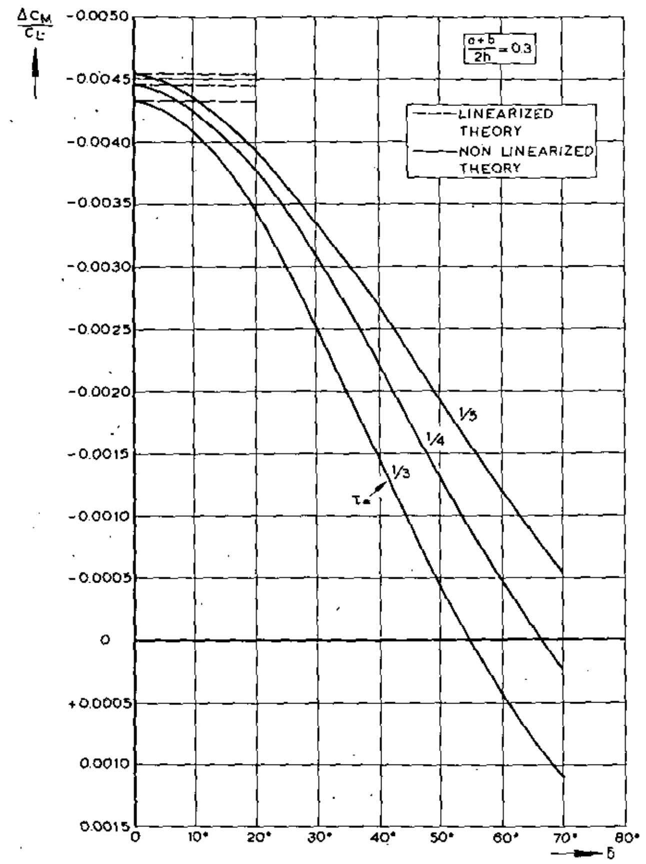

Fig. 14. Tunnel wall corrections for the moment coefficient as function of the angle of flap deflection for three values of τ; $(a+b)/2h=0.3$. The moment is taken about the quarter-chord point.

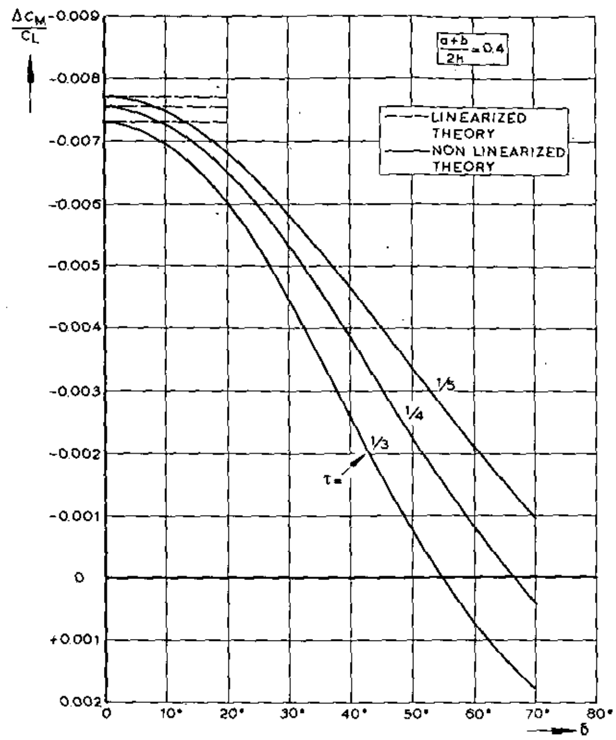

Fig. 15. Tunnel wall corrections for the moment coefficient as function of the angle of flap deflection for three values of τ; $(a+b)/2h=0.4$. The moment is taken about the quarter-chord point.

C.C.L. Class. D 304: D 301

REPORT NLR-TR W. 8

Two-dimensional tunnel wall corrections for a wing with a blown flap between two parallel walls

by

E. M. de Jager

Summary

A linearized, two-dimensional theory has been developed for the determination of the pressure distribution on a wing with a jet-augmented flap between two parallel walls. The pressure distribution is expressed by means of integrals containing the given normal velocity at the wing and the vorticity distribution in the wake. This vorticity distribution is determined by an integral equation, which must be solved numerically.

Graphs presented show the tunnel wall corrections of the aerodynamic derivatives for a flat wing with a flap as functions of the jet momentum coefficient for three values of the ratio of wing chord to tunnelheight and for three values of the ratio of flap to wing chord.

Contents

List of symbols

c_j	jet momentum coefficient
$g(x)$	distance of the jet from center-line of the tunnel
h	semi-height of the tunnel
k	modulus of elliptic functions
l	semi-chord of the wing
n	direction of the outward normal
p	pressure
u	velocity component in x-direction
v	velocity component in y-direction
w	downwash at the wing
x, y	rectangular co-ordinates
z	$x+iy$
C_L	lift coefficient for wing between the walls
C_L^*	lift coefficient for wing in free flight
ΔC_L	tunnel wall correction, $\Delta C_L = C_L^* - C_L$
C_M	moment coefficient for wing between the walls
C_M^*	moment coefficient for wing in free flight
ΔC_M	tunnel wall correction, $\Delta C_M = C_M^* - C_M$
$G(x, y;\ x_p, y_p)$	function of Green
J	momentum flux in the jet
$K(\sigma, \tau)$	kernel function
L	lift of the wing
M	moment of the wing; about quarter-chord point and positive when tail-heavy

R	radius of curvature of the jet	ξ, η	transformed co-ordinates
U	mean velocity outside the jet	ζ	$\xi + i\eta$
U_0	unperturbed velocity at infinity	ρ	density inside the jet
V	mean velocity inside the jet	ρ_0	density outside the jet
β	angle of flap deflection	τ	ratio of flap to wing chord
$\gamma(x)$	vorticity distribution in the wake	$\varphi(x, y)$	velocity potential
δ	thickness of the jet	$\Phi(\xi, \eta;\ \xi_p, \eta_p)$	complex velocity potential

1 Introduction

By blowing a thin jet of high velocity at the trailing edge of a wing into the outer flow, one obtains both a propulsive thrust and an additional lift force induced by the jet momentum flux at the exit of the jet.

This high lift device has been the object of many theoretical and experimental investigations during the last ten years, particularly in England and France, and to a lesser extent in the U.S.A. (see refs. 1, 2, 3, and 4).

At the National Aero- and Astronautical Research Institute, an experimental program has been performed during which lift and moment measurements have been made for a two-dimensional wing-flap system with a jet of small thickness being ejected over the trailing edge flap (flap-blowing).

The purpose of this theoretical investigation is to provide tunnel wall corrections in order to reduce the measured values of the aerodynamic coefficients to free flight conditions.

On developing the theory we have to make some restrictive assumptions, which we shall summarize here shortly. The problem will be treated as if it were a two-dimensional system and therefore the influence of the side walls of the tunnel will not be taken into account. The upper and lower walls of the tunnel are assumed to be parallel.

The thickness of the jet is assumed to be very small and therefore the theory is confined to the case of jets with vanishing thickness, but with finite (non-zero) momentum flux.

Spence (see ref. 5) has pointed out that in this case it is allowed to replace the jet by a single vortex sheet, extending downward to infinity.

We suppose further that the velocity of the outer flow is so small that the fluid may be considered incompressible. Since the theory of a two-dimensional wing with a jet in free flight already leads to an integral equation which is rather difficult to solve (see ref. 6), it is sensible to linearize the equations, as the problem discussed in this report is much more complicated than that of a wing in free flight. Hence we must assume that the wing also is very thin and that the angle of attack and the angle of flap deflection are small. The wing is placed in the middle of the tunnel and the linearized boundary conditions at the wing and in the wake will be prescribed along the centre line of the tunnel.

This report is in some respects an extension of ref. 13 by the author. In the last mentioned report the angle of flap may be large and the theory developed there is non-linearized, while a jet is absent.

2 Representation of the jet by a vortex sheet

The determination of the tunnel wall corrections for a wing with a jet-augmented flap is very much complicated by the presence of the jet in the wake of the wing. Therefore we shall first turn our attention to the physical mechanism of the jet and to its mathematical representation. We shall give here in short the analysis of Preston and Spence (refs. 7 and 5).

A jet of high velocity air is created at some internal point A of the wing and is ducted in such a way as to flow tangentially over the flap of the wing (see sketch a).

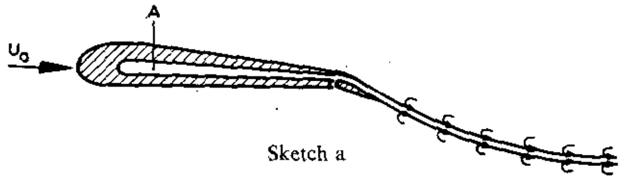

Sketch a

The jet which is not supposed to mix with the outer flow, is represented by two vortex sheets along its boundaries, the strength of each vortex sheet being equal to the difference of the velocities at both sides of the boundary. To investigate more precisely the influence of the jet on the outer flow, we consider an element of the jet, which is approximated by taking the jet boundaries of the element parallel and its radii of curvature equal to $R \pm \frac{1}{2}\delta$, where R is the radius of curvature of the centre line and δ the local thickness of the jet (see sketch b). The element subtends an angle $d\varphi$ at the centre of curvature of the jet.

The application of the Bernouilli-theorem outside and inside the jet yields:

$$p_1 + \tfrac{1}{2}\rho_0 u_1^2 = p_2 + \tfrac{1}{2}\rho_0 u_2^2 \tag{2.1}$$

$$p_1 + \tfrac{1}{2}\rho v_1^2 = p_2 + \tfrac{1}{2}\rho v_2^2 \tag{2.2}$$

where p_1 and p_2 denote the pressures at the boundaries of that jet, u_1 and u_2 the corresponding velocities in the main stream and v_1 and v_2 those in the jet; ρ_0 and ρ are the densities in the main stream and the jet respectively.

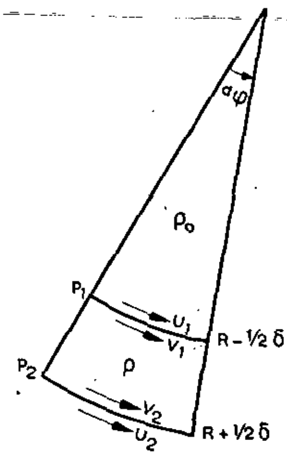

Sketch b

Subtraction of (2.1) and (2.2) gives:

$$u_1^2 - u_2^2 = \frac{\rho}{\rho_0}(v_1^2 - v_2^2) \tag{2.3}$$

Due to the irrotationality of the flow inside the jet we can write:

$$v_1(R - \tfrac{1}{2}\delta) = v_2(R + \tfrac{1}{2}\delta) \tag{2.4}$$

On introducing the mean velocities

$$U = \frac{u_1 + u_2}{2} \tag{2.5}$$

$$V = \frac{v_1 + v_2}{2} \tag{2.6}$$

we can deduce from (2.4)

$$v_1 - v_2 = \frac{\delta \cdot V}{R} \tag{2.7}$$

and hence, from (2.3), (2.5) and (2.6),

$$u_1 - u_2 = \frac{\rho V^2 \delta}{\rho_0 U R} \tag{2.8}$$

From (2.2), (2.6) and (2.7) we derive the relation:

$$p_2 - p_1 = \frac{\rho V^2 \delta}{R} \tag{2.9}$$

which expresses that the pressure jump across the jet acts as a centripetal force on the jet.

The momentum flux in the jet is defined by

$$J = \rho V^2 \delta \tag{2.10}$$

and hence

$$p_2 - p_1 = \frac{J}{R} \tag{2.11}$$

On introducing the momentum coefficient

$$c_j = \frac{J}{\rho_0 U^2 l} \tag{2.12}$$

where l is some characteristic length, relation (2.11) becomes:

$$\frac{p_2 - p_1}{\rho_0 U^2} = c_j \frac{l}{R} \tag{2.13}$$

The jet is represented by two vortex layers; the strengths of the vortices, measured positively in clockwise direction, are given by

$$\gamma_1 \mathrm{d}s_1 = +(u_1 - v_1)(R - \tfrac{1}{2}\delta)\mathrm{d}\varphi \tag{2.14}$$

$$\gamma_2 \mathrm{d}s_2 = -(u_2 - v_2)(R + \tfrac{1}{2}\delta)\mathrm{d}\varphi \tag{2.15}$$

where $\mathrm{d}s_1$ and $\mathrm{d}s_2$ are line elements along the upper resp. lower side of the jet.

When δ is small we may replace the two vortices with strengths $\gamma_1 \mathrm{d}s_1$ and $\gamma_2 \mathrm{d}s_2$ by a single vortex of strength

$$\gamma R \mathrm{d}\varphi = \gamma \mathrm{d}s = \gamma_1 \mathrm{d}s_1 + \gamma_2 \mathrm{d}s_2 \tag{2.16}$$

located along the centre line of the jet, and a doublet of strength

$$mR \mathrm{d}\varphi = \tfrac{1}{2}\delta(\gamma_2 \mathrm{d}s_2 - \gamma_1 \mathrm{d}s_1) \tag{2.17}$$

with the axis along the centre line.

Substitution of (2.14) and (2.15) into (2.16) and (2.17) yields for the strength per unit length of the vortex sheet along the centre line of the jet:

$$\gamma = \frac{\rho V^2 \delta}{\rho_0 U R} - \frac{U\delta}{R} = U\left\{\frac{J}{\rho_0 U^2 R} - \frac{\delta}{R}\right\} \tag{2.18}$$

and for the strength per unit length of the doublet

$$m = \delta\left\{(V - U) + \tfrac{1}{4}\frac{\delta}{R}\frac{J}{\rho_0 U R} - \tfrac{1}{4}\left(\frac{\delta}{R}\right)^2 V\right\} \tag{2.19}$$

Hence, on the assumption that the thickness of the jet is very small, while the momentum flux is non-zero finite, we may disregard the sheet of the doublets and the jet may be replaced by a single vortex sheet of strength:

$$\gamma = \frac{J}{\rho_0 U R} \tag{2.20}$$

When the velocity in the jet is very large in comparison with the velocity in the outer flow, it is allowed to take the momentum flux J constant along the whole jet, and therefore the jet momentum coefficient defined by (2.12) may be taken also as a constant, viz.:

$$c_j = \frac{J}{\rho_0 U_0^2 l} \tag{2.21}$$

where the velocity U is replaced by the unperturbed velocity U_0 of the main stream.

For a detailed analysis the reader is referred to ref. 5.

3 The boundary value problem for the perturbation velocity potential

The wing is placed in the middle of the tunnel. Since we linearize the flow equations, we can prescribe the boundary conditions at the wing and at the jet as follows: the former at a segment along the centre line of the tunnel and the latter at the semi-infinite part of the centre line stretching downward from the trailing edge of the wing to infinity.

The wing-tunnel configuration is indicated in sketch c; l is the semi-chord of the wing and h the semi-height of the tunnel. The point C denotes the hinge axis of the wing flap. Cartesian co-ordinates (x, y) are used and they are defined as indicated in sketch c. Next we introduce a perturbation velocity potential $\varphi(x, y)$, such that the perturbation velocity components $u(x, y)$ and $v(x, y)$ are defined by

$$u = \frac{\partial\varphi}{\partial x} \quad \text{and} \quad v = \frac{\partial\varphi}{\partial y} \tag{3.1}$$

In the region between the tunnel walls $\varphi(x, y)$ satisfies the equation of continuity, which for the case of incompressible flow, reduces to the equation of Laplace, viz.:

$$\frac{\partial^2\varphi}{\partial x^2} + \frac{\partial^2\varphi}{\partial y^2} = 0 \tag{3.2}$$

The boundary conditions at the wing and along the tunnel walls are determined by the condition of tangential flow and hence:

$$\frac{\partial\varphi}{\partial y} = -w(x) \quad \text{for } -l \leqq x \leqq +l;\ y = \pm 0 \tag{3.3}$$

and

$$\frac{\partial\varphi}{\partial y} = 0 \qquad \text{for} \quad y = \pm h \tag{3.4}$$

where $w(x)$ denotes the normal velocity at the wing, taken positively in the downward direction; $w(x)$ is a known function and is determined by the given mean camber line, the angle of attack and the angle of flap deflection of the wing.

We shall first draw our attention to the boundary condition prescribed along the wake of the wing, i.e. for $+l \leqq x < \infty$, $y=0$. In chapter 2 we have shown that thin jets of high velocity may be represented by a single vortex sheet, inducing a pressure jump across the sheet. This pressure jump acts as a centripetal force and hence it is related to the curvature of the sheet by

$$\Delta p = \frac{J}{R}$$

where Δp is positive in the upward direction and R is positive when the sheet is concave.

Describing the jet streamline by the equation

$$y = g(x) \tag{3.5}$$

and using the definition (2.21), the pressure jump across the vortex sheet becomes in linearized approximation:

$$\Delta p = \rho_0 U_0^2 c_j l g''(x) \tag{3.6}$$

Since $y=g(x)$ is a streamline, we can write:

$$g''(x) = \frac{\mathrm{d}}{\mathrm{d}x}\frac{\mathrm{d}g}{\mathrm{d}x} = \frac{1}{U_0}\frac{\partial v(x,0)}{\partial x} \quad \text{for } l \leqq x < \infty \tag{3.7}$$

and hence:

$$\Delta p = \rho_0 U_0 c_j l \frac{\partial v(x,0)}{\partial x} \tag{3.8}$$

By aid of Kutta's condition:

$$\Delta p = \rho_0 U_0 \gamma(x)$$

we obtain for the strength of the vortex sheet replacing the jet:

$$\gamma(x) = c_j l \frac{\partial v(x,0)}{\partial x} \quad \text{for} \quad l \leqq x < \infty \tag{3.9}$$

which is essentially the same formula as (2.20).

Using the definition:

$$\gamma(x) = u(x, +0) - u(x, -0) = 2u(x, +0) \tag{3.10}$$

formula (3.9) can also be written as

$$u(x, +0) = \tfrac{1}{2} c_j l \frac{\partial v(x, +0)}{\partial x} \tag{3.11}$$

The problem of the determination of the velocity field around a profile with a jet between two parallel walls, is now reduced to the derivation of the solution of the boundary value problem for the perturbation velocity potential which, within the region between the tunnel walls, has to satisfy the Laplace equation (3.2), the boundary conditions along the walls, the aerofoil and the wake being given respectively by (3.4), (3.3) and (3.11).

The solution of this boundary value problem is performed in three steps. We decompose the disturbance velocity potential $\varphi(x, y)$ into three parts, viz.:

$$\varphi(x,y) = \varphi_1(x,y) + \varphi_2(x,y) + \varphi_3(x,y) \tag{3.12}$$

where φ_1, φ_2 and φ_3 are defined as follows:

(i) $\varphi_1(x, y)$ is the velocity potential accounting for the given normal velocity $w(x)$ at the wing and the zero normal velocity along the walls, or expressed mathematically:

$$\frac{\partial^2 \varphi_1}{\partial x^2} + \frac{\partial^2 \varphi_1}{\partial y^2} = 0$$

with boundary conditions:

$$\frac{\partial \varphi_1}{\partial y} = -w(x) \quad \text{for} \quad -l \leqq x \leqq +l,\ y = \pm 0 \tag{3.13}$$

and

$$\frac{\partial \varphi_1}{\partial y} = 0 \qquad \text{for} \quad y = \pm h \tag{3.14}$$

(ii) $\varphi_2(x, y)$ is the velocity potential due to the vortex sheet replacing the jet; $\varphi_2(x, y)$ satisfies the Laplace-equation and in order not to disturb the downwash conditions along the aerofoil and the tunnel walls, $\varphi_2(x, y)$ is subjected to the conditions:

$$\frac{\partial\varphi_2}{\partial y} = 0 \quad \text{for} \quad -l \leqq x \leqq +l, \; y = \pm 0 \quad \text{and for} \quad y = \pm h \tag{3.15}$$

(iii) $\varphi_3(x, y)$ is the velocity potential due to the circulation around the aerofoil; $\varphi_3(x, y)$ satisfies the Laplace equation and introduces only a jump in the potential across the aerofoil and the wake.
$\varphi_3(x, y)$ has to satisfy the homogeneous conditions:

$$\frac{\partial\varphi_3}{\partial y} = 0 \quad \text{for} \quad -l \leqq x \leqq +l, \; y = \pm 0 \quad \text{and for} \quad y = \pm h\,. \tag{3.16}$$

This complete boundary value problem is similar to the problem of a harmonically oscillating aerofoil between two parallel walls, which has been solved amongst others by Timman (ref. 8).

The only difference between the two problems consists in the fact, that in the case of the oscillating aerofoil the vorticity distribution in the wake is a known function of x (apart from a multiplicative constant), whereas in the case of an aerofoil with a jet, the vorticity distribution is an unknown function of x.

The derivation of formulae for the potentials $\varphi_1(x, y)$ and $\varphi_2(x, y)$ runs along the same lines as in the mentioned paper by Timman, but $\varphi_2(x, y)$ will now contain the unknown vorticity distribution $\gamma(x)$ in the wake. However, by aid of the boundary condition (3.9) along the wake we can derive an integral equation for $\gamma(x)$, which can be solved numerically.

4 The determination of the perturbation velocity potential

4.1 *The determination of the potential $\varphi_1(x, y)$ due to the normal velocity at the wing*

The potential $\varphi_1(x, y)$ satisfies the Laplace-equation in the region D between the two parallel walls FG and HI (see sketch c) and is submitted to the boundary conditions

$$\frac{\partial\varphi_1}{\partial y} = -w(x) \quad \text{for} \quad -l \leqq x \leqq +l, \; y = \pm 0 \tag{3.13}$$

and

$$\frac{\partial\varphi_1}{\partial y} = 0 \qquad \text{for} \quad y = \pm h \tag{3.14}$$

where $w(x)$ is a given function of x.

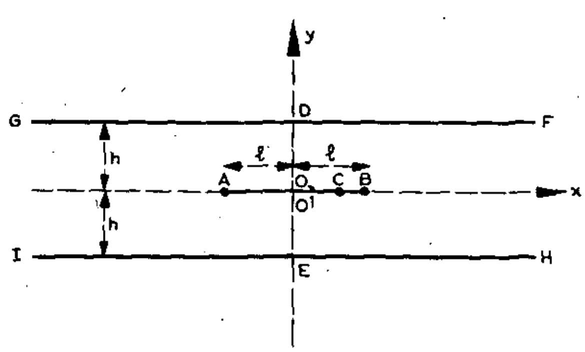

Sketch c

This boundary value problem is a Neumann problem and is solved by means of Green's function. Because of the complexity of the boundaries we shall use a conformal mapping which maps almost all points of the interior of the region D between the tunnel walls into the interior of a rectangle. The transformation formula has been derived in ref. 8 and is defined by:

$$\frac{\mathrm{d}z}{\mathrm{d}\zeta} = -\frac{2hk}{\pi}\,\mathrm{sn}(\zeta, k) \tag{4.1}$$

where $z = x + \mathrm{i}y$ and $\zeta = \xi + \mathrm{i}\eta$; $\mathrm{sn}(\zeta, k)$ is a Jacobian elliptic function with modulus k, determined by the relation:

$$k = \tanh\frac{\pi l}{2h} \tag{4.2}$$

The conformal mapping is illustrated in sketch d, where corresponding points are denoted by the same capitals.

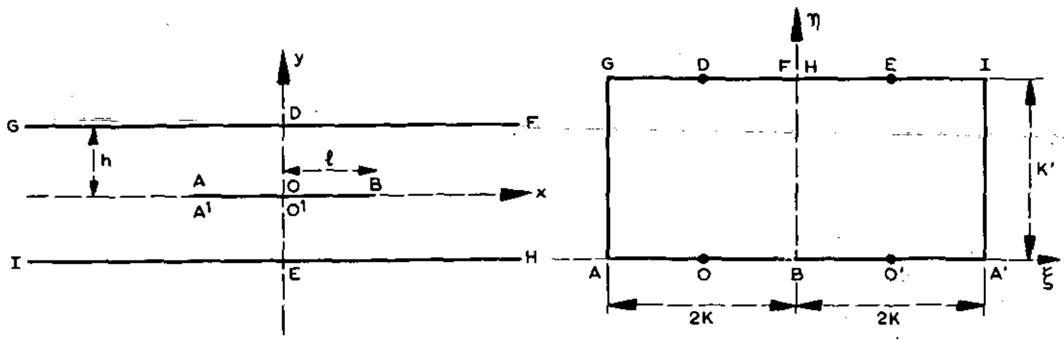

$z=x+iy$ plane Sketch d $\zeta=\xi+i\eta$ plane

The dimensions of the rectangle are $4K$ and K', K and K' being the complete elliptic integrals of the first kind with modulus k resp. $k'=\sqrt{1-k^2}$.

Since the Jacobian elliptic function $\mathrm{sn}(\zeta, k)$ has a real period $4K$ the mapping function $\zeta=\zeta(z)$ is a multi-valued function; the rectangles with corners at the points $\zeta=\pm K \bmod (4K)$ and $\zeta=\pm 2K+iK' \bmod (4K)$ are the images of corresponding Riemann-sheets in the physical plane which intersect along the semi-infinite line A'I.

It may be remarked that not all points, lying between the tunnel walls and not on the wing surface, are mapped into the interior of the rectangle; namely the points on the intersection A'I are mapped on the vertical boundaries of the rectangle.

Therefore it is necessary to apply the method of the function of Green in a somewhat modified way, as will appear in the deduction which follows.

As is well known the potential $\varphi_1(x, y)$ can be expressed by:

$$\varphi_1(x_p, y_p) = -\oint\left\{\frac{\partial\varphi_1}{\partial n} G(x, y; x_p, y_p) - \varphi_1 \frac{\partial G(x, y;\ x_p, y_p)}{\partial n}\right\} ds \tag{4.3}$$

where $G(x, y; x_p, y_p)$ denotes the function of Green; the path of integration is a single closed contour taken along the tunnel walls and the wing, namely the polygon FGAOBO'A'IH; n is the direction of the outward normal along this contour.

The function $G(x, y;\ x_p, y_p)$ is a solution of the equation of Laplace, regular in the area bounded by the polygon except at the point $x=x_p$, $y=y_p$, where it has a logarithmic singularity. Moreover the function $G(x, y;\ x_p, y_p)$ will satisfy some homogeneous boundary conditions which will be specified later on.

After transformation to the ζ-plane we obtain for the velocity potential

$$\varphi_1(x_p, y_p) = -\oint\left\{\frac{\partial\varphi_1}{\partial\nu} G_T(\xi, \eta;\ \xi_p, \eta_p) - \varphi_1 \frac{\partial G_T(\xi, \eta;\ \xi_p, \eta_p)}{\partial\nu}\right\} d\sigma \tag{4.4}$$

where the path of integration is now taken along the sides of the rectangle and ν is the direction of the outward normal; $G_T(\xi, \eta;\ \xi_p, \eta_p)$ is again Green's function and has in corresponding points the same value as the function $G(x, y;\ x_p, y_p)$.

Hence $G_T(\xi, \eta;\ \xi_p\eta_p)$ is a function which also satisfies the equation of Laplace and has a logarithmic singularity for $\xi=\xi_p$, $\eta=\eta_p$.

The boundary conditions for $G_T(\xi, \eta;\ \xi_p, \eta_p)$ are now specified as follows:

$$\frac{\partial G_T}{\partial\nu}(\xi, \eta;\ \xi_p, \eta_p)=0 \tag{4.5}$$

along the line segments AA' and GI and the values of $G_T(\xi, \eta;\ \xi_p, \eta_p)$ along the line segments AG and A'I are the same for points with the same η co-ordinate; hence

$$G_T(-2K, \eta;\ \xi_p, \eta_p)=G_T(+2K, \eta;\ \xi_p, \eta_p) \tag{4.6}$$

These boundary conditions yield for the function $G(x, y;\ x_p, y_p)$ the conditions $\partial G/\partial y=0$ along the wing and along the tunnel walls, and G is continuous across the intersection A'I.

Since $\varphi_1(x, y)$ is antisymmetrical with respect to the x-axis and $\varphi_1(x, y)$ is continuous across the semi-infinite line-segment AG (see sketch d), $\varphi_1(x, 0)$ will be zero for $-\infty < x \leq -l$.

Hence equation (4.4) can be written as

$$\varphi_1(x_p, y_p)=-\oint\frac{\partial\varphi_1}{\partial\nu} G_T(\xi, \eta;\ \xi_p, \eta_p) d\sigma \tag{4.7}$$

Using along the horizontal boundaries of the rectangle the relation:

$$\frac{\partial\varphi_1(\xi,\eta)}{\partial\nu} = \frac{\partial\varphi_1(x,y)}{\partial n}\cdot\left|\frac{\partial n}{\partial\nu}\right| = \frac{\partial\varphi_1(x,y)}{\partial n}\left|\frac{\mathrm{d}z}{\mathrm{d}\zeta}\right| \tag{4.8}$$

and substituting the boundary conditions (3.13) and (3.14) and the transformation formula (4.1) we obtain

$$\frac{\partial\varphi_1(\xi,\eta)}{\partial\nu} = -\frac{2hk}{\pi}\,\mathrm{sn}(\xi,k)w(x) \quad \text{for } -2K<\xi<+2K,\ \eta=0 \tag{4.9}$$

and

$$\frac{\partial\varphi_1(\xi,\eta)}{\partial\nu} = 0 \qquad \text{for } -2K<\xi<+2K,\ \eta=\mathrm{i}K' \tag{4.10}$$

Since $\partial\varphi_1/\partial y$ is continuous across the semi-infinite line-segment AG, $\partial\varphi_1/\partial n$ along AG will differ from $\partial\varphi_1/\partial n$ along A′I only in sign, as n is the direction of the outward normal. Since $\mathrm{sn}(\zeta,k)$ has a period of $4K$, it is clear that

$$\frac{\partial\varphi_1(-2K,\eta)}{\partial\nu} = -\frac{\partial\varphi_1(+2K,\eta)}{\partial\nu} \tag{4.11}$$

Substituting (4.9), (4.10) and (4.11) into (4.7) and using the condition (4.6) we obtain finally for the velocity potential $\varphi_1(x_p, y_p)$ the form:

$$\varphi_1(x_p,y_p) = +\frac{2hk}{\pi}\int_{-2K}^{+2K} w_T(\xi)G_T(\xi,\eta;\ \xi_p,\eta_p)\,\mathrm{sn}(\xi,k)\mathrm{d}\xi \tag{4.12}$$

where $w_T(\xi)$ is defined by

$$w_T(\xi) = w(x) \tag{4.13}$$

for corresponding points.

To obtain the function of Green $G_T(\xi,\eta;\ \xi_p,\eta_p)$, we have to place a source at the point $\zeta=\zeta_p$ and this source is reflected against the lines $\eta=0$ and $\eta=K'$, because the contours of wing and tunnel walls are streamlines. The field of sources is repeated consecutively with period $4K$ in the ξ-direction in order to satisfy the relation (4.6). Hence we have obtained two double-periodic fields of sources, namely at the points $\zeta=\zeta_p+4mK+\mathrm{i}2nK'$ and $\zeta=\bar\zeta_p+4mK+\mathrm{i}2nK'$, where m and n are integers and $\bar\zeta_p$ is the complex conjugate of ζ_p.

The function $G_T(\xi,\eta;\ \xi_p,\eta_p)$ has been determined in appendix A; it turns out that

$$G_T(\xi,\eta;\ \xi_p,\eta_p) = \\ = \frac{1}{2\pi}\mathrm{Re}\left[\ln\left\{\mathrm{sn}\left(\frac{\zeta-\zeta_p}{2},k\right)\mathrm{sn}\left(\frac{\zeta-\bar\zeta_p}{2},k\right)\right\}+2\int_0^{(\zeta-\zeta_p)/2}Z(t)\mathrm{d}t+2\int_0^{(\zeta-\bar\zeta_p)/2}Z(t)\mathrm{d}t\right]+\frac{\xi^2-\eta^2+\xi_p^2-\eta_p^2}{8KK'} \tag{4.14}$$

where $Z(t)$ is the Z-function of Jacobi, defined by:

$$Z(t) = \int_0^t \mathrm{dn}^2(t',k)\mathrm{d}t' - t\,\frac{E(k)}{K(k)} \tag{4.15}$$

$\mathrm{dn}(t',k)$ being a Jacobian elliptic function and $E(k)$ the complete elliptic integral of the second kind, both with modulus k.

The modulus of the elliptic functions to be used in the further development of the theory will mostly be k and therefore we shall omit henceforth the symbol k; when the modulus is not k, it will be indicated explicitly. Substitution of formula (4.14) into (4.12) yields for the velocity potential φ_1:

$$\varphi_1(x_p,y_p) = \\ = \frac{hk}{\pi^2}\int_{-2K}^{+2K} w_T(\xi)\left[\mathrm{Re}\left\{\ln\left(\mathrm{sn}\,\frac{\xi-\zeta_p}{2}\,\mathrm{sn}\,\frac{\xi-\bar\zeta_p}{2}\right)+2\int_0^{(\xi-\zeta_p)/2}Z(t)\mathrm{d}t+2\int_0^{(\xi-\bar\zeta_p)/2}Z(t)\mathrm{d}t\right\}+\frac{\xi^2-\eta^2+\xi_p^2-\eta_p^2}{8KK'}\right]\mathrm{sn}\,\xi\,\mathrm{d}\xi$$

Since $\mathrm{sn}\,\xi$ and $Z(t)$ are odd functions and $w_T(\xi)$ is an even function we can write:

$$\varphi_1(x_p,y_p) = \frac{hk}{\pi^2}\int_{-2K}^{0} w_T(\xi)\,\mathrm{Re}\left\{\ln\frac{\mathrm{sn}\,\dfrac{\xi-\zeta_p}{2}\,\mathrm{sn}\,\dfrac{\xi-\bar\zeta_p}{2}}{\mathrm{sn}\,\dfrac{\xi+\zeta_p}{2}\,\mathrm{sn}\,\dfrac{\xi+\bar\zeta_p}{2}} - 2\int_{(\xi-\zeta_p)/2}^{(\xi+\zeta_p)/2}Z(t)\mathrm{d}t - 2\int_{(\xi-\bar\zeta_p)/2}^{(\xi+\bar\zeta_p)/2}Z(t)\mathrm{d}t\right\}\mathrm{sn}\,\xi\,\mathrm{d}\xi \tag{4.16}$$

Differentiation of this expression to x_p and taking the limit $y_p=+0$ with $-l<x_p<+l$ yields the following formula for the velocity component u_1 on the wing

$$u_1(x_p, +0) = \int_{-2K}^{0} w_T(\xi) P_1(\xi_p, \xi) d\xi \tag{4.17}$$

with $-l<x_p<+l$ and correspondingly $-2K<\xi_p<0$, while

$$P_1(\xi_p, \xi) = -\frac{1}{\pi}\frac{1}{\operatorname{sn}\xi_p}\left\{\operatorname{sn}\xi\,\frac{\operatorname{cn}\xi\operatorname{dn}\xi+\operatorname{cn}\xi_p\operatorname{dn}\xi_p}{\operatorname{cn}^2\xi-\operatorname{cn}^2\xi_p} - Z(\xi)\right\}\operatorname{sn}\xi \tag{4.18}$$

The term $u_1(x_p, +0)$ is necessary for the determination of the pressure on the wing. From equation (3.9) it is apparent, that in order to determine the vorticity in the wake we also need an expression for the velocity component v in the wake.

Therefore we shall also give here a formula for the velocity component v_1, which can be obtained after differentiating (4.16) to y_p, and taking subsequently the limit for $y_p=0$ with $+l<x_p<+\infty$. The result is:

$$v_1(x_p, 0) = \int_{-2K}^{0} w_T(\xi) Q_1(\eta_p, \xi) d\xi \tag{4.19}$$

with $+l\leqq x_p<+\infty$ and correspondingly $0\leqq\eta_p<K'$, while

$$Q_1(\eta_p, \xi) = -\frac{i}{\pi}\frac{1}{\operatorname{sn} i\eta_p}\left\{\operatorname{sn}\xi\,\frac{\operatorname{cn}\xi\operatorname{dn}\xi+\operatorname{cn} i\eta_p\operatorname{dn} i\eta_p}{\operatorname{cn}^2\xi-\operatorname{cn}^2 i\eta_p} - Z(\xi)\right\}\operatorname{sn}\xi \tag{4.20}$$

The reductions for obtaining the formulae (4.17) through (4.20) have been performed in appendix B.

4.2 *The determination of the potential $\varphi_2(x, y)$ due to the vortices in the wake*

Next we shall consider the velocity potential $\varphi_2(x, y)$ due to the vortex sheet representing the jet.

$\varphi_2(x, y)$ satisfies the equation of Laplace and in order not to disturb the downwash conditions along the aerofoil and the tunnel walls, which have already been satisfied by the velocity potential $\varphi_1(x, y)$, $\varphi_2(x, y)$ must be submitted to the homogeneous conditions (3.15):

$$\frac{\partial\varphi_2}{\partial y} = 0 \quad \text{for} \quad -l\leqq x\leqq +l,\ y=\pm 0 \quad \text{and for} \quad y=\pm h$$

The velocity potential at the point (x_p, y_p) due to a unit vortex at the point $(x, 0)$ with $x>l$ in the presence of the wing and the tunnel walls, is obtained in the same way as the function of Green, determined in appendix A. This potential is also obtained by successive reflections of the vortex against the lines $\eta=0$ and $\eta=K'$ and by periodic repetitions with period $4K$ in the ξ-direction. In this case, however, the sign of the vortex is reversed at each reflection in order to satisfy the conditions (3.15); the scheme of the vortex and its reflections is repeated in the ξ-direction with period $4K$ in order to make $\varphi_2(x, y)$ and its derivatives continuous across the semi-infinite line segment A′I (see sketch d).

The total potential of these two double-periodic fields of vortices is determined in appendix C and the result reads:

$$-\frac{1}{2\pi}\operatorname{Im}\left\{\ln\frac{\operatorname{sn}\dfrac{\zeta_p-i\eta}{2}}{\operatorname{sn}\dfrac{\zeta_p+i\eta}{2}} - 2\int_{(\zeta_p-i\eta)/2}^{(\zeta_p+i\eta)/2} Z(t)dt\right\} \tag{4.21}$$

where ζ_p is the image of the point of observation (x_p, y_p) and $i\eta$ that of the point $(x, 0)$ of the wake.

Hence the velocity potential $\varphi_2(x, y)$ due to the vortices with the still unknown strength $\gamma(x)dx$ is given by the expression:

$$\varphi_2(x_p, y_p) = -\frac{1}{2\pi}\int_l^{\infty}\gamma(x)\operatorname{Im}\left\{\ln\frac{\operatorname{sn}\dfrac{\zeta_p-i\eta}{2}}{\operatorname{sn}\dfrac{\zeta_p+i\eta}{2}} - 2\int_{(\zeta_p-i\eta)/2}^{(\zeta_p+i\eta)/2} Z(t)dt\right\}dx =$$

$$+\frac{hk}{\pi^2}i\int_0^{K'}\gamma_T(\eta)\operatorname{Im}\left\{\ln\frac{\operatorname{sn}\dfrac{\zeta_p-i\eta}{2}}{\operatorname{sn}\dfrac{\zeta_p+i\eta}{2}} - 2\int_{(\zeta_p-i\eta)/2}^{(\zeta_p+i\eta)/2} Z(t)dt\right\}\operatorname{sn} i\eta\, d\eta \tag{4.22}$$

with $\gamma_T(\eta)=\gamma(x)$ for corresponding values of x and η.

Differentiation of (4.22) with respect to x_p and taking $y_p = +0$ with $-l \leqq x_p \leqq +l$ yields the following formula for the velocity component u_2 at the wing surface:

$$u_2(x_p, +0) = \int_0^{K'} \gamma_T(\eta) P_2(\xi_p, \eta) \mathrm{d}\eta \tag{4.23}$$

with $-l \leqq x_p \leqq +l$ and correspondingly $-2K \leqq \xi_p \leqq 0$, while

$$P_2(\xi_p, \eta) = -\frac{1}{2\pi} \frac{1}{\operatorname{sn} \xi_p} \left\{ \operatorname{sn} i\eta \, \frac{\operatorname{cn} i\eta \operatorname{dn} i\eta + \operatorname{cn} \xi_p \operatorname{dn} \xi_p}{\operatorname{cn}^2 i\eta - \operatorname{cn}^2 \xi_p} - Z(i\eta) \right\} \operatorname{sn} i\eta \tag{4.24}$$

Differentiating $\varphi_2(x_p, y_p)$ to y_p and taking $y_p = 0$ with $+l \leqq x_p < \infty$ we obtain the downwash in the wake due to the potential φ_2, viz.:

$$v_2(x_p, 0) = \int_0^{K'} \gamma_T(\eta) Q_2(\eta_p, \eta) \mathrm{d}\eta \tag{4.25}$$

with $l \leqq x_p < \infty$ and correspondingly $0 \leqq \eta_p < K'$, while

$$Q_2(\eta_p, \eta) = \frac{-i}{2\pi} \frac{1}{\operatorname{sn} i\eta_p} \left\{ \operatorname{sn} i\eta \, \frac{\operatorname{cn} i\eta \operatorname{dn} i\eta + \operatorname{cn} i\eta_p \operatorname{dn} i\eta_p}{\operatorname{cn}^2 i\eta - \operatorname{cn}^2 i\eta_p} - Z(i\eta) \right\} \operatorname{sn} i\eta \tag{4.26}$$

The reductions for obtaining the formulae (4.23) through (4.26) have been performed in appendix D.

4.3 *The determination of the velocity potential $\varphi_3(x, y)$ due to the circulation*

A suitable potential satisfying zero conditions along the tunnel walls and the aerofoil, and yielding a jump equal to $-4aK$ across the wake is simply given by:

$$\varphi_3(x_p, y_p) = -a(2K + \xi_p) \quad \text{for} \quad -2K < \xi_p < 0 \quad \text{i.e. the upper side of the aerofoil}$$

and

$$\varphi_3(x_p, y_p) = +a(2K - \xi_p) \quad \text{for} \quad 0 < \xi_p < 2K \quad \text{i.e. the lower side of the aerofoil} \tag{4.27}$$

where a is a constant to be determined by aid of the Kutta-condition.

Differentiation with respect to x_p yields for the velocity component u_3 at the upper surface of the wing:

$$u_3(x_p, +0) = +a \frac{\pi}{2hk} \frac{1}{\operatorname{sn} \xi_p} \tag{4.28}$$

with $-l \leqq x_p \leqq +l$ and correspondingly $-2K \leqq \xi_p \leqq 0$.

Differentiation with respect to y_p yields for the downwash v_3 in the wake:

$$v_3(x_p, 0) = +a \frac{\pi}{2hk} \frac{i}{\operatorname{sn} i\eta_p} \tag{4.29}$$

with $+l \leqq x_p < \infty$ and correspondingly $0 \leqq \eta_p < K'$.

We determine now the constant a by substituting the expressions (4.19), (4.25) and (4.29) for the vertical velocity components v into the Kutta-condition, which expresses that

$$\lim_{\eta_p \to 0} (v_1 + v_2 + v_3) \text{ is finite}.$$

One obtains quite easily the result:

$$a = \frac{-2hk}{\pi^2} \int_{-2K}^{0} w_T(\xi) \left\{ \frac{1 + \operatorname{cn} \xi \operatorname{dn} \xi}{\operatorname{sn} \xi} + Z(\xi) \right\} \operatorname{sn} \xi \, \mathrm{d}\xi - \frac{hk}{\pi^2} \int_0^{K'} \gamma_T(\eta) \left\{ \frac{1 + \operatorname{cn} i\eta \operatorname{dn} i\eta}{\operatorname{sn} i\eta} + Z(i\eta) \right\} \operatorname{sn} i\eta \, \mathrm{d}\eta \tag{4.30}$$

5 The pressure distribution on the aerofoil

The pressure distribution Δp on the aerofoil can be obtained from the velocity component $u(x_p, +0)$ along the aerofoil. In linearized approximation the pressure distribution can be written as:

$$\frac{\Delta p(x_p)}{\frac{1}{2}\rho_0 U_0^2} = +\frac{4u(x_p, +0)}{U_0} = \frac{4}{U_0} \left\{ u_1(x_p, +0) + u_2(x_p, +0) + u_3(x_p, +0) \right\} \tag{5.1}$$

or by aid of the equations (4.19), (4.23) and (4.28)

$$\frac{\Delta p(x_p)}{\frac{1}{2}\rho_0 U_0^2} = \frac{4}{U_0} \left\{ \int_{-2K}^{0} w_T(\xi) P_1(\xi_p, \xi) \mathrm{d}\xi + \int_0^{K'} \gamma_T(\eta) P_2(\xi_p, \eta) \mathrm{d}\eta + \frac{a\pi}{2hk} \frac{1}{\operatorname{sn} \xi_p} \right\}.$$

After substituting the expression (4.30) for the constant a and the formulae (4.18) and (4.24) for $p_1(\xi_p, \xi)$ resp. $p_2(\xi_p, \eta)$ we obtain:

$$-\frac{\Delta p(x_p)}{\frac{1}{2}\rho_0 U_0^2} = +\frac{4}{\pi U_0}\left\{\int_{-2K}^{0} w_T(\xi) K(\xi_p, \xi) d\xi + \tfrac{1}{2}\int_0^{K'} \gamma_T(\eta) K(\xi_p, i\eta) d\eta\right\} \tag{5.2}$$

for $-l \leqq x_p \leqq +l$ and correspondingly $-2K \leqq \xi_p \leqq 0$, while the kernelfunction K is given by:

$$K(\sigma, \tau) = \frac{1}{\operatorname{sn}\sigma}\left\{\frac{\operatorname{cn}\sigma \operatorname{dn}\sigma + \operatorname{cn}\tau \operatorname{dn}\tau}{\operatorname{cn}^2\sigma - \operatorname{cn}^2\tau} - \frac{1 + \operatorname{cn}\tau \operatorname{dn}\tau}{1 - \operatorname{cn}^2\tau}\right\}\operatorname{sn}^2\tau \tag{5.3}$$

The first integral on the right-hand side of eq. (5.2) can always be calculated, either exactly or numerically, for any given normal velocity distribution on the wing surface.

However, the second integral on the right-hand side of eq. (5.2) still contains the unknown vorticity distribution $\gamma_T(\eta)$ of the vortex sheet.

This vorticity distribution is related to the downwash in the wake by the jet condition (3.9); since the downwash can be expressed by aid of the formulae (4.19), (4.25) and (4.29), it can be written as the sum of some integrals, containing either the given downwash at the wing or the vorticity distribution in the wake. Hence the jet condition (3.9) can be recast in an integral equation for the unknown vorticity distribution.

After the numerical solution of the integral equation and the substitution of the values of $\gamma_T(\eta)$ into the second term of equation (5.2), we obtain finally the pressure distribution on the wing surface.

6 The integral equation for the vorticity distribution in the wake

The jet condition, valid in the wake, reads according to (3.9)

$$\gamma(x) = c_j l \frac{\partial v(x, 0)}{\partial x} \quad \text{for} \quad l \leqq x < \infty$$

Integrating with respect to x from infinity to a point $(x_p, 0)$ in the wake, one obtains the relation:

$$v(x_p, 0) = v_1(x_p, 0) + v_2(x_p, 0) + v_3(x_p, 0) = -\frac{1}{c_j l}\int_{x_p}^{\infty} \gamma(x) dx \tag{6.1}$$

Substitution of the expressions for $v_i(x_p, 0)$ yields the following integral equation for the vorticity in the wake:

$$\int_{\eta_p}^{K'} \gamma_T(\eta) \operatorname{sn} i\eta \, d\eta = \frac{c_j l}{2hk}\left\{\int_{-2K}^{0} w_T(\xi) K(i\eta_p, \xi) d\xi + \tfrac{1}{2}\int_0^{K'} \gamma_T(\eta) K(i\eta_p, i\eta) d\eta\right\} \tag{6.2}$$

with $0 \leqq \eta_p < K'$, while the kernel function K is defined by the formula (5.3).

The first term on the right-hand side of eq. (6.2) can again be calculated either exactly or numerically for any given normal velocity distribution on the aerofoil

It has to be remarked that the kernel function $K(i\eta_p, i\eta)$ has a singularity for $\eta = \eta_p$ of the type $1/(\eta - \eta_p)$, and the second integral on the right-hand side of (6.2) must be conceived in the sense of Cauchy.

The integral equation (6.2) can be solved numerically; after substitution of the values of $\gamma_T(\eta)$ into (5.2) we obtain numerical values for the pressure distribution and after substitution into the jet condition (6.1), we find the slope of the jet streamline.

7 The limiting case of walls at infinite distance

In the limiting case of walls at infinite distance, viz. $h \to \infty$, the theory reduces to the theory of the wing with jet in free flight.

For $h \to \infty$ the elliptic functions pass into ordinary trigonometric functions.

The conformal transformation (4.1) becomes

$$\frac{dz}{d\zeta} = -l \sin\zeta$$

or

$$z = l \cos\zeta \tag{7.1}$$

The infinite unbounded region around the wing is mapped into the semi-infinite strip $-\pi < \xi < +\pi, \eta > 0$ of the complex ζ-plane.

The wing contour has its image along the real axis of the ζ-plane; the upper side is mapped on the line segment $-\pi < \xi < 0$ and the lower side on the line segment $0 < \xi < \pi$ (see sketch e).

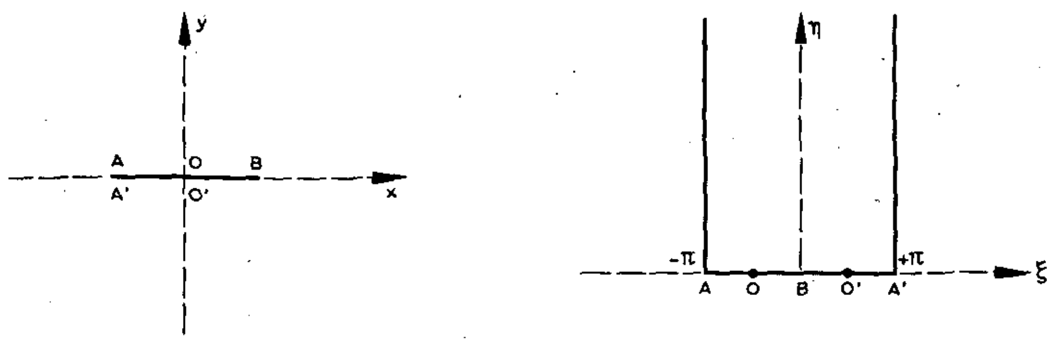

$z=x+iy$ plane Sketch e $\zeta=\xi+i\eta$ plane

Taking the limit $h\to\infty$ or $k\to 0$ (compare (4.2)) and denoting corresponding quantities in free flight by an asterisk, we obtain for the pressure distribution the expression:

$$\frac{\Delta p^*(x_p)}{\frac{1}{2}\rho_0 U_0^2} = +\frac{1}{\pi U_0}\left\{\int_{-\pi}^{0} w_T(\xi)K^*(\xi_p,\xi)\,d\xi+\tfrac{1}{2}\int_0^{\infty}\gamma_T^*(\eta)K^*(\xi_p, i\eta)\,d\eta\right\} \tag{7.2}$$

with $-l\leqq x_p\leqq +l$ and $x_p=l\cos\xi_p$, $-\pi<\xi_p<0$.

The integral equation for the vorticity distribution in the wake reduces to:

$$\int_{\eta_p}^{\infty}\gamma_T^*(\eta)\sinh\eta\,d\eta = \frac{c_j}{\pi i}\left\{\int_{-\pi}^{0} w_T(\xi)K^*(i\eta_p,\xi)\,d\xi+\tfrac{1}{2}\int_0^{\infty}\gamma_T^*(\eta)K^*(i\eta_p, i\eta)\,d\eta\right\} \tag{7.3}$$

with $0<\eta_p<\infty$ and $x_p=l\cosh\eta_p$.

The kernelfunction $K^*(\sigma,\tau)$ occurring in (7.2) and (7.3) becomes now

$$K^*(\sigma,\tau) = \frac{1}{\sin\sigma}\left\{\frac{1}{\cos\sigma-\cos\tau}-\frac{1}{1-\cos\tau}\right\}\sin^2\tau \tag{7.4}$$

Putting $\bar{z}=(1+\cos\zeta)/2$ it can be easily shown that the equations (7.2) and (7.3) are identical to those derived by Spence in ref. 5.

8 The tunnel wall corrections for lift and moment

When numerical values have been obtained for the pressure distribution on the wing by aid of the formulae (5.2) and (7.2) for the cases of tunnel walls and free flight respectively, lift and moment can easily be calculated by numerical integration.

Assuming that the jet at the exit makes an angle β with the direction of the main stream at infinity, the lift of the wing is given by:

$$L=\int_{-l}^{+l}\Delta p(x)\,dx+J\cdot\beta \tag{8.1}$$

and the lift coefficient $C_L=L/\rho_0 U_0^2 l$ by

$$C_L=\int_{-l}^{+l}\frac{\Delta p(x)}{\rho_0 U_0^2 l}\,dx+c_j\cdot\beta \tag{8.2}$$

The moment about the quarter chord point (taken positively in clockwise direction) is defined by

$$M=-\int_{-l}^{+l}(x+\tfrac{1}{2}l)\Delta p(x)\,dx-(x_F+\tfrac{1}{2}l)J\cdot\beta \tag{8.3}$$

where x_F denotes the x-coordinate of the jet exit on the wing; the moment coefficient $C_M=M/2\rho_0 U_0^2 l^2$ is given by:

$$C_M=-\int_{-l}^{+l}\frac{(x+\frac{1}{2}l)\Delta p(x)}{2\rho_0 U_0^2 l^2}\,dx-\frac{(x_F+\frac{1}{2}l)}{2l}c_j\cdot\beta \tag{8.4}$$

Lift and moment coefficients C_L^* and C_M^* for the wing in free flight are defined in the same way and the tunnel wall corrections become thus:

$$\Delta C_L=C_L^*-C_L \tag{8.5}$$

and

$$\Delta C_M=C_M^*-C_M \tag{8.6}$$

9 Application of the theory to a flat wing with jet-augmented flap

The theory, developed in the preceding chapter, has been applied to the flat wing with a jet-augmented flap. The angle of attack of the wing is taken zero, while the angle of flap deflection is β.
The jet-exit is taken at the hinge point of the flap and the jet is blown tangentially over the flap (flap-blowing).

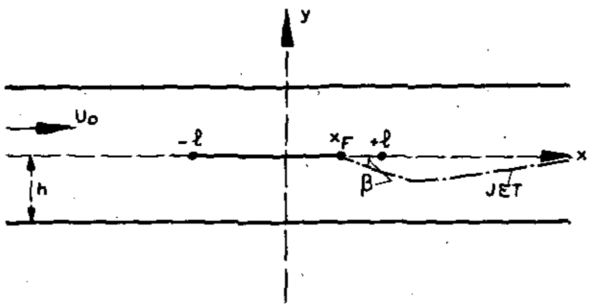

Sketch f

The wing chord is taken again $2l$ and the hinge point of the flap has x-coordinate $x=x_F$. The configuration is indicated in sketch f. The normal velocity $w(x)$ at the wing is given by

$$\begin{aligned} w(x) &= 0 \quad &&\text{for} \quad -l \leqq x \leqq x_F \\ w(x) &= U_0\beta \quad &&\text{for} \quad x_F \leqq x \leqq +l \end{aligned} \tag{9.1}$$

Substitution of this downwash-function into the integral-equation for the vorticity in the wake yields:

$$\int_{\eta_p}^{K'} \gamma_T(\eta)\,\mathrm{sn}\,i\eta\,\mathrm{d}\eta = \frac{c_j l}{2hk}\left\{U_0\beta\int_{-\xi_F}^{0} K(i\eta_p,\xi)\mathrm{d}\xi + \tfrac{1}{2}\int_0^{K'}\gamma_T(\eta)K(i\eta_p, i\eta)\mathrm{d}\eta\right\} \tag{9.2}$$

where $\zeta=-\xi_F$, is the image in the ζ-plane of the hinge-point $z=x_F+\mathrm{i.o}$. The first term on the right-hand side can be calculated.

Inserting equation (5.3), it can be written as:

$$F(\eta_p) = U_0\beta\int_{-\xi_F}^{0} K(i\eta_p,\xi)\mathrm{d}\xi = \frac{U_0\beta}{\mathrm{sn}\,i\eta_p}\int_{-\xi_F}^{0}\left\{\frac{\mathrm{cn}\,i\eta_p\,\mathrm{dn}\,i\eta_p + \mathrm{cn}\,\xi\,\mathrm{dn}\,\xi}{\mathrm{cn}^2 i\eta_p - \mathrm{cn}^2\xi} - \frac{1+\mathrm{cn}\,\xi\,\mathrm{dn}\,\xi}{1-\mathrm{cn}^2\xi}\right\}\mathrm{sn}^2\xi\,\mathrm{d}\xi \tag{9.3}$$

According to formula (4.1) the relation between the x-coordinate of points at the aerofoil and the ξ-coordinate of their images in the ζ-plane is given by:

$$\frac{\mathrm{d}x}{\mathrm{d}\xi} = -\frac{2hk}{\pi}\,\mathrm{sn}\,\xi$$

or after integration:

$$x = \frac{2h}{\pi}\cosh^{-1}\left(\frac{\mathrm{dn}\,\xi}{k'}\right) \tag{9.4}$$

Hence the relation between ξ_F and x_F is:

$$\frac{x_F}{l} = \frac{2}{\pi}\frac{h}{l}\cosh^{-1}\left(\frac{\mathrm{dn}\,\xi_F}{k'}\right) \quad \text{with} \quad 0<\xi_F<2K \tag{9.5}$$

ξ_F can be solved numerically for any given x_F/l by an iteration process. The integral (9.3) can be reduced to the following form:

$$\begin{aligned} F(\eta_p) = \frac{-\mathrm{i}U_0\beta}{\mathrm{sn}(\eta_p,k')}\,\mathrm{cn}(\eta_p,k')\Bigg[&\frac{\mathrm{dn}(\eta_p,k')-\mathrm{cn}^2(\eta_p,k')}{\mathrm{cn}^2(\eta_p,k')}\,\xi_F - \frac{\mathrm{sn}(\eta_p,k')}{\mathrm{cn}(\eta_p,k')}\tan^{-1}\left\{\frac{\mathrm{sn}(\xi_F,k)}{\mathrm{sn}(\eta_p,k')}\,\mathrm{cn}(\eta_p,k')\right\} + \\ &- \frac{\mathrm{dn}(\eta_p,k')}{\mathrm{cn}^2(\eta_p,k')}\,\Pi\left(\varphi_F, \frac{-\mathrm{cn}^2(\eta_p,k')}{\mathrm{sn}^2(\eta_p,k')}, k\right)\Bigg] \end{aligned} \tag{9.6}$$

where Π is the incomplete elliptic integral of the third kind, defined by

$$\Pi(\varphi,\alpha^2,k) = \int_0^{u_1}\frac{\mathrm{d}u}{1-\alpha^2\mathrm{sn}^2 u} \tag{9.7}$$

with $\sin\varphi = \mathrm{sn}\,u_1$.

The function $F(\eta_p)$ can be evaluated by using the well-known Fourier expansions for the elliptic functions of Jacobi and a series expansion to the modulus for the elliptic integral Π. The integral equation for the vorticity distribution is solved subsequently in a numerical way. This integral equation is satisfied in N-points $\eta_{p,n}$ with $0<\eta_{p,n}<K'$, $n=1,2,\ldots N$.

Since the pressure at the wing is influenced more strongly by the vortices in the neighbourhood of the trailing edge than by those further away downstream in the wake, it is recommendable to satisfy the integral equation for the vorticity distribution as good as possible in the neighbourhood of the trailing edge. Therefore we introduce the simple transformation

$$\eta=\frac{t}{1-t}, \qquad \eta_p=\frac{t_p}{1-t_p} \tag{9.8}$$

and hence t and t_p are lying in the interval $(0, K'/(1+K'))$.

Putting for $t_{p,n}$ N equidistant points, we obtain an $\eta_{p,n}$ distribution which is more dense in the neighbourhood of the trailing edge than further away downstream in the wake.

The integrals containing $\gamma_T(\eta)=\gamma_T\{t/(1-t)\}$ are now evaluated by means of the trapezoïdal rule for which the points, dividing the integration interval, are the same as the points $t_{p,n}$, $n=1,\ldots N$.

For $\eta_p=0$(or $t_p=0$), according to (3.9) the integral equation reduces simply to:

$$\int_l^\infty \gamma(x)\mathrm{d}x=c_j l U_0\beta$$

or

$$\int_0^{K'}\gamma_T(\eta)\,\mathrm{sn}\,\mathrm{i}\eta\,\mathrm{d}\eta=-\mathrm{i}\,\frac{\pi}{2}\,\frac{l}{hk}\,c_j U_0\beta \tag{9.9}$$

Hence by satisfying this formula and the integral equation for the vorticity distribution in N points $t_{p,n}$ and by approximating the integrals containing $\gamma_T(\eta)$ by the trapezoïdal rule, we obtain a system of $(N+1)$ linear algebraic equations for the $(N+1)$ unknown values of $\gamma_T\{t_{p,n}/(1-t_{p,n})\}, n=1,2,\ldots N$ and $\gamma_T(0)$.

$\gamma_T(K')$ does not occur as an unknown value, since we know beforehand that $\gamma_T(K')$ equals zero, because $\gamma(x)\to 0$ for $x\to\infty$.

In appendix E it is shown that $\gamma(x)=0(1/x^2)$ for $x\to\infty$ and therefore $\gamma(x)$ is replaced by $(1/x^2)\,\bar\gamma(x)$ or $\gamma_T(\eta)$ by

$$\frac{\pi^2}{h^2}\left\{\ln\frac{\mathrm{dn}(\eta,k')+k}{\mathrm{dn}(\eta,k')-k}\right\}^{-2}\bar\gamma_T(\eta)$$

where the factor of $\bar\gamma_T(\eta)$ has been found by integration of the transformation formula (4.1).

Solution of the set of $(N+1)$ linear algebraic equations yields $(N+1)$ numerical values for $\gamma_T(\eta)=\gamma_T\{t/(1-t)\}$.

In the reduction of the integral equation to a set of $(N+1)$ linear algebraic equations the complication of the kernel $K(\mathrm{i}\eta_p,\mathrm{i}\eta)$ having a Cauchy-singularity at $\eta=\eta_p$ arises. This singularity is isolated by writing

$$\int_0^{K'}\gamma_T(\eta)K(\mathrm{i}\eta_p,\mathrm{i}\eta)\mathrm{d}\eta=\int_0^{K'}\{\gamma_T(\eta)-\gamma_T(\eta_p)\}K(\mathrm{i}\eta_p,\mathrm{i}\eta)\mathrm{d}\eta+\gamma_T(\eta_p)\int_0^{K'}K(\mathrm{i}\eta_p,\mathrm{i}\eta)\mathrm{d}\eta=$$

$$=\int_0^{K'/(1+K')}\left\{\gamma_T\left(\frac{t}{1-t}\right)-\gamma_T\left(\frac{t_p}{1-t_p}\right)\right\}K\left(\mathrm{i}\,\frac{t_p}{1-t_p},\ \mathrm{i}\,\frac{t}{1-t}\right)\frac{\mathrm{d}t}{(1-t)^2}+\gamma_T\left(\frac{t_p}{1-t_p}\right)\int_0^{K'}K(\mathrm{i}\eta_p,\mathrm{i}\eta)\mathrm{d}\eta \tag{9.10}$$

The second integral on the right-hand side of (9.10) can be reduced to a formula being composed of elliptic functions and the first one is numerically approximated by the trapezoïdal rule.

For $t=t_p=t_{p,n}$ the integrand is approximated by:

$$\frac{\gamma_T\left(\dfrac{t_{p,n+1}}{1-t_{p,n+1}}\right)-\gamma_T\left(\dfrac{t_{p,n-1}}{1-t_{p,n-1}}\right)}{t_{p,n+1}-t_{p,n-1}}\lim_{t\to t_{p,n}}\left\{(t-t_{p,n})K\left(\mathrm{i}\,\frac{t_{p,n}}{1-t_{p,n}},\ \mathrm{i}\,\frac{t}{1-t}\right)\right\} \tag{9.11}$$

in which the limit can be calculated easily.

The occurring elliptic functions are evaluated by aid of Fourier-expressions.

Having obtained in this way numerical values for $\gamma_T(\eta_p)=\gamma_T\{t_p/(1-t_p)\}$ the pressure distribution at the aerofoil is determined by substituting these values into equation (5.2), which for the case considered here, reduces to:

$$\frac{\Delta p(x_p)}{\frac{1}{2}\rho_0 U_0^2} = + \frac{4}{\pi U_0}\left\{U_0\delta\int_{-\xi_F}^{0} K(\xi_p, \xi)\,\mathrm{d}\xi + \tfrac{1}{2}\int_{0}^{K'} \gamma_T(\eta) K(\xi_p, i\eta)\,\mathrm{d}\eta\right\} \tag{9.12}$$

Both integrals are evaluated numerically for several equidistant points at the wing surface. As to the first integral one has to distinguish the cases where ξ_p lies inside and where it lies outside the integration interval; when ξ_p lies inside this interval, the integrand has a Cauchy-singularity and the numerical integration is performed after isolating this singularity.

When we have determined in this way the pressure at the aerofoil in several equidistant points, we approximate the pressure distribution finally by the formula:

$$\frac{\Delta p}{\frac{1}{2}\rho_0 U_0^2\beta} = a_0 \operatorname{cotg}\frac{\vartheta}{2} + a_1 \log\left|\frac{\sin\dfrac{\vartheta+\vartheta_F}{2}}{\sin\dfrac{\vartheta-\vartheta_F}{2}}\right| + \frac{\Delta p(l)}{\frac{1}{2}\rho_0 U_0^2\beta} + a_2\sin\vartheta + a_3\sin 2\vartheta + a_4\sin 3\vartheta + a_5\sin 4\vartheta \tag{9.13}$$

where $x/l=-\cos\vartheta$ with $0<\vartheta<\pi$ and $x_F/l=-\cos\vartheta_F$.

The coefficients $a_0, \ldots a_5$ are determined by aid of the values of the known pressure distribution at the wing.

We can now easily determine the aerodynamic coefficients C_L and C_M by substituting (9.13) into the formulae (8.2) and (8.4) and performing the integrations.

The calculations have been performed by aid of the electronic computer *ZEBRA* of the mathematical department of the National Aero- and Astronautical Research Institue.

The aerodynamic coefficients C_L^* and C_M^* for the free flight case are calculated in the same way by taking h very large, i.e. k is very small.

We have not used the formulae (7.2) and (7.3) since the calculations for small values of k can be performed by means of the same program as for the case of tunnel walls.

10 Numerical results

Tunnel wall corrections for the aerodynamic derivatives $\partial C_L/\partial\beta$ and $\partial C_M/\partial\beta$ have been calculated in the way outlined in the preceding chapter.

The ratio l/h of wing chord to tunnelheight has been chosen as 2/21, 4/21 and 6/21 and the ratio τ of flap to wing chord as 15%, 25% and 100%. The jet-momentum coefficient ranges from 0–5.

The integral equation for the vorticity distribution has been satisfied in 15 points in the wake and hence N is taken equal to 15. The pressure distribution at the wing is calculated in the points $x/l=-0.8(0.2)+0.8$.

The values of the aerodynamic derivatives for the case of free flight have been calculated from the formulae, valid for the wing between tunnel walls by taking $l/h=0.025$.

The values of the lift derivative for the wing in free flight ($l/h=0.025$) have been compared with those of Spence (ref. 9) for several values of the jet-momentum coefficient and the agreement appears to be satisfactory.

The aerodynamic derivatives $\partial C_L/\partial\beta$ and $\partial C_M/\partial\beta$ have been plotted for fixed τ as functions of that jet-momentum coefficient c_j for $l/h=0$, 2/21, 4/21 and 6/21 in figs. 1, 3, 5, 7, 9 and 11.

The corresponding tunnel wall corrections

$$\frac{\Delta\dfrac{\partial C_L}{\partial\beta}}{\dfrac{\partial C_L}{\partial\beta}} = \frac{\dfrac{\partial C_L^*}{\partial\beta} - \dfrac{\partial C_L}{\partial\beta}}{\dfrac{\partial C_L}{\partial\beta}} \tag{10.1}$$

$$\frac{\Delta\dfrac{\partial C_M}{\partial\beta}}{\dfrac{\partial C_L}{\partial\beta}} = \frac{\dfrac{\partial C_M^*}{\partial\beta} - \dfrac{\partial C_M}{\partial\beta}}{\dfrac{\partial C_L}{\partial\beta}} \tag{10.2}$$

have been plotted as functions of c_j in the figs. 2, 4, 6, 8, 10 and 12.

As to the case of $\tau=1$, i.e. the case that the jet is blown over a wing with angle of attack β, we have to remark that the moment point is the quarter chord point of the wing and not the point $(-\frac{1}{2}l, 0)$.

A survey of the values of the tunnel wall corrections for some values of c_j, l/h and τ is given in the next table.

$\tau \rightarrow$	0.15		0.25		1		
$c_j \downarrow$	$\dfrac{\Delta \frac{\partial C_L}{\partial \beta}}{\frac{\partial C_L}{\partial \beta}}$	$\dfrac{\Delta \frac{\partial C_M}{\partial \beta}}{\frac{\partial C_L}{\partial \beta}}$	$\dfrac{\Delta \frac{\partial C_L}{\partial \beta}}{\frac{\partial C_L}{\partial \beta}}$	$\dfrac{\Delta \frac{\partial C_M}{\partial \beta}}{\frac{\partial C_L}{\partial \beta}}$	$\dfrac{\Delta \frac{\partial C_L}{\partial \beta}}{\frac{\partial C_L}{\partial \beta}}$	$\dfrac{\Delta \frac{\partial C_M}{\partial \beta}}{\frac{\partial C_L}{\partial \beta}}$	$\dfrac{l}{h}$
0	−0.002	+0.0004	−0.002	+0.0004	−0.003	+0.0004	
1.6	−0.003	+0.0009	−0.003	+0.0009	−0.005	+0.0009	$\frac{2}{21}$
4.8	−0.005	+0.0015	−0.005	+0.0014	−0.006	+0.0014	
0	−0.009	+0.0017	−0.010	+0.0018	−0.014	+0.0018	
1.6	−0.013	+0.0034	−0.015	+0.0037	−0.018	+0.0037	$\frac{4}{21}$
4.8	−0.022	+0.0053	−0.023	+0.0054	−0.027	+0.0055	
0	−0.019	+0.0039	−0.021	+0.0040	−0.031	+0.0039	
1.6	−0.029	+0.0072	−0.031	+0.0077	−0.041	+0.0078	$\frac{6}{21}$
4.8	−0.045	+0.0105	−0.047	+0.0111	−0.055	+0.0112	

As to the case of $l/h = 2/21$ the tunnel wall corrections are very small and the results are not quite reliable due to the fact, that figures cancel out by the subtraction of the results for free flight and tunnel walls.

However, the corrections for $l/h = 4/21$ and $l/h = 6/21$ are certainly sufficiently reliable in order to use them for obtaining aerodynamic derivatives in free flight from the measurements in the tunnel.

11 References

[1] Williams, J., British research on boundary layer control for high lift by blowing. *Zeitschrift für Flugwissenschaften. 6. Jahrgang Heft 5* pp. 143–150 (1958).

[2] Williams, J., British research on the jet-flap scheme. Zeitschrift für Flugwissenschaften. 6. Jahrgang Heft 6 pp. 170–176 (1958).

[3] Poisson-Quinton, Ph., Jousserandot, P., Malavard, L., Jet-induced circulation control. Aero Digest Part I, Sept.; Part II, Oct.; Part III, Nov. 1956.

[4] Jacobs, W., Neuere theoretische Untersuchungen über den Strahlflügel in zweidimensionaler Strömung. Zeitschrift für Flugwissenschaften. 5. Jahrgang Heft 9 pp. 253–259 (1957).

[5] Spence, D. A., The lift coefficient of a thin, jet-flapped wing. Proc. of the Royal Soc. of London, Series A, Vol. 238, 1957.

[6] Davies, H. J., Ross, A. J., A jet deflected from the lower surface of an aerofoil. *Quarterly J. Mech. Appl. Math. Vol. 10 – No. 3, 1957.*

[7] Preston, J. H., Note on the circulation in circuits which cut the streamlines in the wake of an aerofoil at right angles. Report Memor. Aero. Research Comm. London. No. 2957, 1956.

[8] Timman, R., The aerodynamic forces on an oscillating aerofoil between two parallel walls. Applied Sci. Research. Vol. A 3, 1951.

[9] Spence, D. A., The lift on a thin aerofoil with a jet-augmented flap. The Aeron. Quart. Vol. IX, Part 3, 1958.

[10] Betz, A., Konforme Abbildung, Springer-Verlag, Berlin 1948.

[11] Whittaker, E. T., Watson, G. N., A course of modern analysis. Cambridge, University Press.

[12] Byrd, P. F., Friedman, M. D., Handbook of elliptic integrals for engineers and physicists. Springer-Verlag Berlin 1954.

[13] de Jager, E. M., van de Vooren, A. J., Tunnel wall corrections for a wing flap system between two parallel walls. *Report W 7*, National Aero- and Astronautical Research Institute, 1961, Amsterdam.

APPENDIX A

Derivation of Green's function

Green's function $G_T(\xi, \eta;\ \xi_p, \eta_p)$ is the potential at the point (ξ, η) due to two double-periodic fields of unit sources located at the points: $\zeta = \zeta_p + 4mK + \mathrm{i}2nK'$ and $\zeta = \bar{\zeta}_p + 4mK + \mathrm{i}2nK'$, where m and n are integers.

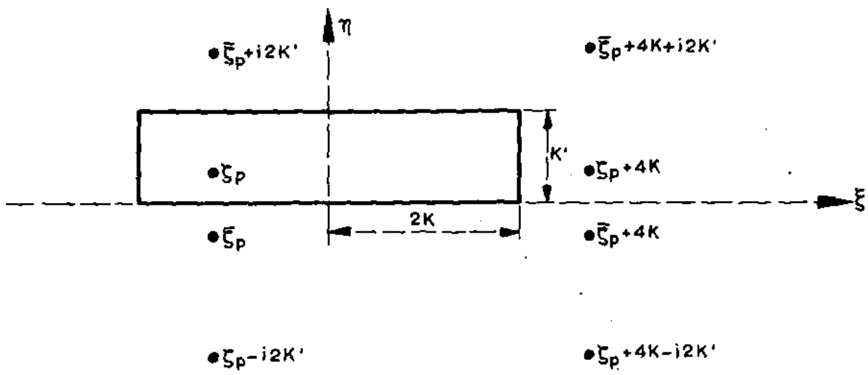

Sketch g: double-periodic fields of sources.

The potentials of these fields are not uniquely determined when they are not submitted to some boundary conditions (see ref. 10, page 291). These conditions are for the case considered here:

(i)
$$\frac{\partial G_T}{\partial \eta} = 0 \quad \text{for} \quad \eta = 0 \text{ and } \eta = K' \tag{A.1}$$

this means that the lines $\eta = 0$ and $\eta = K'$ are streamlines.

(ii)
$$G_T(-2K, \eta;\ \xi_p, \eta_p) = G_T(+2K, \eta;\ \xi_p, \eta_p) \tag{A.2}$$

This condition corresponds with that of equation (4.6) of the text and is explained there.

We introduce the complex potentials $\Phi_1(\xi, \eta;\ \xi_p, \eta_p)$ and $\Phi_2(\xi, \eta;\ \xi_p, \eta_p)$ due to the field of unit sources at the points $\zeta = \zeta_p + 4mK + \mathrm{i}2nK'$ resp. $\zeta = \bar{\zeta}_p + 4mK + \mathrm{i}2nK'$.

Analogously to the theory of ref. 10 we obtain for the potential Φ_1 the expression

$$\Phi_1 = \frac{1}{2\pi} \ln \vartheta_1 \left\{ \frac{\pi(\zeta_p - \zeta)}{2\mathrm{i}K'}, q \right\} = \frac{1}{2\pi} \ln \vartheta_1 \left\{ \frac{\pi(\zeta_p - \zeta)}{2\mathrm{i}K'} \middle| \frac{2\mathrm{i}K}{K'} \right\} \tag{A.3}$$

where ϑ_1 is the first thêta-function of Jacobi and $q = e^{-\pi(2K/K')}$; we have used here the notation of Whittaker-Watson (lit. 11). By aid of Landen's transformation:

$$\vartheta_1(2z\,|\,2\tau) = \frac{\vartheta_4(0\,|\,2\tau)}{\vartheta_3(0\,|\,\tau)\,\vartheta_4(0\,|\,\tau)}\,\vartheta_1(z\,|\,\tau)\,\vartheta_2(z\,|\,\tau) \tag{A.4}$$

and Jacobi's imaginary transformation:

$$\begin{aligned} (-\mathrm{i}\tau)^{\frac{1}{2}}\,\vartheta_1(z\,|\,\tau) &= -\mathrm{i}\,\exp(\mathrm{i}\tau' z^2/\pi)\,\vartheta_1(z\tau'\,|\,\tau') \\ (-\mathrm{i}\tau)^{\frac{1}{2}}\,\vartheta_2(z\,|\,\tau) &= \phantom{-\mathrm{i}}\,\exp(\mathrm{i}\tau' z^2/\pi)\,\vartheta_4(z\tau'\,|\,\tau') \end{aligned} \tag{A.5}$$

with $\tau' = -1/\tau$.

$\Phi_1(\xi, \eta;\ \xi_p, \eta_p)$ reduces to:

$$\Phi_1 = \frac{1}{2\pi}\left[\ln\left\{\vartheta_1\left(\frac{\pi(\zeta - \zeta_p)}{4K}\middle|\frac{K'}{K}\mathrm{i}\right)\cdot\vartheta_4\left(\frac{\pi(\zeta - \zeta_p)}{4K}\middle|\frac{K'}{K}\mathrm{i}\right)\right\} + \frac{\pi(\zeta_p - \zeta)^2}{8KK'}\right] \tag{A.6}$$

where we have omitted an irrelevant constant.

The complex potential Φ_2 is obtained from (A.6) after replacing ζ_p by $\bar{\zeta}_p$. Hence the total potential φ of the two double-periodic fields becomes:

$$\varphi(\xi, \eta;\ \xi_p, \eta_p) = \frac{1}{2\pi}\,\mathrm{Re}\left[\ln\left\{\vartheta_1\left(\frac{\pi(\zeta - \zeta_p)}{4K}\right)\cdot\vartheta_4\left(\frac{\pi(\zeta - \zeta_p)}{4K}\right)\cdot\vartheta_1\left(\frac{\pi(\zeta - \bar{\zeta}_p)}{4K}\right)\cdot\vartheta_4\left(\frac{\pi(\zeta - \bar{\zeta}_p)}{4K}\right)\right\}\right] +$$

$$+\ \frac{1}{16KK'}\,\mathrm{Re}\left[(\bar{\zeta}_p - \zeta)^2 + (\zeta_p - \zeta)^2\right] \tag{A.7}$$

the modulus $(K'/K)\mathrm{i}$ has been omitted for brevity.

This potential has to satisfy the condition $\partial\varphi/\partial\eta=0$ for $\eta=0$ and $\eta=K'$; this can easily be shown by proving that the harmonic conjugate of φ is constant for $\eta=0$ and $\eta=K'$.

The first term of (A.7) is periodic in ζ with period $4K$, but the second term is not, and $\varphi(-2K,\eta;\ \xi_p,\eta_p)\neq\varphi(+2K,\eta;\ \xi_p,\eta_p)$.

The condition (A.1) is however not violated when we add to the potential φ the potential of a uniform parallel flow, viz. $\xi_p\xi/4KK'$. Having done this we finally obtain the function of Green:

$$G(\xi,\eta;\ \xi_p,\eta_p)=\frac{1}{2\pi}\operatorname{Re}\left[\ln\left\{\vartheta_1\left(\frac{\pi(\zeta-\zeta_p)}{4K}\right)\cdot\vartheta_4\left(\frac{\pi(\zeta-\zeta_p)}{4K}\right)\cdot\vartheta_1\left(\frac{\pi(\zeta-\bar\zeta_p)}{4K}\right)\cdot\vartheta_4\left(\frac{\pi(\zeta-\bar\zeta_p)}{4K}\right)\right\}\right]+\frac{\xi_p^2-\eta_p^2+\xi^2-\eta^2}{8KK'} \tag{A.8}$$

Using the well-known relations:

$$\operatorname{sn}(z,k)=\frac{\vartheta_3}{\vartheta_2}\,\frac{\vartheta_1(z\vartheta_3^{-2})}{\vartheta_4(z\vartheta_3^{-2})} \tag{A.9}$$

where $\vartheta_3=\vartheta_3(0)$ and $\vartheta_2=\vartheta_2(0)$ and

$$\ln\vartheta_4\left(\frac{\pi z}{2K}\right)=\ln\theta(z)=\ln\theta(0)+\int_0^z Z(t)\mathrm{d}t \tag{A.10}$$

where $\theta(z)$ denotes the θ-function and $Z(t)$ the Z-function of Jacobi we can write at last:

$$G(\xi,\eta;\ \xi_p,\eta_p)=\frac{1}{2\pi}\operatorname{Re}\left[\ln\left\{\operatorname{sn}\left(\frac{\zeta-\zeta_p}{2}\right)k\operatorname{sn}\left(\frac{\zeta-\bar\zeta_p}{2}\right),k\right\}+2\left\{\int_0^{(\zeta-\zeta_p)/2}Z(t)\mathrm{d}t+\int_0^{(\zeta-\bar\zeta_p)/2}Z(t)\mathrm{d}t\right\}\right]+$$
$$+\frac{\xi^2-\eta^2+\xi_p^2-\eta_p^2}{8KK'} \tag{A.11}$$

which is the same as equation (4.14).

APPENDIX B

Determination of the velocity component u_1 on the wing and the velocity component v_1 in the wake

B.1 *The velocity component u_1 on the wing*

According to equation (4.16) the potential at a point (x_p, y_p) can be written as:

$$\varphi_1(x_p,y_p)=\frac{hk}{\pi^2}\int_{-2K}^{0}w_T(\xi)\operatorname{Re}\left\{\ln\frac{\operatorname{sn}\left(\frac{\xi-\zeta_p}{2}\right)\operatorname{sn}\left(\frac{\xi-\bar\zeta_p}{2}\right)}{\operatorname{sn}\left(\frac{\xi+\zeta_p}{2}\right)\operatorname{sn}\left(\frac{\xi+\bar\zeta_p}{2}\right)}-2\int_{(\xi-\zeta_p)/2}^{(\xi+\zeta_p)/2}Z(t)\mathrm{d}t-2\int_{(\xi-\bar\zeta_p)/2}^{(\xi+\bar\zeta_p)/2}Z(t)\mathrm{d}t\right\}\operatorname{sn}\xi\,\mathrm{d}\xi \tag{B.1}$$

Hence

$$\varphi_1(x_p,+0)=2\frac{hk}{\pi^2}\int_{-2K}^{0}w_T(\xi)\left\{\ln\left|\frac{\operatorname{sn}\frac{\xi-\xi_p}{2}}{\operatorname{sn}\frac{\xi+\xi_p}{2}}\right|-2\int_{(\xi-\xi_p)/2}^{(\xi+\xi_p)/2}Z(t)\mathrm{d}t\right\}\operatorname{sn}\xi\,\mathrm{d}\xi \tag{B.2}$$

with $-l<x_p<+l$ and correspondingly $-2K<\xi_p<0$.

Differentiation to x_p yields:

$$u_1(x_p,+0)=2\frac{hk}{\pi^2}\frac{\mathrm{d}\xi_p}{\mathrm{d}x_p}\int_{-2K}^{0}w_T(\xi)\left\{\frac{\partial}{\partial\xi_p}\ln\left|\frac{\operatorname{sn}\frac{\xi-\xi_p}{2}}{\operatorname{sn}\frac{\xi+\xi_p}{2}}\right|-Z\left(\frac{\xi+\xi_p}{2}\right)-Z\left(\frac{\xi-\xi_p}{2}\right)\right\}\cdot\operatorname{sn}\xi\,\mathrm{d}\xi \tag{B.3}$$

with

$$\frac{\mathrm{d}\xi_p}{\mathrm{d}x_p}=\frac{-\pi}{2hk}\,\frac{1}{\operatorname{sn}\xi_p}$$

Performing the differentiation to ξ_p, the factor of $w_T(\xi)$ in the integrand becomes:

$$-\operatorname{sn}\xi\left\{\frac{1}{2}\,\frac{\operatorname{cn}\frac{\xi-\xi_p}{2}\operatorname{dn}\frac{\xi-\xi_p}{2}}{\operatorname{sn}\frac{\xi-\xi_p}{2}}+\frac{1}{2}\,\frac{\operatorname{cn}\frac{\xi+\xi_p}{2}\operatorname{dn}\frac{\xi+\xi_p}{2}}{\operatorname{sn}\frac{\xi+\xi_p}{2}}+Z\left(\frac{\xi-\xi_p}{2}\right)+Z\left(\frac{\xi+\xi_p}{2}\right)\right\}$$

By aid of the addition formulae for the Jacobian elliptic functions (see ref. 11 or 12) this form becomes after some derivations

$$-\operatorname{sn}\xi\left\{\operatorname{sn}\xi\,\frac{\operatorname{cn}\xi\operatorname{dn}\xi+\operatorname{cn}\xi_p\operatorname{dn}\xi_p}{\operatorname{cn}^2\xi_p-\operatorname{cn}^2\xi}+Z(\xi)\right\} \tag{B.4}$$

Inserting (B.4) into (B.3) we finally obtain:

$$u_1(x_p,+0)=-\frac{1}{\pi}\frac{1}{\operatorname{sn}\xi_p}\int_{-2K}^{0}w_T(\xi)\left\{\operatorname{sn}\xi\,\frac{\operatorname{cn}\xi\operatorname{dn}\xi+\operatorname{cn}\xi_p\operatorname{dn}\xi_p}{\operatorname{cn}^2\xi-\operatorname{cn}^2\xi_p}-Z(\xi)\right\}\operatorname{sn}\xi\,d\xi \tag{B.5}$$

with $-l<x_p<+l$ and correspondingly $-2K<\xi_p<0$.
This is the same expression as given by eqn. (4.17).

B.2 *The velocity component v_1 in the wake*

We obtain $\lim\limits_{\substack{y_p\to+0\\ x_p>l}}\dfrac{\partial\varphi_1(x_p,y_p)}{\partial y_p}$ by applying the operator $-\dfrac{\pi}{2hk}\dfrac{i}{\operatorname{sn} i\eta_p}\dfrac{\partial}{\partial\xi_p}$ to the right-hand side of equation (B.1) and passing subsequently to the limit $\xi_p=-0$.

Performing this operation and using again the addition formulae of the Jacobian elliptic functions we get in quite analogous way as in appendix B.1, the result of eqs. (4.19) and (4.20), viz.:

$$v_1(x_p,0)=-\frac{1}{\pi}\frac{i}{\operatorname{sn} i\eta_p}\int_{-2K}^{0}w_T(\xi)\left\{\operatorname{sn}\xi\,\frac{\operatorname{cn}\xi\operatorname{dn}\xi+\operatorname{cn} i\eta_p\operatorname{dn} i\eta_p}{\operatorname{cn}^2\xi-\operatorname{cn}^2 i\eta_p}-Z(\xi)\right\}\operatorname{sn}\xi\,d\xi \tag{B.6}$$

with $x_p>+l$ and correspondingly $0<\eta_p<K'$.

APPENDIX C

Determination of the potential due to the two double-periodic fields of vortices

A vortex located in the wake has its image at the point $(i\eta_p, 0)$ of the ζ-plane. This vortex is reflected against the lines $\eta=0$ and $\eta=iK'$ and this proces is repeated again for the reflections themselves reversing at each reflection the sign of the vortex.

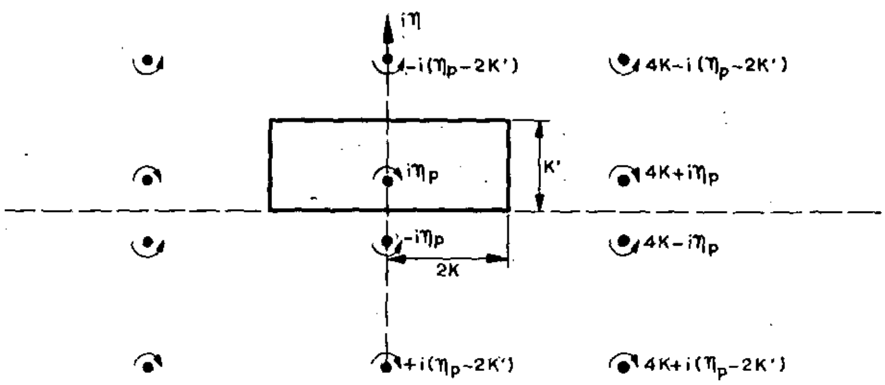

Sketch h: double-periodic fields of vortices.

The vortex row is repeated consecutively with period $4K$ in the ξ-direction. We obtain in this way two double-periodic fields of vortices, viz.: vortices of strength $+1$ in the points $\zeta=+4mK+i(\eta_p+2nK')$ and vortices of strength -1 in the points $\zeta=+4mK-i(\eta_p+2nK')$ with m and n as integers. A vortex strength is defined positively when the rotation of the vortex is in the clockwise sense.

The complex potential of a unit-vortex equals the complex potential of a unit-source multiplied by i.

Hence the complex potential Φ_3 of the vortices located at the points $\zeta = +4mK + \mathrm{i}(\eta_p + 2nK')$ follows immediately from the expression (A.6) for the complex potential of a double-periodic field of sources by replacing in (A.6) ζ_p by $\mathrm{i}\eta_p$ and multiplying the formula with i.

The result is:

$$\Phi_3 = \frac{\mathrm{i}}{2\pi}\left[\ln\left\{\vartheta_1\left(\frac{\pi(\zeta-\mathrm{i}\eta_p)}{4K}\bigg|\frac{K'}{K}\mathrm{i}\right)\cdot\vartheta_4\left(\frac{\pi(\zeta-\mathrm{i}\eta_p)}{4K}\bigg|\frac{K'}{K}\mathrm{i}\right)\right\} + \frac{\pi(\mathrm{i}\eta_p-\zeta)^2}{8KK'}\right] \tag{C.1}$$

The complex potential Φ_4 due to the vortices at the points $\zeta = +4mK - \mathrm{i}(\eta_p + 2nK')$ is obtained from (C.1) by replacing η_p by $-\eta_p$ and multiplying with -1.

The sum of Φ_3 and Φ_4 yields the complex potential of a unit vortex at the point $(0, \mathrm{i}\eta_p)$ in the presence of wing and tunnel walls. Thus

$$\varphi(x, y) = \operatorname{Re}\left[\frac{\mathrm{i}}{2\pi}\left\{\ln\frac{\vartheta_1\left(\frac{\pi(\zeta-\mathrm{i}\eta_p)}{4K}\right)\vartheta_4\left(\frac{\pi(\zeta-\mathrm{i}\eta_p)}{4K}\right)}{\vartheta_1\left(\frac{\pi(\zeta+\mathrm{i}\eta_p)}{4K}\right)\vartheta_4\left(\frac{\pi(\zeta+\mathrm{i}\eta_p)}{4K}\right)} - \pi\frac{\mathrm{i}\eta_p\zeta}{2KK'}\right\}\right]$$

or

$$\varphi(x, y) = -\frac{1}{2\pi}\operatorname{Im}\left\{\ln\frac{\vartheta_1\left(\frac{\pi(\zeta-\mathrm{i}\eta_p)}{4K}\right)\vartheta_4\left(\frac{\pi(\zeta-\mathrm{i}\eta_p)}{4K}\right)}{\vartheta_1\left(\frac{\pi(\zeta+\mathrm{i}\eta_p)}{4K}\right)\vartheta_4\left(\frac{\pi(\zeta+\mathrm{i}\eta_p)}{4K}\right)}\right\} + \frac{\eta_p\xi}{4KK'} \tag{C.2}$$

The function φ must have a periodicity $4K$ and therefore we add the potential of a uniform parallel flow with velocity $-\eta_p/4KK'$; this flow does not violate the condition that the lines $\eta = 0$ and $\eta = \mathrm{i}K'$ have to be streamlines for the velocity field. The potential at the point (x_p, y_p) due to a unit-vortex at the point $(0, \mathrm{i}\eta)$ in the presence of wing and tunnel walls becomes finally:

$$\varphi(x_p, y_p) = -\frac{1}{2\pi}\operatorname{Im}\left\{\ln\frac{\vartheta_1\left(\frac{\pi(\zeta_p-\mathrm{i}\eta)}{4K}\right)\vartheta_4\left(\frac{\pi(\zeta_p-\mathrm{i}\eta)}{4K}\right)}{\vartheta_1\left(\frac{\pi(\zeta_p+\mathrm{i}\eta)}{4K}\right)\vartheta_4\left(\frac{\pi(\zeta_p+\mathrm{i}\eta)}{4K}\right)}\right\} \tag{C.3}$$

By aid of (A.9) and (A.10) this expression may be reduced to

$$\varphi(x_p, y_p) = -\frac{1}{2\pi}\operatorname{Im}\left\{\ln\frac{\operatorname{sn}\frac{\zeta_p-\mathrm{i}\eta}{2}}{\operatorname{sn}\frac{\zeta_p+\mathrm{i}\eta}{2}} - 2\int_{(\zeta_p-\mathrm{i}\eta)/2}^{(\zeta_p+\mathrm{i}\eta)/2} Z(t)\,\mathrm{d}t\right\} \tag{C.4}$$

which is the same as formula (4.21).

APPENDIX D

Determination of the velocity component u_2 on the wing and the velocity component v_2 in the wake

D.1 *The velocity component u_2 on the wing*

The potential due to the vortices in the wake has been given by formula (4.22)

$$\varphi_2(x_p, y_p) = +\frac{hk}{\pi^2}\mathrm{i}\int_0^{K'}\gamma_T(\eta)\operatorname{Im}\left\{\ln\frac{\operatorname{sn}\frac{\zeta_p-\mathrm{i}\eta}{2}}{\operatorname{sn}\frac{\zeta_p+\mathrm{i}\eta}{2}} - 2\int_{(\zeta_p-\mathrm{i}\eta)/2}^{(\zeta_p+\mathrm{i}\eta)/2} Z(t)\,\mathrm{d}t\right\}\operatorname{sn}\mathrm{i}\eta\,\mathrm{d}\eta \tag{D.1}$$

Hence

$$\varphi_2(x_p, +0) = +\frac{hk}{\pi^2}\mathrm{i}\int_0^{K'}\gamma_T(\eta)\operatorname{Im}\left\{\ln\frac{\operatorname{sn}\frac{\xi_p-\mathrm{i}\eta}{2}}{\operatorname{sn}\frac{\xi_p+\mathrm{i}\eta}{2}} - 2\int_{(\xi_p-\mathrm{i}\eta)/2}^{(\xi_p+\mathrm{i}\eta)/2} Z(t)\,\mathrm{d}t\right\}\operatorname{sn}\mathrm{i}\eta\,\mathrm{d}\eta \tag{D.2}$$

with $-l < x_p < +l$ and correspondingly $-2K < \xi_p < 0$.

Since

$$\int_{(\xi_p - i\eta)/2}^{(\xi_p + i\eta)/2} Z(t)\,dt = \ln \frac{\theta\left(\dfrac{\xi_p + i\eta}{2}\right)}{\theta\left(\dfrac{\xi_p - i\eta}{2}\right)}$$

it is clear, that

$$\ln \frac{\operatorname{sn} \dfrac{\xi_p - i\eta}{2}}{\operatorname{sn} \dfrac{\xi_p + i\eta}{2}} - 2\int_{(\xi_p - i\eta)/2}^{(\xi_p + i\eta)/2} Z(t)\,dt$$

is purely imaginary.
Thus

$$\varphi_2(x_p, +0) = \frac{hk}{\pi^2}\int_0^{K'} \gamma_T(\eta)\left\{\ln \frac{\operatorname{sn} \dfrac{\xi_p - i\eta}{2}}{\operatorname{sn} \dfrac{\xi_p + i\eta}{2}} - 2\int_{(\xi_p - i\eta)/2}^{(\xi_p + i\eta)/2} Z(t)\,dt\right\} \operatorname{sn} i\eta\, d\eta \tag{D.3}$$

The differentiation to x_p can now easily be performed; applying the operator $-\dfrac{\pi}{2hk}\dfrac{1}{\operatorname{sn}\xi_p}\dfrac{\partial}{\partial \xi_p}$ to the right-hand side of (D.3) and using the addition formulae for the Jacobian elliptic functions, the result turns out to be:

$$u_2(x_p, +0) = -\frac{1}{2\pi}\frac{1}{\operatorname{sn}\xi_p}\int_0^{K'} \gamma_T(\eta)\left\{\operatorname{sn} i\eta \frac{\operatorname{cn} i\eta \operatorname{dn} i\eta + \operatorname{cn}\xi_p \operatorname{dn}\xi_p}{\operatorname{cn}^2 i\eta - \operatorname{cn}^2 \xi_p} - Z(i\eta)\right\}\operatorname{sn} i\eta\, d\eta \tag{D.4}$$

with $-l < x_p < +l$ and correspondingly $-2K < \xi_p < 0$.

D.2 *The velocity component v_2 in the wake*

We obtain $\lim\limits_{\substack{y_p \to +0 \\ x_p > l}} \dfrac{\partial \varphi_2(x_p, y_p)}{\partial y_p}$ by applying again the operator $-\dfrac{\pi}{2hk}\dfrac{i}{\operatorname{sn} i\eta_p}\dfrac{\partial}{\partial \xi_p}$ to the right-hand side of equation (D.1) and passing subsequently to the limit $\xi_p = -0$.

Performing this operation and using again the addition formulae for the Jacobian elliptic functions we get in a quite analogous way as in the previous appendices B.1, B.2 and D.1 the following expression for $v_2(x_p, +0)$.

$$v_2(x_p, +0) = \frac{-i}{2\pi}\frac{1}{\operatorname{sn} i\eta_p}\int_0^{K'} \gamma_T(\eta)\left\{\operatorname{sn} i\eta \frac{\operatorname{cn} i\eta \operatorname{dn} i\eta + \operatorname{cn} i\eta_p \operatorname{dn} i\eta_p}{\operatorname{cn}^2 i\eta - \operatorname{cn}^2 i\eta_p} - Z(i\eta)\right\}\operatorname{sn} i\eta\, d\eta \tag{D.5}$$

with $x_p > +l$ and correspondingly $0 < \eta_p < K'$.

APPENDIX E

The behaviour of the vorticity distribution at infinity

Assume that $\gamma(x) = 0(x^{-\alpha})$ for $x \to +\infty$ (E.1)
From the jet-condition

$$\gamma(x) = c_j l \frac{\partial v(x, 0)}{\partial x}, \quad x > +l \tag{3.11}$$

it follows immediately that

$$v(x) = 0(x^{1-\alpha}) \quad \text{for} \quad x \to \infty \tag{E.2}$$

Since $v(x)$ becomes zero for x going to infinity, we may conclude that $\alpha > 1$.
The downwash in the wake can be expressed on the other hand by the formula

$$v(x) = \frac{1}{2\pi}\int_{-l}^{\infty} \frac{\gamma(\xi)}{\xi - x}\, d\xi \tag{E.3}$$

where the integral has been taken from the leading edge of the wing to infinity.

From the assumption (E.1) it follows, that there exist constants A and N such that we may write in approximation:

$$v(x) = \frac{1}{2\pi}\int_{-l}^{N} \frac{\gamma(\xi)}{\xi - x}\,d\xi + \frac{A}{2\pi}\int_{N}^{\infty} \frac{\xi^{-\alpha}}{\xi - x}\,d\xi$$

and hence

$$v(x) = 0\left(\frac{1}{x}\right) + \frac{A}{2\pi}\int_{N}^{\infty} \frac{\xi^{-\alpha}}{\xi - x}\,d\xi \quad \text{for} \quad x \to \infty \tag{E.4}$$

By aid of the formula:

$$\frac{1}{\xi^{\alpha}(\xi - x)} = \frac{1}{x^{[\alpha]}}\left\{\frac{1}{\xi^{\alpha-[\alpha]}}\left(\frac{1}{\xi - x} - \frac{1}{\xi}\right)\right\} - \frac{1}{x}\sum_{n=0}^{[\alpha]-2} \frac{1}{x^{n}\xi^{\alpha-n}} \tag{E.5}$$

where $[\alpha]$ is the smallest whole number larger than or equal to α, it is clear that

$$v(x) \infty 0\left(\frac{1}{x}\right) + \frac{A}{2\pi}\frac{1}{x^{[\alpha]}}\int_{N}^{\infty} \frac{1}{\xi^{\alpha-[\alpha]}}\left(\frac{1}{\xi - x} - \frac{1}{\xi}\right)d\xi \tag{E.6}$$

Introducing $\xi = xt$

$$v(x) \infty 0(x^{-1}) + \frac{A}{2\pi}x^{-\alpha}\int_{N/x}^{\infty} t^{[\alpha]-\alpha}\left(\frac{1}{t-1} - \frac{1}{t}\right)dt \tag{E.7}$$

The second term of (E.7) tends asymptotically to zero in a similar way as ($x^{-\alpha}\ln x$) when α is an integer, and as ($x^{-\alpha}$), when α is not an integer. Since $\alpha > 1$, it follows from (E.7) that $v(x) \infty 0(x^{-1})$ and using (E.2) we find that $\alpha = 2$. Hence the vorticity distribution behaves at infinity as $0(x^{-2})$.

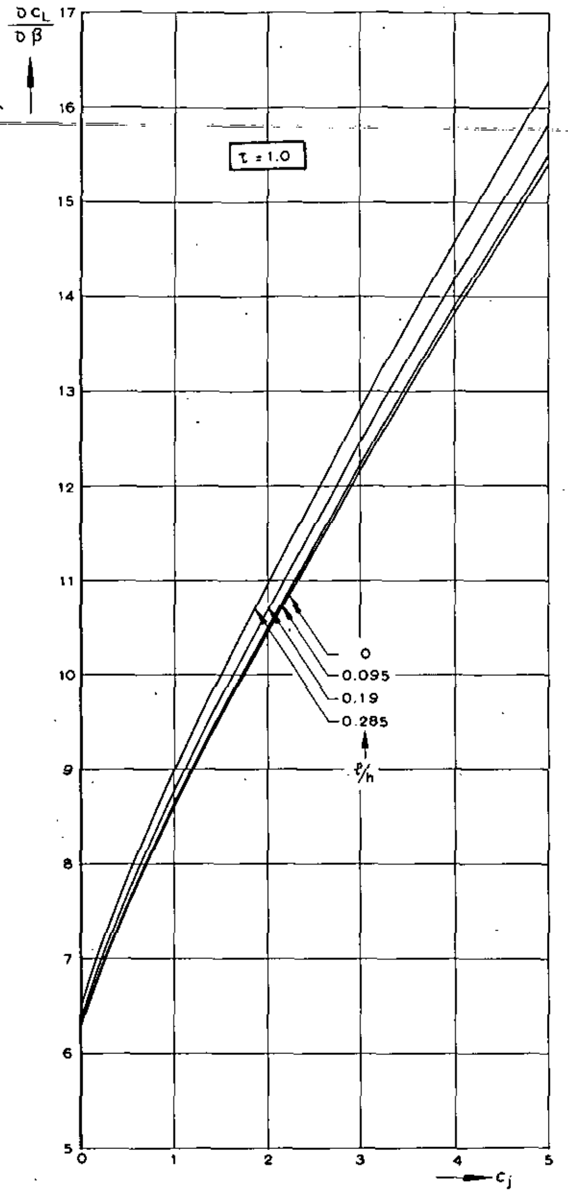

Fig. 1. Lift derivative as function of jet-momentum coefficient.

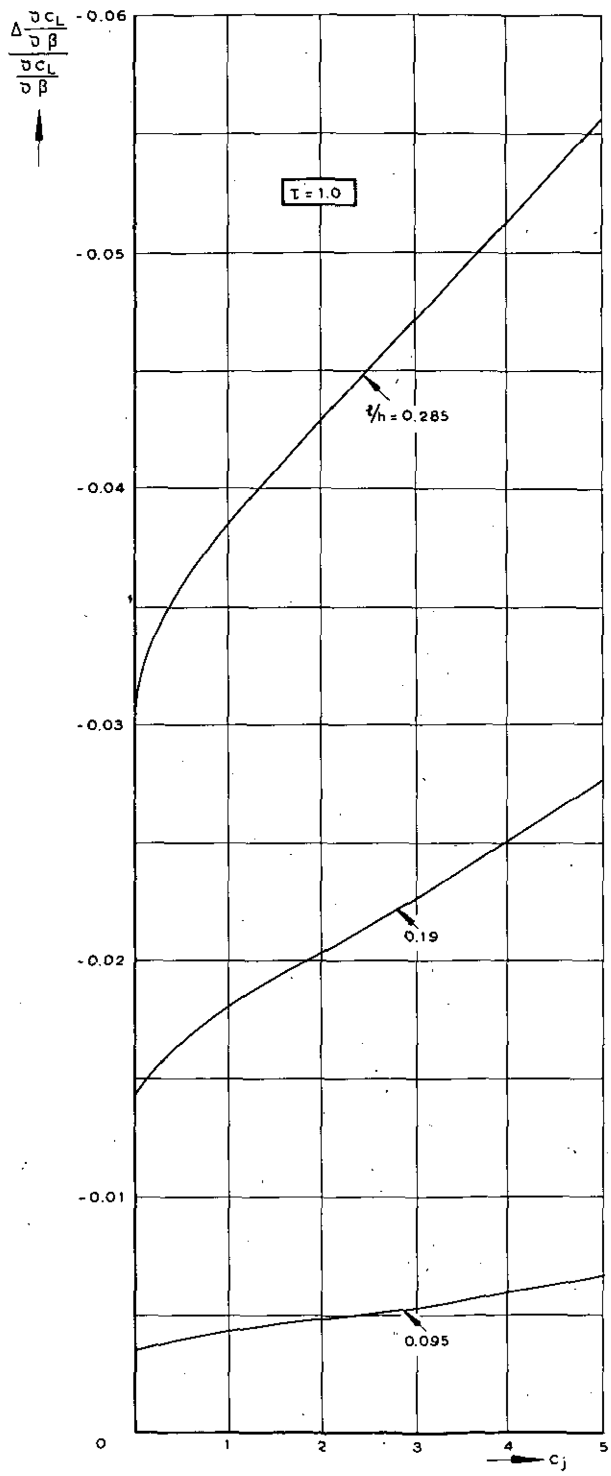

Fig. 2. Tunnel wall corrections for the lift derivative as function of jet-momentum coefficient.

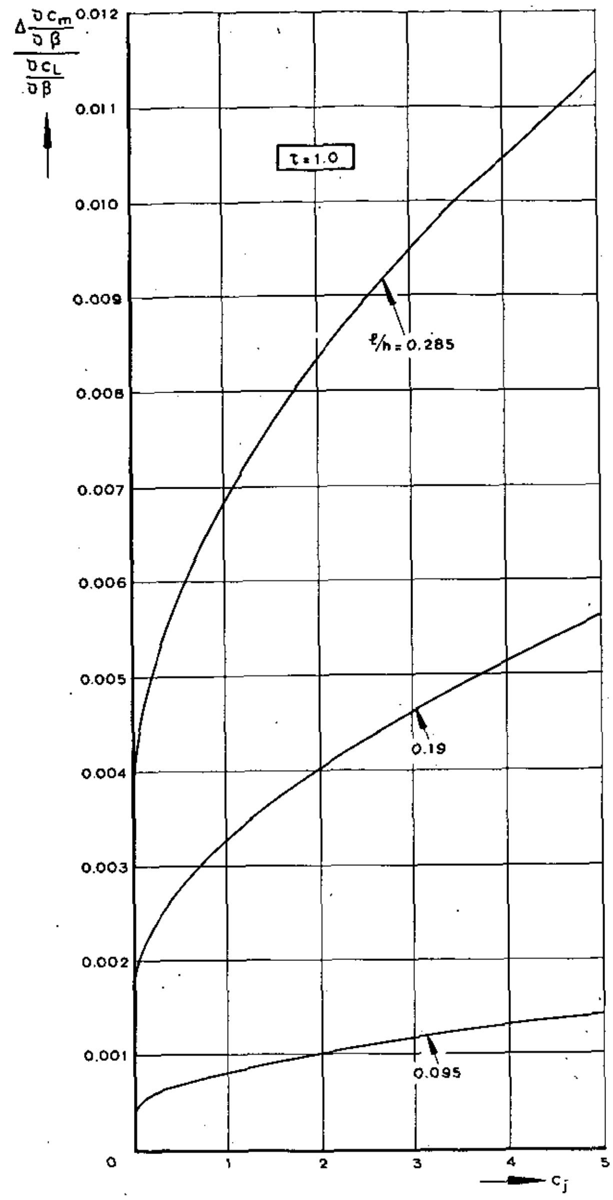

Fig. 4. Tunnel wall corrections for the moment derivative as function of the jet-momentum coefficient.

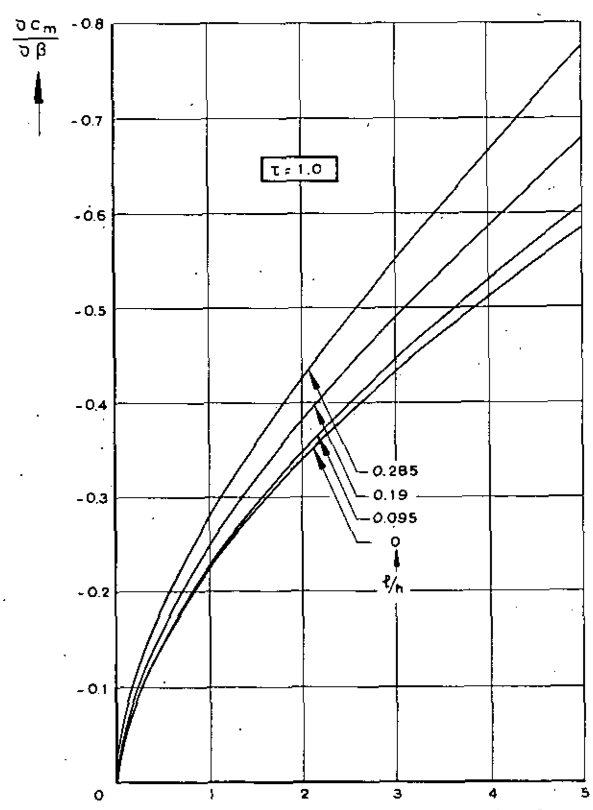

Fig. 3. Moment derivative as function of jet-momentum coefficient.

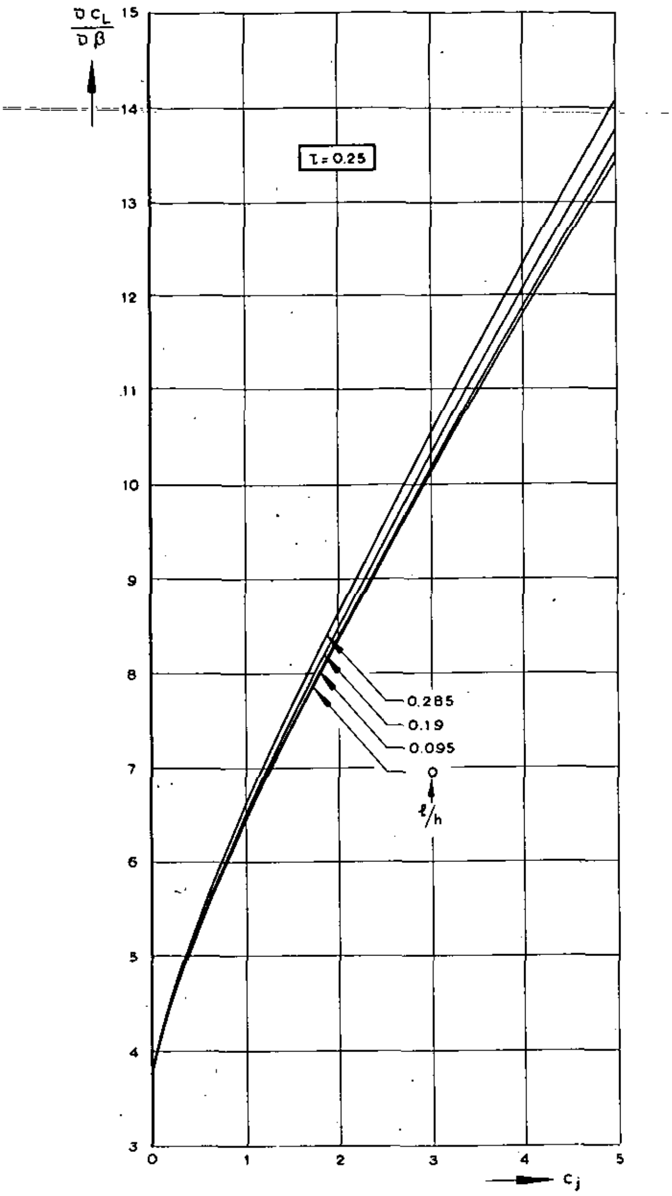

Fig. 5. Lift derivative as function of jet-momentum coefficient.

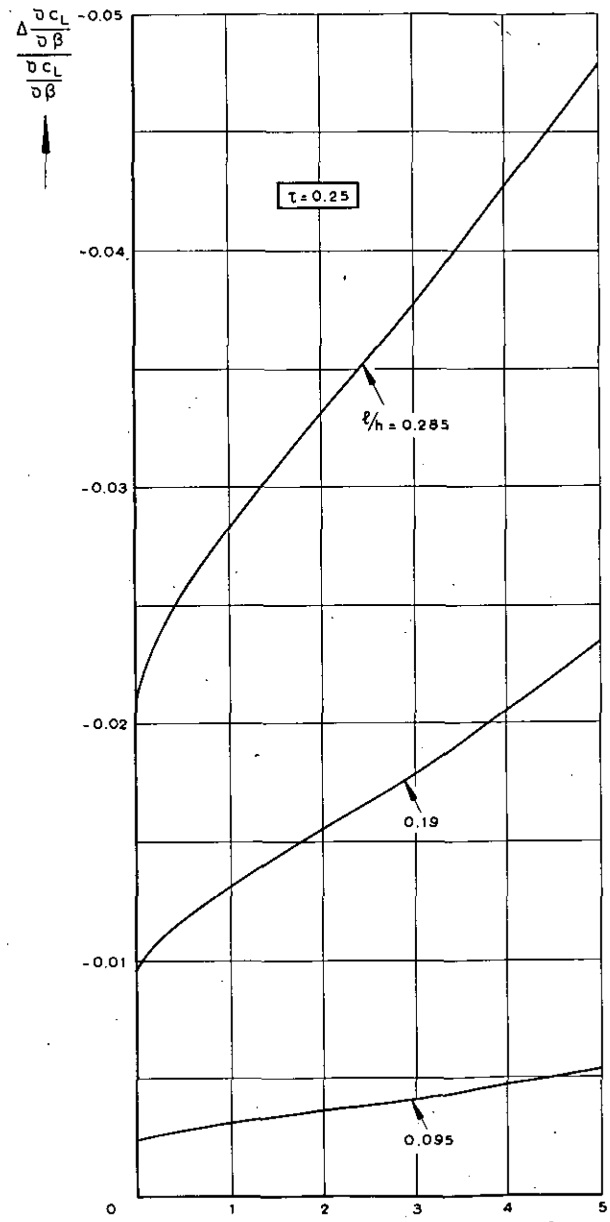

Fig. 6. Tunnel wall corrections for the lift derivative as function of jet-momentum coefficient.

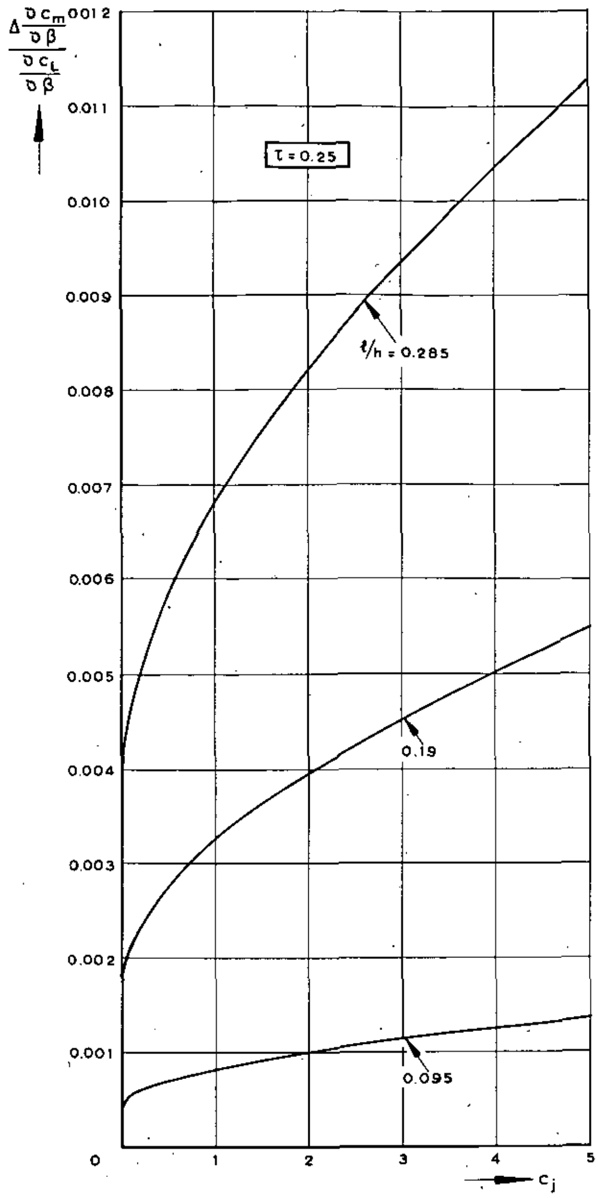

Fig. 8. Tunnel wall corrections for the moment derivative as function of jet-momentum coefficient.

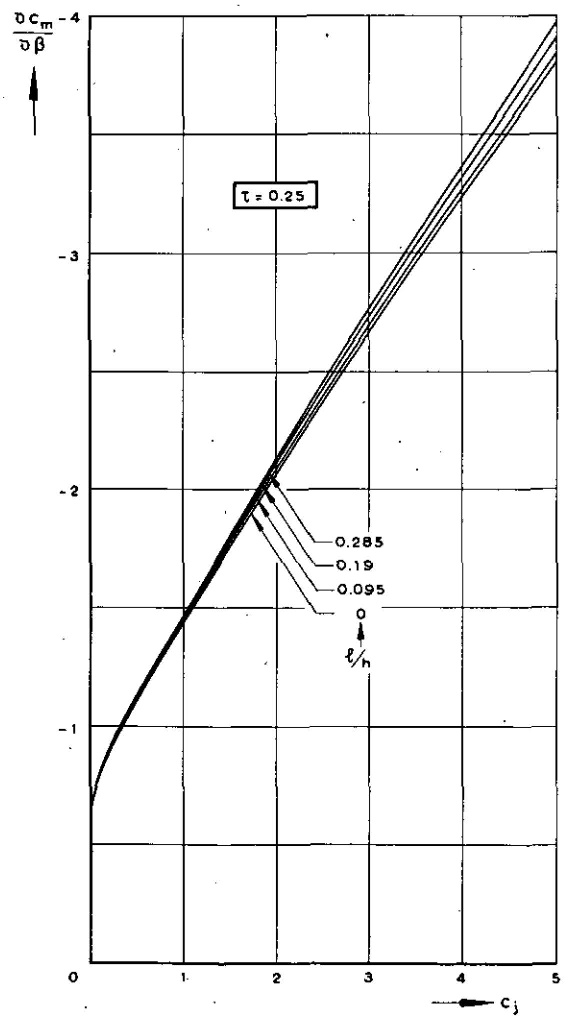

Fig. 7. Moment derivative as function of jet-momentum coefficient.

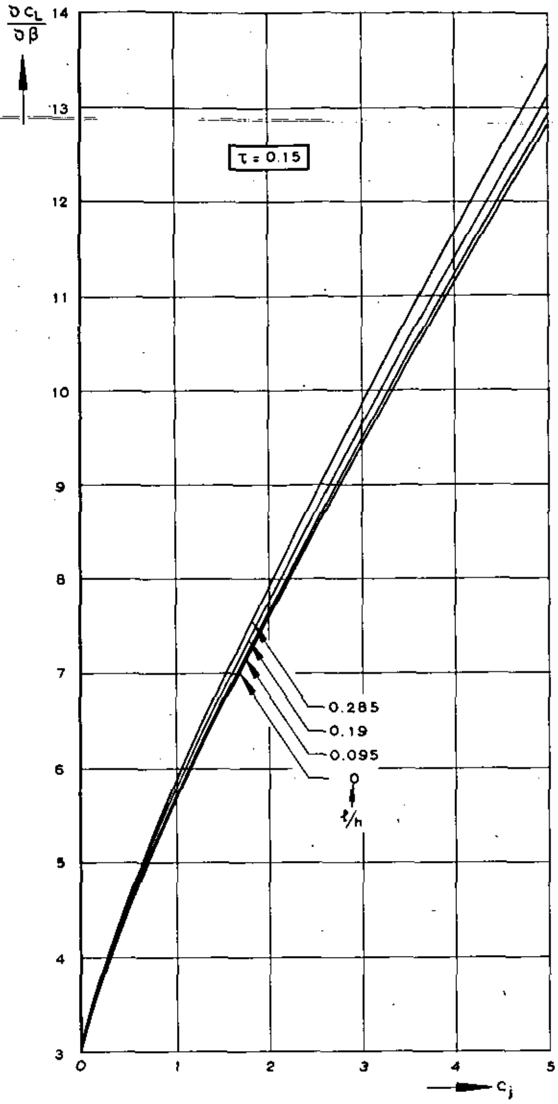

Fig. 9. Lift derivative as function of jet-momentum coefficient.

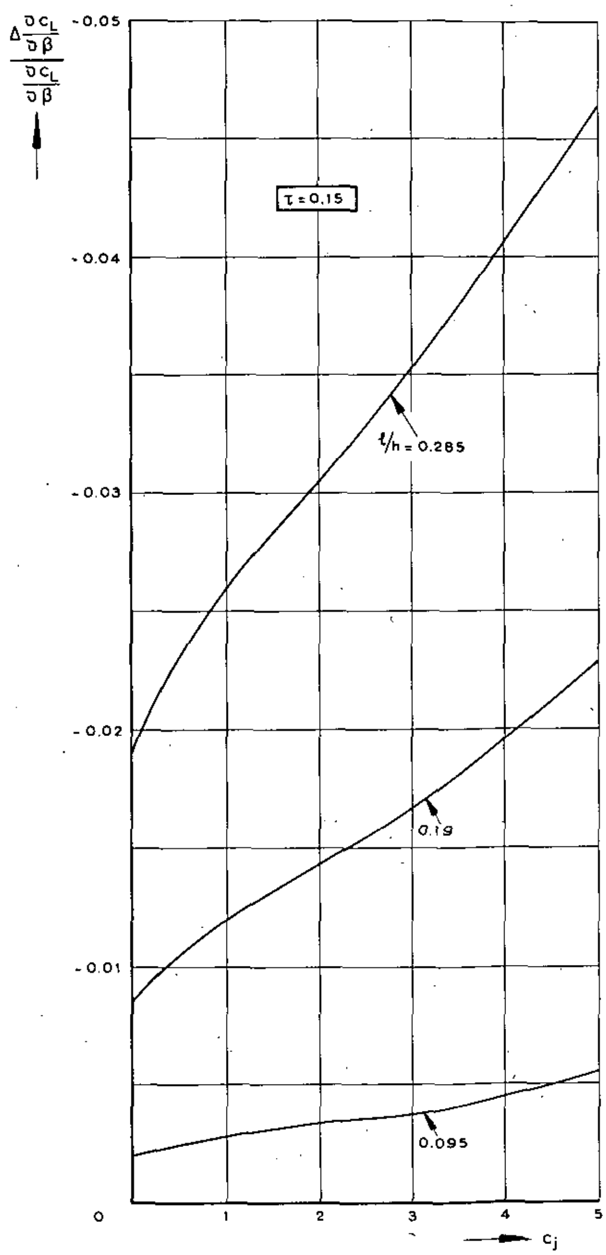

Fig. 10. Tunnel wall corrections for the lift derivative as function of jet-momentum coefficient.

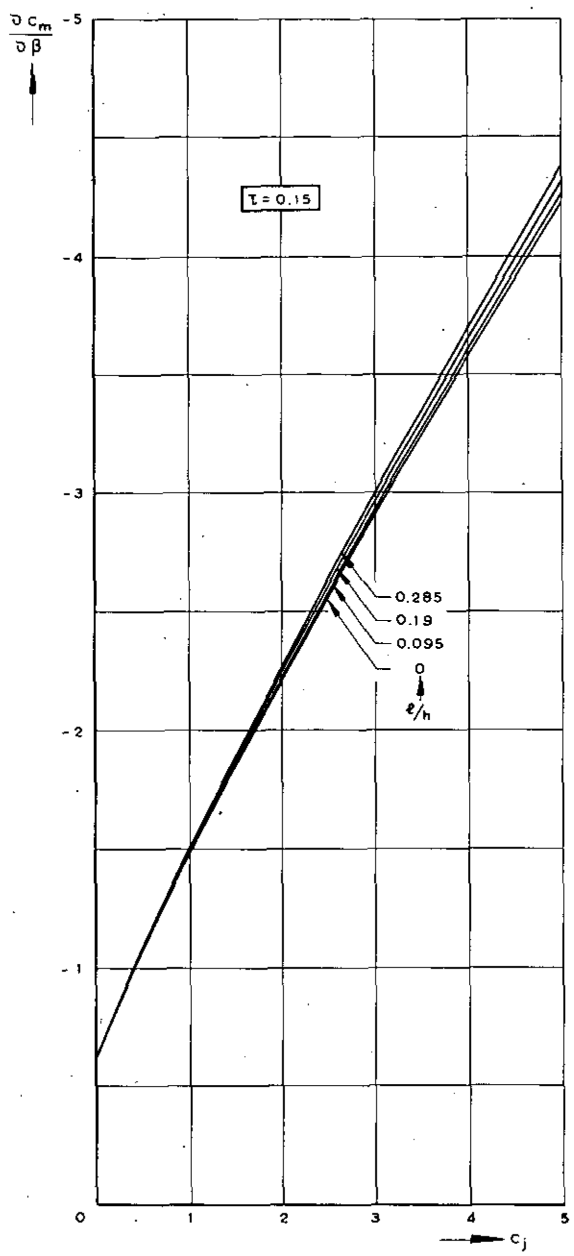

Fig. 11. Moment derivative as function of jet-momentum coefficient.

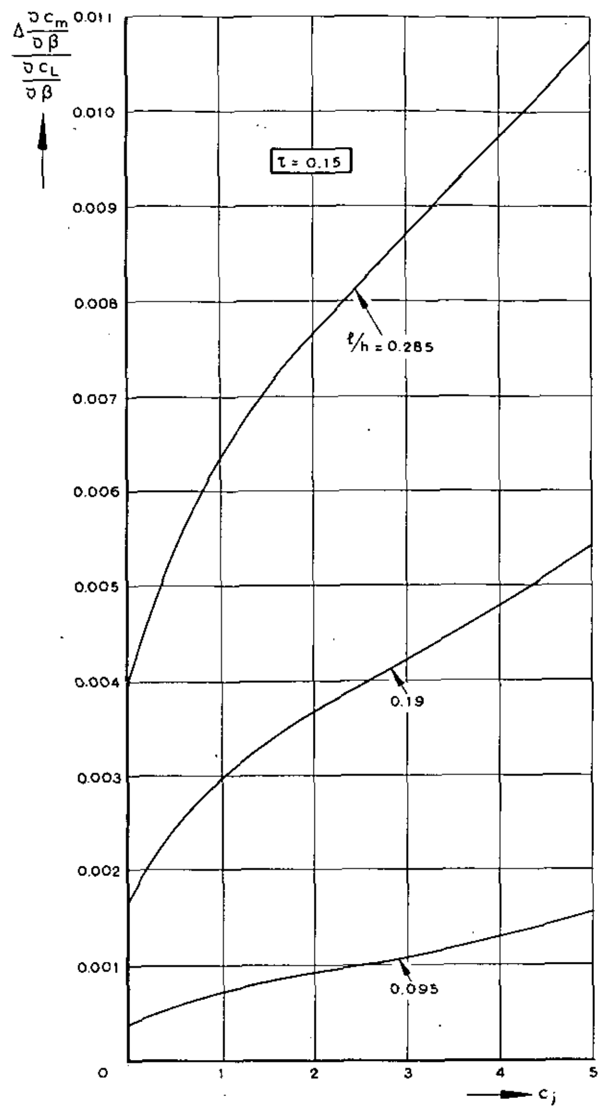

Fig. 12. Tunnel wall corrections for the jet-momentum coefficient.